Gamma rays, cosmic rays and local molecular clouds.

Richardson, K.M.

GAMMA RAYS, COSMIC RAYS AND LOCAL MOLECULAR CLOUDS

by

KENNETH MICHAEL RICHARDSON

A thesis submitted to the University of Durham

for the

Degree of Doctor of Philosophy

April, 1988

ABSTRACT

An estimate of the CO-to-N(H_2) conversion factor X has been obtained using gamma ray data from local molecular clouds at medium latitudes. Evidence is found for the production of low-energy cosmic rays in the cloud environs which complicates the derivation of X, but an interpretation of the results that is consistent with extinction and optically thin molecular emission data is possible and suggests $X \sim (1-2) \times 10^{20}\,\mathrm{mol\,cm^{-2}\,(K\,km\,s^{-1})^{-1}}$. Some variations in cosmic ray intensity not associated with the clouds but in the same line-of-sight may be indicated by the gamma ray analysis.

Differences between the value proposed by COS-B ($X = 2.6 \times 10^{20}$ in the Orion molecular cloud) and the present work are ascribed to their disregard for the production of cosmic rays in or around the clouds.

Several models that might account for the cosmic ray excess are examined in detail. The most promising is that by Morfill (1982) in which electrons are convected into the cloud by Alfvén waves generated by few GeV protons.

The optical and molecular emission data suggest that X is $\sim 1 \times 10^{20}$ in low CO luminosity parts of the cloud and remains $\lesssim 2 \times 10^{20}$ in more luminous regions. At the highest luminosities there is evidence that X declines once again. It is suggested that such a dependence on cloud luminosity arises because X is temperature-dependent, being roughly proportional to T^{-1}. This contention supports the conclusions of Bhat et al. (1986c) that X decreases to about 1×10^{20} in the inner Galaxy, since mean cloud temperatures are higher there than in the solar neighbourhood.

The Massachusetts-Stony Brook virial analysis of inner Galaxy giant molecular clouds is reappraised, leading to $X \lesssim 1 \times 10^{20}$ after allowance has been made for saturation broadening of the CO emission line.

The mass of molecular gas in the inner Galaxy is derived as $\sim 4.5 \times 10^8\,M_\odot$, or about 60% of the HI mass over the same distance interval.

CONTENTS

PREFACE

The work presented in this thesis was carried out between 1986 and 1988 while the author was a research assistant under the supervision of Professor A.W. Wolfendale, F.R.S., in the Physics Department at the University of Durham.

Some of the research was carried out in collaboration with Professor Wolfendale, but the calculations and interpretation are those of the author.

Parts of the thesis have been published as follows:
Richardson K.M. and Wolfendale, A.W., 1988a, Astron. Astrophys., (in press).
Richardson K.M. and Wolfendale, A.W., 1988b, Astron. Astrophys., (in press).
McLaren, I., Richardson, K.M. and Wolfendale, A.W., 1988, Astrophys. J., (in press).

CHAPTER 1
INTRODUCTION

1.1 The CO-to-H_2 Conversion Ratio

The qualitative features of the distribution of molecular gas in the Galaxy are now reasonably well understood, thanks to the efforts of millimetre-wave radio astronomers over the last 15 years. This is of considerable interest for many fields in astrophysics. For example, the distribution of target nuclei in the Galaxy is important in $\gamma-$ray astronomy when trying to unravel the origin of cosmic rays (CR). Similarly, it is now known that star formation takes place almost entirely in Giant Molecular Clouds (GMCs) of about $10^5\,M_\odot$ which contain most of the Galactic molecular material. Understanding the formation of such clouds and the subsequent process of star formation within them or on their periphery are important fields of study in their own right and a necessary pre-requisite for comprehending the structure and evolution of the Galaxy. Furthermore it is clear that GMCs are intimately connected (via star formation and star death) with the processing of the light elements (H, He etc.) into heavier elements. Chemical evolution of the Galaxy is thus closely related to the role GMCs play in Galactic physics. Since they are among the most massive objects in the Galaxy they have a role in determining the velocity dispersion of stars in the Galactic disc, the disruption of open stellar clusters and perhaps the dynamics of the Oort cloud of comets (see Wilkinson, 1987 for an extensive treatment of these topics).

The $J = 1 \rightarrow 0$ rotational transition in ^{12}CO at 112 GHz has been decisive in achieving this understanding. A tracer molecule must be used to infer the large-scale distribution of interstellar molecules because the most common molecule, H_2, is non-polar and difficult to detect directly except in rather unusual conditions. In contrast the millimetre lines of ^{12}CO are easy to detect because it has both high abundance and a weak dipole moment. It is easily excited into emission by collisions with other molecular species in the interstellar medium – principally H_2.

The integrated intensity of the ^{12}CO line along a given line-of-sight is often assumed to be proportional to the column density of molecular hydrogen, $N(H_2)$, in the same direction i.e.

$$N(H_2) = X \int T^r \, dv \text{ molecules cm}^{-2} \tag{1.1}$$

where $T^r(v)$ is the antenna temperature in K at velocity $v\,\mathrm{km\,s^{-1}}$, and the conversion factor X has units molecules $\mathrm{cm^{-2}\,(K\,km\,s^{-1})^{-1}}$. The quantity $\int T^r(v)\,dv$ is henceforth abbreviated to W_{CO} (in $\mathrm{K\,km\,s^{-1}}$).

However, ^{12}CO is usually optically thick, so that equation (1.1) is, a priori, rather unexpected. It is empirically founded on the observation that ^{12}CO (denoted CO) emission tends to mimic that of its isotope ^{13}CO, which is far less abundant and often taken to be optically thin over all but the densest parts of a GMC. Within rather poorly known limits, CO appears to be 'effectively' optically thin! Furthermore the complexity of its line formation process has resulted in considerable disagreement over fundamental issues, such as the mass of gas in the Galaxy. These differences largely centre on the value of the parameter X_{20} $(= X/10^{20})$; estimation of it, using a variety of techniques, forms the major part of the work reported here.

1.2 Previous Results

Figure (1.1) presents the time-history of the parameter X as given by various workers. Many different methods have been used to estimate it, each having its own uncertainties. For example Solomon, Scoville and Sanders (1979), Solomon and Sanders (1980) and

Sanders (1981) used Local Thermodynamic Equilibrium (LTE) arguments (see §2.4) together with assumptions about the abundance of ^{13}CO. Combining this with a $W_{CO}/W_{^{13}CO}$ ratio, which they observed to be roughly constant in the Galactic plane, gave the results shown. Sanders (1981), and Sanders, Solomon and Scoville (1984) (SSS) also derive X_{20} empirically from visual extinction data obtained by star counts and infra-red (IR) measurements in local dark clouds. More recent work by these authors have relied on the virial method for clouds in the inner Galaxy.

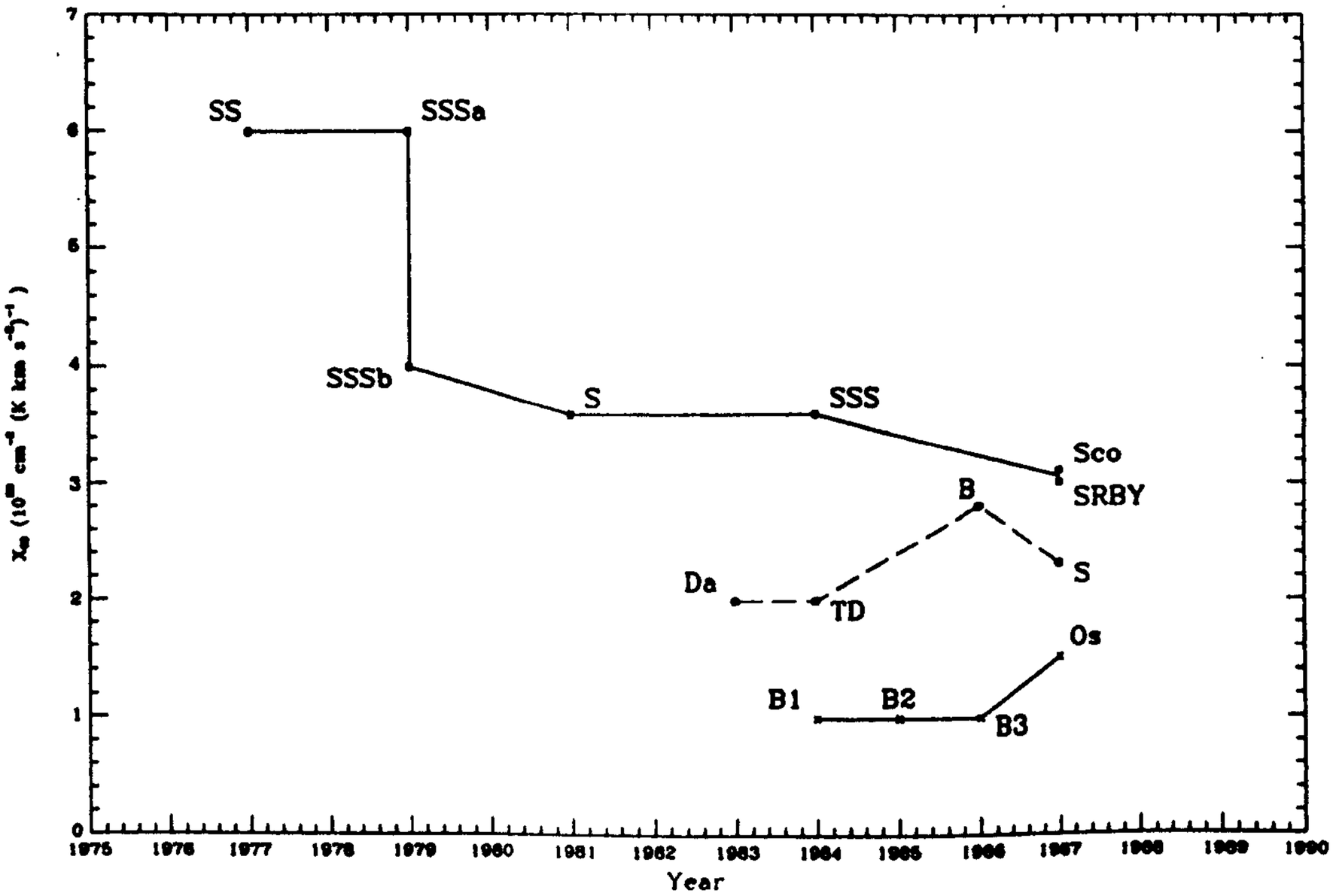

Fig 1.1 The conversion factor X_{20} as estimated by various groups

MSB	Columbia/COS-B	Durham
SS Solomon& Sanders (1980)*	Da Dame (1984)	B1 Bhat et al. (1984)
S Sanders (1981)	S Strong et al. (1987)	Os Osborne et al. (1987)
Sco Scoville et al. (1987)	TD Thaddeus & Dame (1984)	B2 Bhat et al. (1985)
SRBY Solomon et al. (1987)	B Bloemen et al. (1986)	B3 Bhat et al. (1986c)

SSSa Solomon, Sanders & Scoville (1979)
SSSb Solomon, Scoville & Sanders (1979)
SSS Sanders, Solomon & Scoville (1984)
*Conference held 1977.

As can be seen, these early X_{20} estimates were often high. Thus the total mass of molecular gas in the Galaxy deduced was correspondingly large. Fig (1.2) compares the ratio of surface mass densities (in $M_\odot\,pc^{-2}$) of H_2 as a function of R for the various groups in Fig (1.1), using present X_{20} values. It should be noted that though there is general agreement as to the shape of the distribution there are large quantitative differences. These are not entirely due to different values of X_{20} since the azimuthally averaged mid-plane CO emissivities $J_0(z,\mathrm{R})\,\mathrm{K\,km\,s^{-1}\,kpc^{-1}}$ derived by the Columbia and Massachusetts-Stony Brook (MSB) groups are also significantly discrepant. The MSB fit to such an axisymmetric model of Galactic emissivity yields a molecular mass 2.2 times larger than that obtained by Columbia observers in the range $4 < R < 8\,\mathrm{kpc}$. According to Bronfman et al. (1987) this disagreement can be attributed to instrumental calibration (20%), different X values (30%) and different statistical analyses (40%). The most recent work by the Columbia group claims to

be self-consistent in the sense that the observed doubly-integrated CO intensity

$$I(l) = \iint T(l, b, v)\, dv\, db$$

can be recovered from $J(z, \mathrm{R})$. This is not the case for either the MSB analysis or earlier Columbia work, as first pointed out by Bhat et al. (1986c).

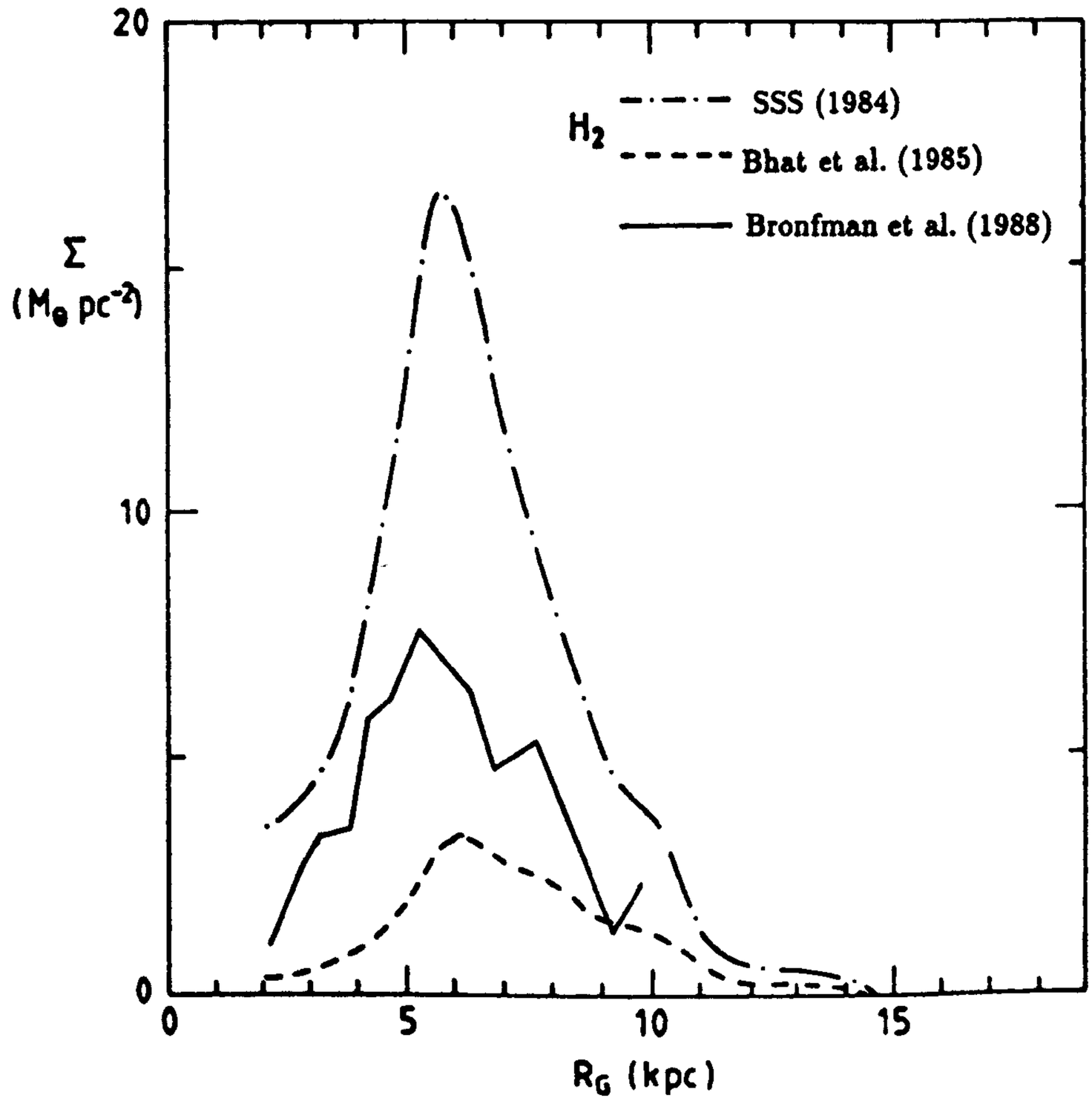

Fig 1.2 Surface density of H_2 as a function of radius from the centre of the Galaxy derived by various groups.

The values of X_{20} denoted COLUMBIA/COS-B in Fig (1.1) are derived from analyses of the diffuse $\gamma-$ray background by the COS-B collaboration. The result is appropriate for GMCs in the inner Galaxy (mainly the molecular ring) and is considerably smaller than the MSB figure. It should be noted that the Columbia observers adopted the COS-B estimate when deriving Σ_{H_2}. The technique and its results will be described in greater detail later; in brief it assumes that the observed $\gamma-$ray intensity is produced by interactions between CRs and nuclei from the Interstellar Medium (ISM) with a small Inverse Compton (IC) contribution. With simplifying assumptions about the large-scale distribution of CRs an estimate of the total gas column density N(H) can be obtained. Providing that the column density of ionised gas along the line of sight is small and CRs are able to penetrate such dense interstellar clouds (see later), then the amount of atomic hydrogen can be estimated from its 21 cm radio emission and X_{20} can be derived from CO data.

However, work at Durham using the same $\gamma-$ray database suggests that even the COS-B figure is too large and $X_{20} = 1.5 \pm 0.5$ is more appropriate for the inner Galaxy. Bhat et al. (1986c), for example, argue that the situation is more complicated than assumed in the COS-B analyses. They find evidence for a decrease in X_{20} toward the inner Galaxy from

X-ray, virial, IR and $\gamma-$ray techniques. For local molecular clouds in the Orion region the COS-B and Durham results are

$E_\gamma > 300\,\mathrm{MeV}$	$X_{20} = 2.6 \pm 1.2$	Bloemen (1985)
$E_\gamma > 100\,\mathrm{MeV}$	$X_{20} = 1.9 \pm 0.3$	Houston and Wolfendale (1985)

The thesis is organised as follows.

- Chapter 2 sketches the theoretical and experimental basis of the work in this thesis.
- Chapter 3 discusses two independent methods and results for a local calibration of the CO-to-H_2 conversion factor.
- Chapter 4 investigates some consequences of the above for models of CR propagation in and near GMCs.
- Chapter 5 uses the virial mass method to determine X_{20} for GMCs in the inner Galaxy.
- Chapter 6 summarises and discusses the present results and examines future prospects.

Chapter 2

THE INTERSTELLAR MEDIUM

2.1 Introduction

This thesis is mainly concerned with the molecular component of the ISM concentrated in massive, cold GMCs. These are, of course, inseparable from the ISM from which they form and into which they presumably disperse. The techniques whereby information can be obtained are varied; several are used in this work in the hope that their assumptions are to some degree independent. It is presumed thereby that if the results agree, more or less, then the assumptions are probably not too important. In order to provide a coherent framework for the separate areas of investigation , a brief review of the ISM together with the theoretical tools used to understand observations of it seems appropriate.

In the so-called three-phase model of McKee and Ostriker (1977) the ISM is composed of atomic (both ionised and neutral), molecular and 'hot' components. The latter is also atomic but originates from the hot gas inside old supernova shells. McKee and Ostriker (1977) argued that the supernova rate was high enough to make this phase dominant i.e., neutral HI was to be found in isolated clouds with dense cores surrounded by warm HI envelopes. Representative parameters of the ISM derived by those authors are given in Table (2.1). However, this picture may be oversimplified; McCray (1987) has suggested, for example, that if clustered type II supernovae from massive population I stars (OB associations) are the driving force for the process, the volume filling fraction of the 'hot' ($T \sim 10^6$ K) component could be less than previously thought. Similarly, Reynolds (1984) claims, on the basis of diffuse H_α emission line data, that a considerable part of the interstellar volume is filled by highly ionised, warm hydrogen. Nevertheless, the McKee-Ostriker model is adopted when required for the remainder of this work and its components are briefly described below.

Table 2.1

	Cloud Core	Cloud Halo		Inter-cloud
	Cold Neutral	Warm Neutral	Warm Ionised	Hot Ionised
H density (cm^{-3})	42	0.37	0.25	0.0035
Ionisation fraction	0.001	0.15	0.68	1.00
Temperature (K)	80	8000	8000	4.5×10^5
Mean radius (pc)	1.6		2.1	
filling factor	0.024	0.05	0.23	0.7

2.2 The Atomic Component

Three phases of atomic gas are thought to exist in approximate pressure equilibrium with the hot component.

(a) Cold ($T \sim 80$ K), neutral HI (CM). The mean pressure from observations of CI fine-structure lines is ~ 3000 cm^{-3} K. Considerable structure is found to exist in this component with, for example, dense ($n \sim 20-50$ cm^{-3}), cold ($T = 30-80$ K) clumps embedded in lukewarm ($T \gtrsim 500$ K), possibly transient envelopes.

(b) Warm ($T \lesssim 8000$ K), neutral HI (WNM). There is no direct evidence of the pressure in this phase.

(c) Warm ($T \sim 8000$ K), ionised H (WIM). The mean pressure from CII fine structure lines is similar to that of the CM.

The CM is probably distributed as discrete clouds ('diffuse clouds') whereas the WNM is seen along most lines of sight. However, 21 cm HI emission does not distinguish between the CM and WNM, and absorption data are needed to identify them. Though vital to an understanding of the physics of the neutral HI component, from a $\gamma-$ray standpoint it is the total column density that is important. Cosmic rays do not distinguish between neutral and ionised gas in $\gamma-$ray production so the WIM may be significant. Unfortunately its distribution is not so well known since, on a large scale, the only information comes from the dispersion measure of pulsar signals, $\mathrm{DM} = \int n_e \, dl$. An estimate of $\overline{n}_e$ requires distances from HI absorption spectra which are only known for a limited number of pulsars. These give $\overline{n}_e \sim .03\,\mathrm{cm}^{-3}$ with a similar figure for the proton density, since most of the interstellar electrons come from the WIM (Heiles and Kulkarni 1987). The scale height is uncertain but is greater than that of pulsars (400 pc); a not unreasonable figure is 1 kpc which gives a vertical column density $N_{\perp,i} \sim 0.5 \times 10^{20}$ and $\Sigma_{\mathrm{H},i} \sim 2\,\mathrm{M}_\odot\,\mathrm{pc}^{-2}$.

Locally the neutral HI and WIM can be approximated by a slab of gas with

$$N_{\mathrm{H}}(b) = N_{\mathrm{H},\perp} / \sin|b|$$

where $N_{\mathrm{H}}(b)$ is the column density toward galactic latitude b and $N_{\mathrm{H},\perp} = < N_{\mathrm{H}}(b) \sin b >$. For the neutral HI, Heiles (1976) gives $N_{\mathrm{H},\perp} \sim 3.7 \times 10^{20}\,\mathrm{cm}^{-2}$ or $\Sigma_{\mathrm{HI}} \sim 5.9\,\mathrm{M}_\odot\,\mathrm{pc}^{-2}$. At least locally, the WIM is a non-negligible part of the atomic component.

The surface density of the neutral HI layer from 21 cm studies in the inner Galaxy is roughly constant for R > 4 kpc and decreases rapidly for R < 4 kpc. Assuming the 21 cm line is optically thin gives $\Sigma_{\mathrm{HI}} \sim 4.5 \times 10^{20}\,\mathrm{cm}^{-2}$ or $\sim 3.6\,\mathrm{M}_\odot\,\mathrm{pc}^{-2}$ (Lockman 1984). This is probably only a good assumption outside the Galactic plane. Kulkarni (1983) estimates an optical depth $\tau \sim 1.25$ so that $\Sigma_{\mathrm{HI}} \sim 6\,\mathrm{M}_\odot\,\mathrm{pc}^{-2}$, comparable to the local value considering the uncertainties. The full width at half maximum is ~ 365 pc and is independent of R. However, in the outer Galaxy, the thickness of the HI layer increases linearly with R, possibly because the stellar density (and therefore potential) decreases rapidly. The total mass of neutral HI in the Galaxy is about $4.8 \times 10^9\,\mathrm{M}_\odot$ (Henderson et al. 1982), with about $1 \times 10^9\,\mathrm{M}_\odot$ lying inside the solar circle (Li et al. 1983).

Within 2 kpc of the sun the mean electron density, ignoring the small contribution from bright HII regions, increases towards the Galactic centre as

$$\overline{n}_e = \frac{.05}{1 + \frac{\mathrm{R}}{\mathrm{R}_\odot}} \tag{2.1}$$

(Lyne et al. 1985). This is to be expected if the WIM is generated by ultra-violet (uv) radiation from hot young stars which are more common in the inner Galaxy. If so, and the trend in equation (2.1) continues into the central regions of the Galaxy, the WIM is even more significant than locally. For this reason the WIM has been invoked to explain the increase in I_γ above expectation from neutral and molecular gas observed at medium latitudes in many regions of the inner Galaxy (Bloemen et al. 1988). However it will probably have little effect on $\gamma-$ray estimates of X_{20} since its spatial distribution is quite unlike that of the molecular gas.

2.3 The Molecular Component

2.3.1 The distribution of H_2 in the Galaxy

Both local and more distant inner Galaxy molecular clouds have been studied in detail in the 2.6 mm CO line. Many of the qualitative features of its large-scale distribution are now reasonably well known. The early surveys of Burton et al. (1975) and Scoville and Solomon (1975) revealed that the radial (i.e., azimuthally averaged) distribution of CO emission had the following features.

- A large maximum in the Galactic centre.
- Weak emission from 0.5 to 4 kpc.
- A broad peak between 4 and 8 kpc.
- Little emission beyond the solar circle.

It was noted that such features were also seen in so-called extreme population I objects as revealed by the large scale distribution of HII regions, supernova remnants, pulsars, $\gamma-$rays etc. However it is quite different from the radial distribution of neutral HI as noted above. Subsequent work in CO and ^{13}CO confirmed the early work and established that the vertical scale height of the molecular gas corresponded roughly to that of the extreme population I objects. (e.g., Cohen and Thaddeus 1977; Burton and Gordon 1978; Cohen et al. 1980; Sanders et al. 1984; Bronfman et al. 1987). It was further shown that most of the molecular mass was contained in molecular clouds of $\sim 10^5 - 3 \times 10^6\,\mathrm{M}_\odot$ (e.g., Solomon et al. 1979; Solomon and Sanders 1980; Stark 1979; Liszt et al. 1981; Dame 1984; Sanders et al. 1985).

Several authors have derived a mass spectrum $\frac{dN}{dM} \propto M^{-3/2}$ (e.g., Dame 1984; Sanders et al. 1985; Solomon et al. 1987) which puts most molecular mass into the largest clouds. Dame et al. (1986), however, argue that this could be misleading because the cloud samples are luminosity biased. Nevertheless, there is a consensus that GMCs of mass $\gtrsim 10^5\,\mathrm{M}_\odot$ contain at least 50% of the molecular gas mass.

Compared to diffuse HI clouds, GMCs are dense and cold. A typical mean density for a $5 \times 10^5\,\mathrm{M}_\odot$ cloud is $n_{\mathrm{H_2}} \sim 100\,\mathrm{cm}^{-3}$ with a dependence on cloud size (R_c) such that $n_{\mathrm{H_2}}(R_c) \propto R_c^{-1}$. Mean cloud kinetic temperatures around 10 K seem appropriate although some variation is found depending on whether the cloud has a heat source (or sources) embedded in it. Solomon and Sanders (1985) separated the inner Galaxy discrete features they observed into a 'cold cloud' and 'warm cloud' population with $T = 10$ K as the dividing line. Interestingly, they found that their 'hot clouds' were more clumped in the longitude-velocity ($l - v$) plane than was the case for their 'cold clouds'. They argued that the 'hot clouds' were probably more confined to spiral arms than the 'cold cloud' population, particularly since the distribution of HII regions chosen from the Downes et al. (1980) survey was rather similar to that of the 'hot clouds'. Scoville et al. (1987) arrive at much the same conclusion.

GMCs appear clumpy even in CO maps. This property had long been suspected since the mean cloud densities observed were often below the minimum required for the collisional excitation of CO ($n \sim 100\,\mathrm{cm}^{-3}$; Blitz 1987). Recent studies of local clouds in ^{13}CO show structure down to the resolution of the telescope. Such granularity is usually invoked when trying to understand why CO emission appears to be optically thin. Thus $T(\mathrm{CO})/T(^{13}\mathrm{CO})$ is often observed to be ~ 5.5 yet the abundance ratio [CO]/[^{13}CO] is usually taken to be ~ 40 in the ISM (c.f. ~ 80 terrestrially). A common model for CO emission from GMCs is of small, optically thick, unresolved clumps that do not shadow each other either spatially or in velocity. However, a satisfactory quantitative analysis of this process has yet to be done.

The internal dynamics of molecular clouds are not well understood. Linewidths for CO averaged over a typical GMC are supersonic ($\sim 5 - 10\,\mathrm{km\,s^{-1}}$) and are much greater than the thermal linewidth of a gas at 10 K (a few tenths of a $\mathrm{km\,s^{-1}}$). There is a well established power-law correlation between cloud size and linewidth, seemingly independent of the line used. Myers and Goodman (1988b) find, for a large range of cloud sizes and using several emission lines,

$$\sigma_{NT} \propto R_{FWHM}^{0.5}$$

where σ_{NT} is the non-thermal velocity dispersion and R_{FWHM} is the cloud size (Full-Width-at-Half-Maximum). Many other authors find similar relations although the details are almost certainly dependent on the line used and definition of cloud size. Furthermore, the method of background subtraction is probably important, particularly for inner Galaxy clouds (see §5.3). Myers and Goodman suggest the correlation arises because the clouds are approximately virialised and magnetically supported against gravity. Other explanations for these observations are discussed in §5.3. Finally, the association of young stars, protostars and other signatures of star forming activity with molecular clouds over the last 10 – 15 years have established GMCs as the major sites of star formation in the Galaxy.

These GMC properties are broadly confirmed by studies of more local molecular material (e.g., Blitz 1978, 1980) where confusion with intense inner Galaxy background emission and instrumental resolution effects are less severe. Furthermore, comparison with extinction measurements of gas column densities are possible for those clouds within a few hundred parsecs. Blitz (1987) has summarised the characteristics of GMCs within 3 kpc – Table (2.2) lists their average properties. In addition

(i) All OB associations form from GMCs. Within 3 kpc of the sun only one GMC has been found without traces of star formation (Maddalena 1986).

(ii) GMCs are surrounded by warm HI envelopes which may contain a comparable mass of gas. This could be partly due to photodissociation and heating of the outer layers of the GMC (Blitz and Thaddeus 1980; Terndrup 1981). For example, Heiles and Kulkarni (1987) give typical parameters for the HI envelopes around Taurus, Perseus and Orion as $N(H) \sim 1.0 \times 10^{21}\,\mathrm{cm^{-2}}$, mass $\sim 1.0 \times 10^5\,M_\odot$ and linear diameter ~ 120 pc.

Table 2.2

Mass	$1 - 2 \times 10^5\ M_\odot$
Mean diameter	45 pc
Projected surface area	$2.1 \times 10^3\,\mathrm{pc^2}$
Volume	$9.6 \times 10^4\,\mathrm{pc^3}$
Volume averaged $n(H_2)$	$\sim 50\,\mathrm{cm^{-3}}$
Mean $N(H_2)$	$3 - 6 \times 10^{21}\,\mathrm{cm^{-3}}$
Local surface density	$\sim 4\,\mathrm{kpc^{-2}}$
Mean separation	~ 500 pc

Evidence of the considerable internal structure of molecular clouds is to be found in ^{13}CO surveys of Orion by Bally et al. (1987) and the Rosette GMC by Blitz and Stark (1986). The latter have demonstrated that at least 60% and perhaps most of the gas in the Rosette molecular cloud (RMC) exists in very dense clumps. A density enhancement of about 100 – 500 times that of a tenuous interclump gas seems likely. Even clumps at the low mass end have an overdensity of around 100, though are probably not gravitationally bound. The

clump mass spectrum $\frac{dN}{dM_c} \propto M_c^{-1.54}$ for $M_c \gtrsim 20\,M_\odot$ suggests (see Table 2.3) that most of the mass is in the largest clumps. Using the mean density of the Rosette ($\bar{n} \sim 25\,cm^{-3}$; Blitz and Thaddeus 1980) and the mean clump density $\overline{n}_c$ from Table (2.3) gives a volume filling factor of ~ 0.03. Of considerable interest for later discussion of the virial theorem is the internal velocity field of the Rosette molecular cloud. Blitz and Stark find the mean clump-to-clump velocity dispersion and clump linewidth to be about $2\,km\,s^{-1}$, though each depends on the clump mass in a different way.

Table 2.3

N	RANGE $M_\odot$	$\langle M \rangle$ $M_\odot$	σ_v km s^{-1}
33	M < 100	59	4.0
26	100 < M < 300	171	3.7
19	300 < M < 1000	524	2.3
8	1000 < M	1650	1.7

Dame et al. (1987) use the first comprehensive, wide-latitude CO survey of the Milky Way to obtain, for molecular gas within 1 kpc of the sun, a mean surface density of Σ_{H_2} and half-thickness $z_{1/2}$ of

$$\Sigma_{H_2} \sim 1.3\,M_\odot\,pc^{-2}$$
$$z_{1/2} \sim 87\,pc.$$

The scale height is comparable to the inner Galaxy analyses of Bronfman et al. (1987) and SSS, and the analysis of the outer Galaxy Carina clouds by Grabelsky et al. (1987) after extrapolation to the solar circle. When corrected for the different X_{20} value preferred here (1.5 against 2.7 used by Dame et al.), the mean local surface density and volume densities are $\Sigma_{H_2} \sim 0.7\,M_\odot\,pc^{-2}$ and $n_{H_2} \sim .05\,mol\,cm^{-3}$.

2.3.2 Physical Conditions in Molecular Clouds

Molecules in the ISM are dissociated primarily by uv radiation from hot young stars. Molecular clouds thus form when the dust opacity becomes sufficiently great to absorb most of the background stellar uv photons. Furthermore, the dominant molecular species – H_2 – is formed on grains because its gas phase reactions are far less efficient under interstellar conditions . The transition from atomic to molecular form seems to be abrupt. Self-shielding of the inner regions of the cloud by its outer layers may be responsible for this. Locally, H_2 and CO are usually found only in clouds with $A_v \gtrsim 0.5\,mag$ (Bally and Langer 1982), which coincides with the condition for a strongly self-gravitating cloud i.e., a gravitational potential energy greater than the external pressure (see Elmegreen 1985). Exclusion of background starlight from the cloud interior removes the heat input to the cloud from the photoelectric effect and from uv ionisation of weakly bound atoms. Thus the temperature drops from $\sim 80\,K$ typical of a diffuse HI cloud to $\sim 10\,K$ inside an inactive cloud.

The formation and composition of a molecular cloud depend on at least three properties of the ISM in which it is immersed.

- Heavy element abundance since:

  (a) Dust is required for shielding molecules from photodissociating stellar radiation.

(b) The molecular formation rate (H_2) is proportional to the surface area of grains or (CO) to the relative densities of C and O.

(c) CO is often the dominant cooling agent in GMCs and the molecular formation rate depends on temperature.

(d) The stellar Initial Mass Function and atmospheric opacity may be sensitive to heavy element abundance with consequences for the external radiation field.

- The local stellar density, which determines the uv flux incident on the cloud.
- The local CR flux. Low energy cosmic rays may play a significant role in the ionisation of atomic and molecular species within the cloud. Thus the local magnetic field, supernova rate etc. could also be important.

In addition H_2 is more strongly self-shielding than CO. Variations in the above properties of the local ISM are likely to affect each molecule differently. Thus, the relative amounts of H_2 and CO will depend in a complicated way on their local environment. In regions of the Galaxy (or in external galaxies) where conditions are far different from solar, the local conversion factor X_{20} might be quite inappropriate (see e.g., Maloney and Black 1988).

Evidence that this is the case in the Galaxy has been presented by Bhat et al. (1986c) who found that X_{20} decreased towards the inner Galaxy, though it was not clear whether this was mainly a metallicity or temperature effect. It is suggested later that temperature plays some role (see §3.4.1) and, furthermore, the high abundance of CO might make its emission relatively insensitive to moderate variations in metallicity or gas/solid phase abundances. Nevertheless, it is unlikely a priori that Nature has conspired in such a complicated way to keep the mean $N(H_2)/W_{CO}$ ratio constant throughout the Galaxy. Since the proof of the pudding is in the eating, the line formation process is now examined to enable closer examination of the apparent 'optical-thinness' of CO emission in later chapters. The treatment follows that given by Spitzer (1978) and Kutner (1984).

2.3.3 Line Formation

CO is the most abundant molecule after H_2 and at least 10 times more abundant than any other molecule. The $J = 1 \rightarrow 0$ transition at 115.27 GHz corresponds to a temperature

$$T = \frac{h\nu_{01}}{k} \sim 5.5\,\mathrm{K} \tag{2.2}$$

which is less than the kinetic temperature typically found inside GMCs. Therefore its higher rotational states are easily populated. In addition, it has a small dipole moment so that its rotational transitions are readily excited into emission above the microwave background even at modest gas densities. However, though CO is abundant and easily detected, its emission is also optically thick. The emergent intensity from a dense, uniform molecular cloud is not linearly related to the number of molecules in the telescope beam.

A. Radiative Transfer

Consider the specific intensity I_ν (in $\mathrm{erg\,cm^{-2}\,s^{-1}\,sr^{-1}\,Hz^{-1}}$) absorbed by a very thin slab of gas. The optical depth τ_ν can be defined so that its increment $d\tau_\nu$ is given by

$$d\tau_\nu = -\frac{dI_\nu}{I_\nu} \tag{2.3}$$

The absorption coefficient κ_ν is the optical depth per unit length so that for z perpendicular to the slab surface

$$d\tau_\nu = \kappa_\nu dz. \tag{2.4}$$

Since the gas will also emit radiation, the total change in intensity is

$$dI_\nu = -I_\nu \kappa_\nu dz + j_\nu dz$$

where j_ν (in $\mathrm{erg\,cm^{-3}\,s^{-1}\,sr^{-1}\,Hz^{-1}}$) is the emissivity coefficient. Therefore

$$\frac{dI_\nu}{d\tau_\nu} = -I_\nu + S_\nu \tag{2.5}$$

where $S_\nu \equiv j_\nu/\kappa_\nu$ is the source function. Integration of equation (2.5) gives

$$I_\nu = I_\nu(0)\mathrm{e}^{-\tau_\nu} + \int_0^{\tau_\nu} d\tau'_\nu\, S_\nu \mathrm{e}^{-(\tau_\nu - \tau'_\nu)}. \tag{2.6}$$

The first term corresponds to absorption of radiation incident on the slab of intensity $I_\nu(0)$ while the second describes emission at τ'_ν which 'sees' an optical depth $\tau_\nu - \tau'_\nu$ to the surface of the cloud.

In radio astronomy it is conventional to define a brightness temperature T_b

$$I_\nu = B_\nu(T_b),$$

and a radiation temperature T^r

$$T^r \equiv \frac{c^2}{2\nu^2 k} I_\nu.$$

$B_\nu(T_b)$ is the Planck distribution function appropriate for blackbody radiation. If the populations of the various excited states are in thermal equilibrium, they will obey the Boltzmann law i.e., for levels i, j with $E_j > E_i$

$$\frac{n_j}{n_i} = \frac{g_j}{g_i} \exp\left(-h\nu_{ij}/kT\right). \tag{2.7}$$

In general, this will not be the case. The concept of excitation temperature may then be useful to describe the departure from thermal equilibrium. This is defined by

$$\frac{n_j}{n_i} = \frac{g_j}{g_i} \exp\left(-h\nu_{ij}/kT_x\right) \tag{2.8}$$

where g_i and g_j are the statistical weights of the i, j rotational states. Note that T_x can in general be different for each excited state.

The higher rotational levels of CO are populated by collisions (mainly with H_2) or by the radiation field in the cloud via emission and absorption of line photons. The excitation temperature describes the coupling of the molecule to these sources. As n_{H_2} increases and collisions begin to dominate $T_x \rightarrow T$ as expected for a Boltzmann distribution at temperature T. Conversely, at low n_{H_2}, $T_x \rightarrow T_b$. It can be shown that if N_i is the column density of molecules in state i and μ_{ij} is the dipole matrix element, then

$$\int \tau_\nu \, d\nu = \frac{8\pi^3 \nu_{ij}}{3hc} |\mu_{ij}|^2 \left[1 - \exp\left(\frac{-h\nu_{ij}}{kT_x}\right)\right] f_i N_{tot} \tag{2.9}$$

where $N_i = f_i N_{tot}$. Assuming j_ν and κ_ν have the same frequency profiles

$$j_\nu/\kappa_\nu \equiv S_\nu = B_\nu(T_x)$$

so that equation (2.6) becomes

$$\Delta T_\nu^r \equiv T_\nu^r - T_0^r = (T_x^* - T_0^r)\left(1 - e^{-\tau_\nu}\right) \tag{2.10}$$

for

$$T_x^* = \frac{c^2}{2\nu^2 k} B_\nu(T_x).$$

Clearly, solving equations (2.9) and (2.10) pose formidable difficulties; an estimate of N_{tot} depends on knowing the physical conditions inside the cloud a priori. Under conditions when radiative and collisional excitation are comparable the equations of radiative transfer and excitation, involving many different levels, are coupled. As an example, for $\tau \sim 1$, a photon emitted by one molecule can be absorbed by another in a phenomenon known as photon trapping. This increases the excitation temperature for that transition since the photon remains 'trapped' in that excited state. In effect, $T_x \rightarrow T$ (thermalises) at lower densities than when there is no trapping. Both high n and τ can therefore produce thermalisation. A useful concept in this case is that of the thermalisation length, which is the mean τ between creation of a photon and its destruction by collisional de-excitation. Clearly if $\tau > \tau_{th}$, most emitted photons do not escape and the level populations tend to Boltzmannian i.e., thermalisation. CO has high abundance and a small τ_{th} so that its excitation temperature is often equal to the kinetic temperature.

However the excitation temperature for ^{13}CO and CO can be quite different. In the former case, assuming its emission is optically thin and noting that the spontaneous decay rate for the transition $J+1 \rightarrow J$ is $A_{J+1,J} \propto J^4/(2J+1)$, then $A_{2,1} \sim 10A_{1,0}$. Collisional de-excitation rates for these levels are roughly equal so that the $J = 1$ level becomes relatively overpopulated and $T_x(1,0) > T_x(2,1)$ (see equation 2.8). However, the much higher optical depth of CO emission suggests that both transitions will be thermalised and that $T_x(\mathrm{CO}) \neq T_x(^{13}\mathrm{CO})$. This must be borne in mind in the following discussion of LTE.

B. Local Thermodynamic Equilibrium

Observations do not yet constrain the problem sufficiently to allow a comprehensive solution of the problem, though useful attempts have been made (see, for example, Kutner and Leung 1985; Kwan and Sanders 1986; Maloney and Black 1988). The difficulties are compounded in GMCs which are very complex objects. There are several alternatives; one is to make the above equations more tractable by assuming LTE. In particular

(i) $T_x = T$ for both CO and ^{13}CO (T is the kinetic temperature here). This effectively decouples the equations of radiative transfer and excitation.

(ii) CO is optically thick ($\tau^{12} \gg 1$) but ^{13}CO is optically thin ($\tau^{13} < 1$).

(iii) Only the ground (0) and first excited rotational states (1) are important.

At millimetre wavelengths, the only important continuum source (upon which the line emission sits) is the 2.7 K microwave background (MWB), so that equation (2.10) becomes

$$T_x^* = \frac{5.5}{\ln\left[1 + \frac{5.5}{\Delta T^r(\mathrm{CO}) + 0.82}\right]}. \tag{2.11}$$

and

$$\tau_\nu(^{13}\mathrm{CO}) = -\ln\left[1 - \frac{\Delta T^r(^{13}\mathrm{CO})}{\Delta T^r(\mathrm{CO})}\right]. \tag{2.12}$$

Solving for $N(^{13}\mathrm{CO})$ from equation (2.9) gives

$$N(^{13}\mathrm{CO}) = \frac{3hf_0}{8\pi^3|\mu_{01}|^2} \int \frac{\tau^{13}(v)\,dv}{[1 - \exp(-h\nu_{01}/kT_x)]} \tag{2.13}$$

where

$$\int \tau_\nu^{13}\, d\nu = \frac{\nu_{01}}{c} \int \tau^{13}(v)\, dv$$

has been used and $f_0 = N_0/N_{tot}$.

Thus $N(^{13}\mathrm{CO})$ can be obtained by substituting equations (2.11) and (2.12) in (2.13). Of course, to derive $N(H_2)$ an abundance ratio must be used, which is not well known. In addition, the assumptions that go into the LTE approximation are often wrong, as noted above. Assumption (i) is particularly suspect. Modelling by Kutner and Leung (1985) suggests $N_{LTE}(^{13}\mathrm{CO})$ can be in error by up to a factor of 3. Several authors (e.g., Dickman 1978, Duvert et al. 1986) have compared N_{LTE} with gas estimates derived from extinction studies. Substantial variations in $N_{LTE}(^{13}\mathrm{CO})/A_v$ were noted by Duvert et al.

It is useful at this point to consider neutral HI 21 cm emission since, for $n_H \gtrsim 1\,\mathrm{cm}^{-3}$, LTE is a reasonable approximation (Spitzer 1978). The background term can be ignored, and equation (2.10) becomes

$$T_b(\nu) = T_s \left(1 - \mathrm{e}^{-\tau_\nu}\right);$$

at these wavelengths, brightness and radiation temperatures are approximately the same. T_s is the excitation temperature, but is called the spin temperature by convention. By equation (2.9)

$$N_{tot} \propto \int T_s\, \tau(\nu)\, d\nu$$

or, considering τ and T_b to be functions of the Doppler velocity v

$$N_{tot} \propto \int \frac{T_b(v)\tau(v)\, dv}{1 - \mathrm{e}^{-\tau(v)}} \tag{2.14}$$

where τ is determined as above. If the emission is optically thin

$$N_{tot} \propto \int T_b(v)\, dv.$$

Many of the concepts sketched here are used in subsequent chapters. Equation (2.14) and its optically thin analogue are used in §3.3 to derive HI column densities from 21 cm data.

2.3.4 Extinction

Another approach, which attempts to avoid the above difficulties, is to correlate integrated CO or ^{13}CO emission with A_v. For an optically thin line and constant T_x this follows directly from equation (2.14). The results for ^{13}CO are no worse than using the LTE assumptions (e.g., Heyer 1986, Cernicharo and Guélin 1987) Even for CO, assumed optically thick in the above, a correlation appears reasonable for low A_v. Thus Frerking et al. (1982) find the correlation breaks down above $A_v = 2\,\mathrm{mag}$ in the Taurus molecular cloud whereas Cernicharo and Guélin find a 3 mag limit. This conclusion is supported by the theoretical calculations of Kutner and Leung (1985). However, a considerable proportion of the mass of a GMC appears to lie inside this range. This may be part of the reason why W_{CO} can be used as a mass tracer on a large scale.

Star counting (and galaxy counting) is one common method for estimating column densities in local dark clouds over reasonably large areas (up to a few square degrees). Molecular clouds within a few hundred parsecs contain substantial amounts of dust. Background stars are therefore obscured and reddened. The amount of obscuration and reddening, measured

via star counts or IR photometry, can be used to estimate the amount of dust in the line-of-sight. The total column density of gas follows provided the dust-to-gas ratio is known. As might be expected, there are many uncertainties (see Cernicharo and Bachiller 1984; Arquilla 1987 and references therein for a more extensive discussion).

The star counting technique commonly uses a grid (reseau) of squares to count the number of stars per square degree down to some limiting magnitude on blue (or red) photographic plates covering the dark cloud. Nearby reference fields, apparently obscuration-free or of (known) uniform extinction, are counted in a similar manner. The limiting magnitude will in the former case be smaller because the light from fainter stars cannot penetrate the dark cloud. Comparison of the limiting magnitudes gives the extinction (m_b or m_r) which are converted to visual extinctions using an assumed value for the selective extinction ratio $R = A_v/E_{B-V} \sim 3.2$.

Errors are substantial at small and large extinctions. The former follows because at low A_v, the uncertainty in A_v is dominated by the extinction assumed for the reference field; Frerking et al. (1982) assert that this error is ~ 0.5 mag and a similar value is obtained by Cernicharo and Bachiller (1984). At high A_v the number of stars per reseau square becomes very small and counting errors are large. The method is useful for $1 \lesssim A_v \lesssim 5$ mag though for the present purposes this restriction is not too severe. A more serious systematic error can arise from residual absorption in the reference field, which must be close enough to the cloud to avoid a significant change in the expected number of stars. For example, Cernicharo and Bachiller claim it is impossible to find reference fields free of obscuration near the clouds they studied in the Taurus and Perseus regions. Also, the conversion from A_v to $N(\mathrm{H})$ presumes that the gas-to-extinction ratio,

$$N(\mathrm{H})/A_v = 1.9 \times 10^{21}\ \mathrm{atoms\,cm^{-2}\,mag^{-1}}$$

measured by Bohlin et al. (1978) towards lightly reddened ($A_v < 1$) stars, can be extrapolated to the conditions inside dense molecular clouds. More distant clouds with substantial numbers of foreground stars are not amenable to the technique. Unfortunately, the clouds in Orion at ~ 500 pc fall into this category.

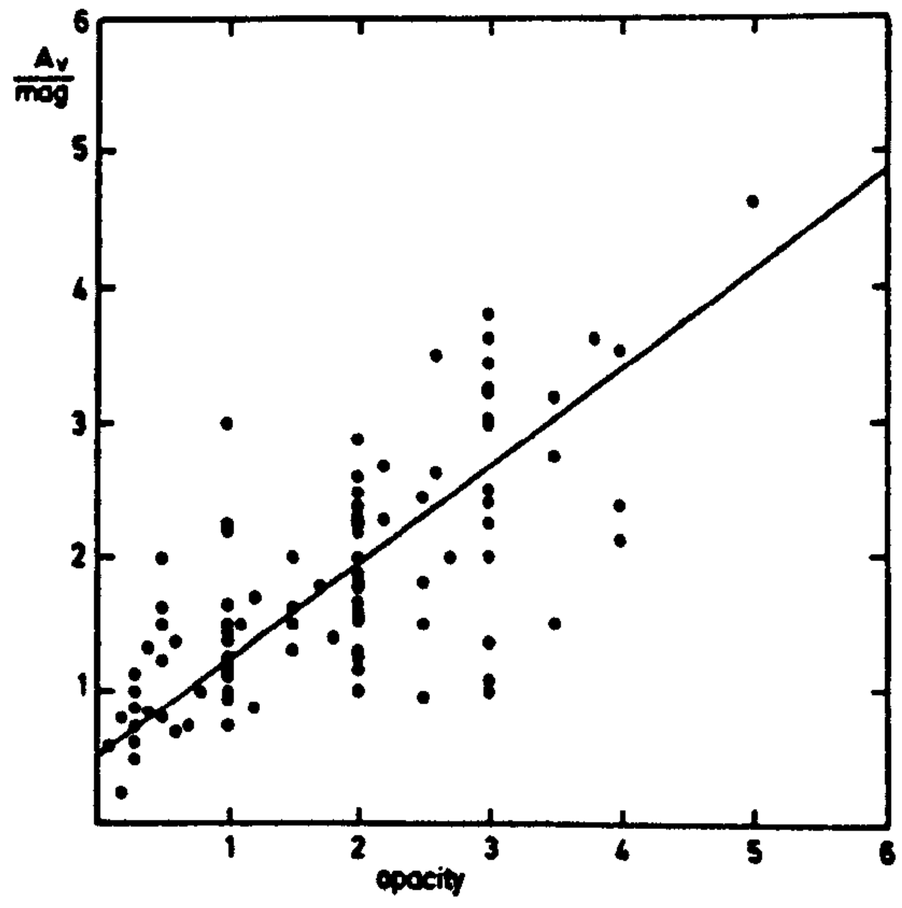

Fig 2.1 Correlation between opacity classes and A_v

On a larger scale, the combined dark cloud catalogue of Feitzinger and Stüwe (1986) and Lynds (1962) covers the Galactic plane roughly in the latitude range $|b| < 40°$. It contains most of the local molecular material of which those in the Orion and Taurus regions are of

particular interest for later work. To cover such a large area, the obscuration was estimated by eye into 6 opacity classes which correlate roughly with visual extinction (Fig. 2.1). The dark cloud atlas and the Columbia CO survey of the Milky Way at comparable resolution are shown in Fig (2.2). Happily, away from the Galactic plane, the maps appear quite similar. Visual extinctions have also been measured using IR photometry towards field stars lying behind the dust cloud. Stars are first classified from absorption features in their spectra. A comparison of the measured continuum level and the intrinsic luminosity for its spectral type gives the reddening caused by the dust cloud. A_v follows by assuming $A_v/E_{j-k} = 4.6$. Much greater column densities of dust can be probed by this technique because IR photons are scattered less than those in the visible waveband. However, the method is limited by the number of suitable stars in the required field, and is biased toward more highly reddened stars.

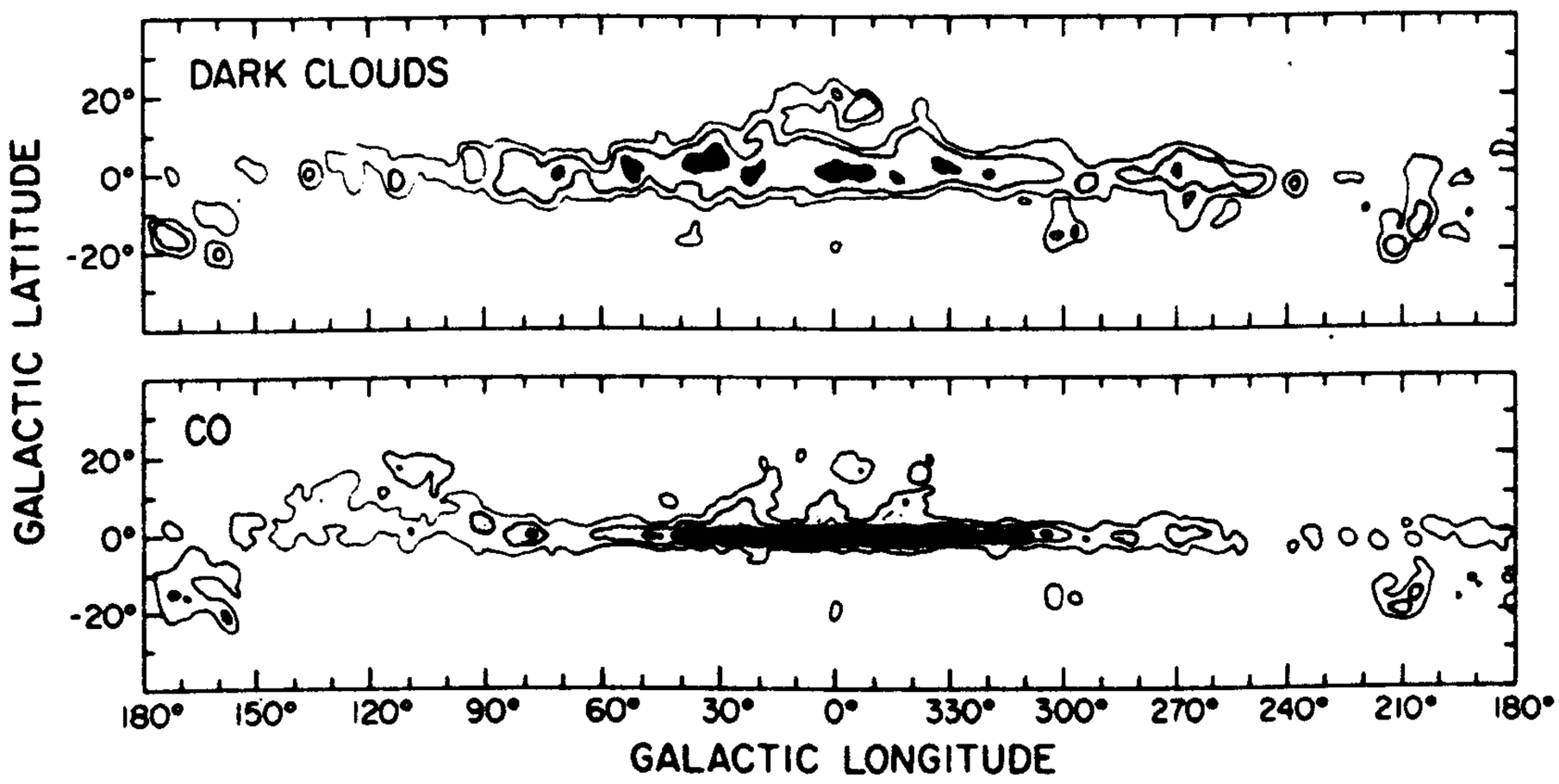

Fig 2.2 (a) Dark Clouds: The Galactic distribution of 2622 dark clouds folded with a Gaussian point spread function of form $\exp(-\theta/\theta_0)$ with $\theta_0 = 2.5°$. Contours at opacity class 1, 2 and 5.
(b) CO: W_{CO} contours from the Milky Way smoothed to an angular resolution of 2.5° (FWHM). Contours at $W_{CO} = 2, 9$ and $23\,\mathrm{K\,km\,s^{-1}}$.

2.4 Cosmic Rays

An exhaustive treatment of the properties of CRs would be out of place here, even though their distribution in the Galaxy was an important motivation for the present work. Nevertheless, a cursory review of what is known is given for later reference. More details can be found in Wolfendale (1983, 1984). The main constituents of the so-called cosmic radiation are protons and helium nuclei (alpha particles).

The energy spectra (Figs 2.3 and 2.4) are not known below $\sim 10^{10}\,\mathrm{eV\,nucleon^{-1}}$ because of solar modulation; at higher energies the spectrum is of power-law form i.e.,

$$N(E)\,dE \propto E^{-\gamma}dE$$

with $\gamma \sim 2.6$ up to $\sim 10^{15}\,\mathrm{eV\,nucleon^{-1}}$ and ~ 3.15 to $10^{19}\,\mathrm{eV}$. There is a small admixture of heavier elements (Fig 2.5); the excess of light elements (Li, Be, B etc.) are understood to be the spallation products of heavier nuclei in the cosmic radiation as they propagate through the ISM for about 10^7 years. Other components of interest – electrons, positrons and $\gamma-$rays are also indicated in Fig (2.3). The energy densities of the various components are listed in Table (2.4). Most CR energy is contained in the region around a few times 10^9 GeV.

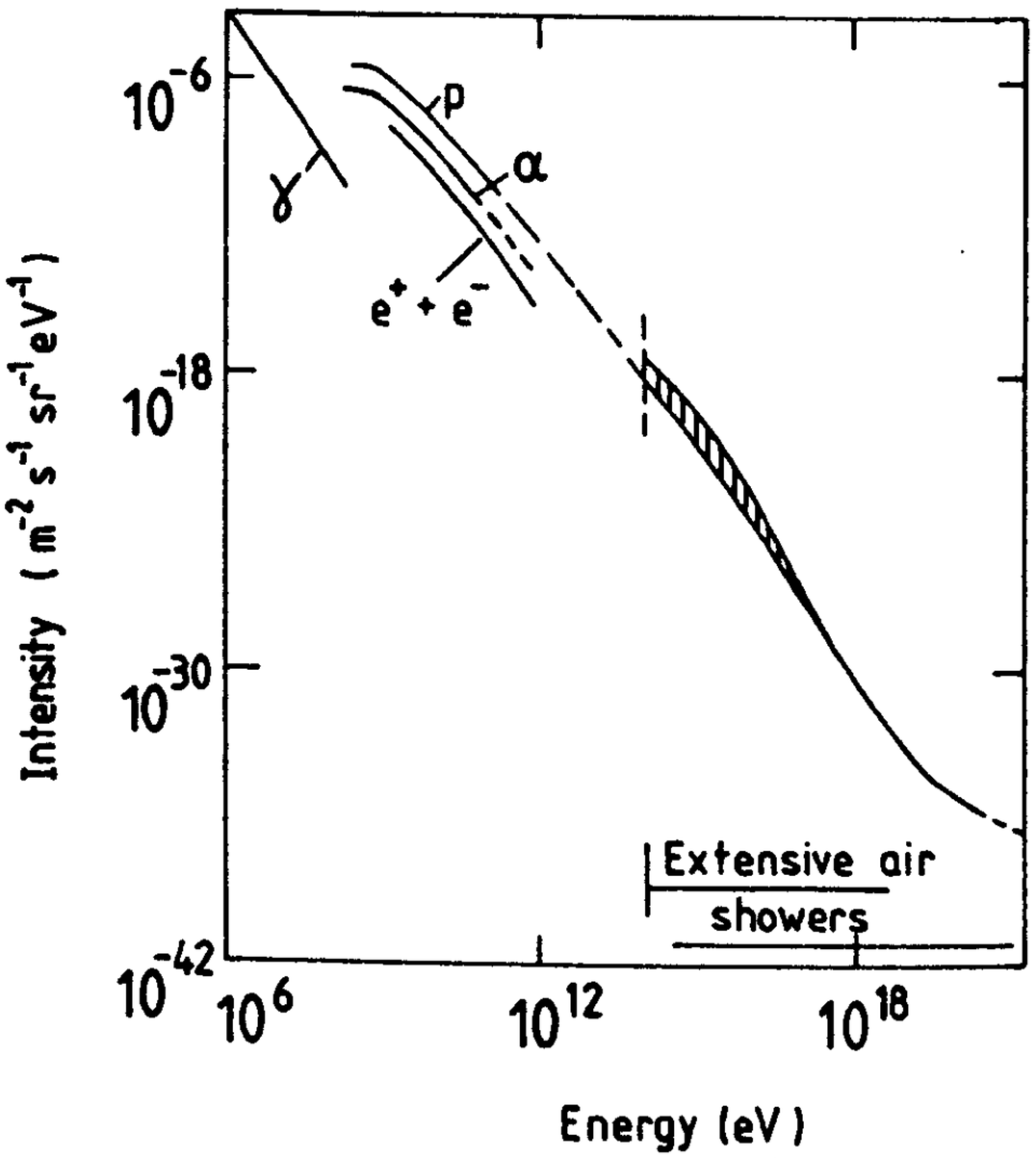

Fig 2.3 Energy spectra of the major components of the cosmic radiation. The mass composition is uncertain in the shaded region but there is general agreement that the particles are mainly protons at the highest energies.

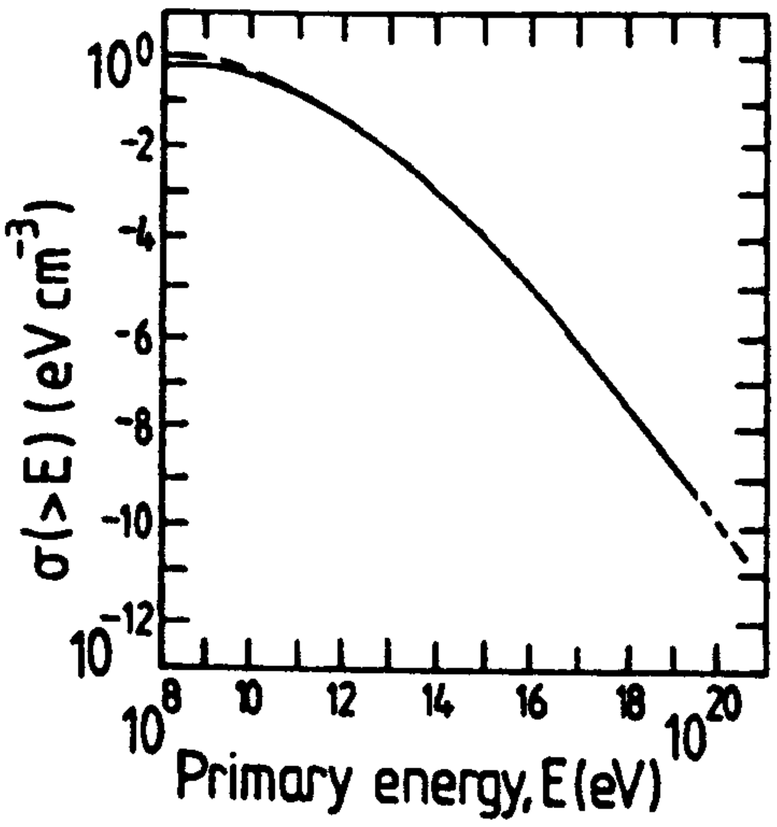

Fig 2.4 Energy densities for the nuclear component of cosmic rays.

Table 2.4

Energy densities of the cosmic ray components near the Earth

Component	(eV)	Energy density (eV cm^{-3})
Protons and heavier nuclei	Above 10^9	$\sim 5 \times 10^{-1}$
	10^{12}	2×10^{-2}
	10^{15}	10^{-4}
	10^{18}	10^{-6}
Electrons and positrons	Above 10^9	$\sim 6 \times 10^{-3}$
	10^{10}	1×10^{-3}
	10^{11}	2×10^{-4}
γ-rays: diffuse background	Above 10^7	$\sim 1 \times 10^{-6}$
	10^8	2×10^{-6}

Cosmic ray nuclei are charged particles and interact with the interstellar magnetic field which is thought to have a significant random component. Their motion is probably diffusive at energies less than 10^{15} eV since their observed isotropy and mass composition cannot be reconciled with straight-line propagation. The standard picture for this process is that the CRs scatter off Alfvén waves generated in the HIM by the bulk streaming motion of the CRs themselves (see the review by Wentzel 1974). The diffusion speed is then comparable to the Alfvén speed

$$v_A = \frac{B_0}{(4\pi\rho)^{\frac{1}{2}}}$$

since if they stream much faster than this they lose energy by exciting Alfvén and hydromagnetic waves. For typical values in the ISM, $B_0 = 3 \times 10^{-6}$ G and $n = 10^{-3}\,\mathrm{cm}^{-3}$, $v_A \sim 10^7\,\mathrm{cm\,s}^{-1}$.

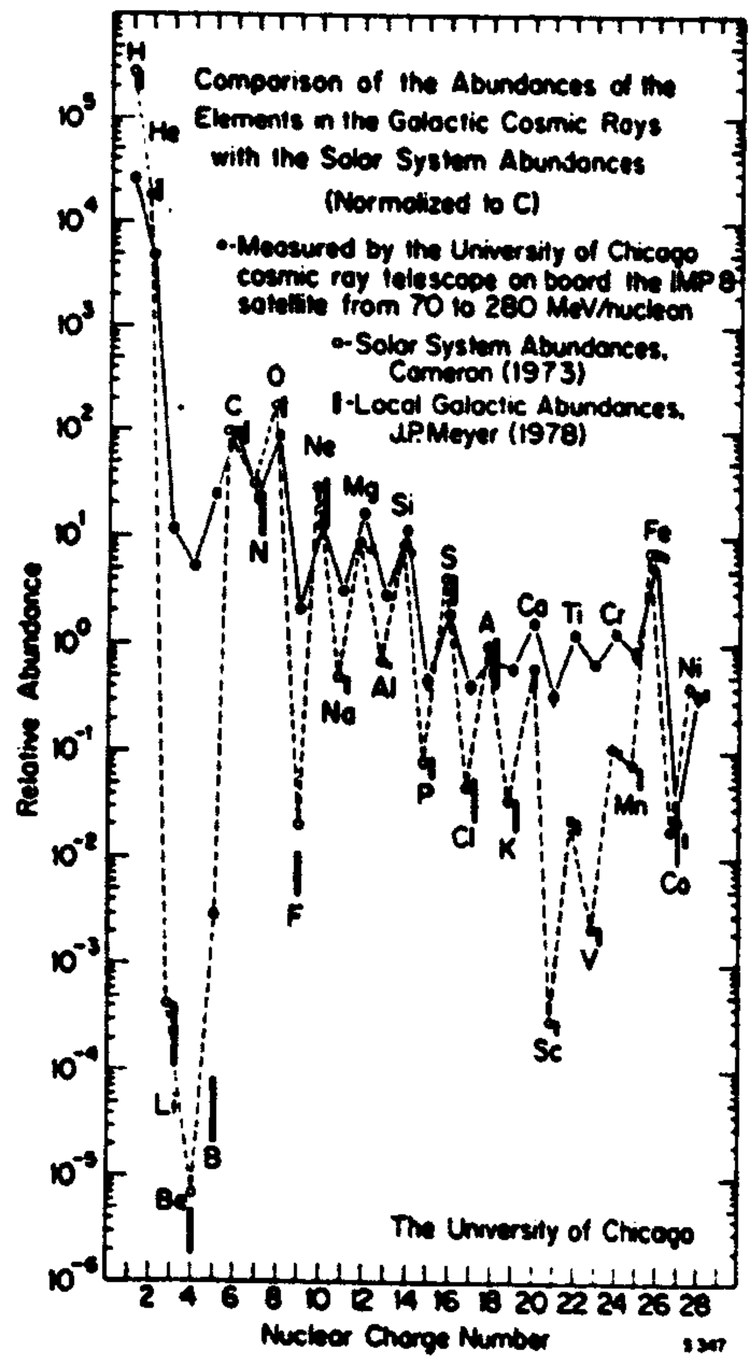

Fig 2.5 Elemental abundances of cosmic rays compared with two compilations of solar system abundances (from Meyer 1981).

A description of the transport equation is given in Longair (1981) and Drury (1983); in

terms of the distribution function f, this is assumed to be

$$\frac{\partial f}{\partial t} + \mathbf{U} \cdot \nabla f = \nabla (\kappa \nabla f) + \nabla \cdot \mathbf{U} C_g f + \frac{1}{p^2} \frac{\partial}{\partial p} \left(p^2 D \frac{\partial f}{\partial p} \right)$$

where $C_g \equiv -\frac{1}{3} p \frac{\partial}{\partial p}$ is the Compton-Getting operator, κ is the (spatial) diffusion tensor, $\mathbf{U}$ the bulk velocity and D the momentum diffusion coefficient. The last term accounts for losses arising from the interaction of the CRs with matter (ionisation, bremsstrahlung etc.). In one dimension, this simplifies to

$$\frac{\partial f}{\partial t} + U \frac{\partial f}{\partial x} = \frac{\partial}{\partial x} \left(\kappa \frac{\partial f}{\partial x} \right) - \frac{\partial}{\partial x} (U C_g f) + \frac{1}{p^2} \frac{\partial}{\partial p} \left(p^2 D \frac{\partial f}{\partial p} \right) \tag{2.15}$$

Equation (2.15) is utilised in §4.3 during the discussion of the Morfill (1982) model for CR convection in GMCs and its application to the results of the $\gamma-$ray analysis of local molecular clouds.

2.5 Gamma Rays

The $\gamma-$ray component of the cosmic radiation is of particular concern here. In the energy range around a few GeV, $I_\gamma / I_{CR} \sim 10^{-6}$. Nevertheless, $\gamma-$rays have major advantages from an observational standpoint since they propagate in straight lines through the Galaxy, unhindered by magnetic fields. At the energies considered here ($\lesssim 5\,\mathrm{GeV}$), propagation is almost without losses since Inverse Compton and pair production processes are negligible.

Contributions to the $\gamma-$rays in the energy range $30 - 5000\,\mathrm{MeV}$, roughly the limits for the SAS-II and COS-B $\gamma-$ray satellites, come from a population of discrete $\gamma-$ray sources (e.g., the CRAB and VELA pulsars) and a diffuse component which arises from interactions between CRs and nuclei of the ISM. Estimates of the effect of unresolved discrete sources are typically $\lesssim 25\%$ of the observed flux. Protheroe et al. (1979), Houston and Wolfendale (1983, 1984) and Fichtel and Kniffen (1984) suggest $10 - 20\%$ as a reasonable figure. Quadrants II and III, and all longitudes for $|b| > 10^\circ$ probably contain no unresolved sources, since they should be readily detectable.

Gamma rays are produced by interactions between CR nuclei and the interstellar gas (denoted collectively as π^0 decay), bremsstrahlung $\gamma-$rays from CR electrons, inverse Compton interactions between CR electrons and the interstellar photon field and synchrotron radiation from electrons spiralling around magnetic field lines. At the energies of interest the last-mentioned process is negligible for the diffuse $\gamma-$ray emission. The inverse Compton contribution is probably small throughout the Galactic plane (Bloemen 1985) and perhaps less than 10% at medium latitudes.

The expected $\gamma-$ray spectrum for the two remaining processes have quite different characteristics. Most π^0 mesons are produced in collisions between CR nuclei and those of the ISM. The simplest case (and the most important) is that of proton-proton collisions i.e.,

$$p + p \rightarrow p + p + \pi^0 + \ldots$$

The threshold kinetic energy for the production of a single π^0 is

$$T \equiv E - m_p = 2 m_\pi \left(1 + \frac{m_\pi}{4 m_p} \right)$$

giving $T = 296\,\mathrm{MeV}$. Note that the units of the equations in this section are such that the speed of light is unity. The emissivity (in $\mathrm{atom}^{-1}\,\mathrm{s}^{-1}\,\mathrm{sr}^{-1}$) can be computed (in principle) as

$$q(E_\gamma)/4\pi = n \int dE_p\, I(E_p)\, \sigma\,(E_\gamma|E_p)$$

where $\sigma(E_\gamma|E_p)$ is the cross-section for the production of a $\gamma-$ray of energy E_γ from the collision of a CR proton of energy E_p with a target nucleus of the ISM, $I(E_p)$ is the intensity of CR protons of energy E_p and n is the volume density of target nuclei. The cross-section can be rewritten as an integral over the energies of neutral pions created in the collision e.g., Stecker (1971):

$$\sigma\,(E_\gamma|E_p) = \int_{E_{\pi,\mathrm{min}}}^{E_{\pi,\mathrm{max}}} dE_\pi \; <m_{\gamma,\pi}>\, f_\pi\,(E_\gamma|E_\pi)\; \sigma_\pi\,(E_\pi, E_p)\,.$$

Here, $<m_{\gamma,\pi}>$ is the average multiplicity of $\gamma-$rays of energy E_γ produced via π^0 decay, $\sigma_\pi\,(E_\pi, E_p)$ is the production cross-section for π^0s of energy E_π and $f_\pi\,(E_\gamma|E_\pi)$ is an energy distibution function giving the probability that a $\gamma-$ray, energy E_γ results from the decay of a π^0 of energy E_π. $E_{\pi,\mathrm{min}}$ and $E_{\pi,\mathrm{max}}$ are the minimum and maximum energies that a π^0 can have and still decay to a $\gamma-$ray of energy E_γ.

The energy distribution function f and integration limits are determined by the kinematics of the π^0 decay. Thus, in the rest frame of the π^0, the decay

$$\pi^0 \rightarrow \gamma_a + \gamma_b$$

produces two photons of energy $E'_\gamma = p' = m_\pi/2$. Transforming to the laboratory frame, where $E_\pi = \gamma m_\pi$, if the π^0 rest frame moves with velocity β_π in the laboratory frame and the $\gamma-$ray moves at an angle θ' with respect to β_π, then

$$E_\gamma(\theta') = \frac{E_\pi}{2}\left[1 + \beta_\pi \cos\theta'\right]. \tag{2.16}$$

Since the π^0 is a spin-zero particle, it decays isotropically in its rest frame, and the angular distribution function is

$$f(\theta', \phi')\, d\theta'\, d\phi' = \frac{1}{4\pi}\, d\Omega\left(\theta', \phi'\right)$$

so that

$$f(\theta')\, d\theta' = \frac{1}{2} \sin\theta'\, d\theta'.$$

Using equation (2.16), the energy distribution function follows as

$$\begin{aligned} f(E_\gamma) &= f(\theta') \left(\frac{dE_\gamma}{d\theta'}\right)^{-1} \\ &= \frac{1}{\sqrt{E_\pi^2 - m_\pi^2}} \end{aligned} \tag{2.17}$$

for $E_{\gamma,\mathrm{min}} < E_\pi < E_{\gamma,\mathrm{max}}$, where, from equation (2.16)

$$E_{\gamma,\mathrm{min}} = \frac{1}{2} E_\pi\,(1 - \beta_\pi) \tag{2.18a}$$

$$E_{\gamma,\mathrm{max}} = \frac{1}{2} E_\pi\,(1 + \beta_\pi)\,. \tag{2.18b}$$

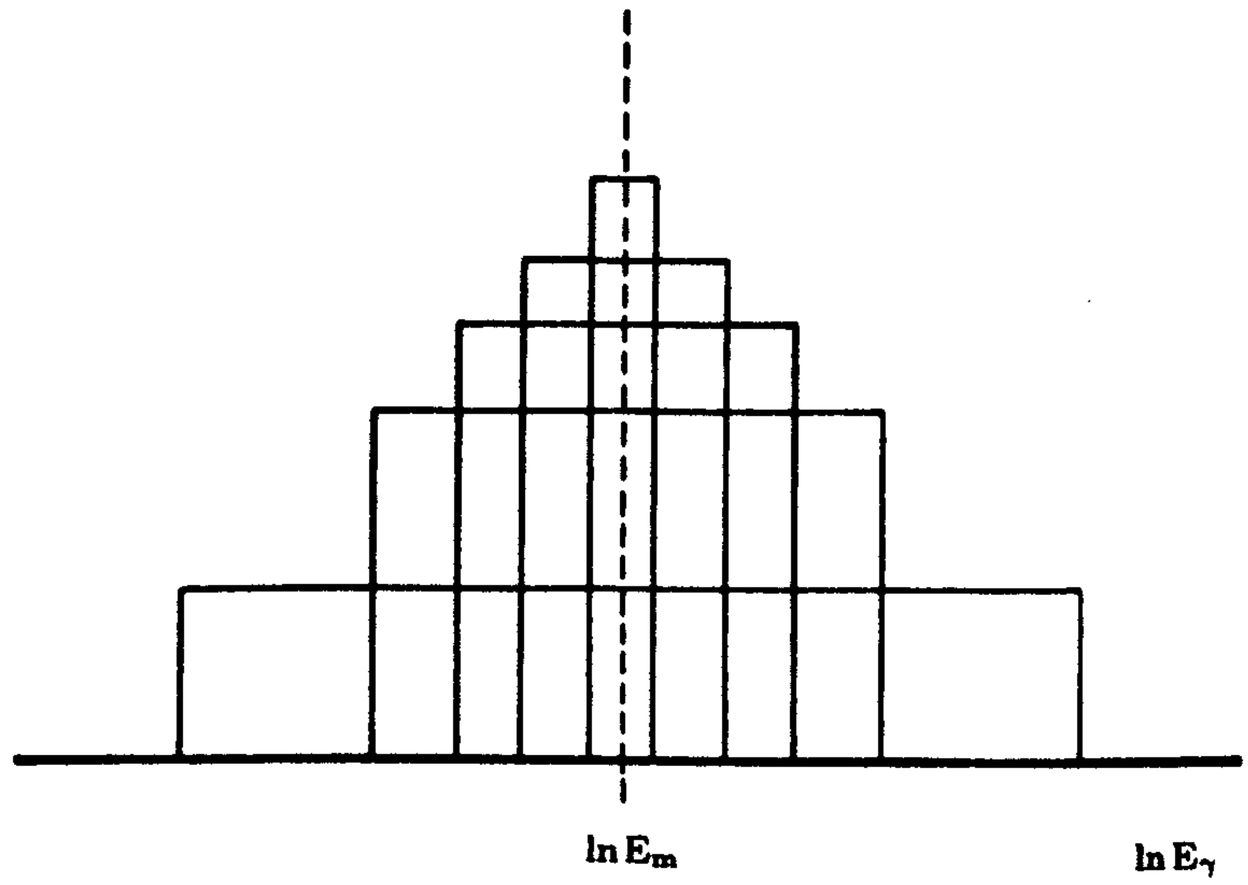

Fig 2.6 Idealised superposition of $\gamma-$ray energy spectra from the decay of π^0s having discrete energies. E_m is the photon energy in the rest-frame of the decaying π^0.

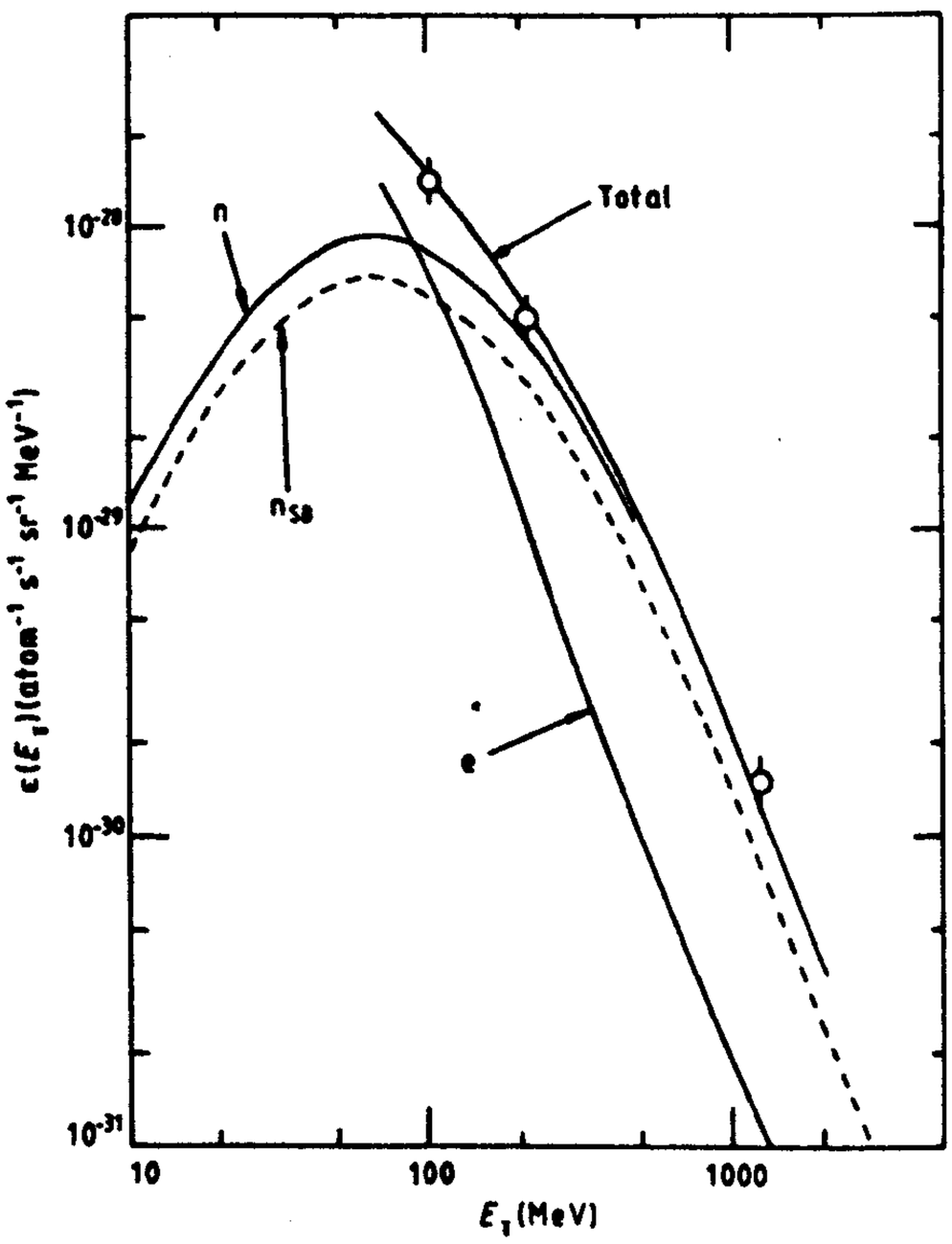

Fig 2.7 Gamma ray emissivity ϵ_γ showing the components for nuclei, n and electrons, e. Also shown is the average of the Stephens & Badhwar (1981) estimates, denoted n_{SB}. The circles represent the COS-B (integrated) emissivities determined by Strong (1985b), plotted at energies that are correct only if the spectrum has the form E_γ^{-2}. The errors shown are 67% limits.

Note that $f(E_\gamma)$ is independent of E_γ. For ultra-relativistic particles, $\beta_\pi \to 1$ so that by equation (2.16), for fixed E_γ,

$$E_\pi \propto \frac{1}{\cos^2 \frac{\theta'}{2}}$$

i.e., $E_{\pi,\mathrm{max}} \to \infty$ for emission of the $\gamma-$rays in the direction of pion motion.The minimum pion energy is obtained by summing equations (2.18) to give

$$E_\pi = E_{\pi,\mathrm{max}} + E_{\pi,\mathrm{min}}. \tag{2.19}$$

Next, multiplying (2.18a) by (2.18b) and eliminating $E_{\gamma,\mathrm{min}}$ from (2.19) gives

$$E_{\pi,\mathrm{min}} E_{\pi,\mathrm{max}} = \frac{m_\pi^2}{4} \tag{2.20}$$

and therefore

$$E_\pi = E_{\gamma,\mathrm{max}} + \frac{m_\pi^2}{4E_{\gamma,\mathrm{max}}}$$

so that the minimum pion energy that can give rise to a $\gamma-$ray of energy E_γ follows as

$$E_{\pi,\mathrm{min}} = E_\gamma + \frac{m_\pi^2}{4E_\gamma}. \tag{2.21}$$

Hence, the $\gamma-$ray emissivity from pion decay is

$$\frac{q_\pi}{4\pi}(E_\gamma) = 2n_{\mathrm{H}} \int dE_p\, I(E_p) \int_{E_{\pi,\mathrm{min}}}^{\infty} dE_\pi \frac{\sigma(E_\pi, E_p)}{\sqrt{E_\pi^2 - m_\pi^2}}. \tag{2.22}$$

Some qualitative features of this result can now be understood.
(i) Equation (2.20) implies that the geometric mean energy of $\gamma-$rays arising from neutral pion decay is independent of the pion energy and equals the energy of the photons in the pion rest frame.
(ii) For a given E_π, the probability distribution function is constant and of width $\beta_\pi E_\pi$ i.e., rectangular. A distribution of pion energies will produce a $\gamma-$ray spectrum which is a superposition of these rectangular functions (see Fig 2.6). The spectrum is symmetric on a log-log plot about $m_\pi/2 \sim 70\,\mathrm{MeV}$.

The cross section $\sigma(E_\pi, E_p)$ is not well known, particularly at high energies. At low energies ($\lesssim 1\,\mathrm{GeV}$), a model that gives a reasonable fit to experimental data is

$$\begin{aligned} p + p &\to \Delta(1.238) + p + \ldots \\ \Delta(1.238) &\to \pi^0 + \ldots \\ \pi^0 &\to \gamma + \gamma \end{aligned}$$

where $\Delta(1.238)$ is the well-known nuclear isobar at $1.238\,\mathrm{GeV}$. In this two-stage process, an additional integration over isobar energies is required to compute the cross section σ; see Stecker (1971) and Dermer (1986) for more details. The contribution from higher energies is usually computed by scaling from lower energy data although this may not be a particularly good assumption. For example, Wdowcyzk and Wolfendale (1987) argue that significant scaling violations probably occur.

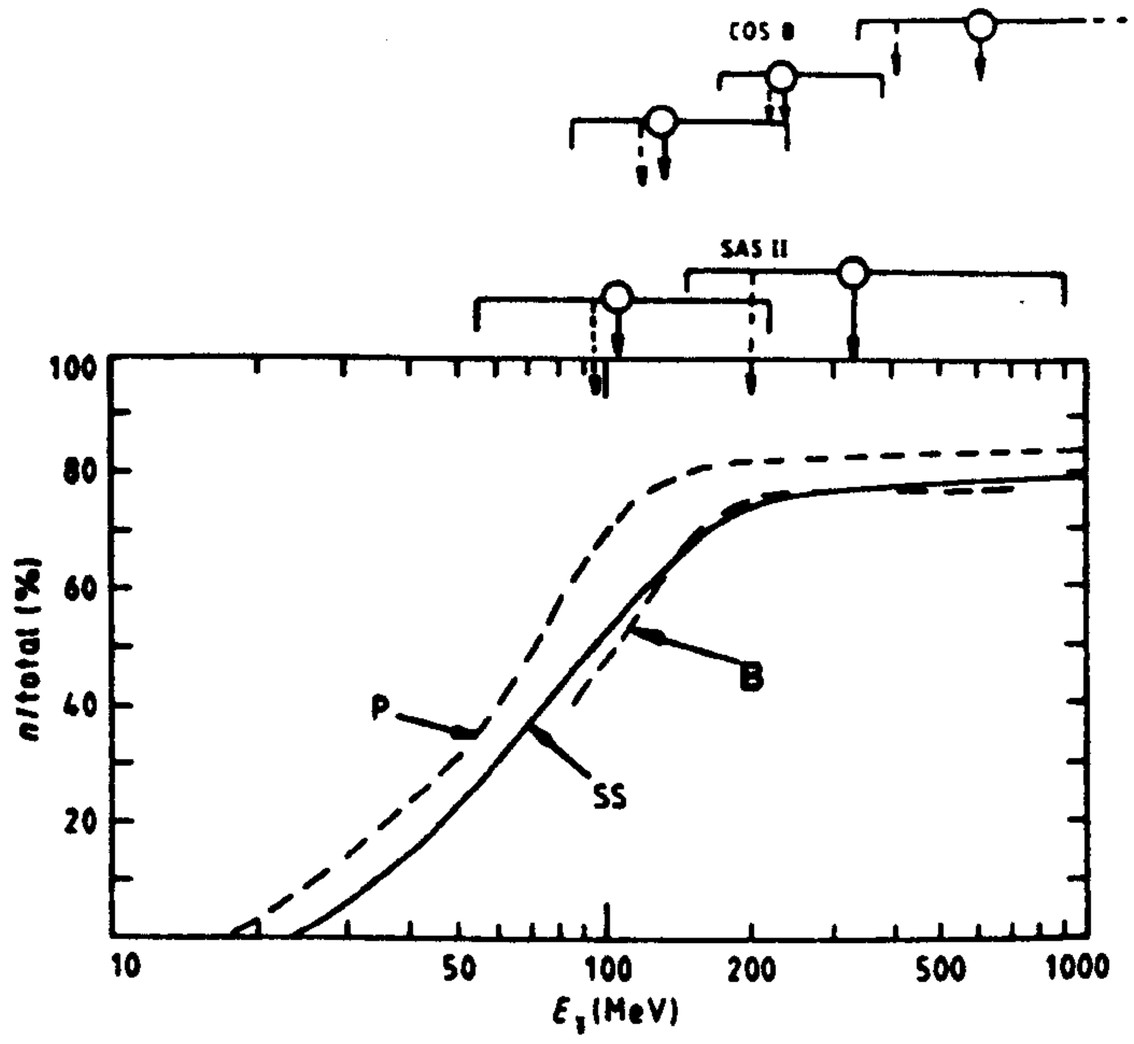

Fig 2.8 The fraction of $\gamma-$rays due to the interactions of cosmic ray nuclei as a function of $\gamma-$ray energy (from Bhat et al. 1986b). The median energy for the SAS-2 and COS-B measurements are indicated ($l = 116° - 136°$). **KEY:** P = Poon (1983)–local spectrum; B = Bhat et al. (1986b) estimate; SS = Sacher & Schonfelder (1984)–anticentre spectrum.

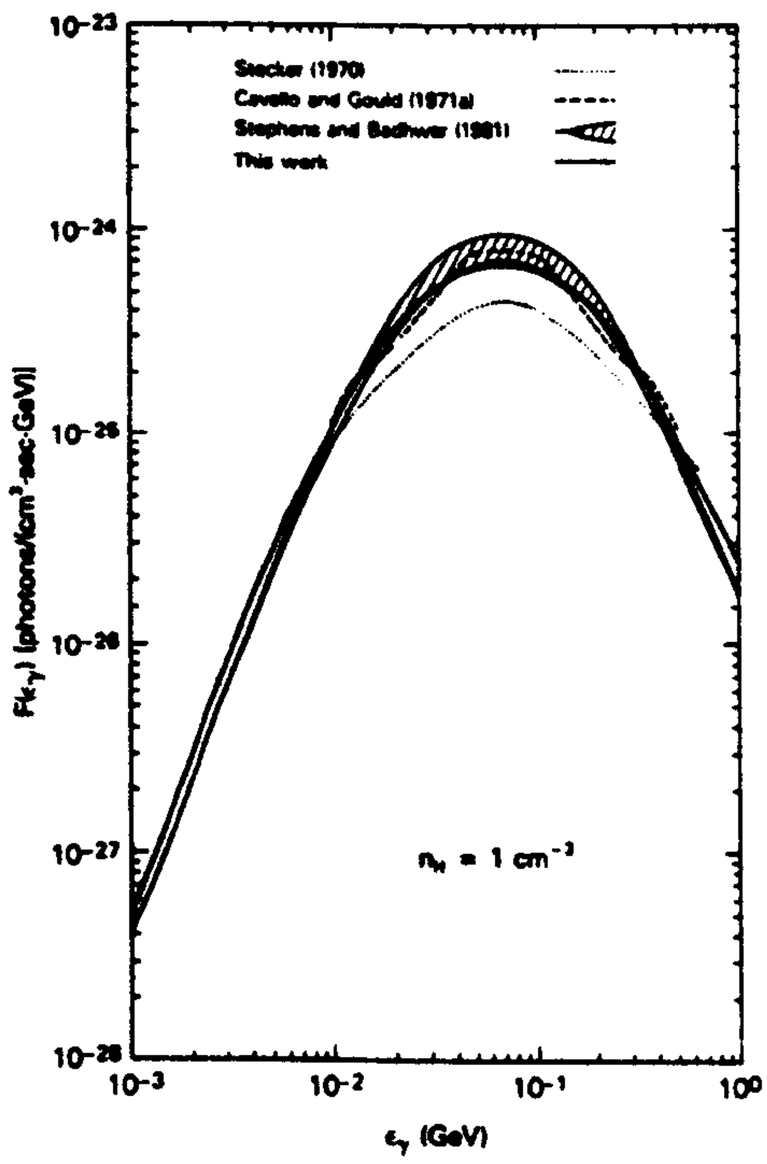

Fig 2.9 The gamma ray emissivity from the interaction of the local demodulated cosmic ray flux with the local ISM assuming $n_H = 1\,\mathrm{cm}^{-3}$. Dermer's calculation (solid heavy line) is shown along with estimates by previous authors.

Fig (2.7) gives one estimate by Bhat et al. (1986b). These authors assumed a π^0 decay emissivity spectrum as given by Stephens and Badhwar (1981) but with absolute normalisation determined by fitting to $\gamma-$ray data.

Of considerable interest for later work is the fraction of $\gamma-$ray flux that can be attributed to nuclei in any given energy range. Fig (2.8) reproduces the results of Bhat et al. (1986b) which suggests that the proton component is dominant at energies $\gtrsim 100\,\mathrm{MeV}$. This corresponds roughly to the two highest COS-B standard energy bands (see below). A recent calculation (Dermer 1986) of the expected emissivity for $\gamma-$rays from π^0 decay is shown in Fig (2.9). Dermer suggests that most diffuse medium energy $\gamma-$rays come from protons with KE between two and several GeV (see Table 2.5). Thus the uncertainties in the solar modulation correction to the proton CR spectrum, important for $E_p \lesssim 1\,\mathrm{GeV}$, are not significant in estimating $q/4\pi$. The SB source function is slightly lower than that of Dermer but only a modest change in Fig (2.7) would result if it was used.

Table 2.5 Fraction of photons coming from protons of various energies

Table 2. Fraction of photons coming from protons of various energies

T_p(GeV)	$0 \leq \varepsilon_\gamma$(GeV) $< \infty$	$0.07 \leq \varepsilon_\gamma \leq 0.15$	$0.15 \leq \varepsilon_\gamma \leq 0.30$	$0.30 \leq \varepsilon_\gamma \leq 1.0$	$1.0 \leq \varepsilon_\gamma \leq 5.0$
$T_p \leq 1$	0.14	0.22	0.17	0.05	0.00
$1 \leq T_p \leq 2$	0.24	0.29	0.29	0.21	0.01
$2 \leq T_p \leq 5$	0.31	0.30	0.32	0.34	0.22
$5 \leq T_p \leq 10$	0.15	0.11	0.13	0.21	0.24
$T_p \geq 10$	0.16	0.08	0.09	0.19	0.53

The bremsstrahlung spectrum is of power law form at the energies of interest here. If n is the number density of nuclei in the production region and $I_e(>E_\gamma)$ is the integrated CR electron intensity for energies $E_e > E_\gamma$, Stecker (1975) gives the emissivity as

$$q_b(E_\gamma) = 4.3 \times 10^{-25} n \frac{I_e(>E_\gamma)}{E_\gamma}\,\mathrm{cm^{-3}\,s^{-1}\,MeV^{-1}} \tag{2.23}$$

The computation of this quantity is uncertain and model dependent; neither n nor I_e are sufficiently well known to make a definitive calculation. The Bhat et al. bremsstrahlung estimate is given in Fig (2.7). Its form (power-law) has been determined by equation (2.23), but it is again normalised to the observed emission.

2.6 Gamma Ray Astronomy

It is appropriate at this point to summarise the main results of this technique in the relevant areas. A brief description of the COS-B satellite and database will be given shortly. It was noted above that $\gamma-$rays could be a valuable tool for establishing the distribution of CR nuclei throughout the Galaxy. In particular, if it were possible to establish the existence of a 'cosmic ray gradient' i.e., a decrease in CR intensity with increasing galactocentric radius, then the Galactic origin model would be considerably strengthened.

Evidence for a gradient in the electron component is substantial (Issa et al. 1980; Bloemen et al. 1984a; Bhat et al. 1984) but not unexpected since extragalactic electrons are excluded by Inverse Compton scattering off the 3 K MWB. It has proved much more difficult to establish a gradient in the proton component. The Durham group (Issa et al. 1980; Bhat et al. 1984, 1986a,b) have consistently argued for a significant large-scale gradient in both the inner and outer Galaxy (see Fig 2.10). Bhat et al. (1986a) also showed that the $\gamma-$ray results were consistent with a supernova remnant (SNR) origin for both electrons and protons. Combining a Monte Carlo simulation of SNR exploding in the Galaxy with the model for

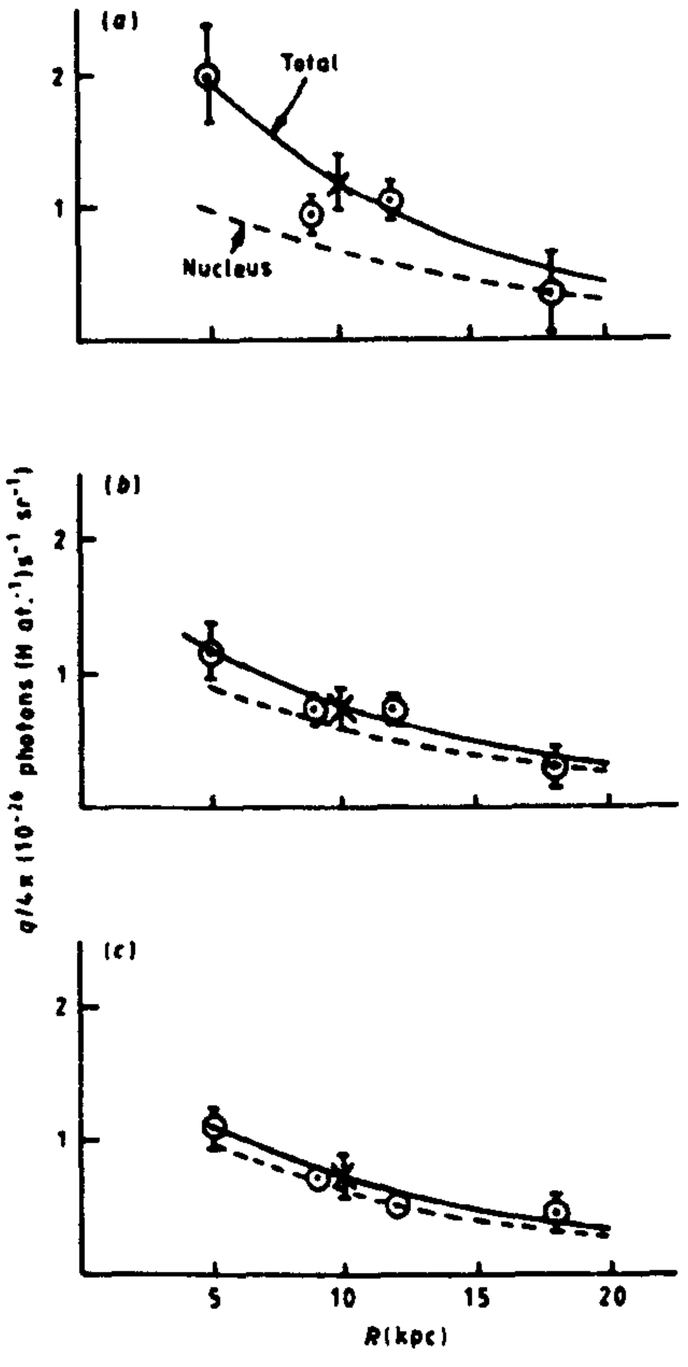

Fig 2.10 Bhat et al. (1986b) $q/4\pi$ values versus galactocentric radius R for (a) 70−150 MeV (b) 150−300 MeV (c) 300−5000 MeV. The circles are from Bloemen (1985) except for the point at smallest R which has been increased by 1.25 to correspond to the Bhat et al. estimate of gas column density. The crosses are from Strong (1985b)

CR acceleration by Blandford and Cowie (1982), they found evidence of similar scale sizes in both model and observed $\gamma-$ray data.

In addition, there is some evidence for an excess in the electron and proton intensity towards the Loop I SNR (Wolfendale and van der Walt 1988) and the Loop III SNR and Vela (Rogers and Wolfendale 1987). However, there are as yet unresolved problems with the analyses – e.g., uncertainties about gas column densities inside the SNR (particularly the contribution of ionised gas and the value of X_{20}) and the energetics and frequency of SNRs. There is also a likely contribution from distributed acceleration (accounting for up to 50% of the CR energy density); see Cowsik (1981), Giler et al. (1987) for more details.

The most recent work by COS-B (Strong et al. 1987) also provides evidence for the reality of the gradient in CR protons. Their technique is to divide the Galaxy into concentric annuli (2−4, 4−8, 8−10, 10−12, 12−15 and $>$ 15 kpc) and to fit the observed $\gamma-$ray distribution to an expected distribution using a maximum likelihood analysis. The model chosen assumes the observed I_γ arises from CR-gas interactions as described above. i.e.,

$$I_\gamma = \sum_i \frac{q_i}{4\pi}\left(\tilde{\mathrm{N}}(\mathrm{HI})_i + 2Y\tilde{W}_{\mathrm{CO},i}\right) + f_{\mathrm{IC}}\tilde{I}_{\mathrm{IC}} + I_b^0 + \sum_k f_k I_k \qquad (2.24)$$

where $q_i/4\pi$ is the $\gamma-$ray emissivity in the ith ring, $\tilde{\mathrm{N}}(\mathrm{HI})_i$ is the column density of HI, Y is an 'effective' $\gamma-$ray value for X, $f_{\mathrm{IC}}I_{\mathrm{IC}}$ is the Inverse Compton emission, I_b^0 is the background and f_k is the flux from the kth point source. The tilde denotes convolution to the COS-B point spread function (see below).

The results are shown in Fig (2.11), taken from Strong et al. (1987). Independent work by Bhat et al. (1986b) and Wolfendale (1986) suggests there is a modest gradient consistent

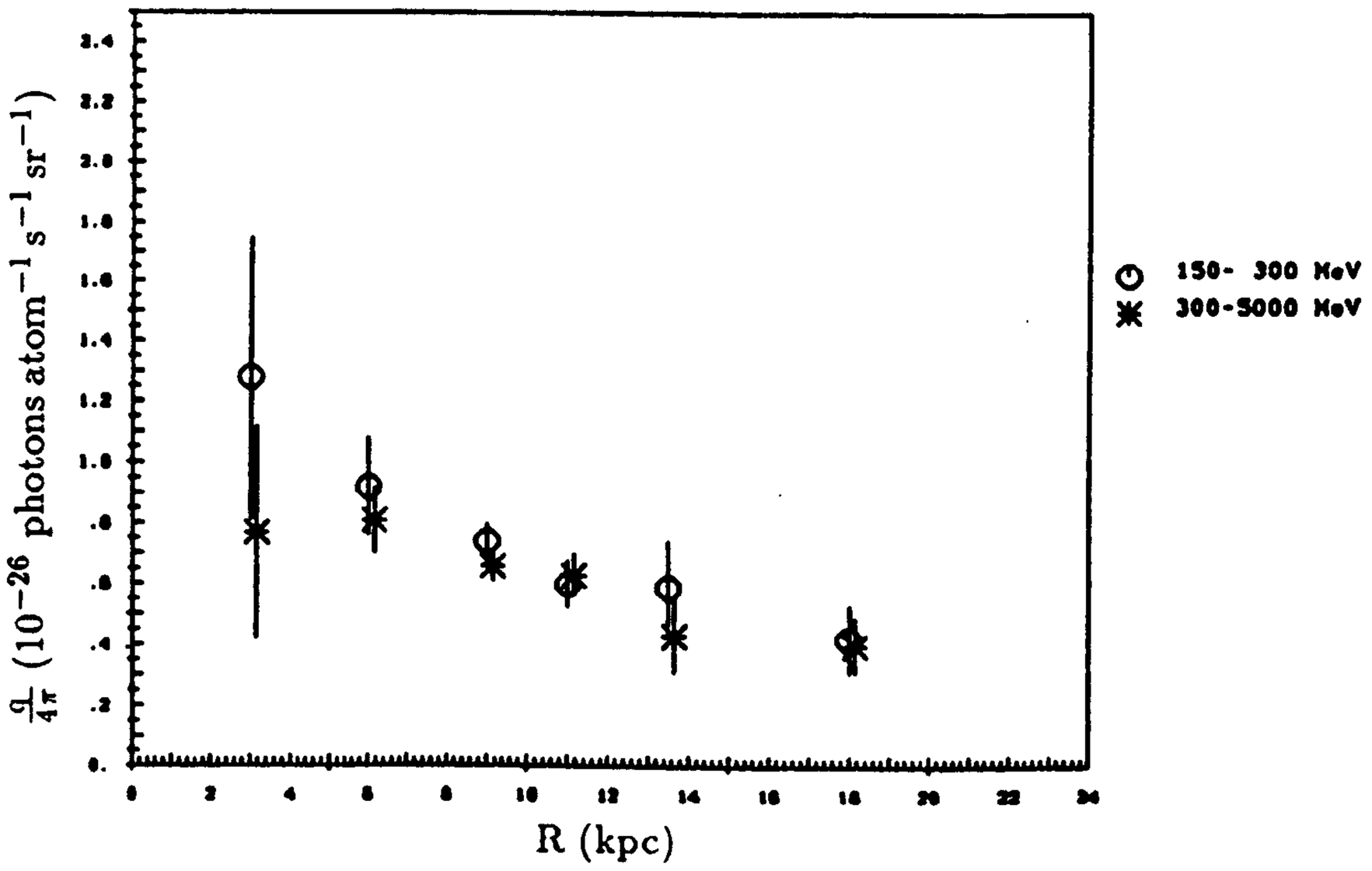

Fig 2.11 Strong et al. (1987) $q/4\pi$ values versus galactocentric radius R for 150–300 and 300–5000 MeV.

with a simple model of CR propagation and a source distribution similar to that of supernova remnants.

The gradient in the proton component is small compared to the distribution of likely sources (e.g., SNR). Bloemen (1987) argues that this may occur if

(a) A transition from diffusion-dominated to convection-dominated propagation at higher energies ($\gtrsim 10\,\mathrm{GeV\,nucleon^{-1}}$) in the outer Galaxy compared to the inner Galaxy ($\sim$ few GeV/nucleon).

(b) Non-linear damping of Alfvén waves (Chin and Wentzel 1972) dominating for $R < R_\odot$ compared to linear damping (Kulsrud and Pearce 1969) for $R > R_\odot$ induced, perhaps, by a radial decrease in the abundance of the WIM.

For CRs confined to a thin disc of scale height $z(R)$, the mean lifetime is

$$\tau_{CR} \sim z(R)^2/\kappa(R, E)$$

where $\kappa(R, E)$ is the (scalar) diffusion coefficient. If the mean value of

$$\kappa(R > R_\odot) < \kappa(R < R_\odot),$$

as suggested in (b) above, and $z(R)^2 \sim$ constant for protons in $\sim 1 - 5\,\mathrm{GeV}$, then clearly the CR lifetime in the outer Galaxy is increased. The γ–ray emissivity will in this case be larger than expected from the distribution of likely Galactic sources (SNRs). Alternatively, if $\kappa \sim$ constant and $z(R)$ increases in the outer Galaxy, the same result follows. This effect may arise from the flaring of the gas and magnetic field observed in the outer Galaxy (see Wolfendale 1984 and references therein).

The COS-B analysis also yields an estimate of the parameter X_{20}. The quantity Y in equation (2.24) gives an upper limit since, among other things, the contribution from unresolved discrete sources has been ignored. Strong et al. (1987) find $Y_{20}(> 150\,\mathrm{MeV}) = 2.3 \pm 0.3$ with no dependence on galactocentric radius. There is some evidence, albeit of low statistical significance, for an apparent energy dependence in Y_{20} (see Fig 2.11). If real, this would suggest a low energy CR excess in the inner Galaxy, perhaps associated with GMCs.

2.7 The COS-B Gamma Ray Satellite

Most recent medium energy $\gamma-$ray satellites have been built around a spark chamber detector, and COS-B was no exception. For $E_\gamma \gtrsim$ few MeV, the most probable interaction with matter is pair production in the Coulomb field of a nucleus. Since the pair production cross-section is proportional to the nuclear charge z^2, a high z element is used to 'materialise' the incoming $\gamma-$ray photon, producing an electron-positron pair. The COS-B spark chamber consisted of 16 1.5 cm 'gaps'; each gap was bounded by orthogonal wire grids, with 3 mm between the grids. Interleaved between the gaps were 12 tungsten ($z = 74$) sheets (see Fig 2.12). The top gap and the lowest three gaps had no tungsten immediately above them. An anti-coincidence shield (A) surrounded the entire spark chamber volume to discriminate against incoming charged particles. In the absence of a pulse from the anti-coincidence shield, the detection of downward-moving electrons in the triggering telescope (B1,B2,C) led to the application of a high-voltage pulse to each gap. Discharges occurred along the electron tracks which could be reconstructed from the spark coordinates detected by the orthogonal wire planes. This information defines the arrival direction of the incoming photon within the angular resolution of the instrument.

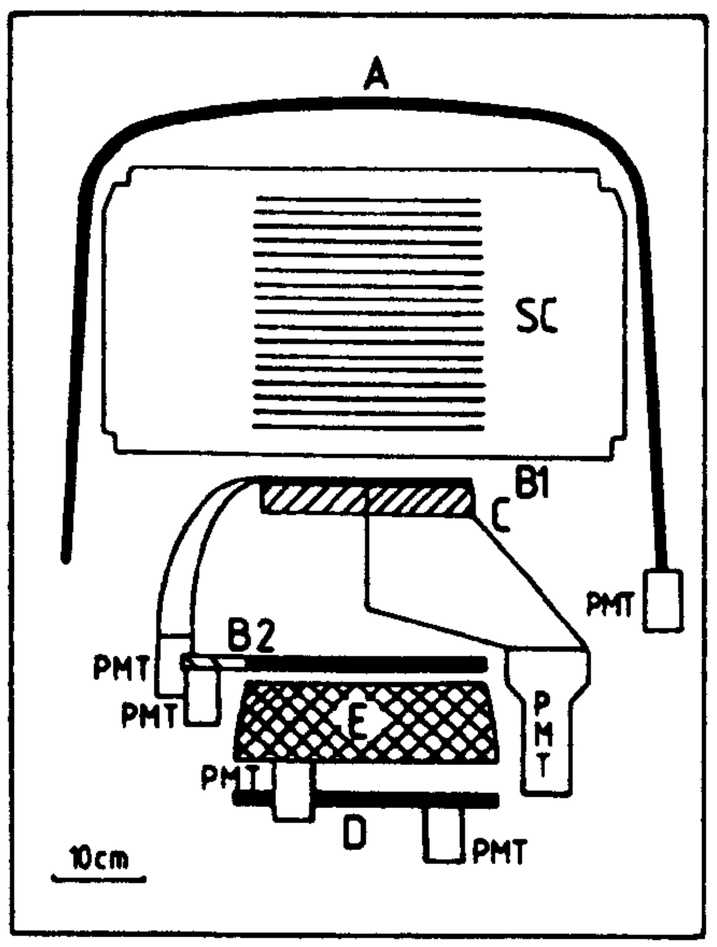

Fig 2.12 Sectional view of the COS-B detector (Bennett et al. 1976).
A: anticoincidence counter; SC: spark chamber; B1,B2: Scintillation counter; C: directional Cerenkov counter; E: energy calorimeter (cæsium-iodide scintillator); D: Scintillator to provide information on high energy events for which the absorption in the calorimeter is incomplete.

The electron (and therefore $\gamma-$ray) energy is measured in the scintillation crystal (E); a pilot plastic scintillator (D) below this monitored leakage of the cascades at the highest energy. The satellite was place in a highly eccentric polar orbit (apogee around 90000 km) to maximise observation time. Thus, the satellite experienced the full CR flux, modulated by the 11 year solar cycle, but unshielded by the earth's magnetic field. The price paid for this was a large instrumental $\gamma-$ray background produced by CR interactions with the material of the telescope and that of the spacecraft in front of the instrument. This background proves to be one of the major sources of uncertainty in the $\gamma-$ray analysis reported here.

The selection criteria applied to the detected events are described by Hermsen (1980); In the present case, the parameters recommended by COS-B for processing the database have been used to construct maps of the $\gamma-$ray sky in the required energy ranges. In most cases, to allow in first order for instrumental energy dispersion, the sensitive area and exposure factors assigned to a particular bin have been estimated using an assumed $\gamma-$ray celestial spectral index of 2. Though the observed spectral index was often slightly different to this,

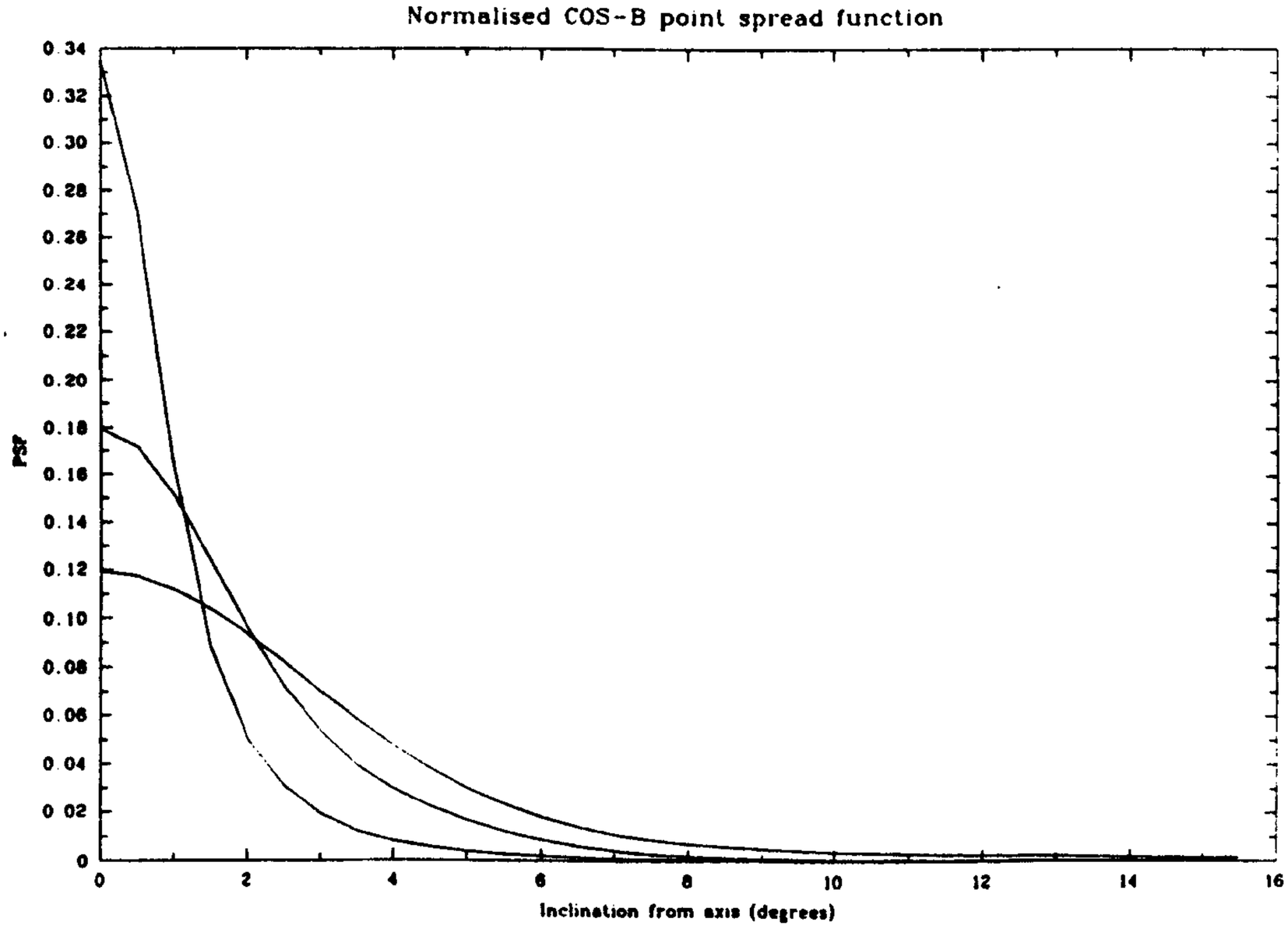

Fig 2.13 The COS-B $\gamma-$ray satellite point spread function (normalised), giving the probability per steradian to measure a photon in a given sky bin at an angle θ from the true incidence direction.

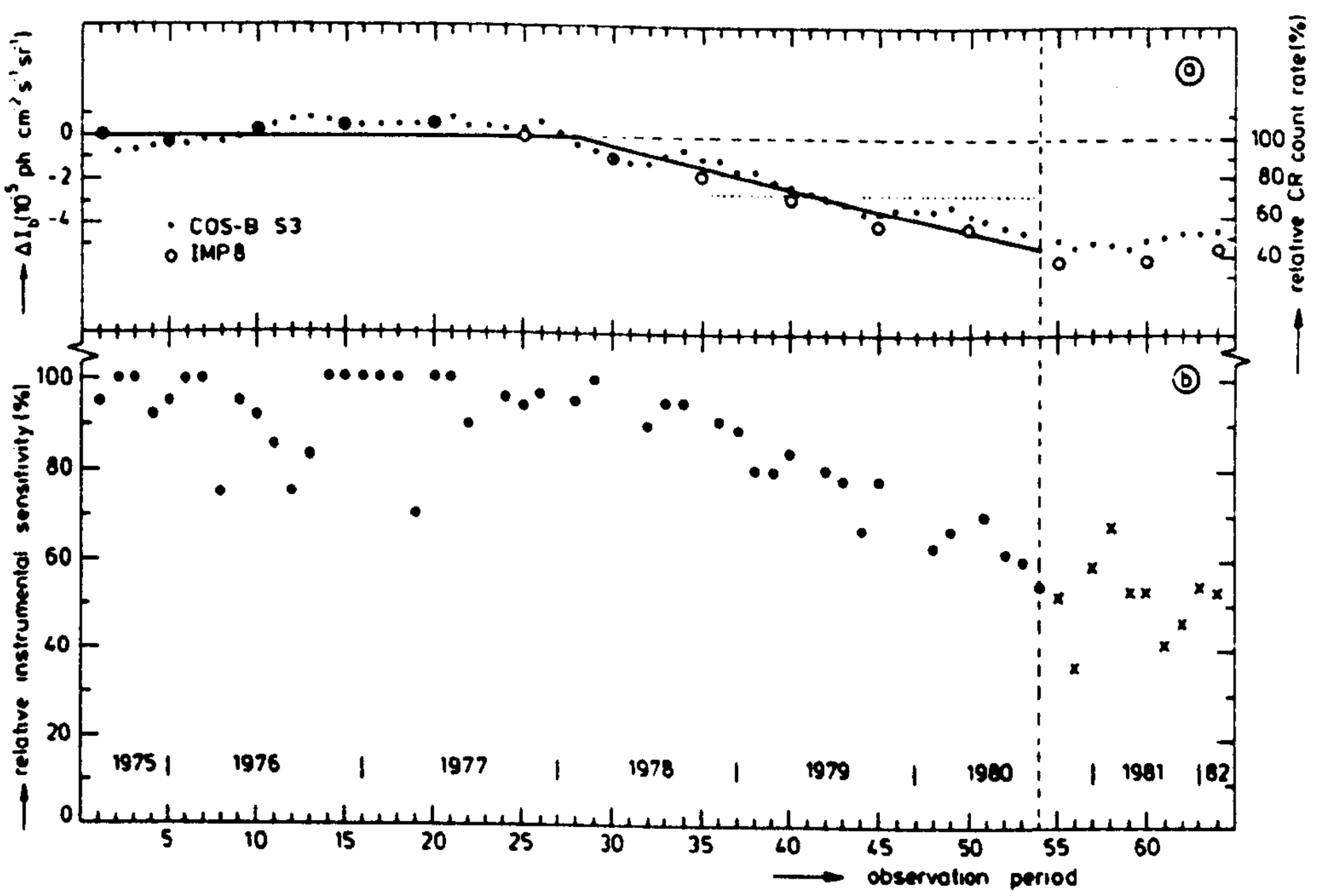

Fig 2.14 (a) Relative variations of the count-rate of cosmic ray particles (RH scale) as measured by the COS-B satellite S3 scaler, and the variation of the instrumental background (70 – 5000 MeV) of COS-B observations (LH scale). The thick curve indicates the smoothed variations of instrumental background from the low-latitude studies of COS-B data.
(b) Relative sensitivities of COS-B as a function of time-in-flight, derived from low-latitude observations. See Bloemen 1985 for details.

the impact on the resulting intensities was small ($\lesssim 10\%$). No iterative correction of the maps was attempted.

The angular resolution of the instrument was limited by multiple scattering of the electrons as they traversed the tungsten plates. Figure (2.13) gives the normalised profile of the point spread function (psf) for the three 'standard' energy bands 70−150, 150−300 and 300–5000 MeV. Note that the resolution is considerably worse at low energies, again because of multiple electron scattering. Details of its derivation are given in Bloemen (1985).

Considerable effort was expended by the COS-B group in estimating long-term trends in instrumental sensitivity and background. Strong et al. (1987a) give details of the in-flight calibration and its incorporation into the final dataset and map-making software used here. However, the estimation of the diffuse background deserves further mention at this point. A long term variation in the background was noted during the years of operation and was correlated, as expected, with changes in the solar-modulated CR flux (see Fig 2.14). In addition, the background was found to vary with inclination to the axis of the telescope. In the map making program supplied, this long-term trend is subtracted from each sky bin so that the 'effective' background is that applicable at the start of the mission. Similarly, the inclination dependence is removed by computing an equivalent 'on-axis' value.

In most COS-B analyses, the background is taken as a free parameter in the fitting procedure. In the present case, only a relatively small part of the observed $\gamma-$ray sky was typically considered. Having regard to the poor counting statistics, it was decided to use the best COS-B deduced background in each energy band. It must be born in mind that absolute intensities are rather sensitive to the background level, though for present purposes this is a minor problem since it is the relative values in different regions of the sky that are important.

CHAPTER 3
THE DERIVATION OF X_{20} IN LOCAL GMCS

3.1 Introduction

There are significant advantages in making a $\gamma-$ray analysis of local molecular clouds. Firstly, the clouds in the Orion-Monoceros, Taurus-Perseus-Auriga and Cepheus regions at $|b| > 10°$ are sufficiently large and close to be resolved by the COS-B satellite, despite its poor angular resolution. Secondly, the contribution from $\gamma-$ray point sources is also probably small (see §2.6). Finally, Inverse Compton emission in quadrants II and III is unlikely to be important.

Table 3.1

Source	ΔE	X_{20}	$\frac{q}{4\pi} \times 10^{-26}$	$I_b \times 10^{-5}$
	MeV	10^{20} mol cm^{-2} (K km s^{-1})$^{-1}$	ph atom^{-1} s^{-1} sr^{-1}	ph cm^{-2} s^{-1} sr^{-1}
[1]Bloemen (1985)	300−5000	2.6 ± 1.2	0.52 ± 0.13	2.0 ± 0.4
"	100 − 5000	3.0 ± 0.7	[2]1.70 ± 0.25	5.1 ± 0.4
[3]HW	100 − 5000	1.9 ± 0.3	[4]2.00 ± 0.28	[5]5.8

(1) Correlation region $198° < l < 222°$; $-25° < b < -5°$

(2) Average of estimates by Strong et al. (1982) and Bloemen et al. (1984a)

(3) Houston and Wolfendale (1985). Correlation region $200° < l < 220°$; $-25° < b < -5°$

(4) Average of several determinations (see Strong and Wolfendale 1981; Strong 1985a)

(5) Strong (1985b); Bloemen (private communication)

The large molecular clouds in Orion and Monoceros have already been the subject of several previous $\gamma-$ray studies using both SAS-2 and COS-B data. The results of some of these are presented in Table 3.1. Houston and Wolfendale (1985) correlated ΔI_γ versus $\left(\frac{q}{4\pi} W_{CO}\right)^\alpha$ where

$$\Delta I_\gamma = I_\gamma - I_b - \frac{q}{4\pi} N(\mathrm{HI})$$

for various values of α inside the $W_{CO} = 1\,\mathrm{K\,km\,s^{-1}}$ contour of the Orion clouds using the COS-B data available at the time. They averaged local emissivity estimates (see Houston 1985) and used the $\gamma-$ray background value derived by COS-B (Strong 1985a) finding $\alpha = 1.7$ and $X_{20} = 1.2 \pm 0.4$, though $\alpha = 1.0$, $X_{20} = 1.8 \pm 0.5$ was not inconsistent with the data. Table (3.2) summarises the main results obtained by Houston (1985) for several combinations of parameters.

Because of the differences with the work of Bloemen et al. (1984b) for the same clouds, Houston (1985) repeated the analysis over the same region as Bloemen et al. using an identical emissivity and background, obtaining $X_{20} = 2.5 \pm 0.4$. As can be seen from Table (3.1), the two results are the same, within errors.

Limited photon statistics led Houston and Wolfendale (1985) to conclude that their result $\alpha > 1$ was not strong evidence for an excess of CRs in the Orion clouds. In fact, they discounted this possibility because previous work by Issa and Wolfendale (1981) had shown the mass ratios between the Orion A and Orion B clouds as measured in $\gamma-$rays

and CO emission were approximately equal. They argued that this result would not follow if the number of cosmic ray sources in the two clouds was different, as might be expected. However, Morfill (1982) has demonstrated that the low energy electron spectrum can be enhanced inside a molecular cloud by CR propagation effects. Thus the equality of mass estimates does not necessarily mean the CR flux in the clouds is not enhanced. The Houston and Wolfendale results are consistent with this picture since electron bremsstrahlung emission is probably a major part of the $E_\gamma > 100\,\mathrm{MeV}$ COS-B energy band.

Table 3.2

α	$I_b \times 10^{-5}$ ph cm^{-2} s^{-1} sr^{-1}	$\frac{q}{4\pi} \times 10^{-26}$ ph atom^{-1} s^{-1} sr^{-1}	X_{20} 10^{20} mol cm^{-2} (K km s^{-1})$^{-1}$
[1]1.7	[2]5.8	[3]2.0	1.3 ± 0.5 (64%)
1.0	"	"	1.9 ± 0.3 (17%)
"	[4]5.1	"	2.2 ± 0.3 (35%)
[1]1.2	"	"	1.8 ± 0.4 (46%)
1.0	[2]5.8	[4]1.7	2.5 ± 0.4
[1]2.3	[5]5.4	2.0	1.0 ± 0.7
1.0	[5]7.8	"	2.7 ± 0.6

(1) Best fit (minimum χ^2) values
(2) Strong (1985b); Bloemen (private communication)
(3) See Table (3.1)
(4) Corresponds to values estimated by Bloemen et al. (1984b)
(5) Fitted during analysis

Bloemen et al. (1984b) used a maximum likelihood technique to estimate $q/4\pi$, X and I_b in the region $198° < l < 222°$, $-25° < b < -5°$ for the two energy ranges $300-5000$ MeV and $100-5000$ MeV. The COS-B intensities were fitted to (c.f. equation 2.24)

$$I_\gamma = A\tilde{\mathrm{N}}(\mathrm{HI}) + B\tilde{\mathrm{W}}_{\mathrm{CO}} + C. \tag{3.1}$$

For the 300–5000 MeV range, which has the highest resolution, all three parameters could be estimated. However, for the other energy band, the convolved HI map was spatially similar to a flat background and the parameters A and C could not be determined independently. In this case, A was set equal to the average local emissivity of Strong et al. (1982) and Bloemen et al. (1984a) i.e., $A = (1.7 \pm 0.25) \times 10^{-26}\,\mathrm{atom^{-1}\,s^{-1}\,sr^{-1}}$. The results are listed in Table (3.1). The value of A for $300-5000$ MeV is consistent with other COS-B estimates of the local $\gamma-$ray emissivity (see, for example, Strong et al. 1982; Bloemen et al. 1984a). However, there seems to be no evidence in Bloemen et al. (1984b) for an excess of CRs in the Orion molecular cloud.

3.2 Local Molecular Clouds

A. Orion and Monoceros.

A well sampled CO survey of the Orion and Monoceros region has been obtained by Maddalena (1986) using the Columbia 1.2 metre telescope at either $\frac{1}{4}°$ or $\frac{1}{2}°$ resolution (FWHM).

The survey region, and outline of the CO emission are shown in Fig (3.1) and (3.2). Almost 12% of the 850 $\deg^2$ area mapped showed CO emission with $T^r > 0.8$ K in the velocity range -10 to 10 $\mathrm{km\,s^{-1}}$, much of it concentrated in the three large clouds denoted Orion A, Orion B and Monoceros R2 in Fig (3.2). Orion A and B are connected by low level emission with no velocity discontinuity, suggesting that they may be physically associated. The Orion OB1 association, located just to the west of the Orion clouds, is probably responsible for the higher T^r(CO) observed on the western cloud edge (see Maddalena 1986 for more details).

Orion A may be rotating about an axis perpendicular to the Galactic plane in a direction opposite to that of the Galaxy. Maddalena (1986), Chin (1978) and Kutner et al. (1977) all found substantial velocity gradients across the cloud. However, the nearby OB 1 association shows no such gradient, as might have been expected if it formed $\sim 10^6 - 10^7$ years ago.

Monoceros R2 also shows considerable evidence of star forming activity, having embedded IR sources, a compact HII region and both H_2 and OH masers. Maddalena (1986) suggests that it may be a less complex, younger version of the Orion nebula region. The cloud subtends $\sim 14\,\deg^2$ and is about 850 pc away, making it comparable in size and luminosity to the Orion complex. However, it may be more centrally condensed than these clouds since most emission comes from the cloud 'core' and little from the envelope. The western edge of the cloud, nearest the star forming region, shows the largest temperature gradient and velocity widths. A velocity gradient across the cloud face may imply rotation in the same sense as Orion A.

Heavy metal (C, O etc.) abundances in the Orion clouds are probably about 50% below solar. This may have implications for the CO to H_2 conversion ratio as argued by Bhat et al. (1985). A difference in X_{20} between the Orion and, say, Taurus clouds (see below) could be expected if this were the case.

B. Taurus, Perseus and Auriga.

The dark clouds in the vicinity of the Taurus region have been recently mapped with the Columbia telescope by Ungerechts and Thaddeus (1986) at an angular resolution of $\frac{1}{2}^\circ$. The three main clouds are:

(i) The northern Perseus-Auriga cloud associated with NGC1499 and NGC1579 at a distance of 350 pc.

(ii) The Taurus clouds in the centre, including an extension into Auriga at 140 pc.

(iii) The Perseus OB2 cloud to the west of Taurus at 350 pc and probably associated with the Per OB2 association. This cloud has the strongest W_{CO} and T^r of the three and is coincident with NGC133, a bright nebula in a region of active star formation.

The Taurus and Auriga clouds cover a total of 200 $\deg^2$, making them the largest molecular clouds in the sky in angular size. However, they are closer than the Orion clouds and are an order of magnitude less massive.

B. Cepheus.

An extensive CO survey in Cepheus ($100^\circ < l < 116^\circ$; $12^\circ < b < 24^\circ$) by Lebrun (1986) established the existence of another major complex of molecular gas at about 500 pc away from the sun and of comparable CO luminosity to those in Orion. However, it is probably less active since it contains no bright IR sources. Lebrun noted the close correspondence in velocity, line shape and width to the HI complex observed by Heiles (1967) and suggested a close connection between them.

C. Other local clouds.

There are significant local complexes closer to the Galactic plane than those described above. These are not dealt with here. However, the distribution of all molecular clouds within 1 kpc of the sun detected by the Columbia telescope is shown in Fig (3.4). Comparing this

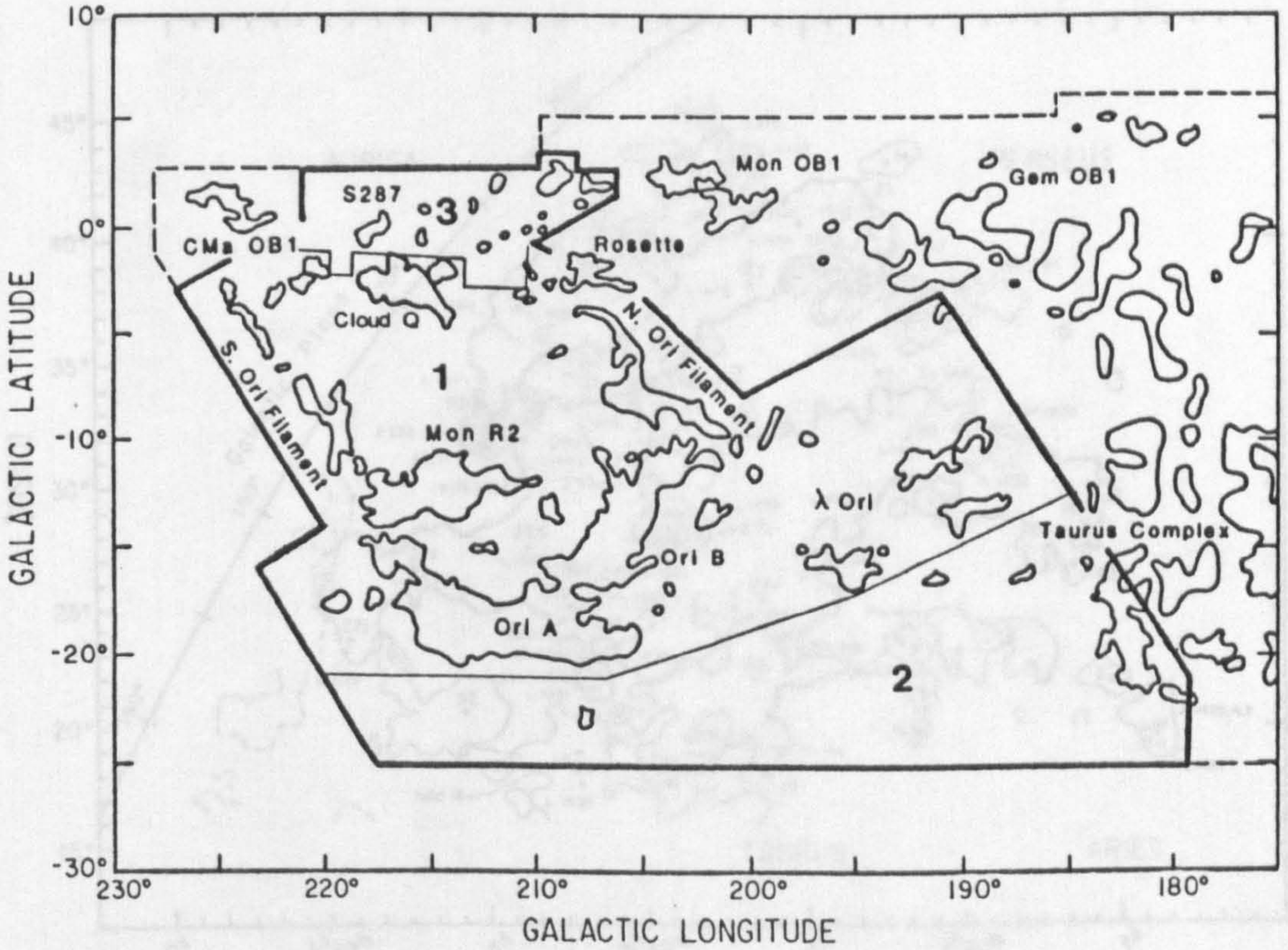

Fig 3.1 The region surveyed in CO by Maddalena (1986) (outlined by the thick solid line). Other large molecular clouds detected by the Columbia telescope are also shown.

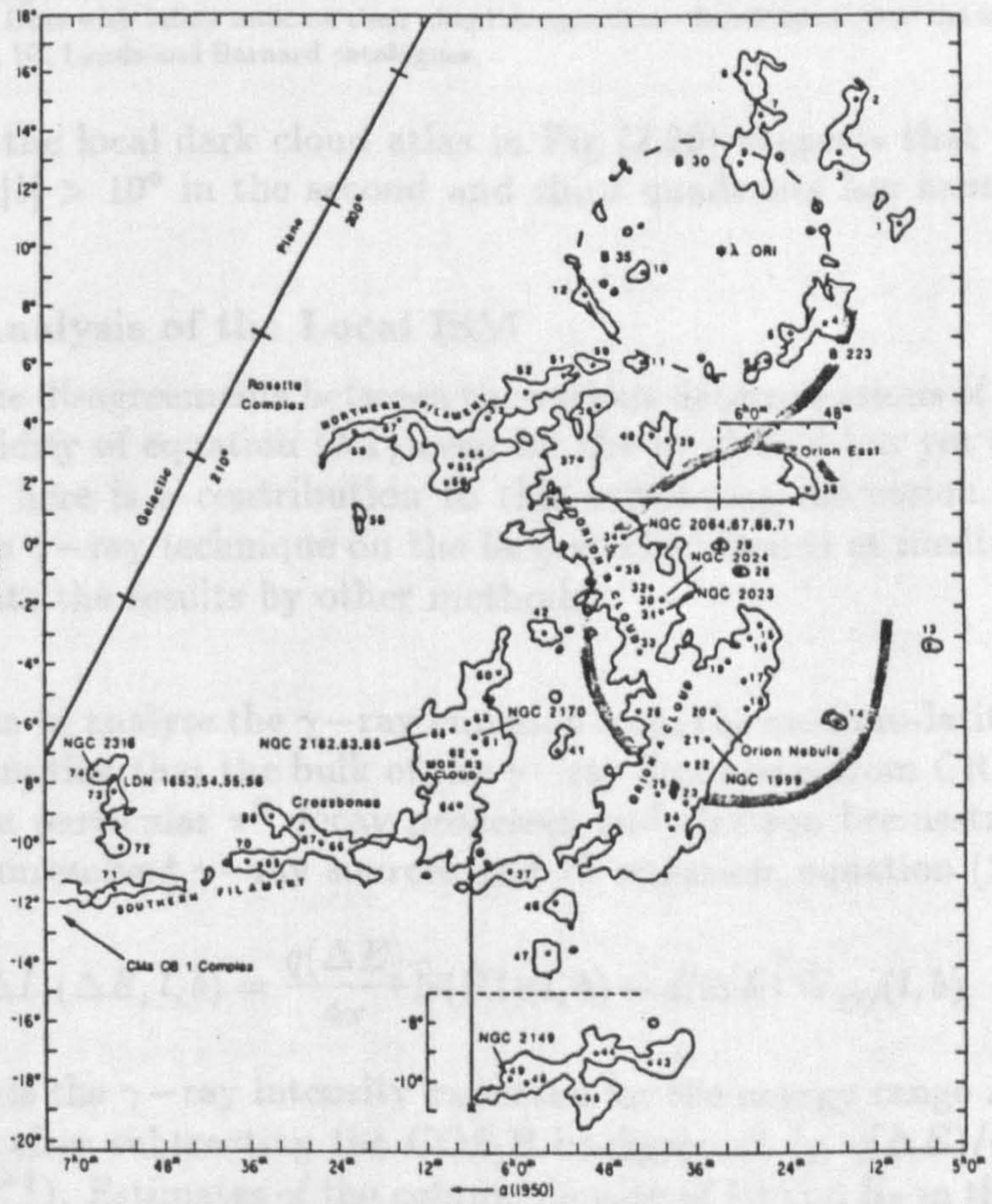

Fig 3.2 Schematic diagram of molecular clouds giving their outline in W_{CO} at the $1.28\,\mathrm{K\,km\,s^{-1}}$ level. Dots with numbers indicate the location of CO emission peaks (see Maddalena 1986 for details). NGC numbers indicate some optically prominent objects that are coincident with CO peaks. The extent of uv emission from Barnard's Loop is shown by the shaded arc.

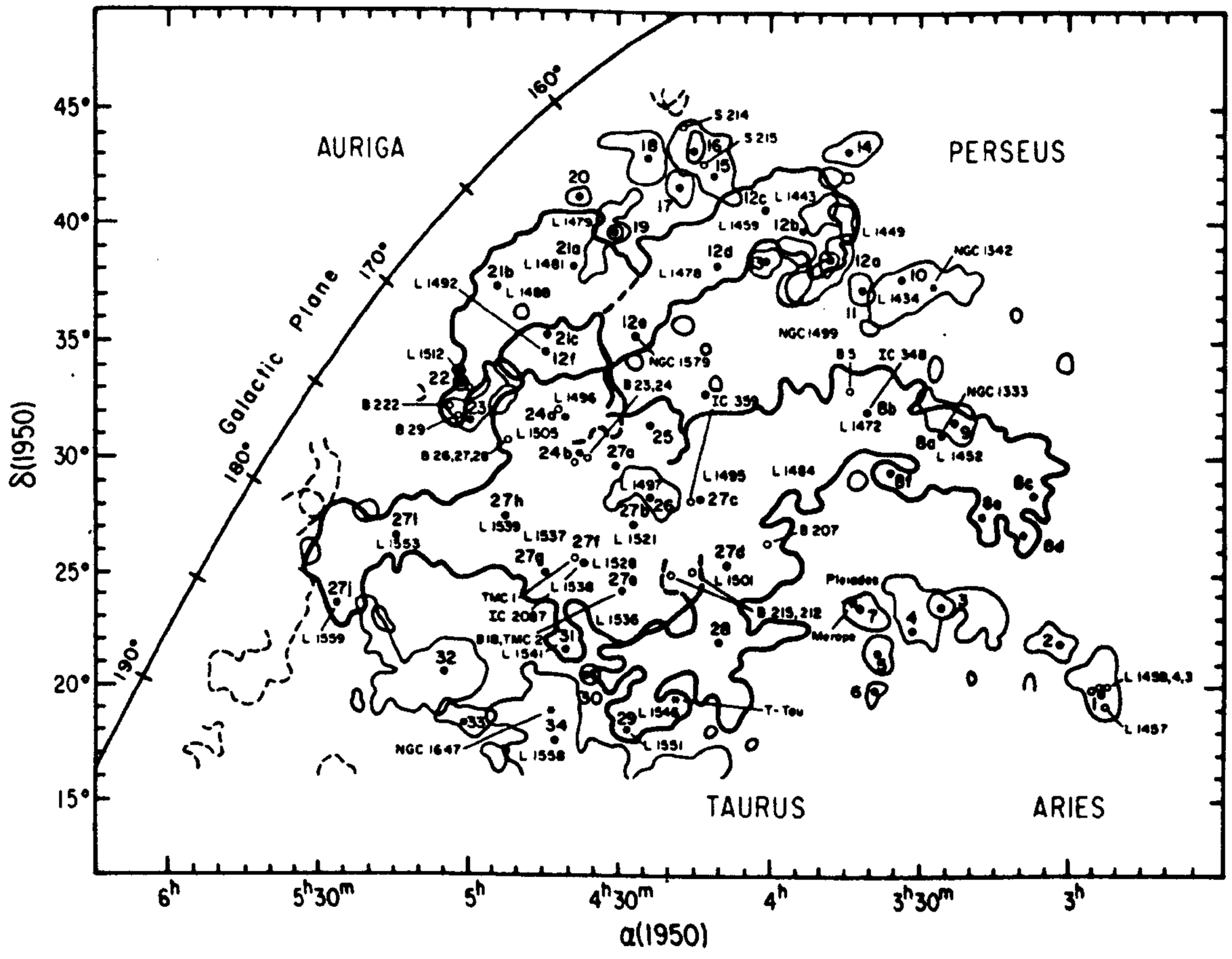

Fig 3.3 Outline of W_{CO} emission at the 0.5 K km s^{-1} level in the Taurus-Perseus-Auriga region found by Ungerechts and Thaddeus (1986). Dots with labels indicate their cloud designations. Small labels give the locations of various objects from the NGC, IC, Lynds and Barnard catalogues.

with Fig (2.2*a*) and the local dark cloud atlas in Fig (2.2*b*) suggests that most of the mass in molecular gas at $|b| > 10°$ in the second and third quadrants has been included in this analysis.

3.3 Gamma ray Analysis of the Local ISM

It is clear from the disagreements between the various determinations of X_{20} that its value and the range of validity of equation (3.1) even for the local ISM has yet to be established. The work described here is a contribution to this continuing discussion. The philosophy adopted is to use the $\gamma-$ray technique on the largest local clouds at medium latitudes, and to try and corroborate the results by other methods.

A. The Method

The model chosen to analyse the $\gamma-$ray emission from the medium-latitude cloud sample is based on the assumption that the bulk of the $\gamma-$ray flux arises from CR interactions with nuclei in the ISM; in particular π^0 decay processes and electron bremsstrahlung. Ignoring contributions from unresolved $\gamma-$ray sources and IC emission, equation (2.24) becomes

$$\Delta I_\gamma(\Delta E, l, b) = \frac{q(\Delta E)}{4\pi}\tilde{\mathrm{N}}(\mathrm{HI})(l,b) + a(\Delta E)\,\tilde{\mathrm{W}}_{\mathrm{CO}}(l,b) \qquad (3.2)$$

where $\Delta I_\gamma(\Delta E, l, b)$ is the $\gamma-$ray intensity expected for the energy range ΔE in the COS-B bin centered on l, b after subtracting the COS-B background I_b; $q(\Delta E)/4\pi$ is the emissivity (in atom^{-1} s^{-1} sr^{-1}). Estimates of the column density of HI and H_2 in the bin are deduced from 21 cm observations and CO emission, convolved to the appropriate psf (denoted by the tilde). The constant $a(\Delta E)$ can be identified with the product $\frac{q(H_2)}{4\pi}X_{20}$ to allow for the possibility of a different $\gamma-$ray spectrum for diffuse HI clouds and dense molecular clouds.

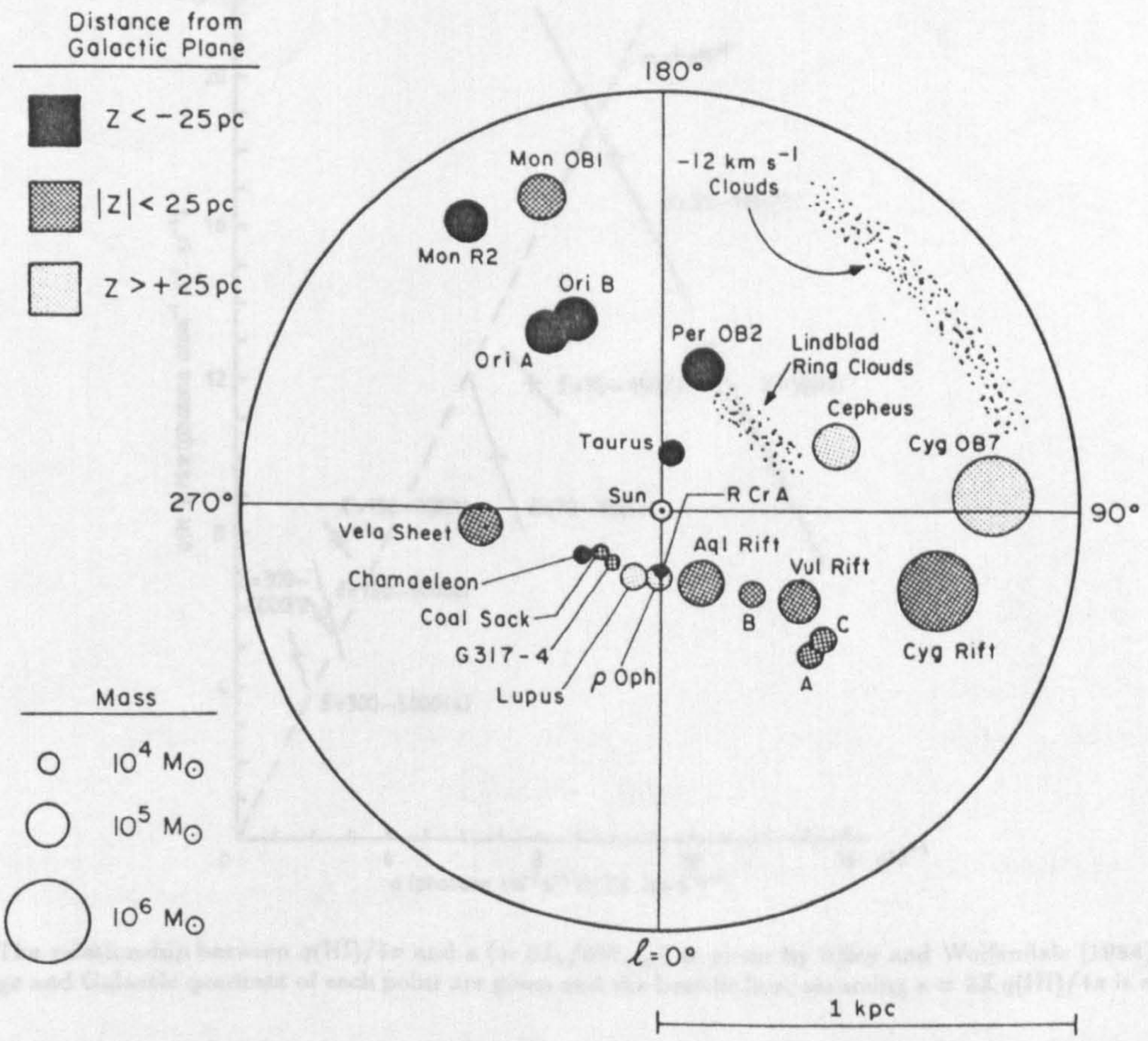

Fig 3.4 The distribution in the Galactic plane of molecular clouds within 1 kpc of the sun as given by Dame et al. (1987). The circle radius is proportional to the cube root of the cloud mass and in most cases is close to the cloud's actual radius. The shading indicates distance from the Galactic plane.

This question has been addressed by several workers. Issa and Wolfendale (1981) searched the available COS-B and SAS-2 data for such an excess from 13 nearby cloud complexes for which rough mass estimates were then available (excess here means relative to the local ISM). Their data included Orion A and B, Monoceros, Taurus and Per OB2. They found evidence for a significant enhancement in CR densities only in the Carina nebula and Cas OB6, with a mean excess for all clouds of 1.3. However, the Orion, Taurus and Per OB2 clouds appeared deficient in CRs relative to the local ISM. On a scale of several kpc Riley and Wolfendale (1984), using COS-B data from the first quadrant (Mayer-Hasselwander et al. 1982), noted that the emissivity spectrum for H_2 was steeper than that of HI. Their fit to the COS-B data (Fig 3.5) implied

$$\frac{q(\mathrm{HI})}{q(\mathrm{H_2})} \propto E^{-0.24},$$

though the error on the index is large. A different trend was suggested by the SAS-2 data; inclusion in the above fit made the errors considerably larger (formally ± 0.25). Riley and Wolfendale also examined the COS-B data of Strong et al. 1982 at medium latitudes ($|b| = 11°$ to $19°$) and found no evidence for a difference in energy spectrum between $\gamma-$ray emission from HI and H_2.

Bloemen et al. (1984a) studied this problem in a large-scale analysis of Galactic $\gamma-$ray emission by requiring the emissivity ratios for the three standard COS-B energy bands to be the same in each of 4 bins of galactocentric radius (see equation 2.24). Their resultant fit implied q(HI) and Y had different spectral shapes, but was poorer (chance probability $= 3 \times 10^{-3}$) than when the Y_j were forced to be the same in all energy bins (chance

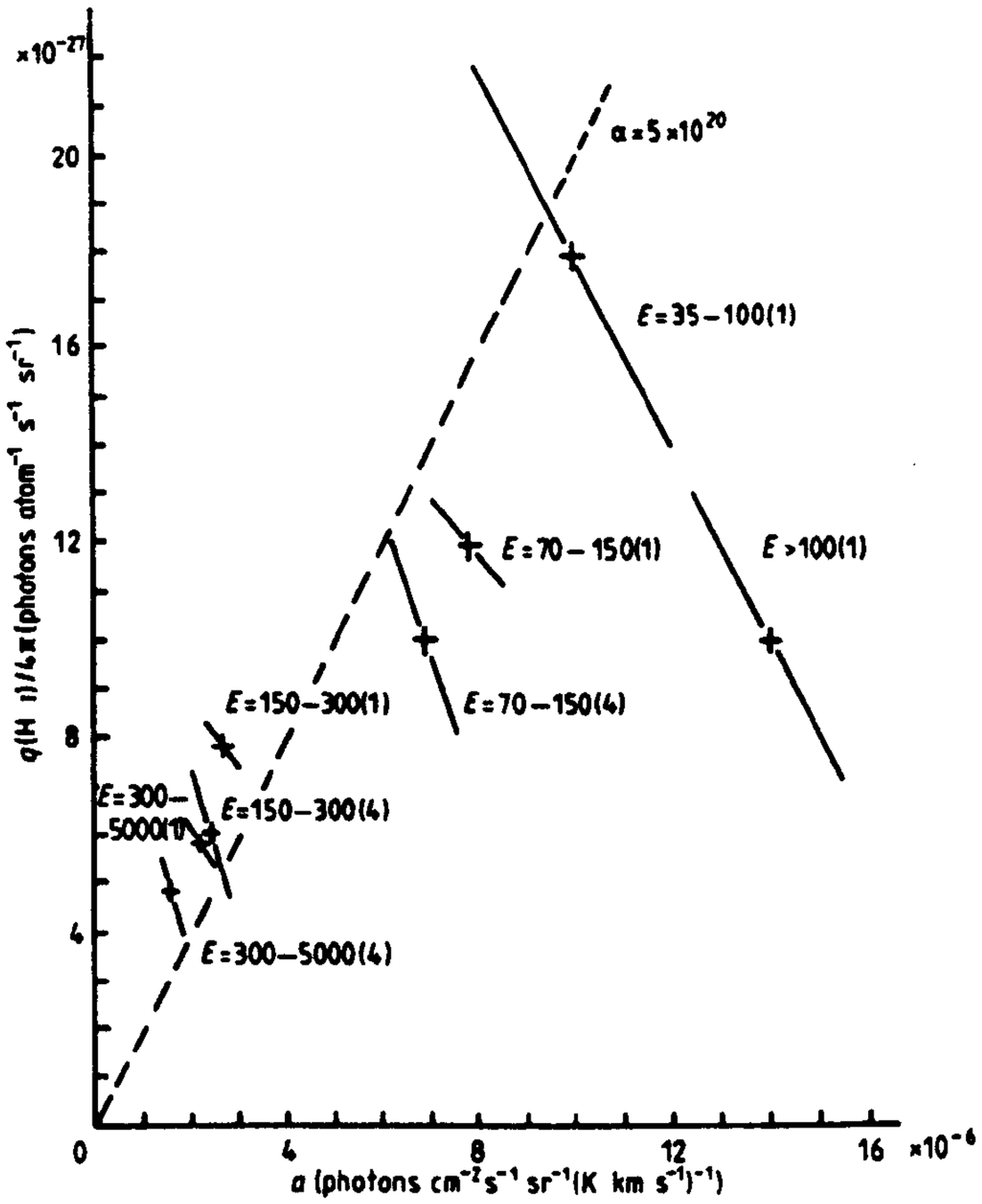

Fig 3.5 The relationship between $q(\mathrm{HI})/4\pi$ and a ($= \partial I_\gamma / \partial W_{CO}$) as given by Riley and Wolfendale (1984). The energy range and Galactic quadrant of each point are given and the best-fit line, assuming $a = 2X\, q(\mathrm{HI})/4\pi$ is shown.

probability $= 6 \times 10^{-12}$); they argued that there was no evidence for $q(\mathrm{H_2}) > q(\mathrm{HI})$. The more recent analysis of Strong et al. (1987) strengthens the evidence for a radial gradient in the higher-energy $\gamma-$ray emissivity, but still argues for equality of HI and H_2 spectra. Nevertheless, there is some (slight) evidence for CR production within inner Galaxy clouds in their results (see §2.6).

Though the evidence is equivocal, there is a theoretical expectation that CR enhancement in GMCs may be significant. The models of Montmerle (1979) and Morfill (1982) can be cited in this regard. Equation (3.2) does not explicitly separate the HI and H_2 emissivities; differences in spectral shape would appear as a modified energy dependence of a relative to $q(\mathrm{HI})/4\pi$.

Before a more detailed discussion of the data used in the analysis, some inadequacies of the model should be noted. Equation (3.2) presumes that the averaging implicitly performed by the fitting procedure makes physical sense i.e., that CR gradients are not too big. Gradients on the kpc scale could not contribute much to variations at these latitudes (see Bhat et al. 1986a), but local production of CRs (in SNRs, GMCs etc.) may produce significant enhancements on small scales. A CR excess not connected with molecular clouds but merely coincidental along the line of sight will complicate the interpretation of the model fits. This difficulty is compounded by the fact that X_{20} appears in equation (3.2) multiplied by $q(\mathrm{H_2})/4\pi$ and can only be separated if $q(\mathrm{H_2})/q(\mathrm{HI})$ is known independently.

Any contribution from the WIM, mentioned in §2.2, is also not explicitly allowed for in the model. Since it is unlikely to be correlated with molecular clouds and I_b has been fixed at its 'best' COS-B value, a general increase in $q(\mathrm{HI})$ may occur. As noted previously, the WIM contribution is probably not negligible; however, other estimates of the local emissivity have ignored this phase, so the results obtained here are at least comparable. Further study of this point is required.

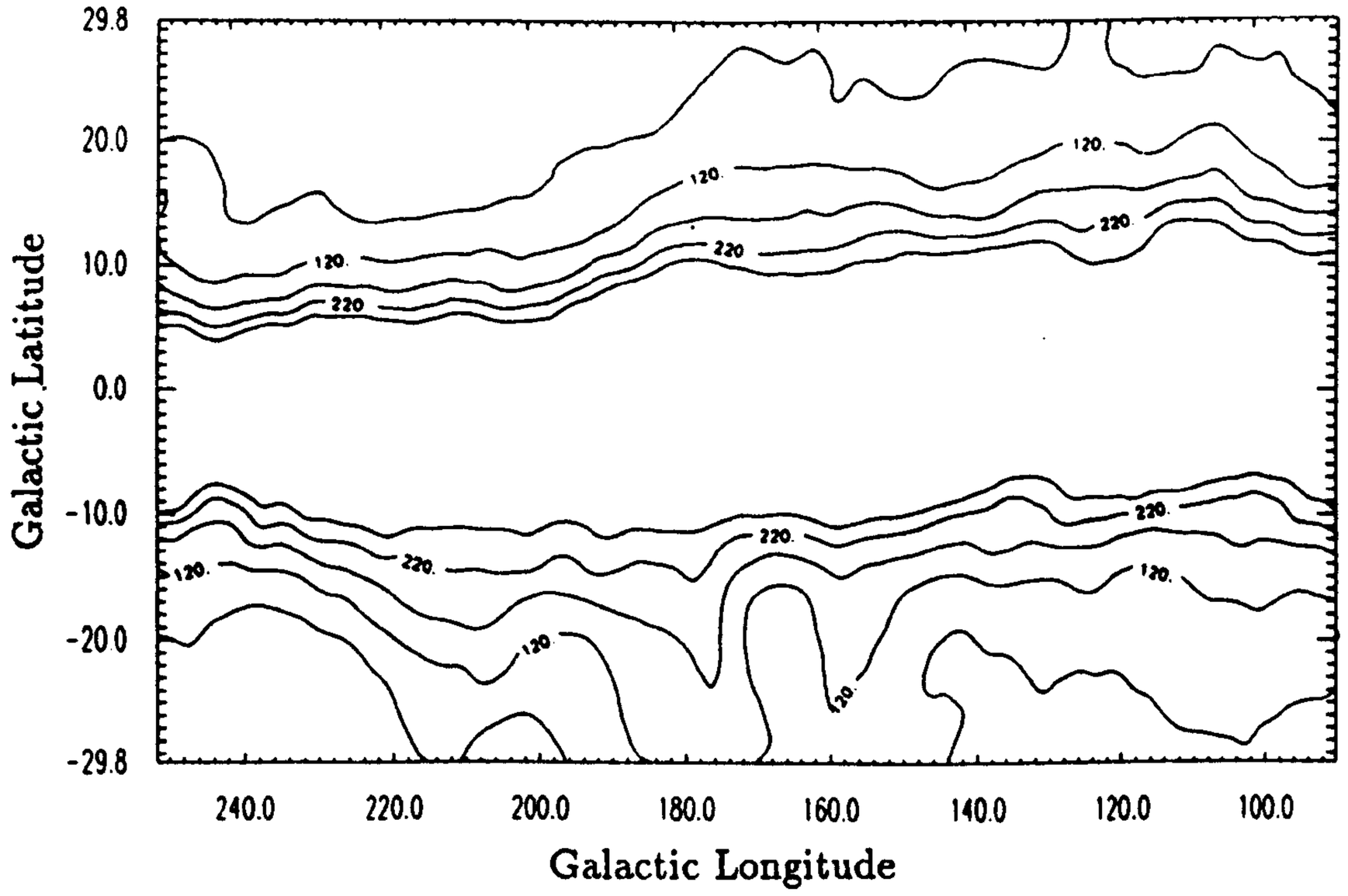

Fig 3.6 Column densities of HI in 1° x 1° bins for the region studied in the $\gamma-$ray analysis. Contours at 70, 120, 170, 220 and 170 x 10^{19} atoms cm^{-2} are shown

B. The Data

Neutral HI column densities for latitudes below 10° have been derived from the 21 cm survey of Heiles and Cleary (1979). Though outside the scope of this work, the region is required for a correct convolution with the rather wide COS-B psf. Saturation effects were corrected using equation (2.14) by assuming a spin temperature of 135 K. This simple approach should not incur too great an error ($\lesssim 30\,\%$ according to Strong et al. 1982), particularly at medium latitudes. Above $|b| = 10°$, the Heiles and Habing (1974) data were used, assuming the emission to be optically thin. The resulting maps were combined and are shown in Fig (3.6).

Contour maps of CO emission, given in the literature for:

- Orion-Monoceros (Maddalena 1986)
- Taurus-Perseus-Auriga (Ungerechts and Thaddeus 1986)
- Cepheus (Lebrun 1986)

were digitised and interpolated with the Sibson (1981) routines. The gas data were then convolved to the resolution of the COS-B instrument for the three 'standard' $\gamma-$ray energy bands i.e., 70 – 150, 150 – 300 and 300 – 5000 MeV and combined. The W_{CO} maps for 300 – 5000 MeV are shown in Fig (3.7). They are compared with the same region from the recently released Columbia combined CO survey in Fig (3.8) which has been convolved to the same resolution. The only significant difference between them is the presence of low level ($W_{CO} \lesssim 0.5\,\mathrm{K\,km\,s^{-1}}$) emission smeared over large angular distances by the COS-B psf. It is shown later that this has no effect on the analysis.

The model was also tested for the 'non-standard' 800 – 5000 MeV band. In this case, there is no psf available with the database, However, Hermsen (1980) and Bloemen (1985) have given an earlier representation of it – viz.

$$f(\theta) = N e^{-(\theta/\theta_0)^{2c}}$$

where θ_0 and c are energy-dependent parameters and N is a normalisation constant. From the data in Bloemen (1985) it is possible to estimate the ratio between θ_0 and c for 300–5000

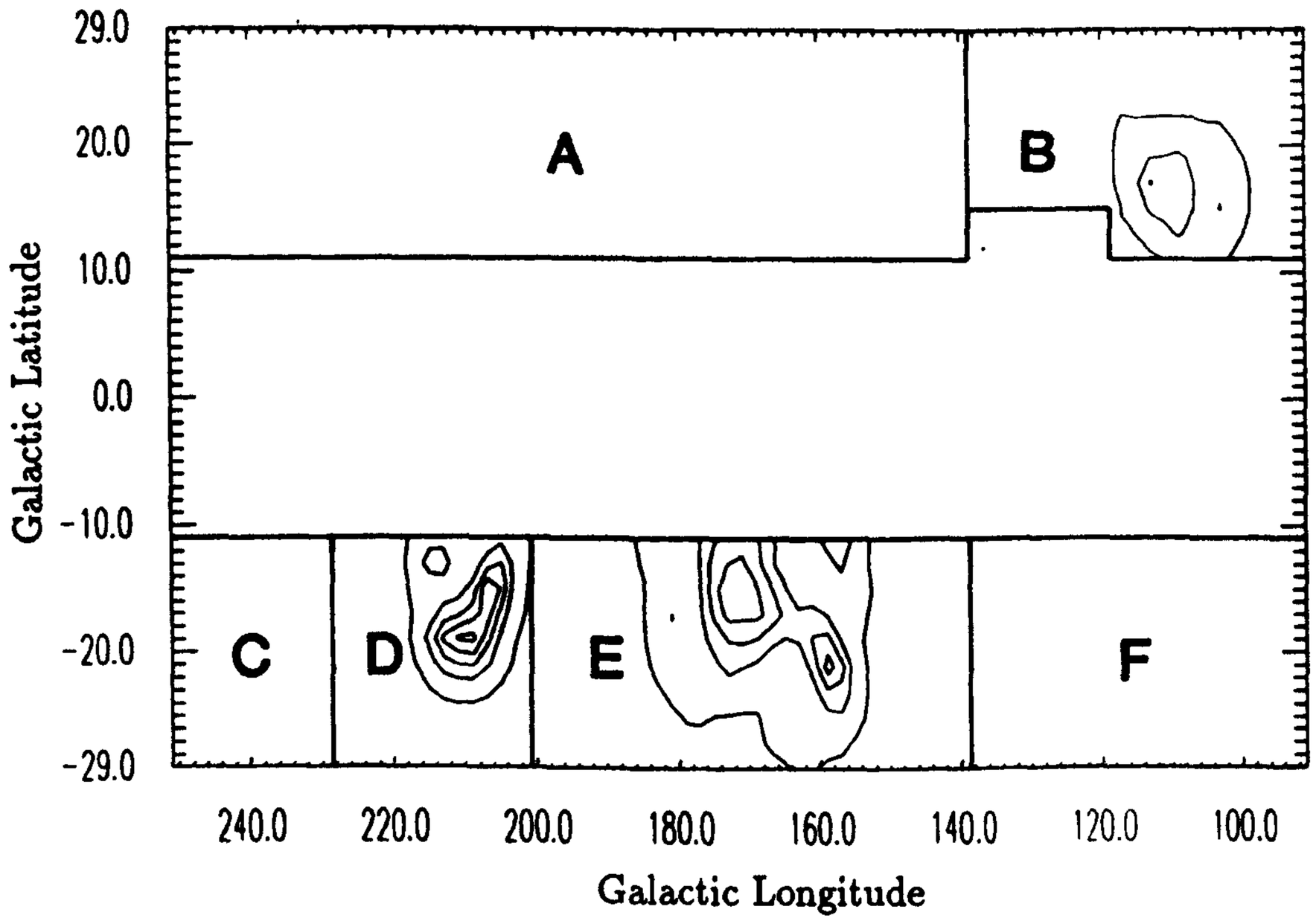

Fig 3.7 Contours of W_{CO} in 2° x 2° bins convolved to the 300–5000 MeV COS-B psf in the region of interest (see text for details). The lowest contour is at 0.5 K km s^{-1} with 2 K km s^{-1} intervals. The l, b extent of the subregions A-F used in the γ–ray analysis are outlined.

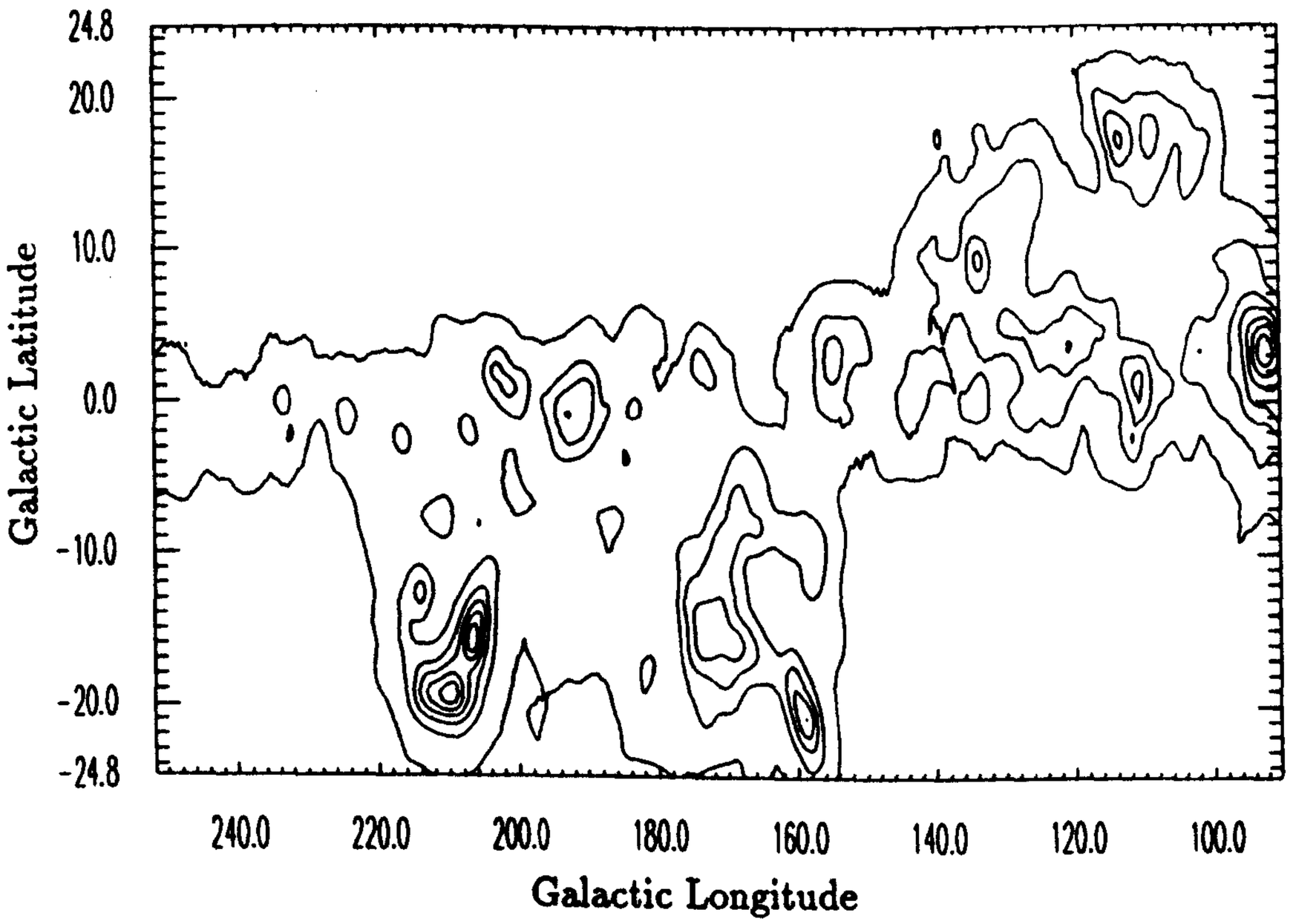

Fig 3.8 W_{CO} from Dame et al. (1987) convolved to 300 – 500 MeV. in 0.5° x 0.5° bins

and 800–5000 MeV as 1.1 and 1.0 respectively. Considering the other uncertainties, and the poor photon statistics at this higher energy, it was decided that the gas data convolved to 300–5000 MeV were sufficiently good representations to use at 800–5000 MeV.

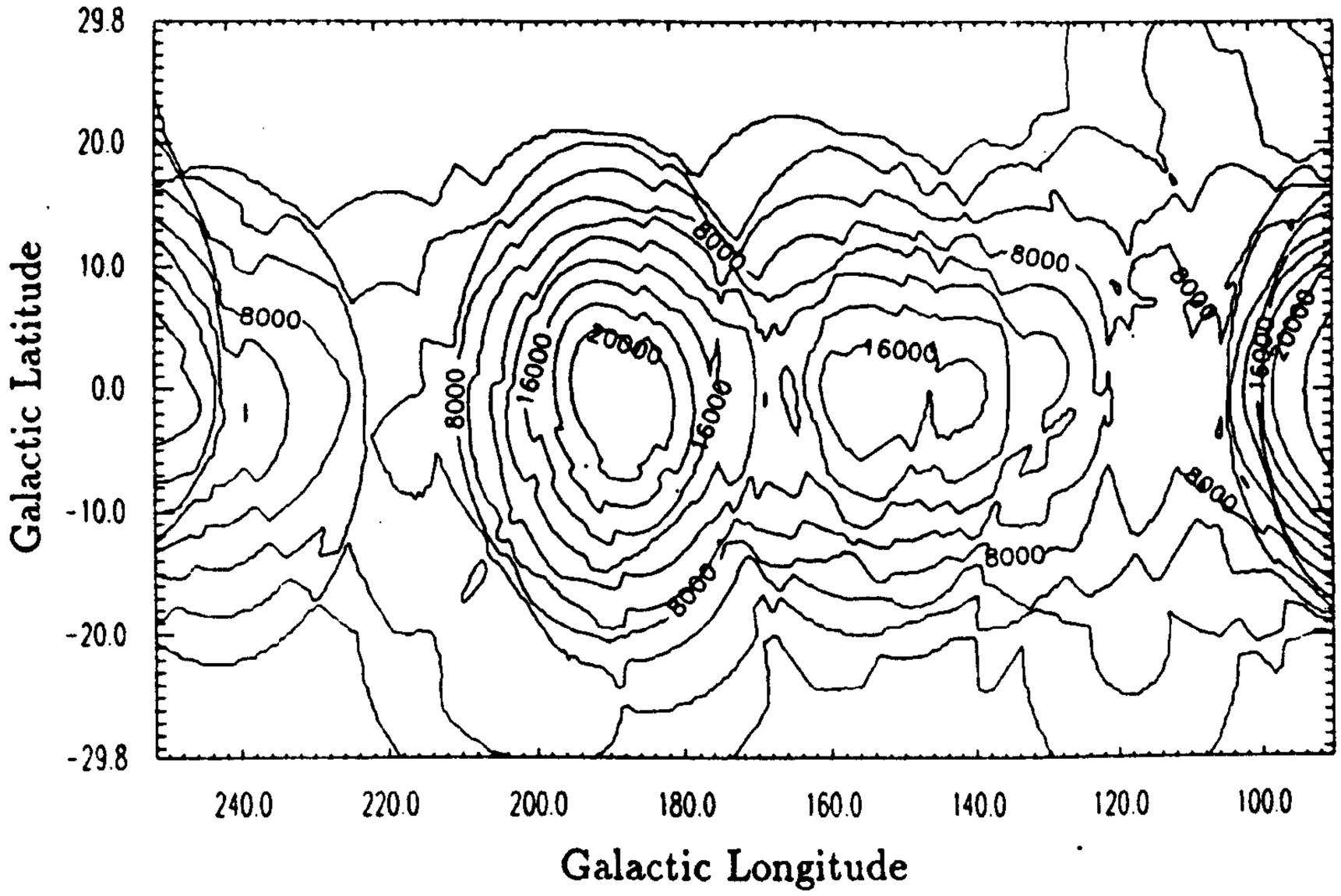

Fig 3.9 COS-B exposure factors (300–5000 MeV) used in the γ–ray analysis. The contour interval is 2000 cm^2 s sr.

Gamma ray maps were constructed with the COS-B supplied software using the following parameters (see the ESTEC manual for details).

- Gamma-class = 2
- Edit class = 1
- Pair opening angle = 90°
- Photon incidence experimental upper limit = 20°
- Inclination dependence parameters:
  (i) $A_2 = 8.55 \times 10^{-4}$
  (ii) $A_4 = -5.63 \times 10^{-2}$
- Assumed differential spectral index of celestial emission = 2.0
- Assumed background differential spectral index = 2.0

Finally, the γ–ray, HI and W_{CO} maps were averaged to 2° × 2° bins. The averaging process had only a marginal impact on the fitted parameters but markedly decreased the computation time. Fig (3.9) gives contours for corrected COS-B exposures towards the region studied.

C. Procedure

The anticentre region containing these medium latitude clouds was divided into 6 subregions. Three contained little CO emission (A, C, and F in Fig 3.7) while the rest contained the molecular clouds (B, D and E). To examine the many permutations possible in a reasonable amount of CPU time, a NAG multi-parameter linear correlation program was used, weighting the data with the COS-B exposure factors. Equation (3.2) was fitted to the data in regions $B + D$, E, $B + D + E$ and in $A + C + F$. Simplified versions of the model were

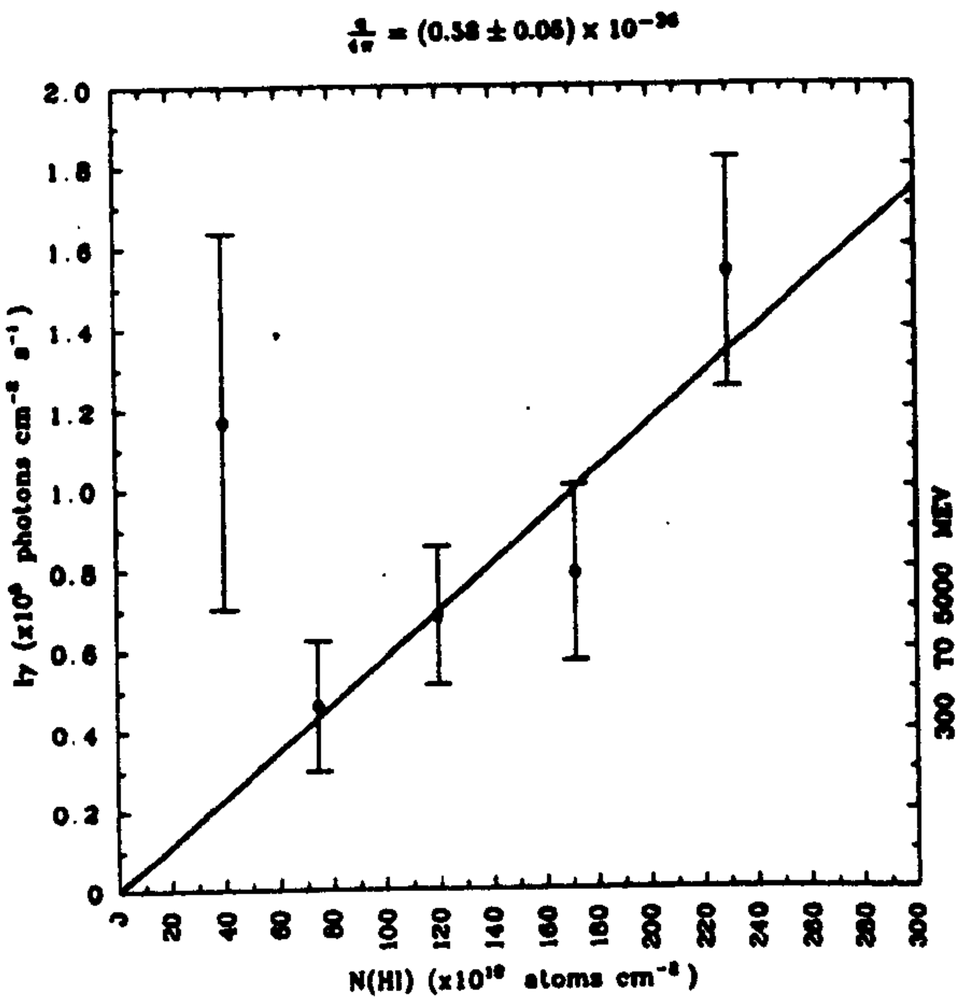

(a)

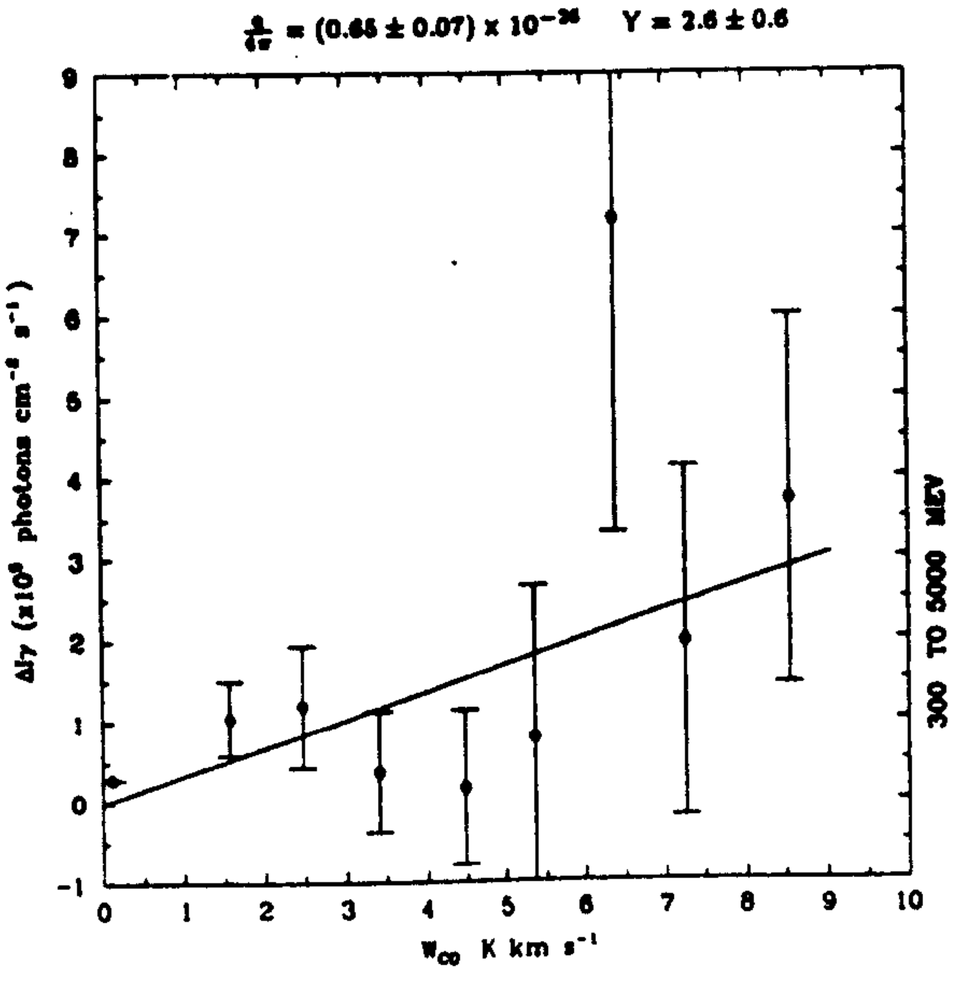

(b)

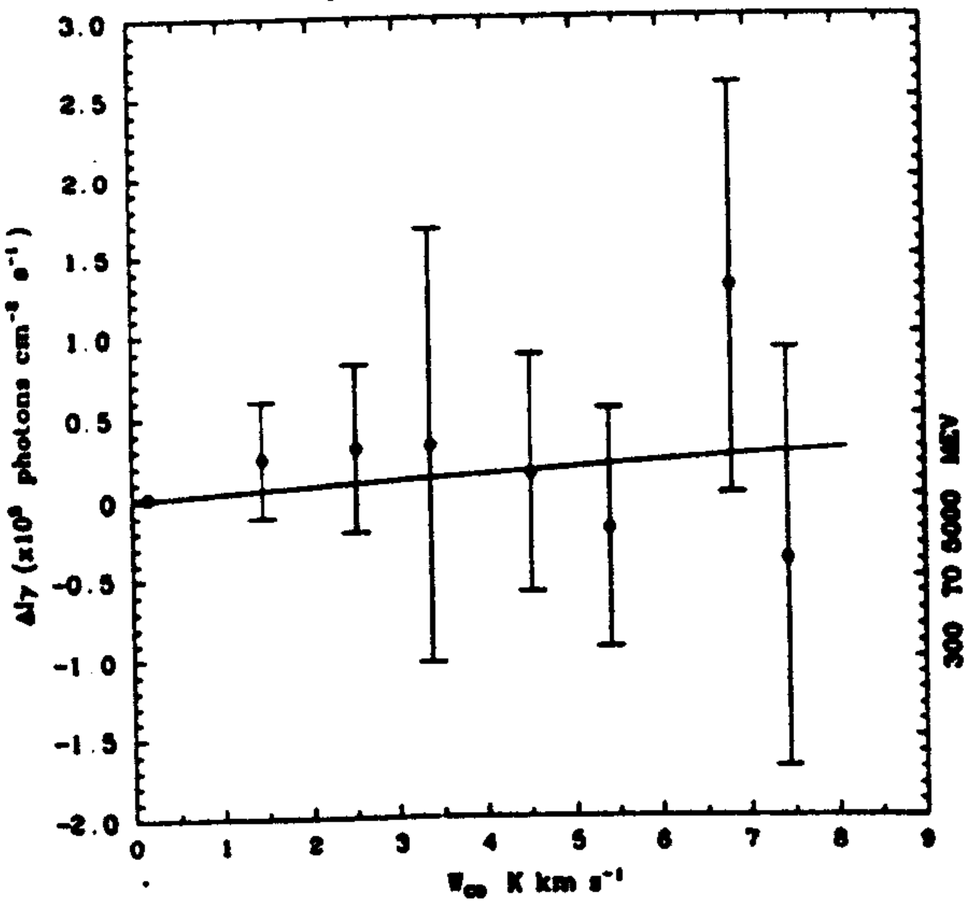

(c)

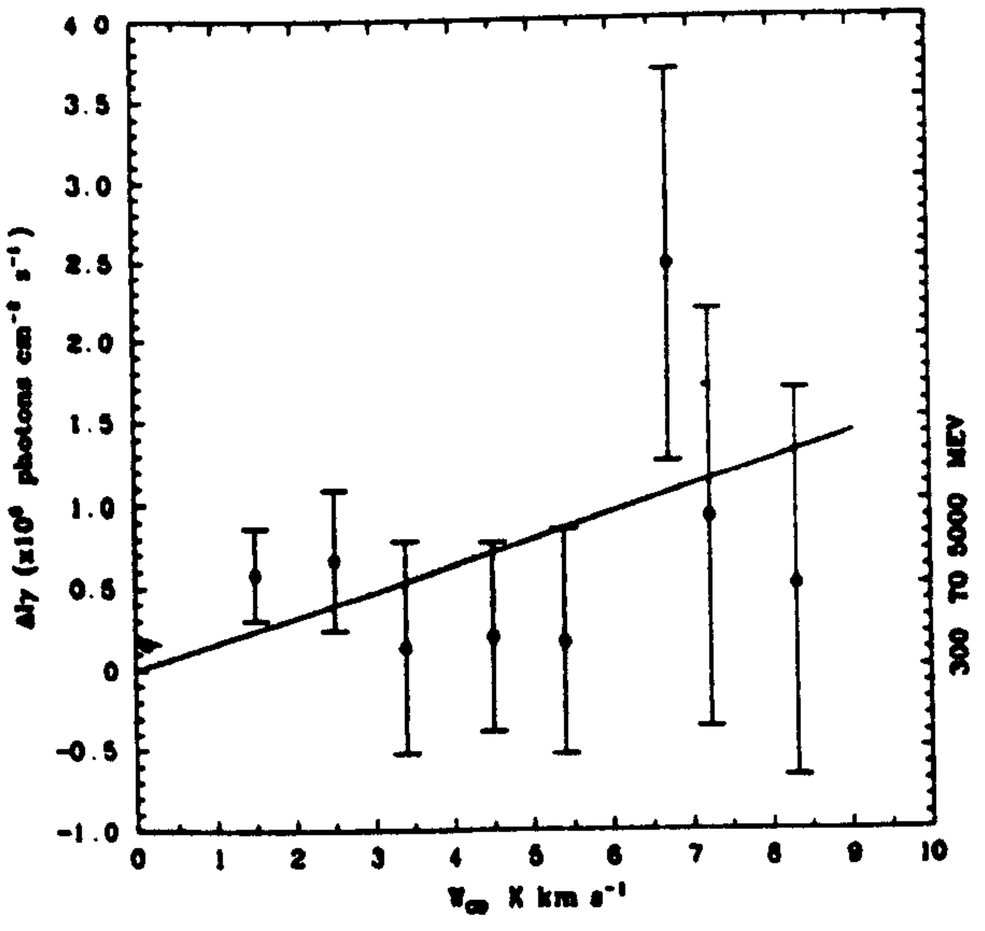

(d)

Fig 3.10 Correlation plots for I_γ ($\equiv I_\gamma(obs) - I_b$) vs N(HI) and ΔI_γ ($\equiv I_\gamma(obs) - (q/4\pi)\mathrm{N(HI)} - I_b$) vs W_{CO} at 300 – 5000 MeV. Errorbars show the (formal) weighted 67% confidence intervals in N(HI) and W_{CO} bins of 50×10^{19} cm^{-2} and 1 K km s^{-1}.
Key:(a) Region $A + C + F$; (b) Region $B + D$; (c) Region E; (d) Region $B + D + E$

also used to test various hypotheses. Firstly, assuming $q(\mathrm{HI})$ for a given ΔE in B, D and E and $A + C + F$ to be identical, the equation

$$\Delta I_\gamma = \frac{q_{A+C+F}}{4\pi}\, 2\mathrm{X}\tilde{\mathrm{W}}_{\mathrm{CO}} \tag{3.3}$$

where

$$\Delta I_\gamma \equiv I_\gamma(obs) - I_b - \frac{q_{A+C+F}}{4\pi}\tilde{\mathrm{N}}(\mathrm{HI}),$$

was used to derive X_{20}. Secondly, assuming $q(\mathrm{HI}) = q(\mathrm{H_2})$ and a fixed value for X_{20}, the data were fitted to

$$\Delta I_\gamma = \frac{q(\mathrm{HI})}{4\pi}\left(\tilde{\mathrm{N}}(\mathrm{HI}) + 2\mathrm{X}\,\tilde{\mathrm{W}}_{\mathrm{CO}}\right) \tag{3.4}$$

in regions $B + D$, E and $B + D + E$ as above.

D. Results

Plots of $\Delta I_\gamma(\mathrm{obs})$ versus $\tilde{\mathrm{W}}_{\mathrm{CO}}$, where

$$\Delta I_\gamma(\mathrm{obs}) \equiv I_\gamma(\mathrm{obs}) - \frac{q(\mathrm{HI})}{4\pi}\tilde{\mathrm{N}}(\mathrm{HI})) - I_b,$$

using the best fit parameters from equation (3.2) are given in Fig (3.10) for $\Delta E = 300 - 5000\,\mathrm{MeV}$. Others are shown in Appendix (A). Table (3.3) presents the details of the full model fit to the $\gamma-$ray data along with the quantity

$$\mathrm{Y}_{20} \equiv \frac{a}{2}\left(\frac{q(\mathrm{HI})}{4\pi}\,10^{20}\right)^{-1}$$

which can be identified with X_{20} if $q(\mathrm{HI}) = q(\mathrm{H_2})$. Figure (3.11) summarises the derived emissivities. They are plotted so that an E_γ^{-2} spectrum would appear as a horizontal line.

It can immediately be seen that there is evidence for fluctuations of CRs on small (i.e., cloud-sized) scales at those CR energies contributing significantly to $E_\gamma < 800\,\mathrm{MeV}$. At $70 - 150$ and $300 - 5000\,\mathrm{MeV}$, q_{B+D} and q_E are distinct at the 95% confidence level. Variations between the 'molecular cloud' regions and $A + C + F$ are revealed in the ratios q_E/q_{A+C+F} and q_{B+D}/q_{A+C+F} also given in Table (3.3). There is an apparent excess in region E relative to $A + C + F$ (predominantly HI) in all except the 800–5000 MeV band. Furthermore, it appears on the line-of-sight towards both the nearby Taurus-Auriga clouds, and the more distant Per OB2 cloud. Removing Per OB2 from the correlation hardly changes the fitted parameters at all. Evidence for an enhancement in the Orion clouds ($B + D$) is more marginal. However, the 'goodness-of-fit' is a strong function of the HI emissivity (see below), suggesting the excess may be real in this case also.

There is considerable dispersion in the fits for the combined 'CO-free' ($A + C + F$) region which implies that there may be substantial CR fluctuations even here. No evidence is found for this if the sub-regions are considered separately (see Table A.1). There is unlikely to be any contribution from molecular material in $A + C + F$ and an average of A, C and F is therefore appropriate when comparing 'molecular clouds' with nearby areas,

To test the significance of the excess relative to $A + C + F$ the simplified model (equation 3.3), which assumed emissivities to be the same in all regions was used. Details of the fit and plots of $\Delta I_\gamma(\mathrm{obs})$ vs W_{CO} can be found in Appendix (A.2). In each case the fit was of substantially poorer quality compared to the full model. For E, at 800–5000 MeV, the fit was so bad that the excess in $q(\mathrm{HI})$ can probably be considered significant. In $B + D$, the enhancement apparently disappears at these energies.

Table 3.3

Region	ΔE	$\frac{q}{4\pi} \times 10^{-26}$	Y_{20}	R
	MeV	ph atom^{-1} s^{-1} sr^{-1}	10^{20} mol cm^{-2} (K km s^{-1})$^{-1}$	
$B+D$	70–150	1.31 ± 0.14 (±0.27)	2.3 ± 0.8 (±1.9)	0.61
"	150–300	0.90 ± 0.08 (±0.16)	1.3 ± 0.6 (±1.1)	0.65
"	300–5000	0.65 ± 0.07 (±0.14)	2.6 ± 0.6 (±1.2)	0.62
"	800–5000	0.28 ± 0.05 (±0.10)	3.2 ± 1.1 (±2.2)	0.44
E	70–150	1.69 ± 0.12 (±0.23)	−0.1 ± 0.4 (±0.8)	0.73
"	150–300	1.06 ± 0.08 (±0.15)	0.9 ± 0.4 (±0.7)	0.73
"	300–5000	0.99 ± 0.06 (±0.12)	0.2 ± 0.4 (±0.6)	0.74
"	800–5000	0.36 ± 0.04 (±0.08)	0.4 ± 0.5 (±1.4)	0.52
$B+D+E$	70–150	1.54 ± 0.09 (±0.17)	0.5 ± 0.4 (±0.6)	0.67
"	150–300	0.98 ± 0.05 (±0.11)	1.1 ± 0.3 (±0.6)	0.70
"	300–5000	0.84 ± 0.05 (±0.09)	0.9 ± 0.3 (±0.5)	0.68
"	800–5000	0.33 ± 0.03 (±0.07)	1.3 ± 0.5 (±1.0)	0.47
$A+C+F$	70–150	1.01 ± 0.08 (±0.17)		0.40
"	150–300	0.77 ± 0.05 (±0.17)		0.46
"	300–5000	0.58 ± 0.05 (±0.10)		0.38
"	800–5000	0.30 ± 0.04 (±0.08)		0.30
q_{B+D}/q_{A+C+F}	70–150	1.30 ± 0.18 (±0.35)		
"	150–300	1.17 ± 0.13 (±0.27)		
"	300–5000	1.12 ± 0.33 (±0.31)		
"	800–5000	0.93 ± 0.21 (±0.41)		
q_E/q_{A+C+F}	70–150	1.67 ± 0.18 (±0.36)		
"	150–300	1.38 ± 0.14 (±0.28)		
"	300–5000	1.71 ± 0.14 (±0.36)		
"	800–5000	1.20 ± 0.21 (±0.42)		

Note: 95% confidence intervals, as estimated by the t-test, are given in brackets; R is the multiple correlation coefficient.

There is no independent evidence for $q(H_2)$ that would permit an unambiguous estimate of X_{20} from the parameter a in equation (3.2). However, providing there is no coincidental CR enhancement along the line-of-sight, $q(H_2) < q(HI)$ for all three 'standard' energy bands (as required for a constant X_{20}), is unsatisfactory since exclusion of CRs of the relevant energies from the molecular cloud is unlikely on theoretical grounds. The reverse, $q(H_2) > q(HI)$, is not unreasonable in Orion but would suggest $X_{20} \sim 0$ in Taurus. Thus, as a first approach, $q(HI) = q(H_2)$ is assumed in the molecular cloud regions. Figure (3.12a) plots 95% confidence intervals for Y_{20} vs E_γ, along with the range of X_{20} derived below from extinction and other data.

E. Discussion

If no large fluctuations were observed between 'cloud' and 'cloud-free' regions (equivalent to a uniform CR flux on the size-scales considered here), there would be no difficulty in deciding what value of X_{20} was appropriate. This assumption is inherent in the analyses by COS-B of the Orion region (see below). Now the situation appears more complicated and difficult to interpret.

Before proceeding, it is worth asking if the results described above do not arise from problems with the γ−ray, CO or HI data. This appears unlikely for several reasons. Firstly,

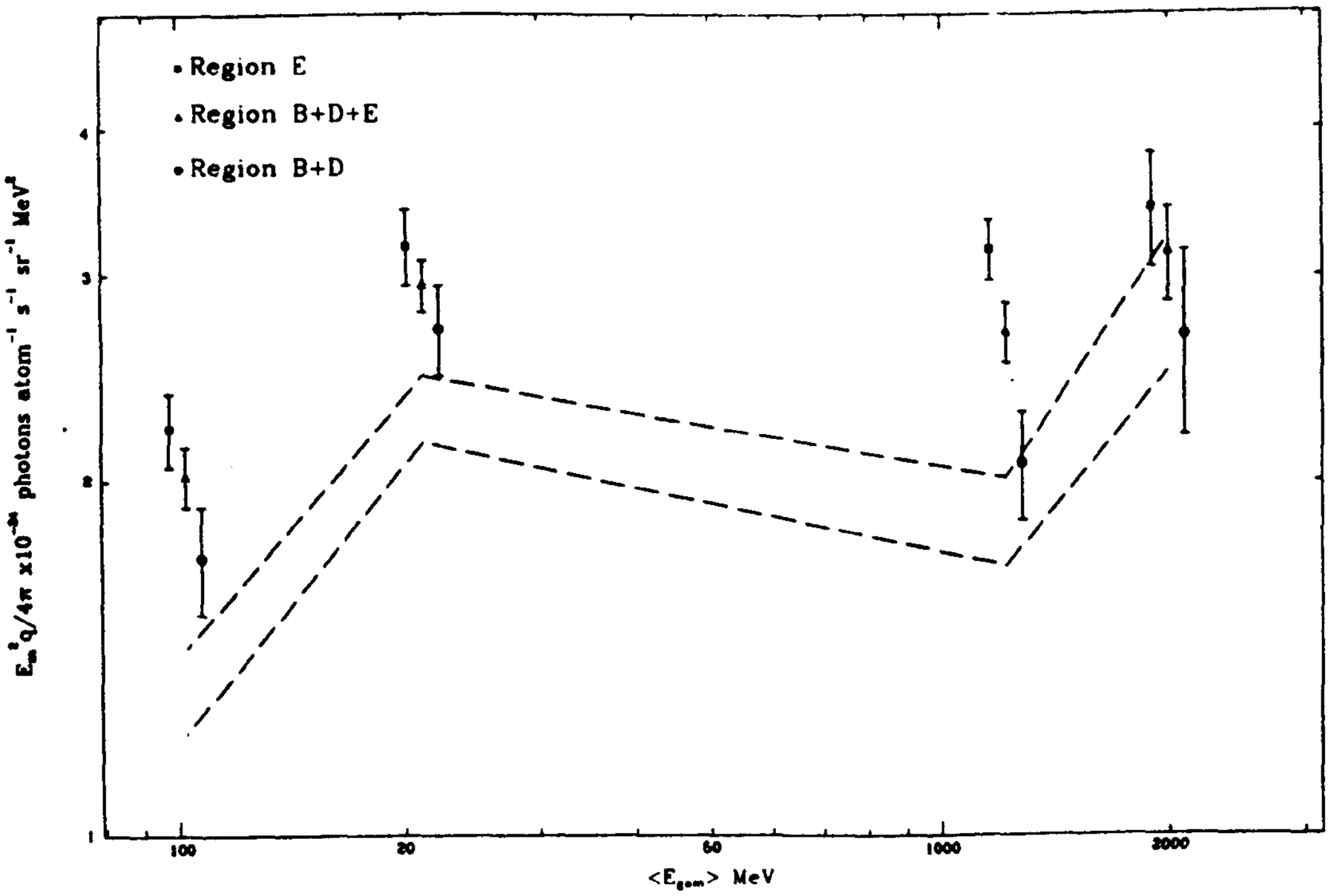

Fig 3.11 Emissivities derived in a 2-parameter fit (equation 3.2) plotted so that an E_γ^{-2} spectrum would appear as a horizontal line. To aid clarity of presentation, only the central point of a given energy band is plotted at the band rms energy. Dotted lines indicate the 1σ limits for the region $A + C + F$ and the errorbars show the formal 67% confidence intervals for the estimated parameters.

systematic errors in the HI data are small ($< 10\%$) since the gas is optically thin at medium latitudes. It is more difficult to quantify possible errors in the COS-B database, and the manner in which it was used here. Strong et al. (1987a) suggest that residual calibration errors are of the same order ($\lesssim 10\%$). Variations in the isotropic background between the above regions are certainly possible, since the contributions to each come from several observation periods (e.g., 7 in Orion). However, the background value obtained by Bloemen et al. (1984b) in Orion, $(2.0 \pm 0.4) \times 10^{-5}\,\mathrm{cm^{-2}\,s^{-1}\,sr^{-1}}$, is comparable with that assumed here. Furthermore, a correlation for $A + C + F$ in which the background was also determined produced results similar in magnitude to the COS-B estimates in each of the three 'standard' energy bands, namely $Ib = (7.6 \pm 0.3)$, (2.7 ± 0.2) and $(2.3 \pm 0.2) \times 10^{-5}\,\mathrm{cm^{-2}\,s^{-1}\,sr^{-1}}$. There is some doubt about the 800–5000 MeV background adopted ($0.74 \times 10^{-5}\,\mathrm{cm^{-2}\,s^{-1}\,sr^{-1}}$), since it is extrapolated from the lower energy intervals assuming an E_γ^{-2} spectrum. Unfortunately, poor statistics and small areas of sky prevented a useful correlation estimate in the present analysis. The emissivities derived above using the extrapolated background are surprisingly high, but since relative values are the main concern in this case, the absolute value is not too important. It seems unlikely that systematic errors as large as 50%, the size of the effect observed here, are possible in every energy band. However, Bloemen et al. (1988) have estimated

$$I_b(800-5000\,\mathrm{MeV}) = 1.04 \times 10^{-5}\,\mathrm{cm^{-2}\,s^{-1}\,sr^{-1}}$$

by combining all high latitude COS-B observations ($b > 30°$) and subtracting contributions from HI (21 cm) and ionised gas (uncertain). Further work in this area is desirable.

Assuming the results to be genuine, several scenarios are possible from the above though none is unambiguous:
(i) The simplest interpretation of the Orion results is that the excess Δq(HI) relative to $A+C+F$ is not significant and $q(\mathrm{HI}) = q(\mathrm{H_2})$ i.e., the CR flux is uniform over the entire gas column towards the cloud. Then $\mathrm{Y_{20}} = \mathrm{X_{20}}$ and conclusions similar to those of Bloemen et

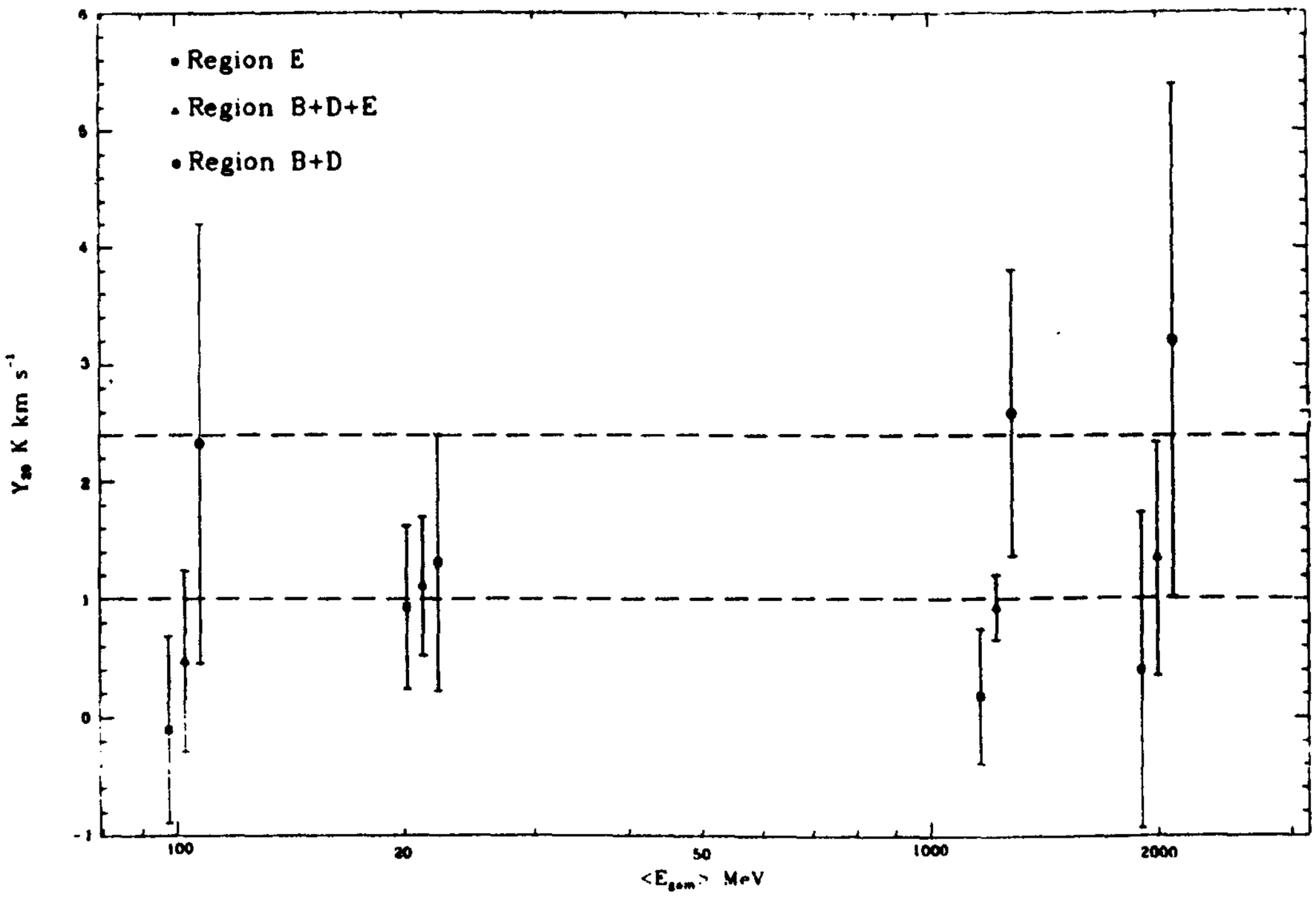

(a)

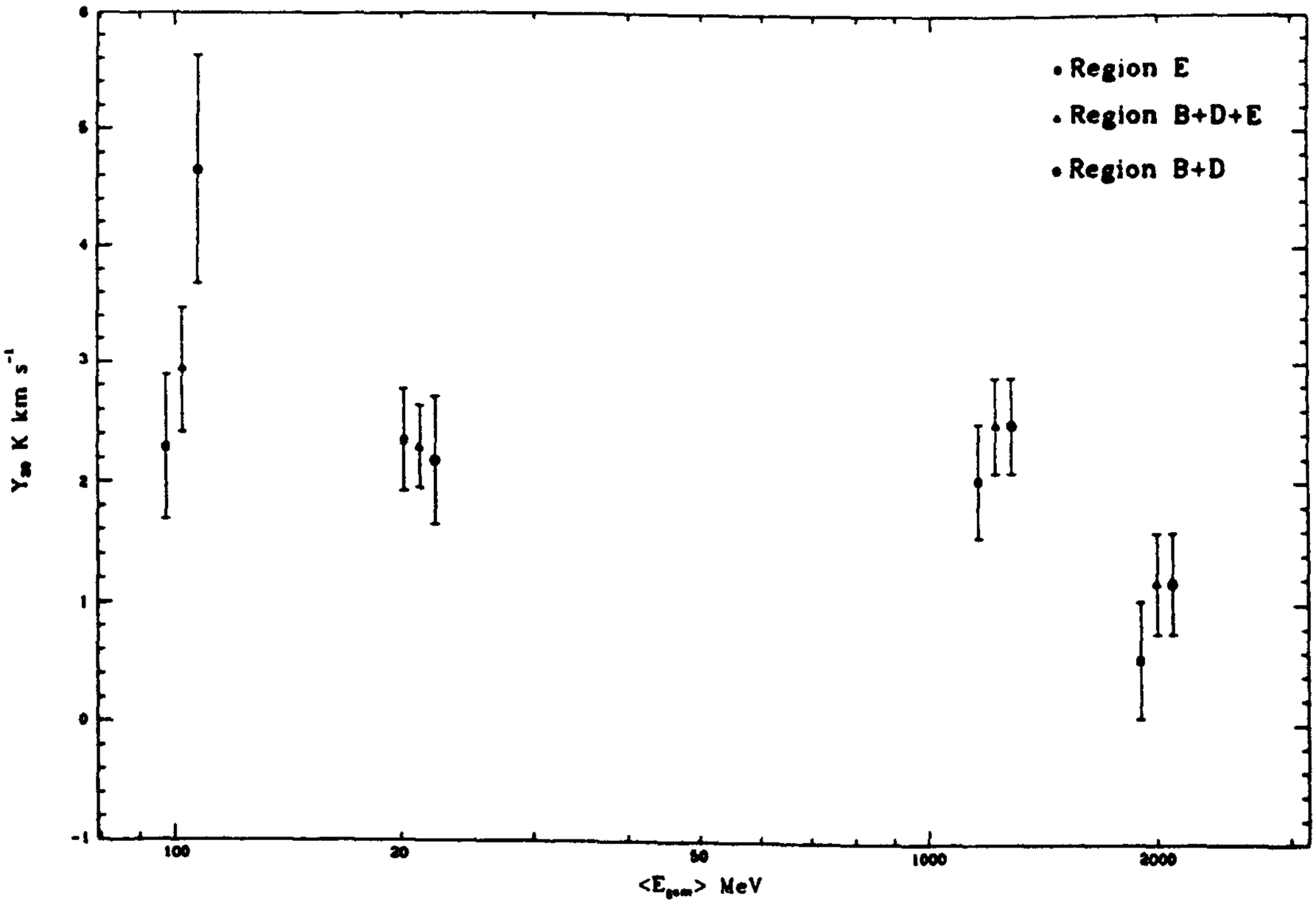

(b)

Fig 3.12 (a) The parameter Y_{20} (K km s^{-1}), estimated with equation 3.2, plotted against the rms energy (< E_{gam} >) of the 70−150, 150−300, 300−5000 and 800−5000 MeV bands. Error bars show formal 95% confidence intervals and the dotted lines give the range of X_{20} found in §3.4.
(b) As in (a) except that Y_{20} was determined in a 1-parameter fit to the data, with emissivities fixed at the values found in region $A + C + F$. Error bars give the 67% confidence intervals.

al. (1984b) are obtained. These authors found $X_{20} = 2.6 \pm 1.2$ for $\Delta E_\gamma = 300 - 5000\,\mathrm{MeV}$. Their estimated emissivity was slightly lower than here (0.52 ± 0.13 c.f. 0.65 ± 0.07 in units of $10^{-26}\,\mathrm{atom^{-1}\,s^{-1}\,sr^{-1}}$), largely due to a smaller background ($2.0 \times 10^{-5}\,\mathrm{cm^{-2}\,s^{-1}\,sr^{-1}}$) to be compared with $2.2 \times 10^{-5}\,\mathrm{cm^{-2}\,s^{-1}\,sr^{-1}}$ assumed in this work.

However, this picture does not work well in region E (Taurus), where vanishingly small values of X_{20} result which are inconsistent with the several estimates of the conversion factor derived below from other data. It can, of course, be argued that Δq(HI) is real but not connected with the cloud, suggesting a local CR excess coincident along the line-of-sight. This would explain why it appears in an apparently identical manner toward Perseus even though this cloud is much further away than the others in region E. However using equation (3.4) and forcing X_{20} to take more reasonable larger values does not reduce Δq(HI) substantially with any reasonable X_{20} (see Figs 3.13 for plots of q(HI) vs X_{20} derived in this way at $300 - 500\,\mathrm{MeV}$). A coincidental CR excess must again be invoked in this case. Furthermore, the quality of the fit is poor compared to the full two-parameter model for $X_{20} \gtrsim 1$ (in region E), as estimated by an F-test on residuals.

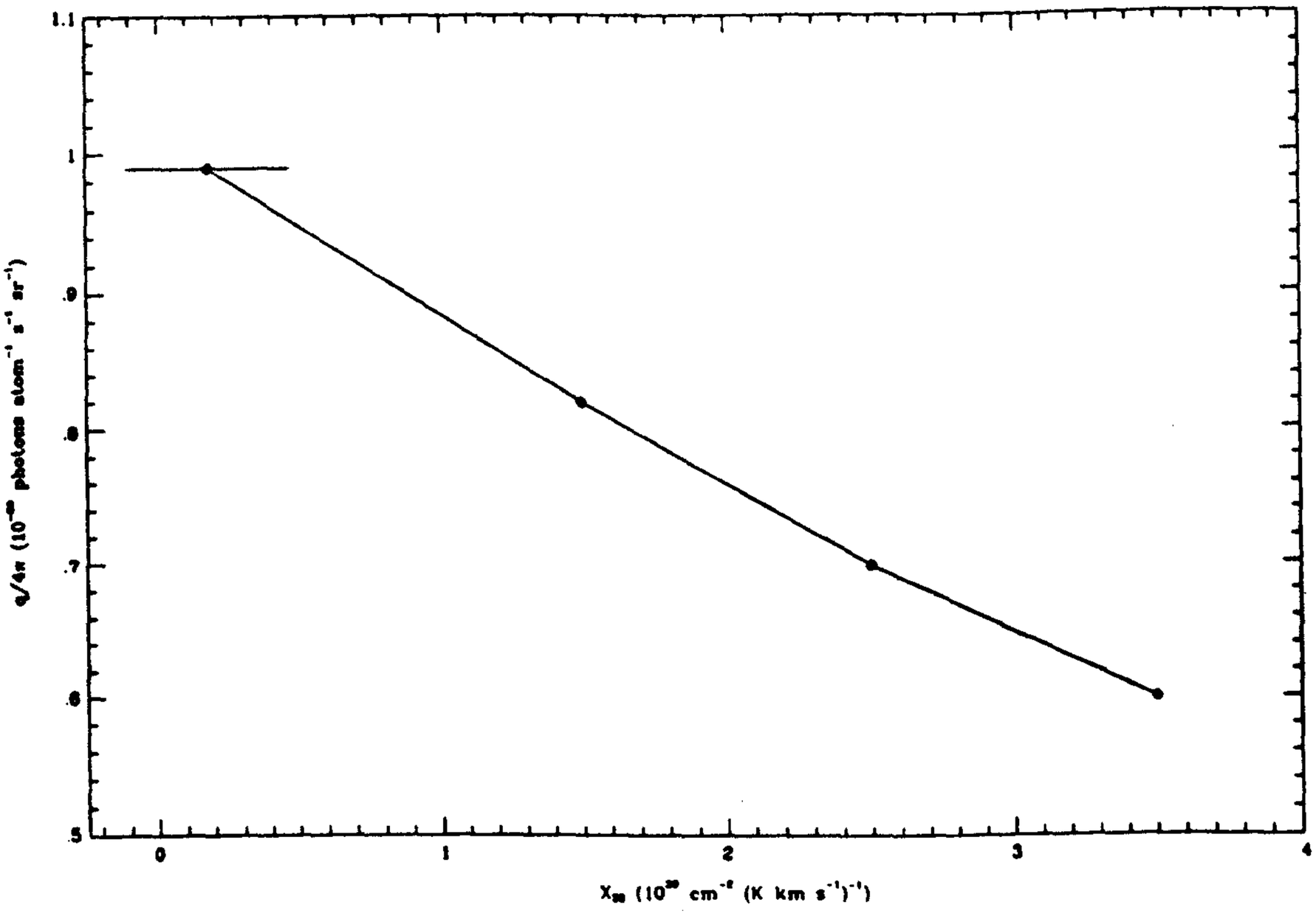

Fig 3.12 q(HI)$/4\pi$ for $300-5000\,\mathrm{MeV}$ derived using a 1-parameter fit to the $\gamma-$ray and gas data in region E for $X_{20} = 1.5$, 2.5 and 3.5. The best fit 95% confidence interval for X_{20} is indicated.

If the Δq(HI) in Orion are now considered both significant and associated with the cloud the interpretation is more complicated . Y_{20} becomes an upper limit for X_{20}, because the observed emissivity refers to the line-of-sight, a considerable fraction of which presumably has a 'normal' value (corresponding to that in $A + C + F$). To estimate this effect, consider the model depicted in Fig (3.14). Then

$$q_{\mathrm{HI}}\mathrm{N(HI)} = q_1\mathrm{N}_1 + q_2\mathrm{N}_2 + q_1\mathrm{N}_3$$

where N(HI) is the total HI column density through the cloud. Foregound, background and 'envelope' contributions are N_1, N_3 and N_2, with associated emissivities q_1, q_1 and q_2 respectively ($q_2 > q_1$); q_{HI} is the emissivity estimated in the fit to the model of $\gamma-$ray emission. Assuming $\mathrm{N}_1 = a\mathrm{N(HI)}$, $\mathrm{N}_2 = b\mathrm{N(HI)}$ and $\mathrm{N}_3 = c\mathrm{N(HI)}$ then

$$q_{\mathrm{HI}} = (a + c)q_1 + bq_2.$$

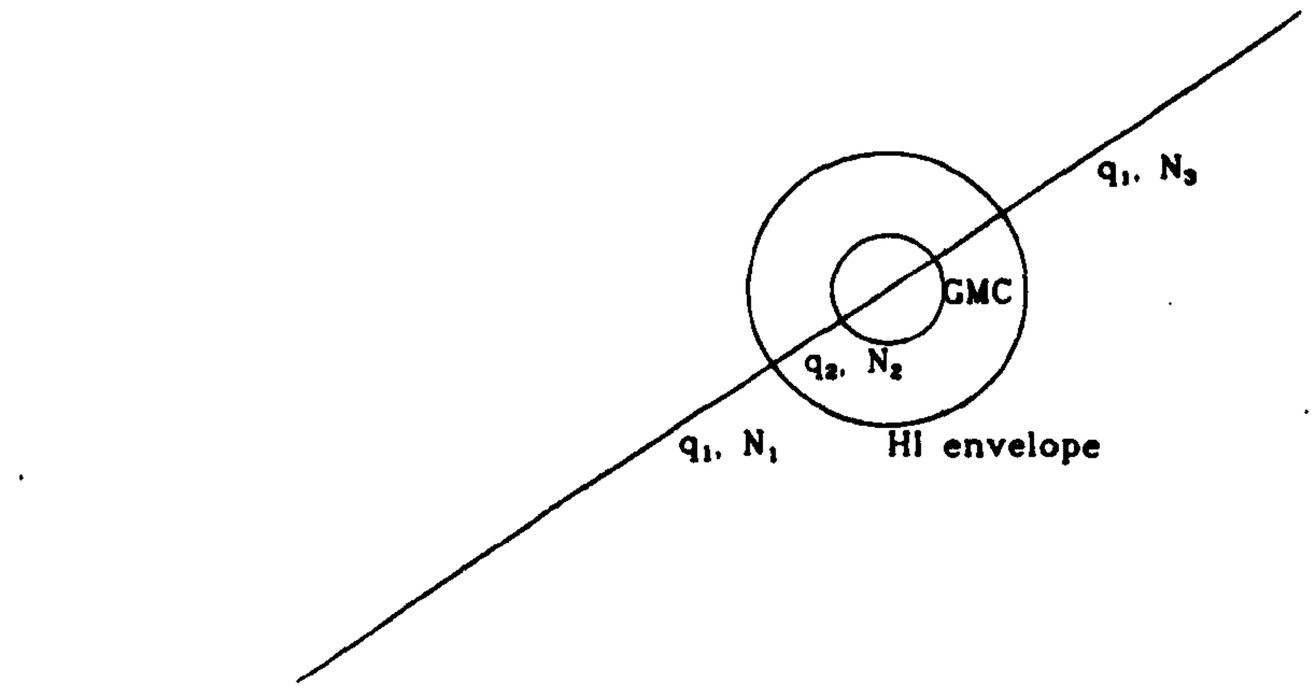

Fig 3.14 A model for the $\gamma-$ray emission of a molecular cloud embedded in a neutral HI cloud of emissivity q_2, surrounded by an ISM of emissivity q_1. N_1, N_2 and N_3 are the foreground, 'envelope' and background HI column densities on a typical line-of-sight through the cloud

To estimate q_2, the fractional column densities inside (b) and outside $(a+c)$ the cloud must be known. The total HI column density towards Orion is $\sim 2 \times 10^{21}\,\mathrm{cm}^{-2}$; a reasonable figure is $b = 0.5$ since, according to §2.3, the HI envelope around Orion has a column density $\mathrm{N(HI)} \sim 1 \times 10^{21}\,\mathrm{cm}^{-2}$. Therefore,

$$q_2 = 2q_{\mathrm{HI}} - q_1$$

giving $q_2 \sim 1.6$ and $1.0 \times 10^{-26}\,\mathrm{atom}^{-1}\,\mathrm{s}^{-1}\,\mathrm{sr}^{-1}$ for the $70-150$ and $150-300\,\mathrm{MeV}$ bands. Clearly this is only illustrative, but it highlights the problem. If the $\gamma-$ray excess (Δq) is confined to only a small fraction of the line-of-sight, the actual emissivity in the cloud can be substantially larger than q_{HI}.

The conversion factor $\mathrm{X_{20}}$ is derived, assuming $q_2(\mathrm{HI}) = q(\mathrm{H_2})$, by dividing the fitted parameter a (equation 3.2) by $q_2(\mathrm{HI})$. Agreement between $\mathrm{X_{20}}(\gamma)$ and other estimates may be closer in this case for the Orion clouds. There is a problem at $800-5000\,\mathrm{MeV}$ since $\Delta q(\mathrm{HI})$ is much reduced but $\mathrm{X_{20}}$ shows no signs of falling. However, the fit is rather poor in this band, largely because there are only about one third the number of photons relative to other energies. Considering the uncertainties with I_b, it might be argued that the absolute value of the high energy result is of reduced significance.

Nevertheless, the difficulties in region E noted above are even greater with this approach because the HI emissivities are already large, and $\mathrm{X_{20}}$ is further reduced.

(ii) A second possibility is to insist that $\mathrm{X_{20}}$ is known well enough from independent measurements to use in deriving $q(\mathrm{H_2})$ from the quantities a. Of course, this inverts the argument that $\gamma-$ray estimates, being independent of assumptions about the dust-to-extinction ratio or LTE arguments, is the best available technique. Clearly the $\gamma-$ray method has its own disadvantages.

Values of $\mathrm{X_{20}}$ in the range $1.0-1.5$ appear typical and results for $\mathrm{X_{20}} = 1.5$ appear in Fig (3.15) and Table (A.3) . In Orion $q(\mathrm{H_2})$ is about twice that derived in $A+C+F$ except at $150-300\,\mathrm{MeV}$ and $q(\mathrm{HI}) < q(\mathrm{H_2})$ must be assumed since the HI envelope is too small to allow equality. For Taurus, on the contrary, the $q(\mathrm{H_2})$ are unreasonably small.

These considerations suggest that, in region E particularly, the model used here fails rather spectacularly. Too little is known about fluctuations in CR intensity in the ISM generally, and around molecular clouds in particular, to expect more from such simplistic assumptions.

(iv) The assumption that

$$q(\mathrm{HI})_{A+C+F} = q(\mathrm{H_2})_{B+D} = q(\mathrm{H_2})_E$$

was discussed by Richardson and Wolfendale (1987). They argued that the quantities Y_{20}, as defined above, may give a reasonable estimate for X_{20} when extrapolated to the highest energies, and they deduced a value $X_{20} = 1.5$ for all clouds from these considerations. The assumption implicit in their analysis was that the CR intensities in the neutral HI outside the GMC were reasonably uniform, and any enhancement observed towards the molecular gas may indicate low-energy CR production there. It is now evident that this is not necessarily a useful assumption. The data are consistent with an excess at low energies but fluctuations in CR flux between regions, and perhaps on similar distance scales along the line-of-sight, produce a poor fit (see Table A.2) and make definitive conclusions even more difficult.

(iii) Figure (3.12*a*), when considered in this context, suggests another approach. The range of X_{20} values from extinction and other data is not inconsistent with the results of a $\gamma-$ray analysis at the 95% confidence level. The observed fluctuations must be ascribed to local variations in the CR flux not properly accounted for in the model. This is assumed to be the case in the following discussion, and its consequences are explored. Until more data are available, these conclusions should be regarded as provisional.

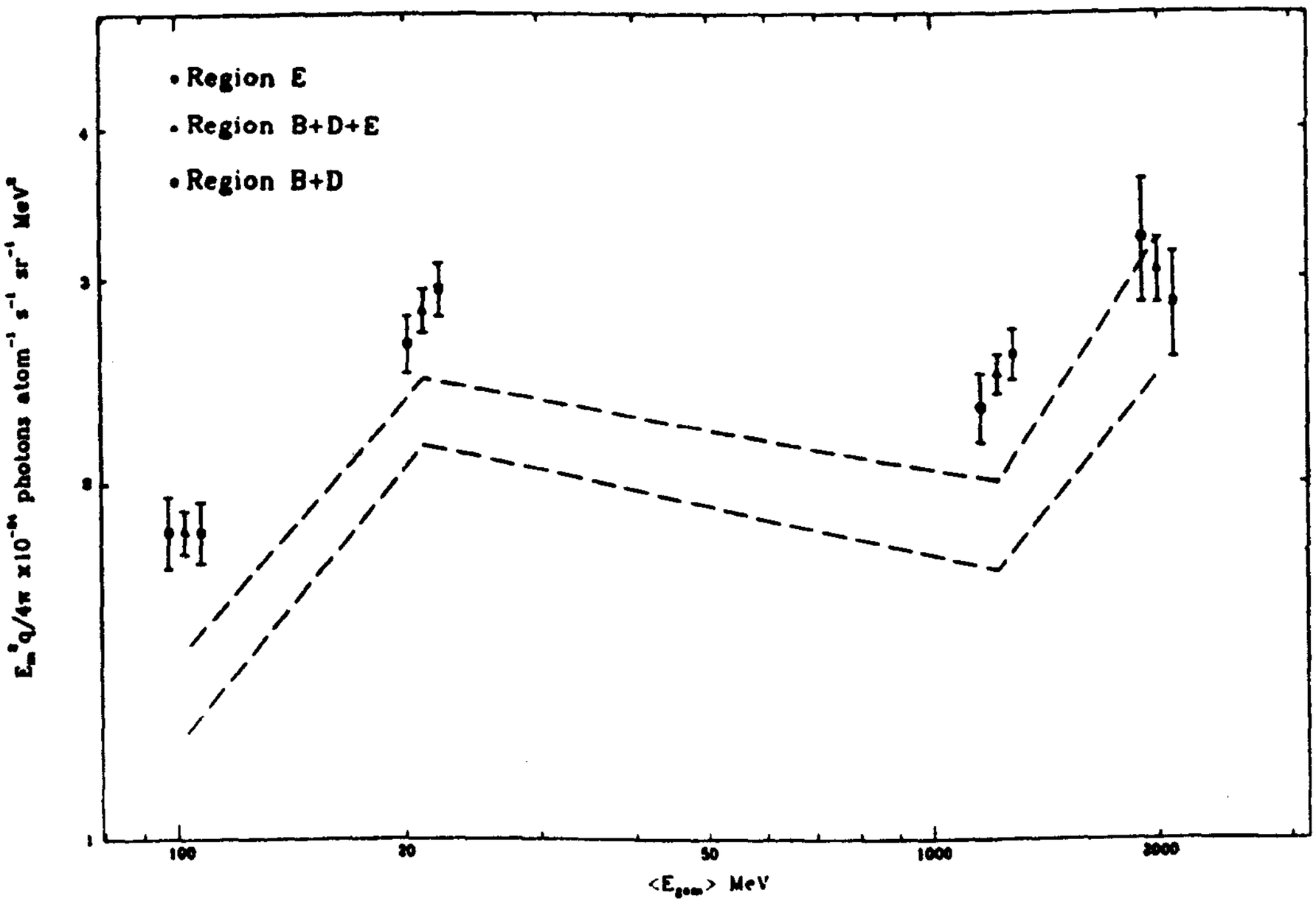

Fig 3.15 As for Fig 3.11 except that $q/4\pi$ has been determined using a 1-parameter fit with $X_{20} = 1.5$.

Equation (3.4) has already been used to compute q(HI) towards the cloud regions. The results for $X_{20} = 1.5$ indicate an excess emissivity (see Fig 3.15), but of more moderate proportions. Naturally, the problems mentioned above concerning Taurus etc. remain, and some part of Δq(HI) should probably be ascribed to coincidence. Unfortunately there is no supporting evidence for this in either long wavelength radio emission (e.g., 408 MHz data) or in X-rays. In fact Orion would seem to be a more likely candidate for a CR enhancement in the line-of sight from the X-ray standpoint (see Fig 3.16 taken from Heiles and Kulkarni 1987). Distributed acceleration processes (e.g., Giler et al. 1987), perhaps from old SNR shells not seen in the radio or X-ray emission, may be one explanation for the Taurus results.

A small excess appears in the highest energy band, but the spectrum is steeper than in $A+C+F$ implying localised production of low energy CRs. Some of this might be associated with the molecular clouds and a discussion of likely processes is given in Chapter 4.

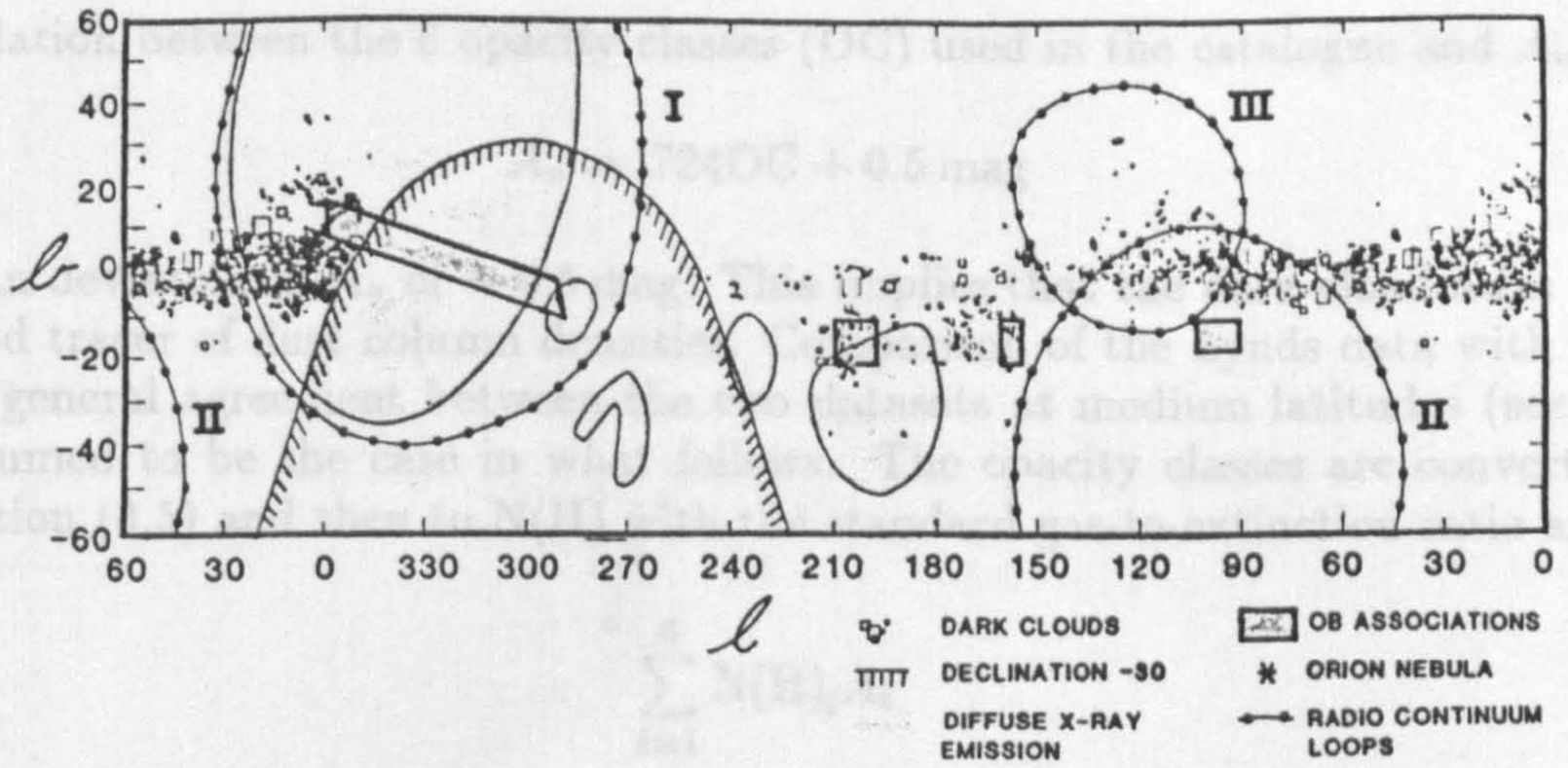

Fig 3.16 Sketches of prominent OB associations, dark clouds, regions of enhanced diffuse X-ray emission, and radio continuum loops (from Heiles & Kulkarni 1987).

3.4 X_{20} Estimates from Extinction and Other Data

As pointed out in the previous section, variations in CR intensities in the local ISM make it difficult to deduce a definitive value for X_{20}. Estimates are now sought using the visual extinction and LTE methods described in section 2.3. Of course, the former technique is restricted to clouds closer than Orion, but data are available for parts of the Taurus molecular clouds and can usefully be compared with the $\gamma-$ray analysis. Surveys in the ^{13}CO $J = 1 \rightarrow 0$ and formaldehyde $J = 1$ doublet lines have been made in Orion and LTE assumptions can be used to estimate masses; comparison with M_{CO} permits an estimate of X_{20}. Smaller dark clouds have been extensively studied in CO and extinction, and provide useful corroborative evidence though it must be borne in mind that conditions in these small clouds could be quite different from those in GMCs.

Clouds of quite varied physical characteristics are examined here. An important question to ask in the context of the $\gamma-$ray analysis is whether the conversion factor varies significantly from cloud to cloud. For example, a strong dependence on kinetic temperature is indicated by the Kutner and Leung (1985) and Maloney and Black (1988) theoretical studies. One way of investigating such effects is to characterise the CO emission of a cloud by the median value of its area-integrated W_{CO} contours $< W_{CO} >$. Provided CO traces the cloud mass, this parameter is related to the 'median' or 'half-mass' contour, knowledge of which is decisive in determining the mass of molecular gas in the cloud since most of a cloud's mass resides 'near' this value. It is important in $\gamma-$ray analyses of molecular clouds for the same reason; provided there are no CR or $\gamma-$ray sources in the cloud, the bulk of its $\gamma-$ray emission arises from those regions containing most of the mass.

Available evidence from the extinction technique often implies that CO fails as a tracer of mass for $A_v \gtrsim 2 - 3$ mag, presumably because of optical depth effects. Theoretical models suggest that high values of $< W_{CO} >$ may arise because the cloud is heated, by a nearby OB association for example, and not necessarily because $N(H_2)$ is large. In this case, variations in X_{20} might be expected at high $< W_{CO} >$.

3.4.1 Extinction Measurements in Local Dark Clouds

A. Lynds (1962).

All the molecular clouds considered for the $\gamma-$ray analysis are contained in the dark cloud catalogue of Lynds (1962). However, cloud shapes are not given in the catalogue and a correlation analysis between CO and opacity is not possible. Feitzinger and Stüwe (1986)

derive a relation between the 6 opacity classes (OC) used in the catalogue and A_v viz.

$$A_v = .724\mathrm{OC} + 0.5\,\mathrm{mag} \tag{3.5}$$

with a mean deviation in A_v of ~ 0.5 mag. This implies that the dark cloud atlas is a moderately good tracer of dust column densities. Comparison of the Lynds data with CO maps suggests a general agreement between the two datasets at medium latitudes (see Fig 2.2). This is assumed to be the case in what follows. The opacity classes are converted to A_v using equation (3.5) and then to N(H) with the standard gas-to-extinction ratio and

$$\sum_{i=1}^{6} \mathrm{N(H)}_i A_i$$

is computed where $\mathrm{N(H)}_i \equiv$ the total gas column density corresponding to the ith opacity class. This defines a sub-area of the cloud, $\sum_{i=1}^{6} A_i$, where A_i is the area assigned to each opacity class in the given cloud. The W_{CO} maps, taken from Maddalena (1986), Ungerechts and Thaddeus (1987) and Lebrun (1986) were integrated over an identical area defined by the highest possible W_{CO} contour. Column densities of HI were computed inside this same boundary in the same way.

In principle, the latter (HI) value should be subtracted from $\sum_{i=1}^{6} \mathrm{N(H)}_i A_i$ to derive the area-integrated H_2 column density. However, since zero-point errors are probably greater in these data than in the conventional star-counting technique, two values are calculated for each X_{20}; one with all the HI subtracted, and the other with none. The 'true' estimates of X_{20} lie somewhere within this range. The results for several GMCs are shown in Fig (3.20). It should be borne in mind that the mean deviation in A_v quoted by Feitzinger and Stüwe (1986) for equation (3.5) corresponds to a 25% dispersion in X_{20} for the Taurus clouds, and about 10% in Orion.

B. Cernicharo and Guélin (1987).

The Taurus cloudlet HCL2, covering $\sim 1.5° \times 1.5°$, was observed in CO, ^{13}CO and C^{18}O. An extinction map for a similar $1° \times 1°$ area was obtained using star counts. The reference field selected was not absorption-free, since this was not available on the same photographic plate. Instead a region of apparently uniform absorption (1.1 ± 0.5 mag) was chosen and corrected for the decrease in sensitivity between the centre and edge of the plate.

Fig (3.17) reproduces their data. A rough linear correlation between W_{CO} and A_v is apparent for $A_v < 3$ mag. The authors obtain a best (least squares) line given by

$$W_{CO} = (5.0 \pm 0.5)\big(A_v - (0.5 \pm 0.23)\big)\,\mathrm{K\,km\,s^{-1}} \tag{3.6}$$

for $0.5 < A_v < 3$ mag. In order to compute $\mathrm{N(H_2)}$ and then X_{20}, it is first necessary to remove any HI along the line-of-sight that is included in the A_v estimate. This is an uncertain quantity, but is particularly important at the moderate A_v values where CO is likely to be useful as a mass tracer. It is usually assumed that all the gas along a line-of-sight is molecular; clearly there is a danger that X_{20} may be overestimated in this case and it is necessary to see if the effect is significant.

The reference field is uncertain in most cases by ~ 0.5 mag. Up to this amount of HI may have thus already been 'subtracted' from obscured positions in the molecular cloud. By comparison, using the data from *A* above, Orion, Taurus and Perseus have mean HI column densities corresponding to 1.0, 0.8 and 0.7 mag respectively over those parts of the cloud where opacity was detected. An approximate correction to the data can be made by

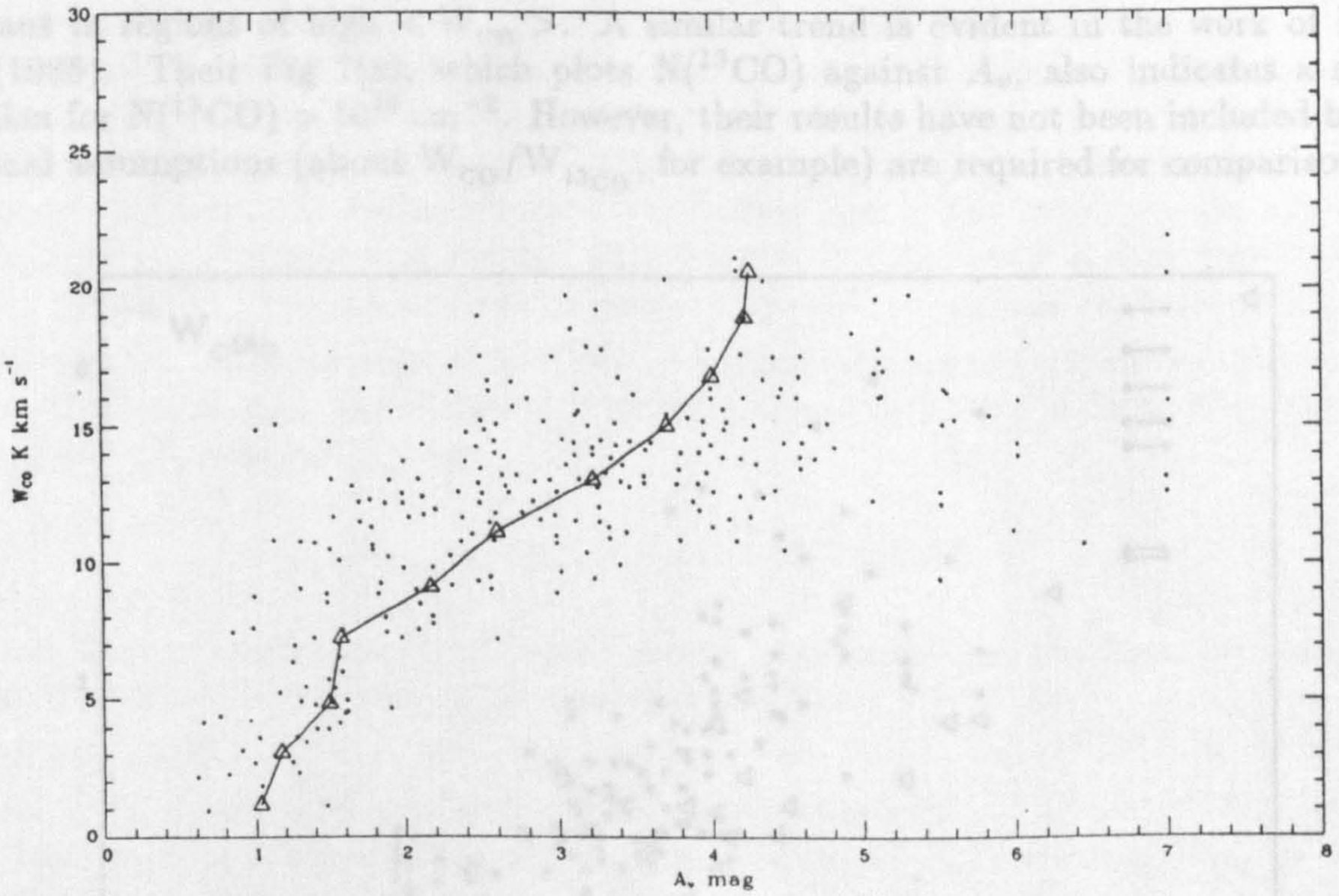

Fig 3.17 W_{CO} versus visual extinction as given by Cernicharo and Guélin (1987) (small points) for HCL2; $2\,\mathrm{K\,km\,s^{-1}}$ bin medians are shown by the large points.

assuming N(HI) to be constant over the small area of the survey and equal to the value of A_v at $W_{CO} = 0$. Thus equation (3.6) becomes

$$W_{CO} = (10.0 \pm 1.0)N(H_2)/19 \times 10^{20}.$$

Computing X_{20} is now straightforward and gives $X_{20} = 1.9 \pm .2$.

The dispersion in the data is large and X_{20} is estimated another way by binning in W_{CO} and calculating bin medians ($< W_{CO} >$, $< A_v >$; see Fig 3.17). The conversion factor is estimated from the ratio $< A_v > / < W_{CO} >$ for each bin assuming an HI 'correction' of 0.5 mag. The results are given in Fig (3.20). Similar numbers are obtained for $< W_{CO} >$ less than $16\,\mathrm{K\,km\,s^{-1}}$ (corresponding to $A_v \lesssim 2\,\mathrm{mag}$) if cumulative medians are used instead.

Three W_{CO} regions are apparent in the data. For $< W_{CO} >$ less then $10\,\mathrm{K\,km\,s^{-1}}$ there is a rough linear correlation between W_{CO} and A_v. Between $10 - 16\,\mathrm{K\,km\,s^{-1}}$ the dispersion in A_v becomes very large, indicating CO to be a very poor tracer of molecular gas in this regime. Clearly, CO is not 'effectively optically thin' in all parts of the cloud. In this case, at least, the model of non-overlapping clumps in space and velocity breaks down, though it may be necessary to invoke it to explain the linear relation seen at low A_v. The median trend, indicated by the line in Fig (3.17), could indicate X_{20} rising to a maximum, but with large errors on the indicated H_2 column densities along a particular line-of-sight. An alternative explanation, considered in more detail below, is that including points with large A_v is invalid and results in an overestimate of X_{20}.

In the three highest W_{CO} bins, the dispersion is somewhat reduced. Regretfully, the evidence is not strong and may arise because of the paucity of data at large W_{CO} and A_v. Hot clumps in the most obscured part of the cloud clearly exist, as might be expected. However, the relative contribution of such clumps to the cloud luminosity is the point at issue. Consequently, conclusions must be a little guarded until more information is available. Nevertheless, the trend in medians implies X_{20} declines or remains small, giving some support to the theoretical expectation that heating by young stars associated with the clouds is

important in regions of high $< W_{CO} >$. A similar trend is evident in the work of Duvert et al. (1986). Their Fig 7(a), which plots N(^{13}CO) against A_v, also indicates a smaller dispersion for N(^{13}CO) $> 10^{16}\,cm^{-2}$. However, their results have not been included because additional assumptions (about $W_{CO}/W_{^{13}CO}$, for example) are required for comparison here.

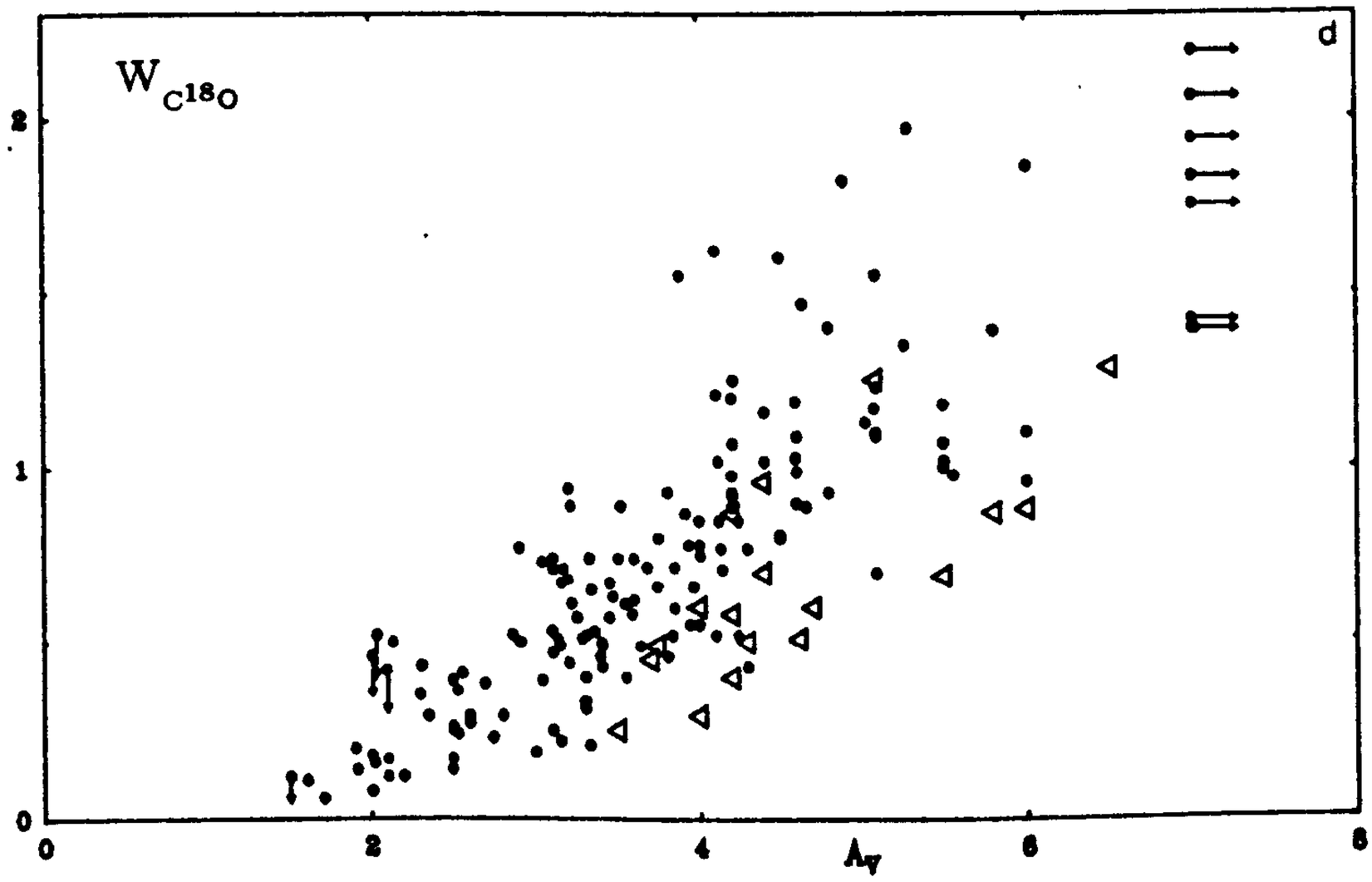

Fig 3.18 $W_{C^{18}O}$ **versus visual extinction in HCL2. open triangles correspond to double profiles; the authors estimate that these points must be shifted** ~ 1.5 **mag to the left before comparing with the othe data points.**

The $C^{18}O$ observations by Cernicharo and Guélin, reproduced in Fig (3.18), are of interest here. An approximately linear relation to $A_v \sim 6$ mag suggests the proportionality law of Bohlin et al. (1978) may well extend to much higher gas column densities. Furthermore, Cernicharo and Bachiller (1984) compared blue and red star counts in a region of the Taurus molecular cloud containing HCL2 and estimated a value of R close to the canonical value of 3.2. This evidence for a 'normal' extinction curve is also supported by the starlight reddening measurements of Vrba and Rydgren (1985), who obtained $R = 3.1$ for 6 Taurus stars in the range $A_v = 1 - 3.2$ mag, and by Guetter (1977) who found $R = 3.2$ towards Per OB2.

C. Frerking, Langer and Wilson (1982).

These authors used IR photometric data to estimate A_v towards field stars in ρ-Oph and Taurus. Much higher column densities were probed in this way, but the method is biased toward highly reddened stars and only a limited number of measurements in widely separated directions are usually possible.

Sanders, Solomon and Scoville (1984) used the FLW ^{13}CO data to derive an empirical value for X_{20}, concluding that $X_{20} = 0.50(W_{^{13}CO})^{0.89}$. They argue that a mean value for $W_{^{13}CO}$ in the molecular ring is $\sim 7\,K\,km\,s^{-1}$ (Liszt et al. 1981). Assuming the ratio $W_{CO}/W_{^{13}CO} \sim 5.5$ for these same clouds and the usual gas-to-extinction ratio, SSS find $X_{20} \sim 2.8$. A value of $X_{20} \sim 5.2$ is derived in similar fashion by SSS from the Dickman (1978) $W_{^{13}CO}$ data. It should be noted in passing that, using their assumptions, the inner Galaxy mean value of W_{CO} is around $40\,K\,km\,s^{-1}$, much higher than that found in the Orion clouds.

However, Bhat et al. (1986c) estimate $< W_{^{13}CO} > \sim 2.1$ locally, after extrapolating the Liszt et al. data to R = 10 kpc. This can be compared with their figures for Mon OB2, Mon OB1 and CMa OB1 ($< W_{^{13}CO} > = 1.7$, 1.8 and $1.5\,K\,km\,s^{-1}$ using the data in Blitz 1978

and assuming $W_{CO}/W_{^{13}CO} = 5.5$). It should also be noted that the SSS values are upper limits since HI along the line of sight has been ignored. An identical approach with the more uniform Cernicharo and Guélin dataset, but with the HI 'subtracted' as above, yields $X_{20} = 1.2 \pm 0.2$ for $0.5 < A_v < 3$ mag. Guélin and Cernicharo (1988) have published ^{13}CO data for several clouds in Taurus, from which follows $\overline{X}_{20} = 0.6$. However, the assumption that $W_{CO}/W_{^{13}CO}$ = constant is suspect, especially at low A_v (see Fig 3 in Cernicharo and Guélin). Where CO data are available it seems preferable to try and calibrate this directly.

Unfortunately, the Frerking et al. Taurus observations are not useful because there are few points at small A_v. The situation is slightly better in ρ-Oph; a fit to the data in the linear regime ($A_v < 10$ mag) gives

$$W_{CO} = (5.8 \pm .9)\big(A_v - (1.24 \pm 1.02)\big)$$

with a correlation coefficient of 0.9 for 13 points. Assuming that the constant term arises because of residual HI and zero-point errors implies $X_{20} = 1.6 \pm 0.2$.

D. Dickman (1978).

Small dark clouds from the Lynds catalogue were mapped in CO and ^{13}CO. Estimates of total gas column densities were derived from star counts. Correlating W_{CO} vs A_v (see Fig 3.19) for $A_v < 2$ mag yields

$$W_{CO} = (5.72 \pm 1.70)A_v + (4.16 \pm 2.08).$$

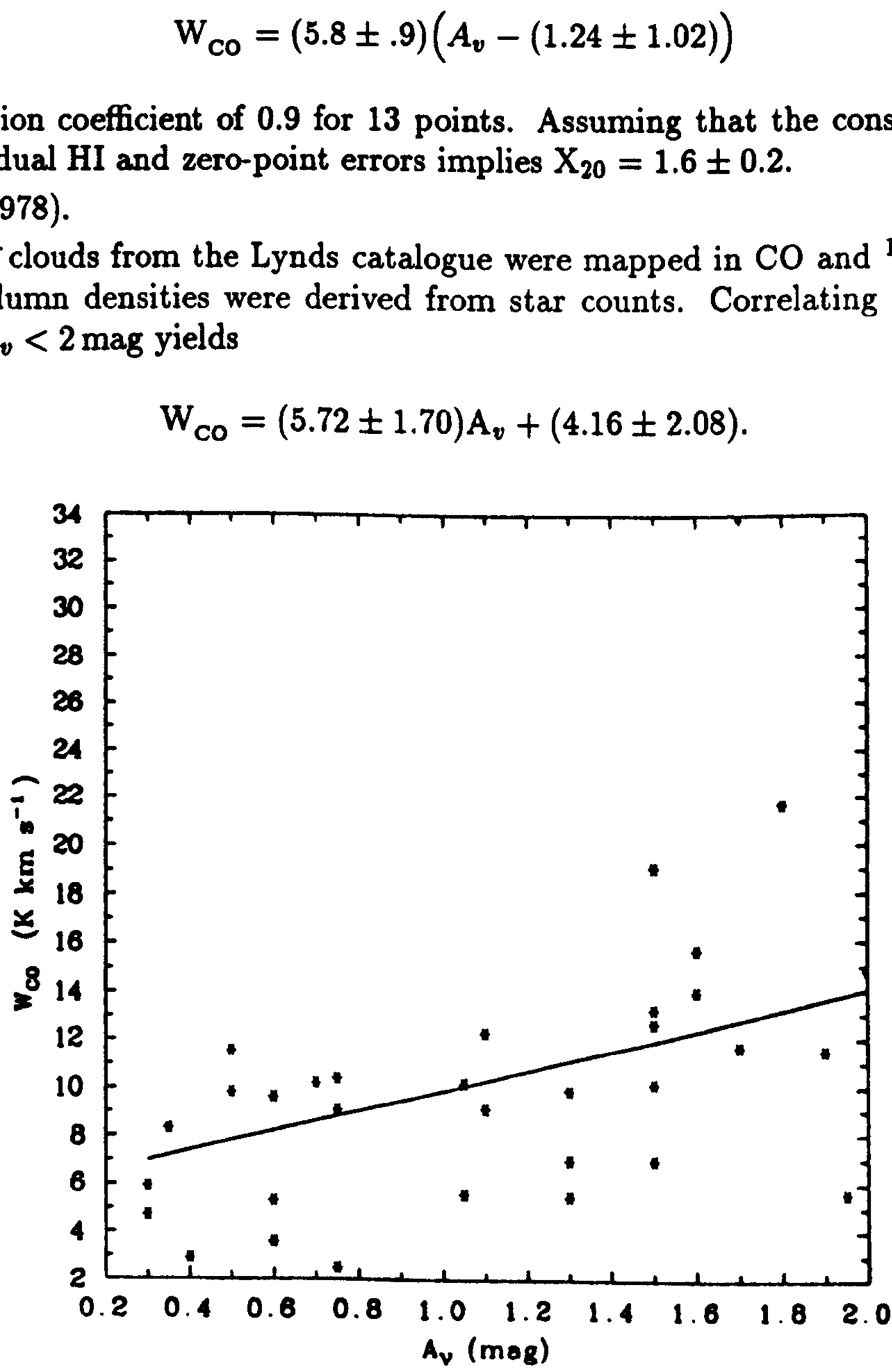

Fig 3.19 W_{CO} versus visual extinction for those clouds with $A_v < 2$ mag observed by Dickman (1978). The line gives the best-fit to the data.

The constant term in this case is greater than zero. It is assumed here to arise from the wide variety of conditions encountered in the cloud sample, causing significant scatter

in W_{CO}. The slope of the relation then implies $X_{20} = 1.7 \pm 0.5$. If the data are binned as above and a curve fitted to the cumulative medians a more satisfactory fit ensues i.e.

$$< W_{CO} >= 7.6 < A_v > -.9,$$

suggesting $X_{20} = 1.25$.

E. Lebrun and Huang (1984).

Extinction data towards the Ophiuchus-Sagittarius region

$$10° < b < 24°$$
$$10° < l < 40°$$

were derived from the star counts of van Hoof (1969). The authors correlated W_{CO} vs $\Delta N(H) = N(H) - N(HI)$ where N(H) is the total gas column density from extinction, and found $X_{20} = 1.1 \pm 0.5$ for $< W_{CO} >= 1.0$. They also found evidence of a 'normal' gas-to-extinction ratio i.e., $5.8 \times 10^{21}\,cm^{-2}\,mag^{-1}$ which is similar to the Bohlin et al. (1978) value of $5.4 \times 10^{21}\,cm^{-2}\,mag^{-1}$.

F. de Vries (1987).

Fifteen small, high latitude molecular clouds, associated with the diffuse IRAS 'cirrus' were studied in detail using 100 μm IR, CO and 21 cm HI observations. Assuming the 100 μm flux density per H atom to be the same in both neutral HI and molecular gas, de Vries computes values for X_{20}. Despite a considerable scatter, all values are low compared to more massive clouds in Taurus and Orion with a mean for all determinations of 0.5 ± 0.15. The median W_{CO} value is not given and is taken to be that of one cloud in his sample.

Though these clouds differ substantially from GMCs in that the gas and dust is heated mainly by the stellar radiation field, they may not be too dissimilar from the less dense regions around more massive molecular clouds. The author suggests that the low values probably arise because of high cloud temperatures ($\sim 20\,K$) and relatively small CO optical depths.

G. LTE masses in Orion.

A large fraction of the Orion A and B clouds have been mapped in both CO and ^{13}CO by Maddalena (1986), from which column densities and masses were obtained using the standard LTE assumptions of §2.3. For a $4.8\,deg^2$ area in Orion B (25% of the area observed in CO) Maddalena derived a LTE mass of $0.2 \times 10^5\,M_\odot$. In Orion A ($11.3\,deg^2$ in ^{13}CO or 39% of the CO area) he found $0.4 \times 10^5\,M_\odot$. The CO data have been used as an estimator of the LTE mass in those parts of the cloud not observed in ^{13}CO giving total masses of 0.5×10^5 and $0.3 \times 10^5\,M_\odot$ in Orion A and B respectively. Comparison with the Maddalena CO-derived mass gives $X_{20} = 1.2$. Curiously, Maddalena derives $X_{20} = 0.9$ by correlating $N_{LTE}(H_2)$ with W_{CO} but states that this is low because his assumed $N(^{13}CO)/N(H_2)$ ratio (2×10^{-6}, derived by Dickman 1978 from CO and extinction studies of local dark clouds) was too large. It is perfectly true that the ^{13}CO abundance varies from cloud to cloud, perhaps by a factor of ~ 2, but Maddalena presents no evidence for this assertion in the Orion clouds. The present work suggests that the Dickman abundance is probably about right.

Cohen et al. (1983) have also obtained maps of the Orion clouds in the 4.8 GHz, $J = 1$ doublet line of formaldehyde (H_2CO). The molecule is of low abundance and is optically thin, permitting a similar LTE analysis. Applying the same method as above gives a mean conversion factor of $X_{20} = 1.4$, consistent with the ^{13}CO line.

The average of all the Orion figures is $X_{20} = 1.3$, substantially smaller than the interpretation (i) of the $\gamma-$ray analysis in §3.3*E*.

3.5 Summary and Conclusion

Figure (3.20) presents the above data as a function of $< W_{CO} >$. There is a tendency for X_{20} to be low (~ 1) in those clouds with small $< W_{CO} >$, but to increase to between $1 - 2$ for $< W_{CO} >= 5 - 20\,\mathrm{K\,km\,s^{-1}}$, where the large local molecular clouds in Taurus and Orion 'reside'. However, at the highest values of $< W_{CO} >$, X_{20} remains roughly constant though there is some indication that it decreases again. This may be because such intense CO emission reflects 'contamination' by high temperature regions such as those undergoing star formation, rather than high gas column densities.

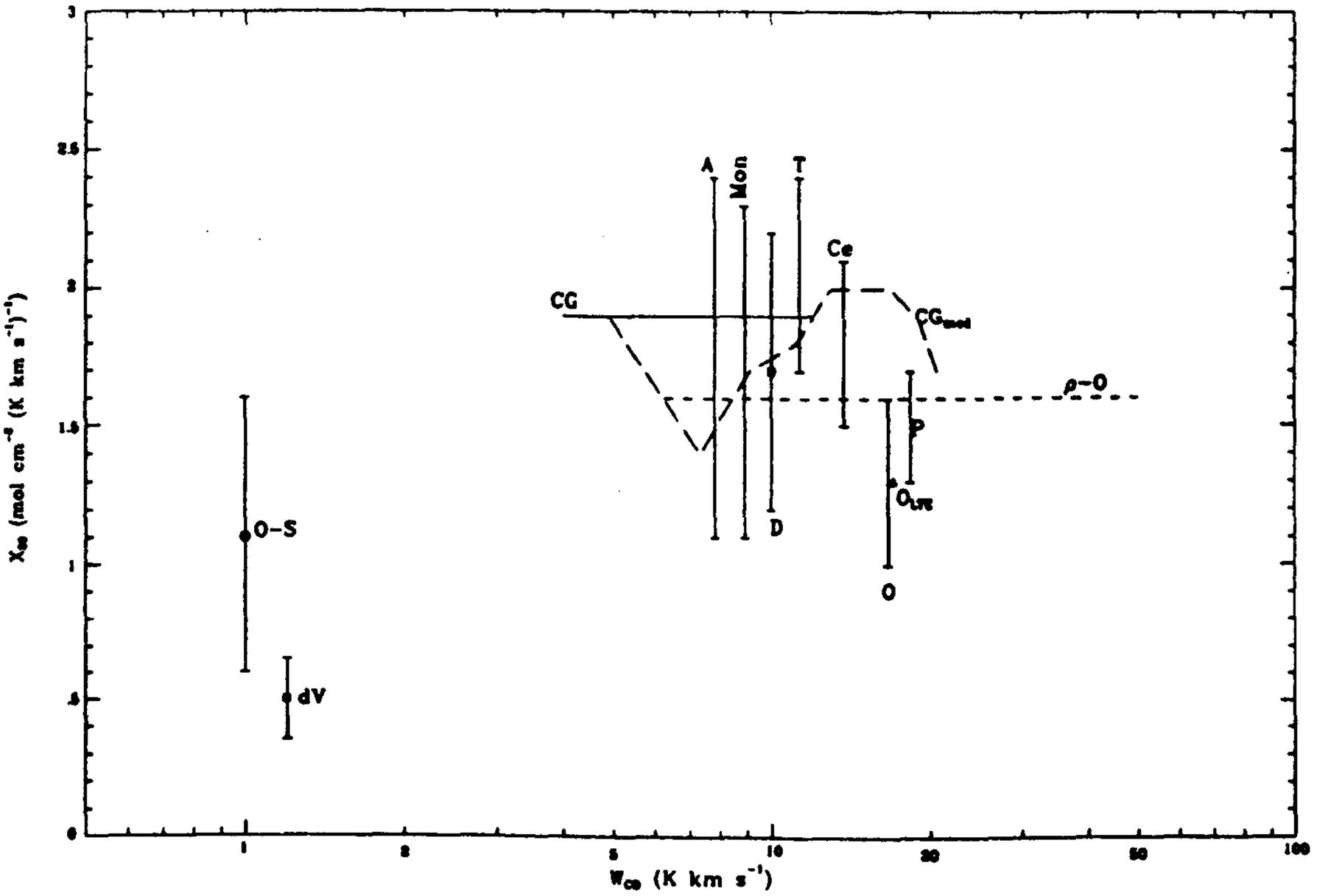

Fig 3.20 The CO-to-N(H_2) conversion factor X_{20} versus median W_{CO} estimated from a variety of sources – see discussion in text.
Key: *dV*, de Vries; *O-S*, Ophiuchus-Sagittarius; *ρ-O*, ρ-Ophiuchus; *D*, Dickman; *T*, Taurus; *P*, Perseus; *O*, Orion; *Ce*, Cepheus; *CG*, Cernicharo & Guélin (HCL2); O_{LTE}; Orion (LTE analyses).

Theoretical work by Maloney and Black (1988), van Dishoeck and Black 1987 and Kutner and Leung 1985 supports a decrease in X_{20} with increasing temperature. The latter claim

$$X_{20} \propto T^{-1.3}$$

under certain conditions, which is not inconsistent with the results presented in Fig (3.20). Solomon et al. (1985) and Scoville et al. (1987) have found evidence that GMC cloud 'cores', defined by some minimum W_{CO} contour, can be categorised as 'warm' ($\overline{T} > 10\,\mathrm{K}$) or 'cold' ($\overline{T} < 10\,\mathrm{K}$) where $\overline{T}$ is an average kinetic temperature over the telescope beam and velocity bin width used ($\sim 5\,\mathrm{K\,km\,s^{-1}}$ in Scoville et al. 1987). If the variation with T is confirmed, these two components will have different X_{20} values, and their relative contribution to the total Galactic H_2 mass becomes an important consideration.

Sanders et al. (1984) attempted to derive X_{20} using the Dickman (1978) and Frerking et al. (1982) ^{13}CO data in local dark clouds and extrapolating to the mean $W_{^{13}CO}$ value observed in the inner Galaxy (see above). However, using CO data directly implies that this will give a substantial overestimate of the mass of gas inside the solar circle where clouds typically have $\overline{W}_{CO} \sim 40\,\mathrm{K\,km\,s^{-1}}$ (SSS, assuming their canonical $W_{CO}/W_{^{13}CO}$ ratio). According to

Fig (3.20), the true value for X_{20} in these clouds could be much less than the SSS value of 3.6 if heating contributes significantly to Galactic CO luminosity.

It is useful at this point to consider in some detail the conclusions of the cloud modelling by Kutner and Leung (1985). These authors solved the CO line transfer problem for the simplified case of a static, spherically symmetric cloud when the characteristic size of a 'turbulent element' is much less than the photon mean free path (the microturbulent approximation). Turbulent velocities were assumed to be of the form $v_{turb} \propto R^{1/2}$, as found by several authors (see Chapter 5). Between 6 and 7 rotational levels could be excited in their models, but the clouds are assumed not to have internal heat sources.

The microturbulent approximation is known to produce self-reversed line profiles in many cases, contrary to observation (Dickman 1985). However, Kutner and Leung argue that their approach is sufficient for computations of integrated intensities, and allows a non-LTE excitation solution while accounting for the non-local nature of the line-transfer process.

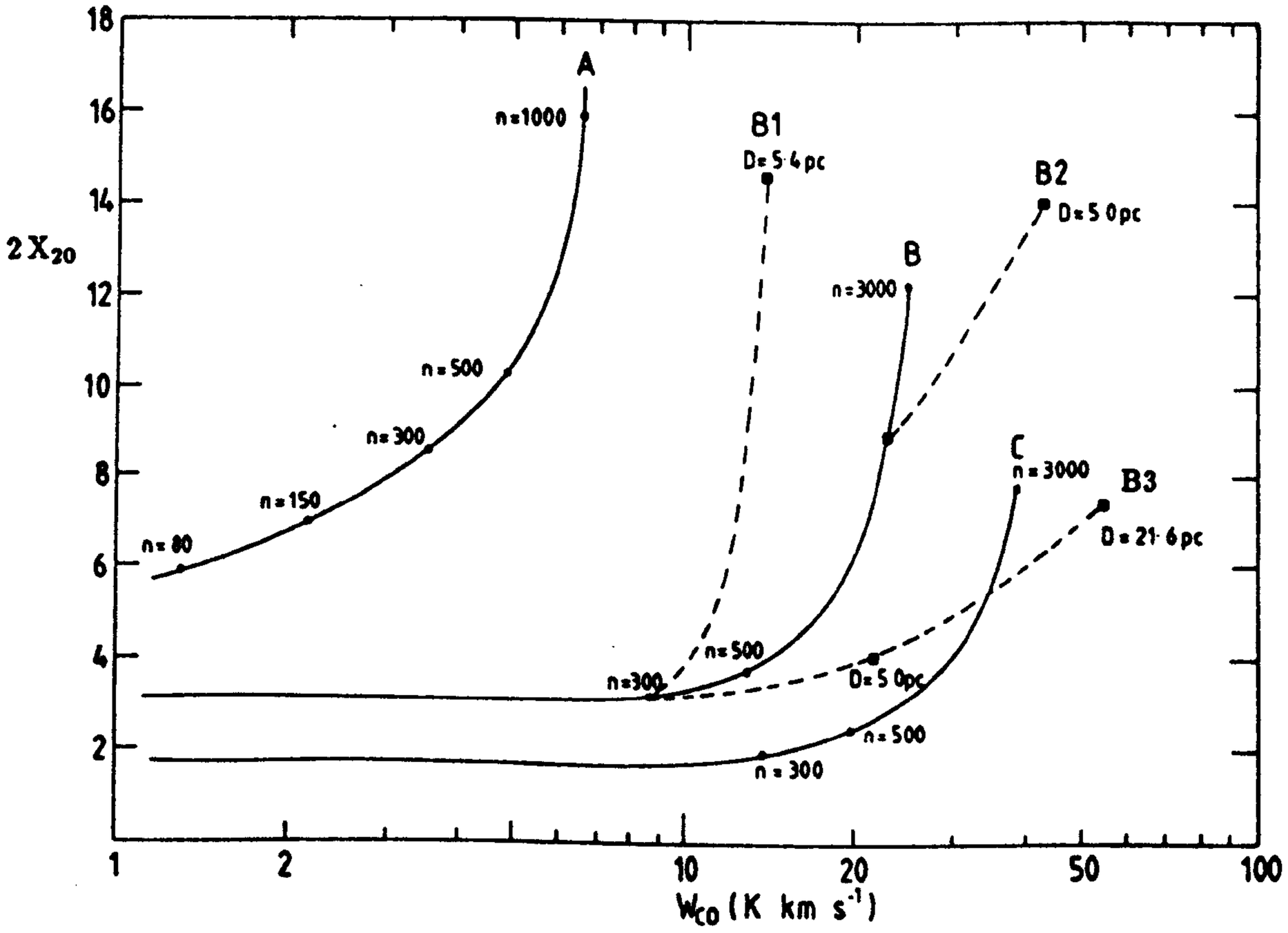

Fig 3.21 X_{20} vesus W_{CO} based on the Kutner & Leung (1985) model cloud calculations (see text). All models shown have $[CO]/[H_2] = 5 \times 10^{-5}$.
Key: A,B,C; diameter $D = 1.6\,pc$, $v_{turb} = 0.6\,km\,s^{-1}$, $T = 6$, 13, 20 K respectively. Variable density.
B1; $n = 300\,cm^{-3}$, $v_{turb} = 0.6\,km\,s^{-1}$, $T = 13\,K$, variable D.
B2; $n = 300\,cm^{-3}$, $T = 13\,K$, variable D, v_{turb}.
B3; as for B2 but with $n = 2000\,cm^{-3}$

The transfer equations are solved for uniform, isothermal clouds of fixed CO fractional abundances and radii. The authors give W_{CO} as a function of $N(H_2)$ for values of these parameters usually encompassing those of GMCs, though cloud radii are small (up to a maximum of about 21 pc). The quantity X_{20}, computed from their results, is shown in Fig (3.21) for a cloud of diameter 1.6 pc, $v_{turb} = 0.6\,km\,s^{-1}$ and $[CO]/[H_2] = 5 \times 10^{-5}$, denoted A, B and C in the figure. Kutner and Leung also give results for clouds of fixed density ($n = 300$ and $2000\,cm^{-3}$) but variable radius, allowing an estimate of the trend to larger diameters (curves B1, B2 and B3). Note that v_{turb} is allowed to vary along B2, but

remains fixed ($0.6\,\mathrm{km\,s^{-1}}$) along B1. This is probably more appropriate for different lines of sight through one cloud.

Kutner and Leung conclude that CO is useful as a mass tracer for

$$N(H_2) \lesssim 5 \times 10^{21}\,\mathrm{cm^{-2}}$$

and

$$n(H_2) \lesssim 300\,\mathrm{cm^{-3}},$$

corresponding to the 'envelopes' of GMCs. This is probably not too restrictive in local clouds, since most of the mass resides in such an envelope. Figure (3.21) therefore only uses column densities below $5 \times 10^{21}\,\mathrm{cm^{-2}}$.

However, GMCs are far from being uniform, isothermal spheres; Blitz (1987) has observed the Rosette molecular cloud in ^{13}CO at high resolution and found that most of the gas mass is contained in dense clumps ($\bar{n} \sim 10^3\,\mathrm{cm^{-3}}$). The term 'envelope' as conventionally used may therefore not be very appropriate and will be used here to mean $N(H_2) \lesssim 5 \times 10^{21}\,\mathrm{cm^{-2}}$ rather than a smooth, diffuse gas. Line transfer calculations in such a medium pose formidable difficulties. Furthermore, no chemical effects have been included in the Kutner and Leung model though these are likely to be very important (van Dishoeck and Black 1987). Therefore, only qualitative conclusions about the variation in X_{20} with $< W_{CO} >$ can be made.

The main trend indicated by Fig (3.21) is that X_{20} remains constant (and relatively small) whenever the CO line is not so saturated as to render it useless as a H_2 tracer e.g., curve B ($T = 10\,\mathrm{K}$). Scaling the cloud to 5 pc along B2 and B3 imply the useful range of W_{CO} varies, but X_{20} doesn't change much. For a cloud of diameter $\sim 20\,\mathrm{pc}$, nearer to typical GMC dimensions, CO appears to be useful out to $40 - 50\,\mathrm{K\,km\,s^{-1}}$, though the line saturates at smaller volume densities. A similar conclusion follows for different lines of sight through one cloud (B1); saturation again becomes important at smaller W_{CO} values. It can be seen that there is a rapid variation of X_{20} with T. The dependence on CO abundance is weaker, however.

The general behaviour of Fig (3.20) can be understood in terms of this model. An embedded or nearby heat source will produce a substantial temperature gradient throughout the cloud. If it is surrounded by a diffuse HI cloud, as appears likely, the temperature could decline from $\sim 80\,\mathrm{K}$ outside (e.g., in the WIM of §2.2) to $\sim 10\,\mathrm{K}$ in the envelope of the cloud, rising once more closer to the heating source. Providing column densities remain small enough to avoid saturating the line, X_{20} would then first increase from a relatively small value, only to decline once more as heating begins to dominate.

A similar X_{20} variation would be expected between the 'warm' and 'cold' cores seen by Solomon et al. (1985), or if there is on average a mean temperature difference between inner and outer Galaxy clouds (Kutner and Mead 1981). The upper curve (A) suggests that CO is a poor mass indicator for very cold, dense clouds.

Kutner and Leung make the important point, on the basis of their model, that it is not useful to calibrate X_{20} in regions where the line is heavily saturated. If, by good fortune, most Galactic GMC mass lies near $N(H_2) \sim 5 \times 10^{21}\,\mathrm{mol\,cm^{-3}}$, this is where it should be calibrated. The mass of dense cloud cores will, of course, be underestimated, but that is not important. These considerations suggest that some of the variation seen in Fig (3.20) might arise from simply overestimating X_{20} in the more opaque cloud regions. A corollary can be added; a local calibration for regions of moderate A_v and $< W_{CO} >$ should be extrapolated with care to regions of very high $< W_{CO} >$ which are likely to be dominated by local or general heating effects, and for which the conversion factor may well be significantly reduced.

The relative contribution of the 'cold' and 'warm' core clouds to the total CO luminosity and molecular mass can now be addressed. Scoville et al. (1987) have analysed the MSB CO survey in a similar manner to Solomon et al. (1985), dividing the emission features they see into '4 K clouds', 'hot cores' and 'HII clouds'. The 'HII clouds' are substantially larger, and therefore more massive, than the entire cloud ensemble i.e.,

$$\overline{D}(\mathrm{HII}) \sim 52\,\mathrm{pc}$$
$$\overline{D}(4\mathrm{K}) \sim 18\,\mathrm{pc}.$$

Not surprisingly, they have higher mean temperatures. The Kutner and Leung model suggests that the appropriate X_{20} for such clouds, which contribute heavily to the total Galactic mass (§2.3), is smaller than for the general inner Galaxy cloud population. This tendency would favour the smaller values for X_{20} suggested by Fig (3.21).

The main result of the foregoing discussion is the realisation that the $\gamma-$ray analysis is greatly complicated by substantial CR variations, on 10 pc scales, in the local ISM at medium latitudes. In Orion, Monoceros and Cepheus it is possible to achieve reasonable agreement (at the 95% level) between the various estimates of X_{20}. A value around $X_{20} = 1.0 - 1.5$, coupled with a considerable excess in the low-energy $\gamma-$ray emissivity along the line-of-sight towards the clouds, seems appropriate.

Agreement is more elusive in the Taurus region. Extinction estimates imply X_{20} in the range $1 - 2.5$. At the same confidence level as above, the $\gamma-$ray analysis requires $X_{20} \lesssim 1.0$, again with a substantial enhancement in q(HI) towards these clouds. This lower result for X_{20} is difficult to understand theoretically; it may arise because a coincidental CR excess in that direction dominates the correlation. In any event it highlights the difficulties encountered by $\gamma-$ray estimates of X_{20} when there are noticeable fluctuations in the CR intensity on these distance scales. It seems likely, considering the evidence from other methods, that the variation reflects the error of the method. Consistency is more difficult to achieve with the higher, universal values of X_{20} favoured by COS-B, or the even larger values of the Massachussets-Stony Brook group.

Derivation of X_{20} based on extinction and optically thin molecular lines suggests there may be difficulties associated with the assumption that X_{20} is constant everywhere within the Galaxy. The conversion ratio probably depends on a number of factors, the most important of which may be temperature, although other parameters which correlate well with temperature (stellar radiation flux, low energy CR flux and, to a lesser extent, metallicity) could also be important.

Using the latest W_{CO} survey of Dame et al. (1987), the total mass of H_2 for R = 2 to 10 kpc can be derived, namely $6.5 \times 10^8\,M_\odot$ for $X_{20} = 1.5$ and constant throughout the Galaxy. This can be compared with $\sim 30 \times 10^8\,M_\odot$ estimated by SSS and $12 \times 10^8\,M_\odot$ from Dame et al. who both assume X_{20} to be independent of R. The Dame et al. result is reduced to $9.9 \times 10^8\,M_\odot$ if the new COS-B figure for X_{20} is used, not too far from the upper limit here. Adopting the variation of R suggested by Bhat et al. (1986c), derived from a mean temperature and metallicity gradient, the inner Galaxy molecular mass falls to $4.5 \times 10^8\,M_\odot$.

The CR variations are of great interest in their own right. The next chapter examines the possibility that part of the variation arises from a CR enhancement in the clouds themselves.

CHAPTER 4
COSMIC RAY PRODUCTION IN MOLECULAR CLOUDS

4.1 Introduction

The $\gamma-$ray analysis in Chapter 3 provided evidence of excessive $\gamma-$ray fluxes associated with local molecular clouds. The effect was mainly confined to the $70-150$, $150-300$ and $300-5000$ MeV energy bands, being much reduced at $800-5000$ MeV and it is apparent that a casė can be made for an enhancement of those CRs contributing substantially to them. This is of considerable interest from a CR standpoint; several models have predicted such a connection between CR production and molecular clouds. The contrary case, CR exclusion from clouds, would appear to be ruled out by the Chapter 3 results. Skilling and Strong (1976) have argued that exclusion from GMCs of $\sim 10^5$ $M_\odot$ is only likely for CRs of energy $E \lesssim 50$ MeV. However the models must account for the magnitude of the effect, its spectral shape and the strong correlation with neutral HI rather than with CO alone.

4.2 Cosmic Ray Energetics in Molecular Clouds.

A precondition for the validity of any model is that the processes considered must produce at least as much energy as is observed in CRs. A total CR energy density of about $0.5\,\mathrm{eV\,cm^{-3}}$ (Wolfendale 1983) gives $\sim 10^{49}$ erg in CRs of $E_{CR} \gtrsim 1$ GeV within a typical GMC of radius 50 pc and mass 10^5 $M_\odot$, providing there is no CR exclusion from the cloud. About 4×10^{47} erg of this would presumably be in electrons of energy $E_e \gtrsim 100$ MeV for a CR spectral index $\gamma = 2.6$.

Of particular interest here are those electrons dominating the $\gamma-$ray emission between $70-300$ MeV. For example, considering the lowest COS-B band (70–150 MeV) and assuming emission via bremsstrahlung processes, this turns out to be electrons with energies of $\sim 100-300$ MeV; such electrons account for about 65% of all CR electrons with $E_e \gtrsim 100$ MeV. If the differential electron intensity in the GMC (I_c) were enhanced by some factor $\beta > 1$, so that $I_c = \beta\, I_e^{\mathrm{ISM}}$, then for $\gamma = 2.6$, the CR excess in the cloud relative to the ISM is $\beta - 1$, with a $\gamma-$ray enhancement of the same size at low energies, where bremsstrahlung probably dominates. Therefore, doubling the $70-150$ MeV emission requires a modest 2×10^{47} erg in electrons of the appropriate energy. Of course, above ~ 300 MeV, where protons and nuclei may become important via π^0 decay, the excess will fall rapidly unless the cloud proton spectrum is also of greater magnitude than that of the surrounding ISM. Note that in this discussion, the 'cloud' may consist of the molecular gas plus any attendant HI 'halo', and the ISM from the CR propagation standpoint, is dominated by its hot, ionised component (HIM) as in §2.2.

Such energies can be compared with the gravitational energy available from cloud formation processes. Assuming that it condensed out of a spherical ball of gas, this will be of order

$$\mathrm{PE}_{form} \sim \frac{GM_c^2}{R_c} = 2 \times 10^{49}\,\mathrm{erg}.$$

If the cloud is clumpy, as observation suggests, some of this energy may end up as random clump kinetic energy. The total KE_{rand} for clumps of mass m_i and velocity v_i is

$$\mathrm{KE}_{rand} = \frac{1}{2}\sum_i m_i v_i^2 \sim M_c(\Delta V)^2$$

where ΔV is the mean clump-clump velocity dispersion. For $\Delta V \sim 2\,\mathrm{km\,s^{-1}}$ (Blitz 1987), $\mathrm{KE}_{rand} \sim 10^{49}$ erg, so that some 50% of the formation energy is available for 'investment' in

CRs. Any mechanism using cloud collapse as an energy source for CR acceleration would need about 10% efficiency.

The translational energy of the cloud complex might also be considered as driving the CR acceleration process with $\mathrm{KE}_{trans} \sim 10^{50}\,\mathrm{erg}$ for $V_{trans} \sim 10\,\mathrm{km\,s^{-1}}$ (Blitz 1987), though it is difficult to see how this might work. However, a variant of this whereby accretion of gas from the HIM compresses CRs in the cloud and enhances the low energy CR flux is more plausible (see §4.4). A crude lower limit to the infall rate can be obtained by considering a cloud moving uniformly with velocity V_c through the ISM. The infall rate is given by

$$\dot{m} \sim 4\pi R_c^2 \rho_{\mathrm{HIM}} V_c$$

so that

$$\begin{aligned}\frac{dT}{dt} &= \frac{d}{dt}\left(\frac{1}{2}MV_c^2\right)\\ &\sim \frac{1}{2}\dot{m}V_c^2\\ &\sim 10^{33}\,\mathrm{erg\,s^{-1}}\end{aligned}$$

for $\rho_{\mathrm{HIM}} = 3 \times 10^{-3} m_{\mathrm{H}}\,\mathrm{g\,cm^{-3}}$ and V_c as above. Over 10^7 yr (the canonical CR disc residence lifetime), the KE available is $\sim 10^{47}$ erg, which is roughly the energy required.

Supernova shock acceleration processes have long been considered likely candidates for CR sources. It is therefore of interest to estimate the efficiency required to deposit CRs of the above energy in a GMC. The energy released per supernova explosion is assumed to be distributed throughout the Galactic disc. If the mean time between explosions is τ_{SN} and the total energy in the disc of supernova origin is E, then

$$\dot{E} = \frac{E_{\mathrm{SN}}}{\tau_{\mathrm{SN}}} - \frac{E}{\tau_L}$$

where τ_L is the timescale for CRs to escape from the disc. In the steady state, $\dot{E} = 0$ so that

$$E = E_{\mathrm{SN}}\left(\frac{\tau_L}{\tau_{\mathrm{SN}}}\right).$$

The average energy per GMC ($\overline{E}_{\mathrm{CR}}$) is then $\epsilon_{FF} E/N$ where ϵ_{FF} is the GMC volume filling factor for the disc, and N is the number of GMCs in the disc. Taking

$$\begin{aligned}\tau_L &= 10^7\,\mathrm{yr}\\ \tau_{\mathrm{SN}} &= 30\,\mathrm{yr}\\ E_{\mathrm{SN}} &= 10^{51}\,\mathrm{erg}\\ \epsilon_{FF} &= .008\end{aligned}$$

and $N = 10^4$ (Sanders et al. 1985; Cowie 1981), then

$$\overline{E}_{\mathrm{CR}} = 2.7 \times 10^{50}\eta\,\mathrm{erg}.$$

Hence, comparing with the figure derived above, $\eta \sim 4\%$ is needed for the solar neighbourhood energy density.

Supernova remnants are known from their synchroton emission to contain energetic electrons. It has been demonstrated that isolated, nearby remnants contain an excess of CR electrons and protons – e.g., Rogers and Wolfendale (1987), for a region around the Vela pulsar; Bhat et al. (1985) and Wolfendale and van der Walt (1988) for Loop I. Thus GMCs associated with SNRs would be excellent candidates for enhanced $\gamma-$ray emission from this standpoint.

4.3 Convection of Low Energy Electrons

Morfill (1982) has proposed that low energy (few MeV) protons and alpha-particles streaming into a cloud, (defined as in §3.1), to offset cloud ionisation losses could generate Alfvén waves in a surrounding HIM. The waves propagate into the cloud in the direction of CR momentum transport where they are damped by ion-neutral friction. In the HIM, where the wave-field is generated, electrons, protons and alpha-particles can all resonate with them if the gyroradius of the CRs $r_g \sim \lambda_A$. The resonant frequency is

$$\nu_{res} = \frac{v_A}{\lambda_A} \sim \frac{v_A}{r_g} \propto \frac{1}{R_{\rm CR}}$$

since $r_g \propto R_{\rm CR}$ (the CR rigidity). Therefore

$$\nu_{res} \propto R_{\rm CR}^{-1}$$

and two different CR species can resonate with the same Alfvén wave if they have the same rigidity. This is true, for example, for 5 MeV protons ($p \sim 100\,{\rm MeV}/c$) and electrons of the same momentum ($E_e \sim 100\,{\rm MeV}$).

The flux of low energy CRs (MeV nucleons, $\lesssim 50\,MeV$ electrons) in the ISM is very uncertain because of solar-modulation effects. However, they can be produced inside the cloud by N-N interactions, mainly 'knock-on' and π^0 decay, between high energy ($\gtrsim 0.5\,{\rm GeV}$) nucleons and the matter in the cloud. These higher energy CRs are unaffected by solar modulation, and their intensity near the solar system is much better known.

As the secondary electrons propagate out of the cloud into the HIM they are scattered by the waves and gain energy each time they are reflected (Fermi acceleration). The electron flux in the cloud can be enhanced provided the electron energy density is less than that of the few MeV protons; otherwise, electrons streaming out of the cloud inhibit access by the MeV protons. There is an upper limit on the energy of electrons generated in this manner. This is set by the cloud column density since, if it is too small, ionisation losses in the cloud become unimportant and the generation of the wave field does not occur. Column densities $\sim 10^{22}\,{\rm cm}^{-2}$, close to the 'half-mass' contour of the Orion and Taurus clouds, correspond to the absorption range of $\sim 50\,{\rm MeV}$ protons and $\sim 200\,{\rm MeV}$ alpha-particles. Including the alpha-particles implies that the mechanism may generate electrons up to $\sim 600\,{\rm MeV}$ in these clouds. Higher-order resonances could increase this limit somewhat.

Losses in the inter-cloud medium can be ignored, even though the particles spend most of their time there, because plasma densities and magnetic fields are low. Inside the cloud, the electrons lose energy mainly via ionisation and bremsstrahlung (producing $\gamma-$rays!). Since electrons of around 100 MeV have much larger absorption ranges than cloud column densities (unlike the few MeV protons), they can traverse the cloud many times, as required for the Fermi acceleration process to work.

Morfill argues that the cloud can be treated as a δ-function in space since CR cloud traversal times are small compared to timescales for particle transport in the HIM. Thus, in region I (Fig 4.1), equation (2.15) becomes for an equilibrium distribution

$$\frac{\partial}{\partial x}\left(-v_A f_1 - \kappa \frac{\partial f_1}{\partial x}\right) = 0 \qquad (4.1)$$

where $\kappa(p)$ is the unknown diffusion coefficient and v_A is the Alfvén speed (taken to be $10^7\,{\rm cm}\,s^{-1}$ in the HIM). The solution for an isolated cloud i.e., no contribution from its

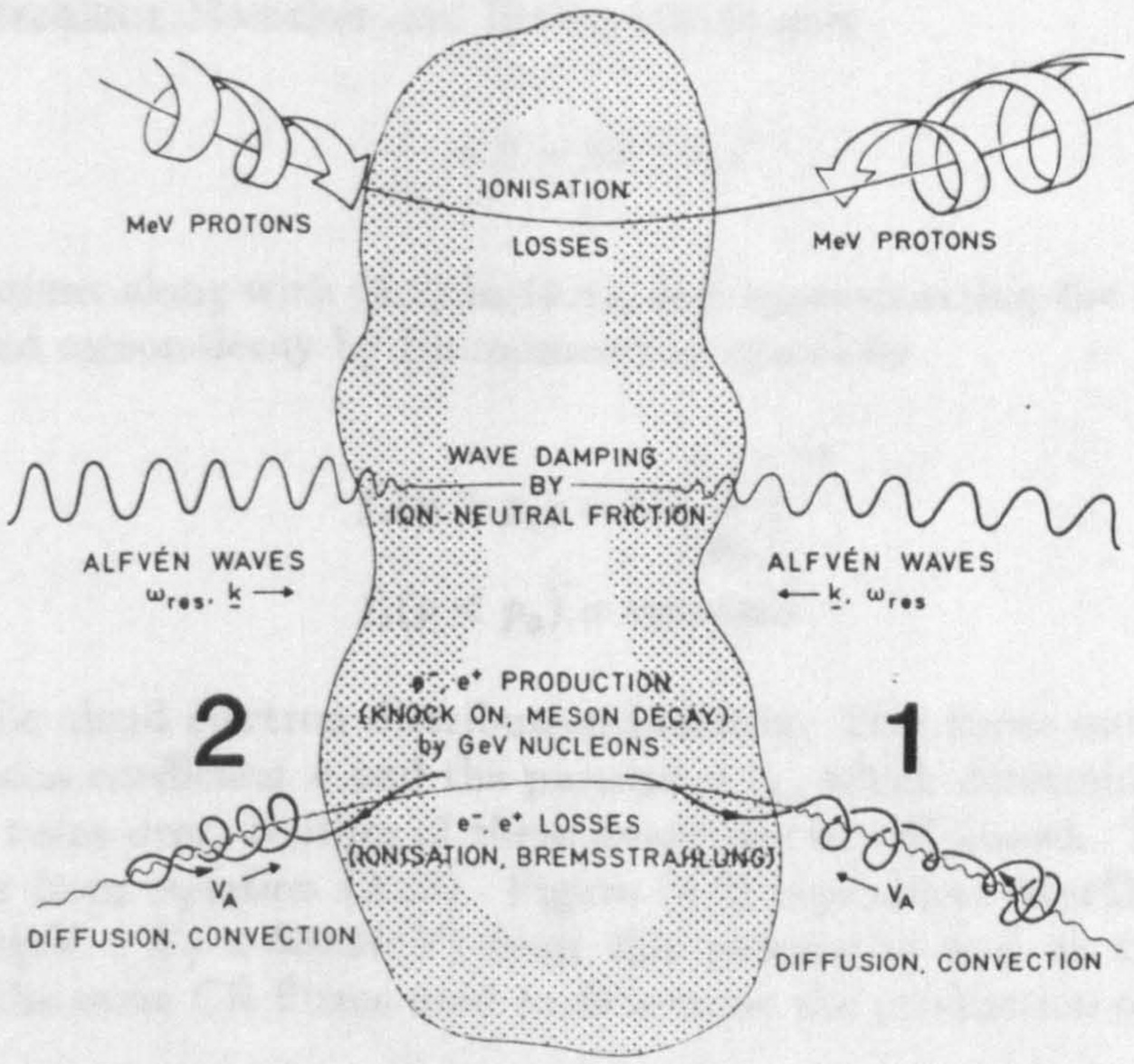

Fig 4.1 Schematic diagram showing the model used by Morfill (1982) to describe particle transport near GMCs. The physical processes involved are also indicated.

'nearest neighbours', is

$$f_1 = A \exp\left(-\int_0^x \frac{v_A}{\kappa} dx'\right) \tag{4.2}$$

where A is a constant to be determined by the boundary conditions at the 'cloud' (at $x = 0$) and with the requirement that the solution is symmetric about $x = 0$ i.e., $f_2(-x) = f_1(x)$.

A solution can be obtained for the δ-function cloud by formally integrating across the discontinuity at $x = 0$, namely

$$\frac{l f_s}{\tau_s} + [uf]_{-\epsilon}^{\epsilon} = \left[\kappa \frac{\partial f}{\partial x}\right]_{-\epsilon}^{\epsilon} - [uC_g f]_{-\epsilon}^{\epsilon} + \frac{1}{p^2}\frac{\partial}{\partial p}\left[p^2 D l f_c\right]_{-\epsilon}^{\epsilon} \tag{4.3}.$$

In this equation, l is the 'size' of the cloud, f_s is the source distribution function and τ_s^{-1} is the rate of particle injection into the cloud. Utilising $u(\epsilon) = -v_A$, $u(-\epsilon) = v_A$, and taking the limit $\epsilon \to 0$ gives

$$2\left[v_A C_g f_1 + \kappa \frac{\partial f_1}{\partial x}\right]_{x=0} = \frac{l}{\tau_i} f_c + \frac{l}{\tau_b} f_c - S \tag{4.4}$$

where $S \equiv (l/\tau_s) f_s \sim c f_s$ and the fact that the $[uf]$ term in equation (4.3) is small has been used. Morfill argues that the last term in equation (4.3) can be replaced by the ionisation and bremsstrahlung loss terms f_c/τ_i and f_c/τ_b respectively without a significant loss of accuracy.

The ionisation loss rate is assumed to be (Ginzburg and Syrovatskii 1964)

$$\frac{1}{\tau_i} = 2.52 \times 10^{-14} n \left(\frac{1}{p}\right)(6.27 + \ln p)\ \mathrm{s}^{-1}$$
$$\approx 2.52 \times 10^{-14} \frac{n}{p}\ \mathrm{s}^{-1}$$

while for bremsstrahlung Marscher and Brown (1978) give

$$\frac{1}{\tau_b} = 8 \times 10^{-16} n \, \mathrm{s}^{-1}.$$

Using these equations along with (4.2) in (4.4), and approximating the source functions for both knock-on and meson-decay by (in momentum space) by

$$f_s(p > p_0) = G \left(\frac{p}{p_0} \right)^{-c}$$

$$f_s(p < p_0) = \text{constant}$$

Morfill obtains the cloud electron distribution function. This turns out to be independent of both the diffusion coefficient κ and the parameter p_0, which determines where the model source spectrum turns over. Neither of these quantities is well known. The bremsstrahlung emissivity follows from equation (2.23). Figure (4.2) reproduces Morfill's expected $\gamma-$ray intensity (for $1\,\mathrm{MeV} < E_\gamma < 600\,\mathrm{MeV}$) from this process as well as that from π^0 decay, computed using the same CR fluxes used to determine the production of electrons.

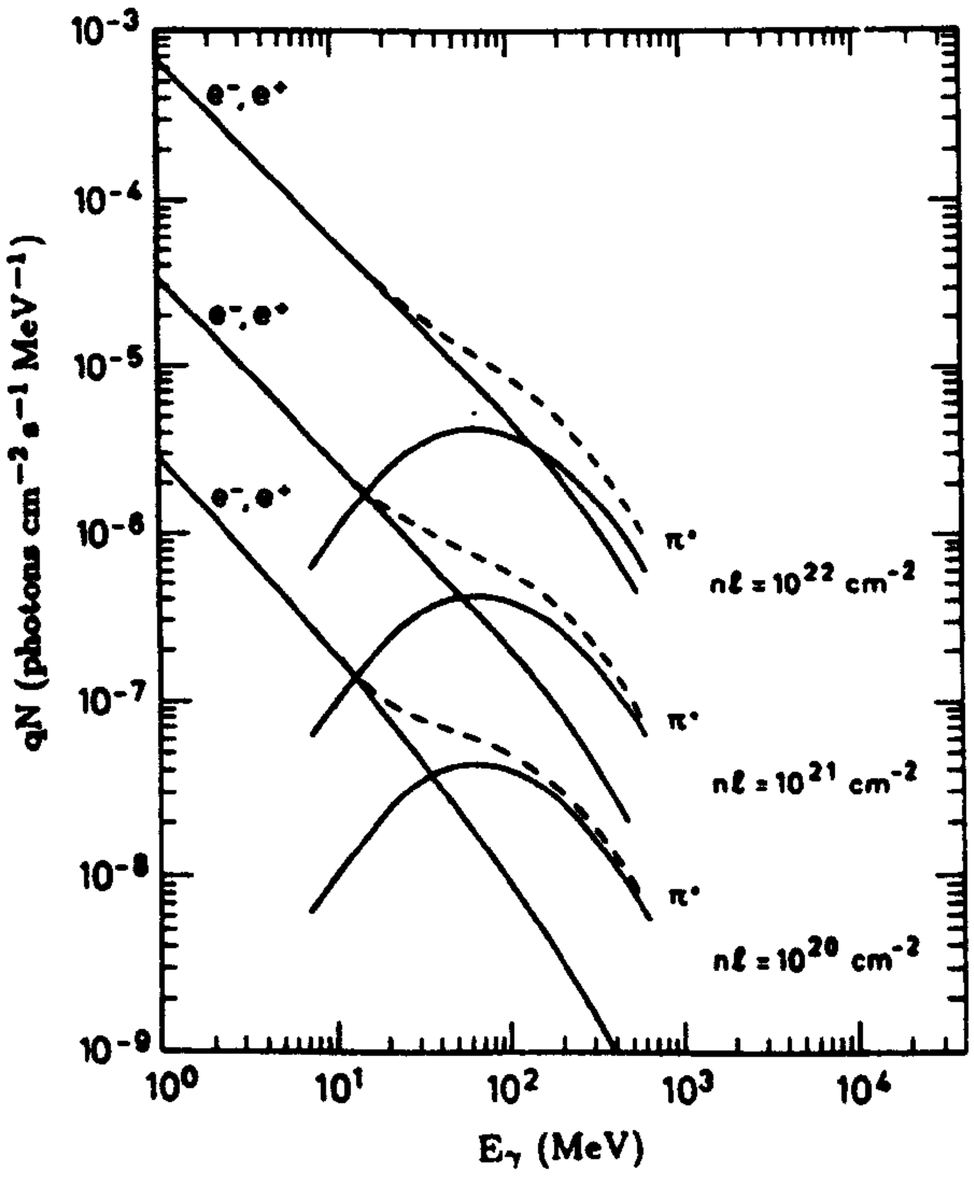

Fig 4.2 Gamma ray emission for the Morfill model due to secondary electron bremsstrahlung as well as π^0 decay. Spectra are given for clouds with column densities N(HI) = 10^{20}, 10^{21} and 10^{22} cm^{-2} respectively.

The acceleration is energetically possible since Morfill's estimated electron energy density is

$$\epsilon_e(E_e < 300\,\mathrm{MeV}) \sim 2.7 \times 10^{-3}\,\mathrm{eV\,cm^{-3}}$$

for a cloud with $< N >= 10^{22}\,\mathrm{cm^{-2}}$, less than the energy density ϵ_p for those protons in the correct rigidity range, $E_p \lesssim 10\,\mathrm{MeV}$, which generate the Alfvén waves (see Fukui and Hayakawa 1981; Hartquist and Morfill 1983).

From Fig (4.2) it is straightforward to estimate the contribution to the emissivities for the COS-B energy bands. Figure (4.3) shows the results for 70$-$150 and 150$-$300 MeV as a

function of column density. The median CO contour in Orion is $\sim 15\,\mathrm{K\,km\,s^{-1}}$, corresponding to a gas column density of about $4.5 \times 10^{21}\,\mathrm{cm^{-2}}$ (for $X_{20} = 1.5$). This should perhaps be increased by $\sim 25\%$ because of the HI envelope, but the effect is small. The enhancements for these bands are 0.24×10^{-26} and $0.16 \times 10^{-26}\,\mathrm{atom^{-1}\,s^{-1}\,sr^{-1}}$ respectively according to Fig(4.3). It is necessary to scale Morfill's GeV proton spectrum to that observed locally; as a rough estimate, it is assumed that π^0 decay contributes about 35% to the $\gamma-$ray emissivity at 70–150 MeV in region $A+C+F$ (see Table 3.3). Morfill's spectrum gives a π^0 emissivity in this band of $0.26 \times 10^{-26}\,\mathrm{atom^{-1}\,s^{-1}\,sr^{-1}}$ so his bremsstrahlung predictions must be increased by $(1.01 \times 0.35)/0.26 = 1.36$. Thus the emissivity in the molecular cloud is enhanced by

$$\Delta q(70/150) = (1.36 \times 0.24) \times 10^{-26} = 0.33 \times 10^{-26}\,\mathrm{atom^{-1}\,s^{-1}\,sr^{-1}}$$

so that

$$\frac{q}{4\pi}(70/150) = (1.01 + 0.33) \times 10^{-26} = 1.34 \times 10^{-26}\,\mathrm{atom^{-1}\,s^{-1}\,sr^{-1}}.$$

Similarly

$$\frac{q}{4\pi}(150/300) = 0.99 \times 10^{-26}\,\mathrm{atom^{-1}\,s^{-1}\,sr^{-1}}.$$

The corresponding figures for the dark clouds in Taurus, Auriga and Perseus, where $<N>= 2.1 \times 10^{21}\,\mathrm{cm^{-2}}$ are

$$\frac{q}{4\pi}(70/150) = 1.24 \times 10^{-26}\,\mathrm{atom^{-1}\,s^{-1}\,sr^{-1}}$$
$$\frac{q}{4\pi}(150/300) = 0.90 \times 10^{-26}\,\mathrm{atom^{-1}\,s^{-1}\,sr^{-1}}.$$

These are summarised in Table (4.1) along with the results from the analysis in Chapter 3.

Table 4.1

Region	ΔE (MeV)	Emissivity (10^{-26} ph atom^{-1} s^{-1} sr^{-1})		
		(a)	(b)	(c)
Orion	70–150	1.34	1.31 ± 0.14	1.39 ± 0.15
"	150–300	0.99	0.90 ± 0.08	0.88 ± 0.05
Taurus	70–150	1.24	1.69 ± 0.12	1.39 ± 0.08
"	150–300	0.90	1.06 ± 0.08	0.98 ± 0.05

(a) Enhancements predicted by Morfill (1982) added to the estimates from regions $A + C + F$ of §3.3

(b) Cloud emissivity derived from a two-parameter fit to the $\gamma-$ray data

(c) Derived from a one parameter fit; X_{20} fixed at 1.5

It was pointed out in Chapter 3 that the best fit solution in Taurus predicts unreasonably small values for $q(H_2)$ and it was doubtful that Δq(HI) derived from the correlation could all be associated with the molecular clouds in that region. However, for the case where X_{20} was forced to have the value 1.5, the Morfill model accounts for almost all the excess in both energy bands for all molecular cloud regions. If the emissivity is higher in the cloud than along the line-of-sight, the Morfill predictions are low by up to 50%. Nevertheless, considering the uncertainties, the agreement is reasonable. Consequently, the results seem encouraging and merit further attention. It is worth emphasising that an increased CR flux in a neutral HI cloud associated with the molecular gas is to be expected in this model.

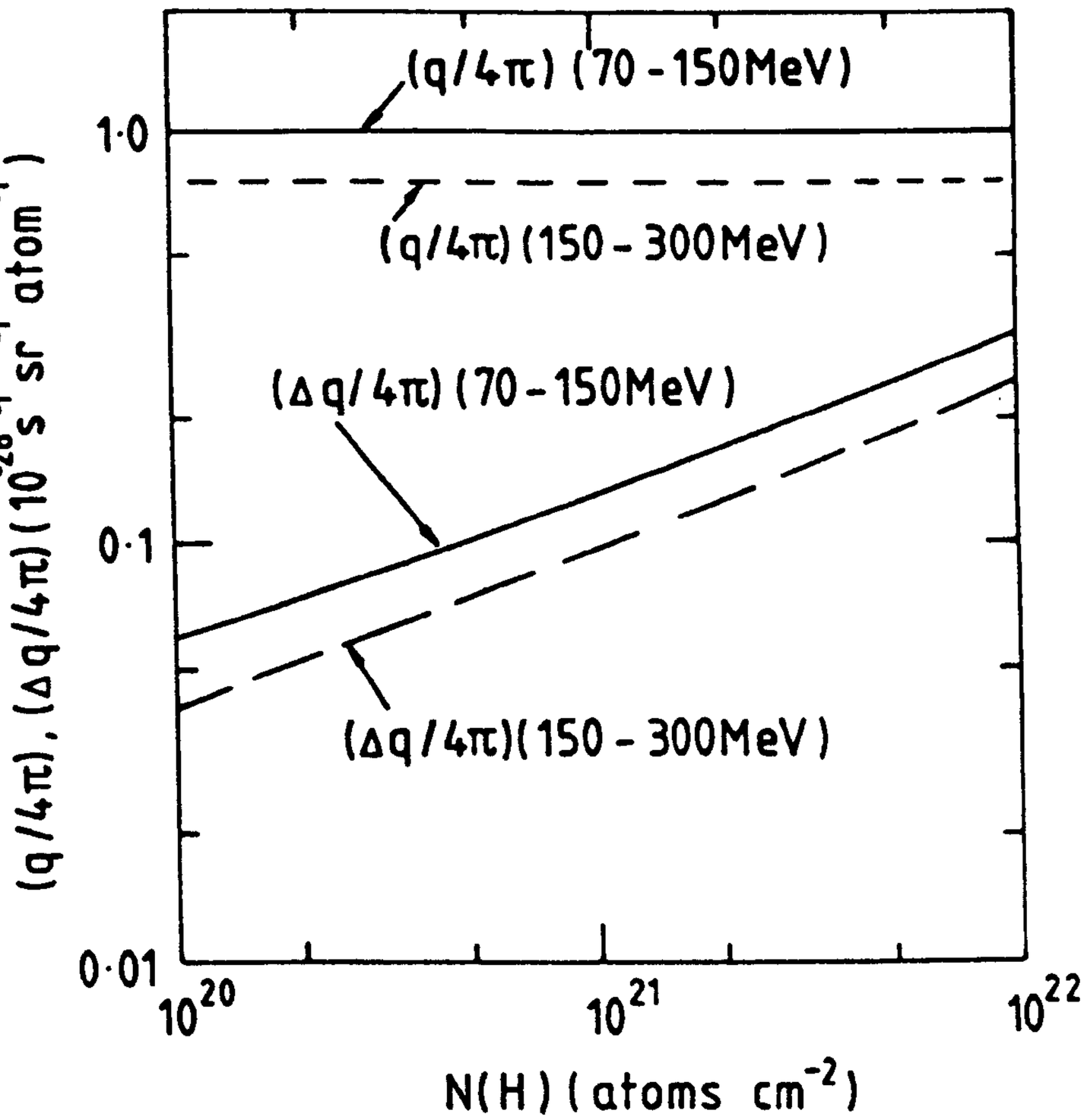

Fig 4.8 Incremental values of the $\gamma-$ray emissivity derived using the model of Morfill (1982). Emissivity values found well away from the clouds (regions $A + C + F$ in §3.3) are also shown.

4.4 Cosmic Ray Modulation by Cloud Accretion and Evaporation

Völk (1983a, b) has suggested that evaporation/accretion of gas onto cold interstellar clouds (HI or molecular) immersed in the HIM might modulate cloud CR intensities. Cowie and McKee (1977) found a critical radius below which cold interstellar clouds evaporate, since radiation losses are smaller than the conductive heat flux from the hot ISM. Thus, according to these authors, a spherical cold cloud of density $\sim 10\,\mathrm{cm}^{-3}$ and radius $1 < Rc < 10\,\mathrm{pc}$ in a medium of density $\sim 3 \times 10^{-3}\mathrm{cm}^{-3}$ and temperature $\sim 5 \times 10^{6}\,\mathrm{K}$ evaporates supersonically with an internal pressure $\sim (2-6) \times p_{\mathrm{HIM}}$ where

$$p_{\mathrm{HIM}} \sim 10^{-13}\,\mathrm{dynes\,cm}^{-2}.$$

The CR energy density is

$$\epsilon_{\mathrm{CR}}(E_{\mathrm{CR}} \gtrsim 1\,\mathrm{GeV}) \sim 0.5\,\mathrm{eV\,cm}^{-3}$$

and since, for a relativistic gas,

$$p_{\mathrm{CR}} = \frac{1}{3}\epsilon_{\mathrm{CR}},$$

then $p_{\mathrm{CR}} \sim 10^{-13}\,\mathrm{dynes\,cm}^{-2}$. Furthermore, for a typical ISM magnetic field strength ($B \sim 10^{-6}\,\mathrm{G}$),

$$p_B = \frac{B^2}{8\pi} \sim 10^{-13}\,\mathrm{dynes\,cm}^{-2}$$

so that $p_{\mathrm{CR}} \sim p_B \sim p_{\mathrm{HIM}}$ i.e., these components are in approximate pressure equilibrium.

The internal pressure in the evaporating cloud is therefore much greater than p_B or p_{CR}, and the outflow speed (v_{out}) is greater than the Alfvén speed v_A in the HIM since

$$v_A = \frac{B}{\sqrt{4\pi\rho_{HIM}}}$$

and

$$v_{out} > c = \sqrt{\frac{p_{HIM}}{\rho_{HIM}}}$$

where c is the sound speed, ρ_c the mass density of the cloud and ρ_{HIM} is the mass density of the HIM. Therefore

$$\frac{v_{out}}{v_A} > \frac{c}{v_A} \gtrsim 1$$

Since $c \sim 200\,\mathrm{km\,s^{-1}}$, parallels can be drawn with the solar wind ($v \sim 100\,\mathrm{km\,s^{-1}}$) which effectively excludes CRs of $E_{CR} \lesssim 1$ GeV from the solar cavity (dimension $\sim 10^{-3}$ pc). Scaling this to the clouds of radius ~ 10 pc implies that all but the highest energy CRs may be excluded from the cloud. If HI clouds tend to be small ($R_c < 10$ pc) – say, in the outer Galaxy – then CR and $\gamma-$ray intensities might be below expectation.

For clouds larger than the critical radius, radiative heat loss is sufficient to offset the heat flux from the HIM, and a static equilibrium is possible. In this case Völk suggested that accretion onto such large clouds might occur and perhaps play an important role in preserving the mass balance between these two phases of the ISM. He argued that the flow speed is less than the Alfvén speed as follows. The gas flow onto the accreting cloud is subsonic since it is driven by the gas pressure gradient (between the hot and cold gases). Since the CR pressure is substantial, the flow is strongly influenced by it. If the flow speed is greater than v_A, so that the relative flow speeds between the gas and CRs streaming out of the cloud is also greater than v_A, an Alfvén wave field is generated around the cloud which convects CRs back into the cloud in much the same manner as in §4.3. Except at very low energies they do not cool efficiently, and they are compressed sufficiently to decelerate the incoming flow until it is sub-Alfvénic. In this steady state situation, CRs can stream outwards through the accretion flow.

Therefore the CR and gas pressure inside the cloud ($p_{g_i} + p_{CR_i}$) equals the CR, gas and flow pressure outside the cloud ($p_{g_o} + p_{CR_o} + \rho_{HIM} u_\infty^2$) where $u_\infty \lesssim v_A$ i.e.,

$$p_{CR_i} - p_{CR_o} = \rho_{HIM} u_\infty^2 + p_{g_o}. \tag{4.5}$$

The internal gas pressure (p_{g_i}) has been set to zero since clouds of $R_c \gtrsim 10$ pc, $T \sim 10$ K and mass $\gtrsim 10^4\,M_\odot$ are likely to have neglible or even negative internal pressures (corresponding to cloud collapse) for reasonable values of the magnetic field strength (Spitzer 1978).

For an Alfvénic flow, an approximate pressure equilibrium between the streaming gas and magnetic field is likely, as in the HIM, so that $\rho_{HIM} u_\infty^2 \lesssim p_B$. Substituting in equation (4.5) then gives

$$\begin{aligned} p_{CR_i} - p_{CR_o} &\lesssim p_{g_o} + p_B \\ &= p_{g_o}\left(1 + \frac{p_B}{p_{g_o}}\right) \\ &\sim 2p_{g_o}. \end{aligned}$$

Since

$$p_{CR_o} \sim p_{g_o} = p_{HIM},$$

this reduces further to $p_{CR_i} \sim 3p_{g_o}$. The flow speed is less than $v_A \sim 3 \times 10^6\,\mathrm{cm\,s^{-1}}$ for the HIM, so that an estimate of $\dot{E}$ is obtained by setting

$$v_\infty = v_A$$
$$n_\infty = 3 \times 10^{-3}\,\mathrm{cm^{-3}}.$$

For $R_c = 50\,\mathrm{pc}$, this turns out to be $\dot{E} = 2 \times 10^{34}\,\mathrm{erg\,s^{-1}}$, corresponding to

$$E_{\mathrm{CR}} \sim 6 \times 10^{47}\,\mathrm{erg}$$

over $10^7\,\mathrm{yr}$. Comparing this with the results of §(4.1) suggests the model is energetically viable for electrons, but not for protons. Since electrons are unimportant dynamically, the model makes no predictions about them. If they do participate in the process, however, it appears that they could be accelerated to quite high energies as indicated by the following argument. In equilibrium, CRs diffuse out of the cloud with velocity $\lesssim v_A$, so that the diffusion coefficient near the cloud is given by

$$K \lesssim R_c v_A \sim 5 \times 10^{26}\,\mathrm{cm^2\,s^{-1}}$$

for $R_c \sim 50\,\mathrm{pc}$ and $v_A \sim 3 \times 10^6\,\mathrm{cm\,s^{-1}}$. Note that this requires a process of wave production around the cloud since the canonical Galactic value is $K \sim 10^{28}\,\mathrm{cm^2\,s^{-1}}$.

In the limit of large amplitude waves

$$K \sim \frac{1}{3} c r_g = \frac{1}{3} \frac{P}{B}$$

where r_g is the particle gyroradius, P the rigidity and B the magnetic field strength. For P in GV and $B = 3\,\mu\mathrm{G}$ this is

$$K = P_{\mathrm{GV}} \times 10^{22}\,\mathrm{cm^2\,s^{-1}}$$

so the process 'works' to high energies. This might explain some of the excess seen in the higher $\gamma-$ray bands, but a more quantitative assessment is required before the validity of this model is established. Nevertheless, it would predict that $\gamma-$ray emission from the inner Galaxy, where GMCs are common, could be enhanced by roughly the amount observed in local clouds perhaps accounting for the Riley and Wolfendale (1984) result (see §3.3).

4.5 SNOBs

These objects, conceived as SNRs linked with OB associations and their surrounding molecular gas, were proposed by Montmerle (1979) as candidates for a class of COS-B $\gamma-$ray 'sources'. He argued that $\gamma-$ray emission was likely from SNOBs on several grounds.

(i) They had a similar scale height to that of the COS-B sources.

(ii) Relativistic electrons are known to be associated with SNRs. However, CR nuclei might also be important providing that the supernova shock acceleration mechanism works. Since this requires injection into the shock of energetic (MeV) nuclei, he suggested that they might come from the flaring of stars in the OB association.

(iii) They were rich in gas which could provide a target for the CR electrons and protons, producing $\gamma-$rays via bremsstrahlung or π^0 decay respectively. The cloud might also assist in confining the CRs near the source by scattering off Alfvén waves generated in the surrounding HIM as they stream out (see above). Such waves are strongly damped in the neutral clouds, but limit the speed of the CRs in the HIM to about v_A.

It was originally proposed that up to half of the first COS-B source catalogue could be of this type. However, the original catalogue was over-optimistic. Several 'sources' are now well explained by CR irradiation of a clumpy ISM (e.g., Li and Wolfendale 1981; Houston and Wolfendale 1983; Simpson and Mayer-Hasselwander 1987). Nevertheless, the model has several attractive features, particularly on a large scale, and the evidence for it is reviewed before commenting on its relevance to the present work.

In the Galactic Centre direction the SNOB candidates for the remaining unidentified 2CG sources are those associated with the SNR CG78.2 + 2, W28 (Montmerle 1985) and the Carina nebula (Morfill et al. 1984). These lie roughly within the error boxes ($\sim 1°$ radius) of the COS-B sources 2CG078+01, 2CG006-00 and 2CG299-00 respectively, although Montmerle (1985) suggests the latter could be caused by stellar wind shocks driven by the Wolf-Rayet stars in the Carina Nebula.

The same concept can be extended to include supernovae exploding some distance away from a GMC (say, $\lesssim 10\,\mathrm{pc}$) and interacting when they are older and larger than the case above. Then the ρ-Oph cloud, being overtaken by the North Polar Spur (Loop I), might also be considered a candidate for 2CG353+16 (e.g., Morfill et al. 1984) though uncertainties in the cloud mass easily encompass the case of no enhancement above the local emissivity. A further 2 likely SNOBs (Cygnus Loop and IC443 are likely to be below the COS-B detection threshold. The above authors estimate that more than 250 such SNOBs with CR enhancements three times the solar neighbourhood value might be expected throughout the Galaxy, with more than 20 within 5 kpc of the sun. Thus, this mechanism may be important in understanding a major class of $\gamma-$ray objects detectable by the next generation of $\gamma-$ray telescopes. Several may already have been detected, as indicated above.

Although the model is unlikely to be useful for the local GMCs considered here insofar as none of the clouds examined has an associated supernova, it may be relevant to the larger scale result of Riley and Wolfendale (1984) Returning to the local clouds, Taurus is particularly 'inert' from the standpoint of stellar activity, but shows a similar enhancement as Orion. For this reason also, CR acceleration by stellar wind shocks from the OB stars associated with the HII region M42 in the Orion complex, as has been suggested for both ρ-Oph (Cassé and Paul 1980) and Carina (e.g., Montmerle 1981), can probably be excluded though it is feasible on energetic grounds.

4.6 Summary

The evidence presented in the previous chapter indicated a higher average CR intensity at low energies in several local GMCs compared to nearby, predominantly HI regions. Riley and Wolfendale (1984) have suggested that this feature might be present throughout the Galaxy.

Several explanations have been considered. The model of Morfill (1982) gives results roughly consistent with observation and needs to be taken seriously. An alternative scenario by Völk is interesting, at least in a qualitative sense, in that it may account for the small excess seen at higher $\gamma-$ray energies ($300-5000$, $800-5000\,\mathrm{MeV}$).

Some other models have not been considered – e.g., that of Ormes (1987) and Berezinsky et al. (1985) – and some, or all, may be important in various contexts. Clearly the presence of such acceleration mechanisms complicates the $\gamma-$ray technique considerably, and great care is required in its interpretation. It offers a new insight, however, into the reasons for the (small) difference between the value of X_{20} derived by COS-B and the Durham workers.

CHAPTER 5
VIRIAL ESTIMATES OF MOLECULAR CLOUD MASS

5.1 Introduction

It has been argued in previous chapters, using both $\gamma-$ray and extinction data as well as LTE arguments, that $X_{20} \sim 1 - 1.5$ in local GMCs. The reasons for the disagreement with the COS-B estimates of X_{20} were studied in some detail, and it was concluded that their slightly higher value in the Orion cloud flowed from a disregard of CR production in GMCs. The complexity of the $\gamma-$ray picture prevented an unequivocal determination of the magnitude of X_{20}, however.

Evidence for much higher values of the conversion factor has been presented recently by Scoville et al. (1987) and Solomon et al. (1987) (SRBY). These authors use the MSB Galactic Plane CO Survey (8° to 90° in longitude and -1° to $+1^\circ$ in latitude) and the virial theorem to derive $X_{20} = 3$ (SRBY) and $X_{20} = 3.1$ (Scoville et al.) for inner Galaxy clouds of mass around $5 \times 10^5\,M_\odot$, near the median mass of the SRBY sample. Disagreement with the analysis of Bhat et al. (1986c), who derived $X_{20} \sim 1.0$ for $R = 5 - 6$ kpc, is even sharper than that presented here.

In this chapter, the virial theorem technique is scrutinised in detail and re-applied to the MSB survey to try and clarify the discrepancy.

5.2 The Virial Theorem

For an isolated system, of density ρ, the virial theorem can be expressed as (Spitzer 1978)

$$\frac{1}{2}\frac{D^2 I}{Dt^2} = 2E_t + E_I + \Omega + E_M \tag{5.1}$$

where $I \equiv \int \rho r^2\, dV$ is the generalised moment of inertia, $E_t \equiv \frac{1}{2}\int \rho v^2\, dV$ is the total kinetic energy of the system, $E_I \equiv 3\int P\, dV$ is related to the internal energy of the fluid, $E_M \equiv \frac{1}{8\pi}\int B^2\, dV$ is the magnetic energy and surface terms have been ignored. The total gravitational potential energy, Ω, is defined by

$$\Omega \equiv -\int \rho \mathbf{r} \cdot \nabla\phi\, dV.$$

If the system is not isolated and external masses have a significant gravitational effect on it, then Ω cannot be so identified; furthermore, surface effects (pressure, magnetic fields etc) may become important.

In many cases, GMCs are presumed to be isolated (in the sense of the virial theorem), non-rotating, in equilibrium and to have negligible support from magnetic fields. With these assumptions, equation (5.1) becomes

$$2E_t + \Omega = 0 \tag{5.2}$$

since the internal energy of the gas in GMCs is small compared to the kinetic energy of large-scale motion and gravitation. If the system is spherically symmetric and of density

$$\rho(r) = \rho_0 r^{-\alpha}$$

with $\alpha < 3$ then, using the definition of Ω

$$\int_0^{R_c} r^{2-\alpha} v(r)^2\, dr = \int_0^{R_c} r^{-\alpha}\left(r\frac{\partial\phi}{\partial r}\right) r^2\, dr$$

where v is the fluid velocity and ϕ the gravitational potential. The above equation can be written

$$M_c = \left(\frac{5-2\alpha}{3-\alpha}\right) \frac{<v^2> R_c}{G} \tag{5.3}$$

where $<v^2>$ is the mean square of the random gas velocities averaged over the cloud and G is the gravitational constant. Given the above assumptions, an estimate of the GMC mass requires an estimate of $<v^2>$ and of the cloud 'radius' R_c. If the velocity field is Gaussian and isotropic with (one-dimensional) dispersion σ_v then $<v^2>= 3\sigma_v^2$ and

$$\sigma_v^2 = \frac{(\Delta v)^2}{8 \ln 2},$$

where Δv is the velocity FWHM. Therefore equation (5.3) becomes

$$\begin{aligned} M_c &= \frac{3}{8 \ln 2} \left(\frac{5-2\alpha}{3-\alpha}\right) \frac{(\Delta v)^2 R_c}{G} \\ &= k(\alpha)(\Delta v)^2 R_c. \end{aligned} \tag{5.4}$$

Values of $k(\alpha)$ for $\alpha = 0,\ 1$ and 2 are given in Table (5.1).

Table 5.1

α	$k(\alpha)$
0	210
1	190
2	126

Molecular linewidths arise not only from large-scale dynamical cloud motions but also from thermal and line-transfer effects. They provide a convenient way of measuring Δv, but any saturation line broadening must be removed before using in equation (5.4) if substantial overestimates of cloud mass are to be avoided. Thermal linewidths are only a few tenths of a $\mathrm{km\,s^{-1}}$ and are important in small cloud cores and dark globules (see Dickman and Clemens 1983; Myers and Goodman 1988a). For GMCs, linewidths are typically tens of $\mathrm{km\,s^{-1}}$, and thermal broadening can be ignored.

5.3 Application to Molecular Clouds

Equation (5.3) is the form of the virial theorem used by many authors, including SRBY and Scoville et al. Clearly, several assumptions have gone into its derivation. Even if these prove to be reasonable, there are additional difficulties with the choice of molecular line and its relation to R_c and Δv.

A. Equilibrium

The first question that must be clarified is whether molecular clouds are sufficiently close to virial equilibrium for the application of equation (5.2) to be meaningful. It is likely that GMCs are disturbed on timescales that are short in comparison to their dynamical relaxation time (see e.g., Kutner 1984). Supernova explosions, young stars, stellar winds, HII region shocks and cloud-cloud collisions increase the velocity dispersion but cannot be accounted for in an equilibrium model. Similarly, GMCs are unlikely to be dynamically isolated in the Galactic disc, particularly in the inner Galaxy where many of the MSB survey clouds are

to be found. Tidal effects which introduce shearing forces may be important there and lead to complete disruption in certain circumstances. Some support for the importance of such processes can be found in the observed irregular and extended structure of GMCs, which imply they are not often dynamically relaxed systems.

B. Magnetic fields

Consideration of the role of magnetic fields in molecular cloud support has received a new impetus with recent measurements of field strengths from Zeeman splitting of HI and OH lines in several dark clouds. These have also been inferred in dense cores associated with compact HII regions from similar measurements in OH maser lines (see Myers and Goodman 1988a and references therein, particularly their Table 1). Typical values in molecular clouds are around 30 μG for clouds of size $\gtrsim 1$ pc.

Mouschovias and co-workers have long argued that magnetic fields of this order were to be expected for self-gravitating, magnetically supported clouds (see Mouschovias 1987 for a review). In such a case, the supersonic linewidths seen in GMCs are essentially caused by Alfvén wave disturbances generated, for example, by contraction of cloud fragments or clump-clump collisions. Mouschovias argues that the Alfvén speed of such clouds is given by

$$v_A \sim \left(\frac{GM}{R}\right)^{\frac{1}{2}} \sim (\pi G \sigma R_c)^{\frac{1}{2}}$$

where σ is the mass surface density of the cloud. This model therefore requires equation (5.4) to hold approximately for molecular clouds and predicts the $\Delta v \propto R_c^{0.5}$ relation often observed, providing σ varies slowly between GMCs. The work of Heyer (1986) and Myers and Goodman (1988b) provide further evidence that magnetic fields play an important, perhaps even decisive, role in the internal dynamics of GMCs.

C. Linewidth

Whatever the origin of GMC velocity fields (turbulent cascades, magnetic fields etc.) they are commonly investigated with molecular emission lines. If optical depth scales roughly as abundance, CO will be insensitive to the physical conditions and kinematics throughout the observed gas column and can provide little information on cloud velocity structure unless the medium is very clumpy. Evidence that this is so has already been summarised. The questions are immediately posed

(i) what are the limits within which optical depth effects are unimportant both with respect to estimating column densities and linewidths.

(ii) does the line adequately sample the velocity field of the cloud.

It was noted in §3.4 that W_{CO} was proportional to A_v only for $A_v \lesssim 3$ mag in Taurus and $A_v \lesssim 10$ mag in ρ-Oph. The limiting magnitudes are significantly larger for the rarer isotopic species ^{13}CO and $C^{18}O$, suggesting that optical depth plays an important role in column density estimates in local clouds at least. It is not implausible to suppose that they affect linewidths similarly.

With regard to point (i), in the LTE microturbulent approximation, saturation broadening can be calculated exactly. Spitzer (1978) derives an expression for optical depth i.e., for the $J = 1 \rightarrow 0$ transition

$$\tau_\nu = \frac{N_0 8\pi^3 \nu_{01}}{3hc} |\mu_{01}|^2 \left[1 - \exp\left(-\frac{h\nu_{01}}{kT_x}\right)\right] \phi(\Delta\nu) \qquad (5.5)$$

where the notation is as in equation (2.9). Assuming a Gaussian velocity field (microturbulence) and Doppler broadening, the line profile can be written

$$\phi(\Delta\nu) = \frac{\lambda_{01}}{2(\pi \ln 2)^{\frac{1}{2}}} \exp\left(\frac{-v^2 4 \ln 2}{(\Delta v)^2}\right) \qquad (5.6)$$

with Δv the intrinsic linewidth (FWHM), v the velocity offset from the line centre and λ_{01} the central wavelength. Substituting in equation (5.5) and using

$$\left[1 - \exp\left(-\frac{h\nu_{01}}{kT_x}\right)\right] \sim \frac{h\nu_{01}}{kT_x}$$

(since $T_x \sim T \sim 10\,\mathrm{K}$), the peak line opacity is

$$\tau_p = \frac{8\pi^{\frac{5}{2}}}{3h}(\ln 2)^{\frac{1}{2}}|\mu_{01}|^2 \left(\frac{h\nu_{01}}{kT}\right)^2 \frac{\mathrm{N_{CO}}}{\Delta v} \tag{5.7}$$

where f_0 (§2.3.3) has been approximated by $f_0 \sim h\nu_{01}/2kT$ (Kutner 1984).

From equation (2.10)

$$T^r(\nu) = (T - T_0)(1 - \mathrm{e}^{-\tau_\nu})$$

so that

$$T_p \equiv T^r(\nu_{peak}) = (T - T_0)(1 - \mathrm{e}^{-\tau_p})$$

and

$$T^r(\nu_{1/2}) = \frac{1}{2}T_p = (T - T_0)(1 - \mathrm{e}^{-\tau_{1/2}}).$$

Therefore

$$\tau_{1/2} = -\ln\frac{1}{2}\left(1 + \mathrm{e}^{-\tau_p}\right) \tag{5.8}$$

and using equation (5.6)

$$\tau_{1/2} = \tau_p \exp\left(\frac{-(\frac{1}{2}\Delta v_{obs})^2 4\ln 2}{(\Delta v)^2}\right) .$$

Solving for the observed linewidth Δv_{obs} gives

$$\frac{\Delta v_{obs}}{\Delta v} = \frac{1}{(\ln 2)^{\frac{1}{2}}}\left[\ln\left(\frac{\tau_p}{-\ln\frac{1}{2}\left(1 + \mathrm{e}^{-\tau_p}\right)}\right)\right]^{\frac{1}{2}} .$$

In the limit of small optical depth, $\Delta v_{obs} \rightarrow \Delta v$, while for large optical depths,

$$\Delta v_{obs} \rightarrow \Delta v \left(\frac{\ln\tau_p}{\ln 2}\right)^{\frac{1}{2}} .$$

Thus, $\tau(\mathrm{CO}) \sim 40$ implies $\Delta v_{obs}/\Delta v \sim 2$, leading to an overestimate in the virial mass by a factor of 4 if the approximation is valid.

Leung et al. (1982) give results for non-LTE calculations in the microturbulent approximation which, they suggest, is probably reasonable for moderate optical depths. They find, for $\tau \lesssim 2$,

$$1.4 \lesssim \frac{\Delta v_{obs}}{\Delta v} \lesssim 1.9$$

giving overestimates in virial mass of between 2 and 4.

However, Dickman and Clemens (1983) argue that the breakdown of the microturbulent model – i.e., when there exist turbulent length scales comparable to the photon mean free path – reduces saturation broadening. Line profiles calculated under these assumptions (so-called 'mesoturbulence') show less self-reversal than the microturbulent case,

so the theoretical evidence is equivocal. Nevertheless it can be tested observationally by comparing, for example, Δv(CO) and $\Delta v(^{13}\mathrm{CO})$ suitably averaged over typical GMCs.

The strongest observational evidence for saturation line broadening comes from the ^{13}CO observations of the Rosette molecular cloud by Blitz and Stark (1986) and Blitz (1987), and those of Falgarone and Pérault (1987) in the Galactic plane and Taurus region. Other comparisons of linewidth available in the literature refer to individual lines of sight and are not so compelling. Even so, they are comparable to the above, implying the effect could be significant. Table (5.2) presents some recent values.

Table 5.2

Type of Cloud	Ratio (Δv_{FWHM})
Inner Galaxy	
Sanders (1981)	0.74
Martin et al. (1984)	0.53 – 0.71
Liszt et al. (1981) (^{13}CO)	0.74
Sanders et al. (1984) (CO)	
Local Clouds	
With associated heating sources	
Blitz (1987)	0.83
Maddalena (1986)	0.66
Blitz et al. (1982)	0.60
No heating sources	
Falgarone & Pérault (1987) (^{13}CO)	0.71*
Dame et al. (1986) (CO)	
Mean	0.70
(Mean)^2	0.49

* Derived from the ratio of σ_v values.

The choice of a less abundant, more optically thin line may conflict with (ii) above, since it can only be detected in the central, denser regions of the cloud. Thus, either most of the mass must be contained within the extent of the observed line, or the behaviour of the linewidth out into the lower density regions must be inferred. Aarseth and Saslaw (1972) show that the effect of excluding the outer regions leads to overestimates of total mass if they are in equilibrium.

The mass in the outer layers seen in CO but not in ^{13}CO can be included in the virial calculation either by simple scaling – e.g., by using R_c(CO) rather than $R_c(^{13}\mathrm{CO})$ – or, if possible, using $R_c(^{13}\mathrm{CO})$ and the method adopted in §3.4. The former approach will again overestimate the cloud mass, since it assumes $\Delta v(^{13}\mathrm{CO})$ applies in the lower density regions, contrary to the Aarseth and Saslaw arguments. The overestimate using the latter approach is presumably smaller. This technique is in sharp contrast to that of SRBY and others who assume CO is 'effectively' optically thin everywhere because it produces Gaussian line profiles, characteristic of such lines. However, evidence has already been presented that the model for 'optically thin' CO emission of dense, non-overlapping, clumps is only valid up to moderate gas column densities.

D. Departures from spherical symmetry

Giant molecular clouds are far from spherically symmetric, in contrast to the assumption

that underpins equation (5.3). In practice, a 'radius' is estimated from the spatial distribution of CO emission according to some scheme, and spherical symmetry is assumed to be a reasonable approximation. Often, an effective radius is calculated using $R_c \propto A^{\frac{1}{2}}$, where A is the projected area of a limiting CO contour.

If the cloud is in equilibrium but departs from spherical symmetry, then equation (5.3) does not produce too large an error provided the ratio of maximum to minimum dimension is about 3. This can be seen from the expression given by Maddalena (1986)

$$M_{vc} = 83.8 L (\Delta v)^2$$

for a uniform cylinder of length L and diameter $\delta \ll L$. If it is in fact assumed to be a uniform sphere with $R_c = \sqrt{\frac{A}{\pi}}$ (where $A = L\delta$), then the ratio of its computed virial mass M^*_{vir} to its actual virial mass is

$$\frac{M^*_{vir}}{M_{vir}} = \frac{2\pi}{5}\sqrt{\frac{\pi\delta}{L}}.$$

For $L = 3\delta$ the Maddalena expression is probably reasonable and

$$\frac{M^*_{vir}}{M_{vir}} = \frac{2\pi}{5}\sqrt{\frac{\pi}{3}} \sim 1.2\ .$$

The SRBY survey contains $\sim 18\%$ of clouds with $L > 3\delta$, so that equation (5.3) holds to within 20% or better for all clouds therein.

E. The influence of cloud definition on cloud parameters

The operational definition of a GMC in the inner Galaxy is a thornier question since the cloud complexes are observed against a background consisting of many smaller or more distant clouds. In many cases, several GMCs lie along the same line-of-sight with consequent problems of line blending. This is particularly true in the molecular ring region where cloud density is high, and near the terminal velocity where velocity crowding is severe.

Two approaches have been used to overcome this difficulty in recent surveys of 1st quadrant CO emission. The first, used by SRBY, Scoville at al. (1987) and Myers et al. (1986), essentially chooses some minimum antenna temperature (T_{min}) to define cloud boundaries. Owing to the complex nature of the emission, there are substantial differences over the choice of T_{min}, and the subsequent computation of velocity dispersion, cloud size and luminosity.

Myers et al. set all emission with $T_{min} < 2\,\mathrm{K}$ to zero and then integrated over $20\,\mathrm{km\,s^{-1}}$ windows. They estimate that 'cloud' luminosity decreases by about 60% as T_{min} is increased from 1.5 to 2.5 K. According to these authors, blending becomes a severe problem at $T_{min} = 1\,\mathrm{K}$, while small clouds are 'lost' if $T_{min} = 3\,\mathrm{K}$. The choice of constant T_{min} for all clouds was made on the basis of simplicity despite the much higher background for $l < 30°$.

SRBY utilised $T_{min} = 4\,\mathrm{K}$ except for the confused region $8° < l < 32°$ and $v > 60\,\mathrm{km\,s^{-1}}$, where the smallest non-blended T_{min} was selected. Given T_{min}, each 'cloud' was enclosed in an l-b-v box; cloud luminosities and l,b,v dispersions were calculated by including all emission within the box down to 1 K, despite having previously noted that large sections of the Galactic plane are blended at the 3 K level. The authors estimate that this increased the l,b dispersions by about 15%, and σ_v by about 50%

Scoville et al. defined cloud boundaries by 4 K contours in l,b,v space containing local emission maxima. Cloud size and velocity dispersions were computed only from observations with $T_{min} > 4\,\mathrm{K}$. They estimated how these values might vary with T_{min} by choosing three clouds in relatively unconfused parts of the $l-v$ plane and repeated their calculations of $A^{\frac{1}{2}}$ and σ_v for several values of T_{min}. Their data and best fit curve is reproduced in Fig (5.1).

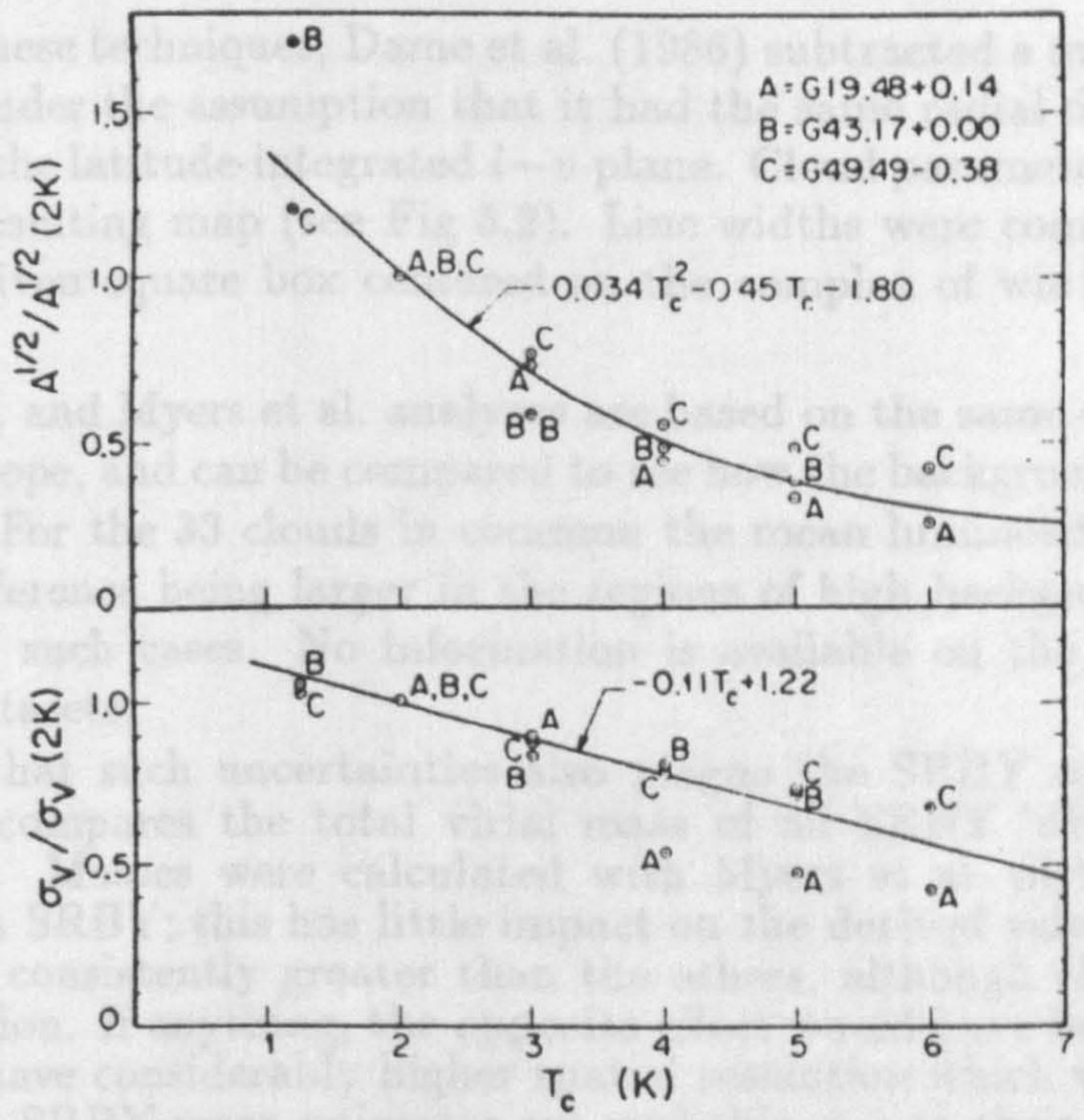

Fig 5.1 Growth curves for cloud size (defined as the square root of the projected area) and velocity dispersion as derived by Scoville et al. (1987) for 4 'HII region' clouds with variable T_c (T_{min} in the text). The clouds were selected because they were in relatively unconfused areas of the $l - v$ plane.

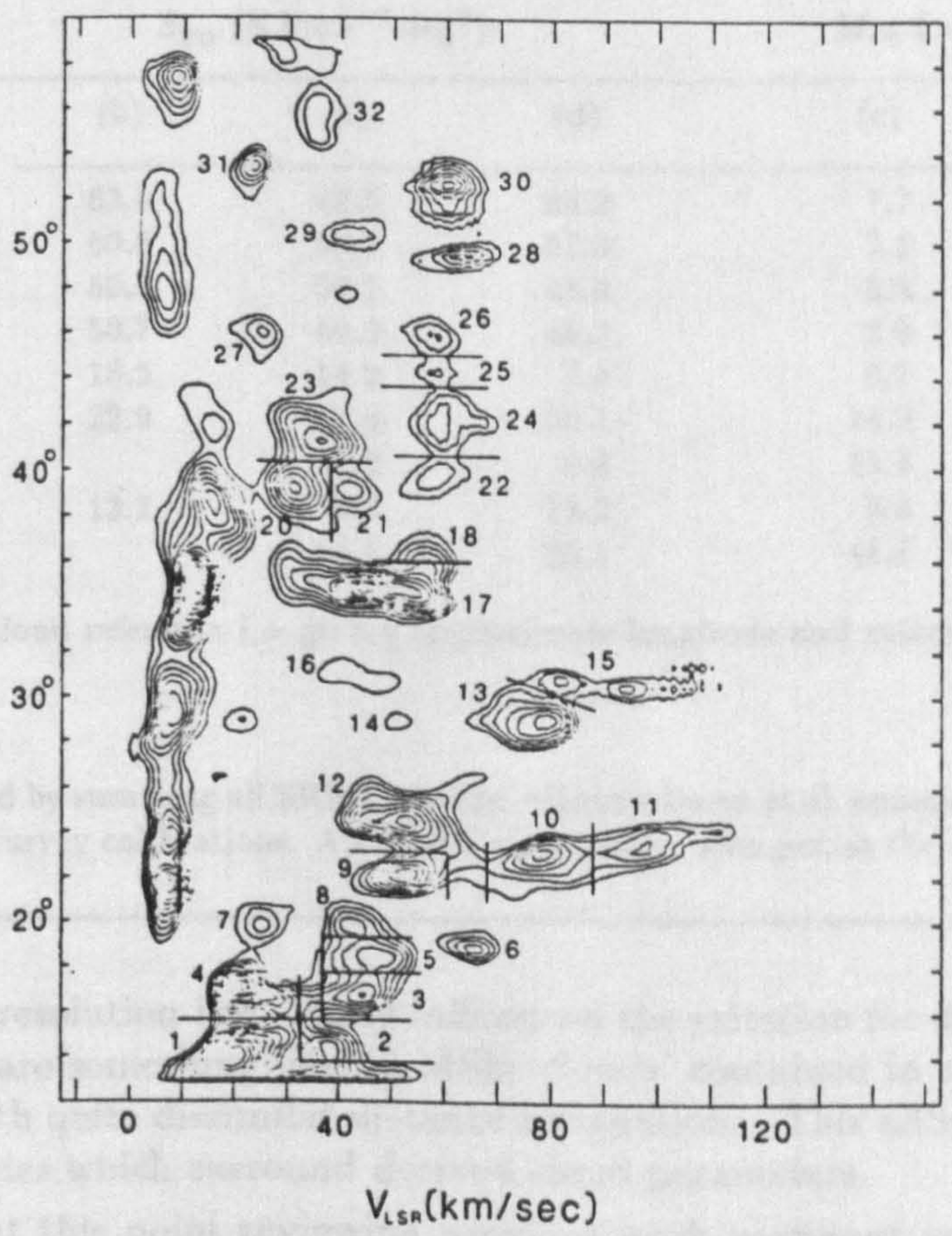

Fig 5.2 $l - v$ map resulting from the Dame et al. (1986) technique of subtracting a model background from the observed $l - v$ map. The model background (see Dame 1984) was scaled so that 75% of the total emission in the observed map was removed. Contour intervals are 0.25 K deg.

In contrast to these techniques, Dame et al. (1986) subtracted a model of the background emission, derived under the assumption that it had the same radial distribution as the total CO emission, from the latitude-integrated $l-v$ plane. Cloud parameters were then estimated directly from the resulting map (see Fig 5.2). Line widths were computed by averaging all spectra within a given square box centered on the complex of width equal to its angular radius.

The Dame et al. and Myers et al. analyses are based on the same data set, obtained with the Columbia telescope, and can be compared to see how the background subtraction method affects the results. For the 33 clouds in common the mean luminosity ratio (Myers/Dame) is 1.6 ± 0.9, the difference being larger in the regions of high background. Variations of up to 3.7 are noted in such cases. No information is available on the variation of linewidth between the two datasets.

An indication that such uncertainties also plague the SRBY results can be found in Table (5.3) which compares the total virial mass of all SRBY 'clouds' located within a Myers et al. cloud. Masses were calculated with Myers et al. distances, which differ in some instances with SRBY; this has little impact on the derived values. Clearly, the SRBY mass estimates are consistently greater than the others, although cloud luminosities show no consistent variation. If anything, the opposite effect would have been expected, since the MSB observations have considerably higher spatial resolution which would assist in defining a 'cloud'. The large SRBY mass estimates are probably due to their method of deriving σ_v which is particularly susceptible to line blending and background confusion.

Table 5.3

*Cloud	S_{CO} (K km s^{-1} deg^2)			M_{vir} ($\times 10^5$ M$_\odot$)	
	(b)	(c)	(d)	(c)	(d)
17,44	63.0	42.5	25.2	7.7	12.4
17,22	60.8	59.7	61.0	7.5	6.7
18,48	50.0	50.1	43.0	5.8	20.5
19,65	50.7	49.3	48.2	8.9	30.3
20,26	15.5	14.2	7.4	0.7	1.4
49,59	22.9	17.4	50.1	14.0	39.1
46,59		16.2	9.8	15.4	15.3
44,60	13.2	6.2	13.2	9.0	16.4
42,63		14.8	25.1	48.8	41.9

(a) Myers et al. (1986) cloud reference l, v giving approximate longitude and velocity of emission features

(b) Myers et al. (1986)

(c) Dame et al. (1986)

(d) SRBY: S_{CO} computed by summing all SRBY 'clouds' within a Dame et al. emission feature after allowing for the difference in survey calibrations. All SRBY clouds have been put at the distances given in Dame et al.

The difference in resolution has clearly influenced the criterion for deciding what constitutes a cloud. There are something like 10 MSB 'clouds' contained in an average Columbia 'cloud', sometimes with quite dissimilar distance assignations. This adds yet another dimension to the uncertainties which surround derived cloud parameters.

It is worthwhile at this point reviewing previous work pertinent to points *A*, *B* and *C* above. Myers and Goodman (1988b) analysed $N(H)_3$, ^{13}CO and CO data from 120 clouds ranging in size from 0.1 – 100 pc. They found the median ratio of the kinetic ($2E_t$) and gravitational (Ω) terms in equation (5.3) to be 1.2 (see Fig 5.3, taken from that paper).

Clearly, if equation (5.3) were exactly satisfied, this ratio would be unity so the authors argue that this might reflect a small contribution from non-equilibrium line-broadening.

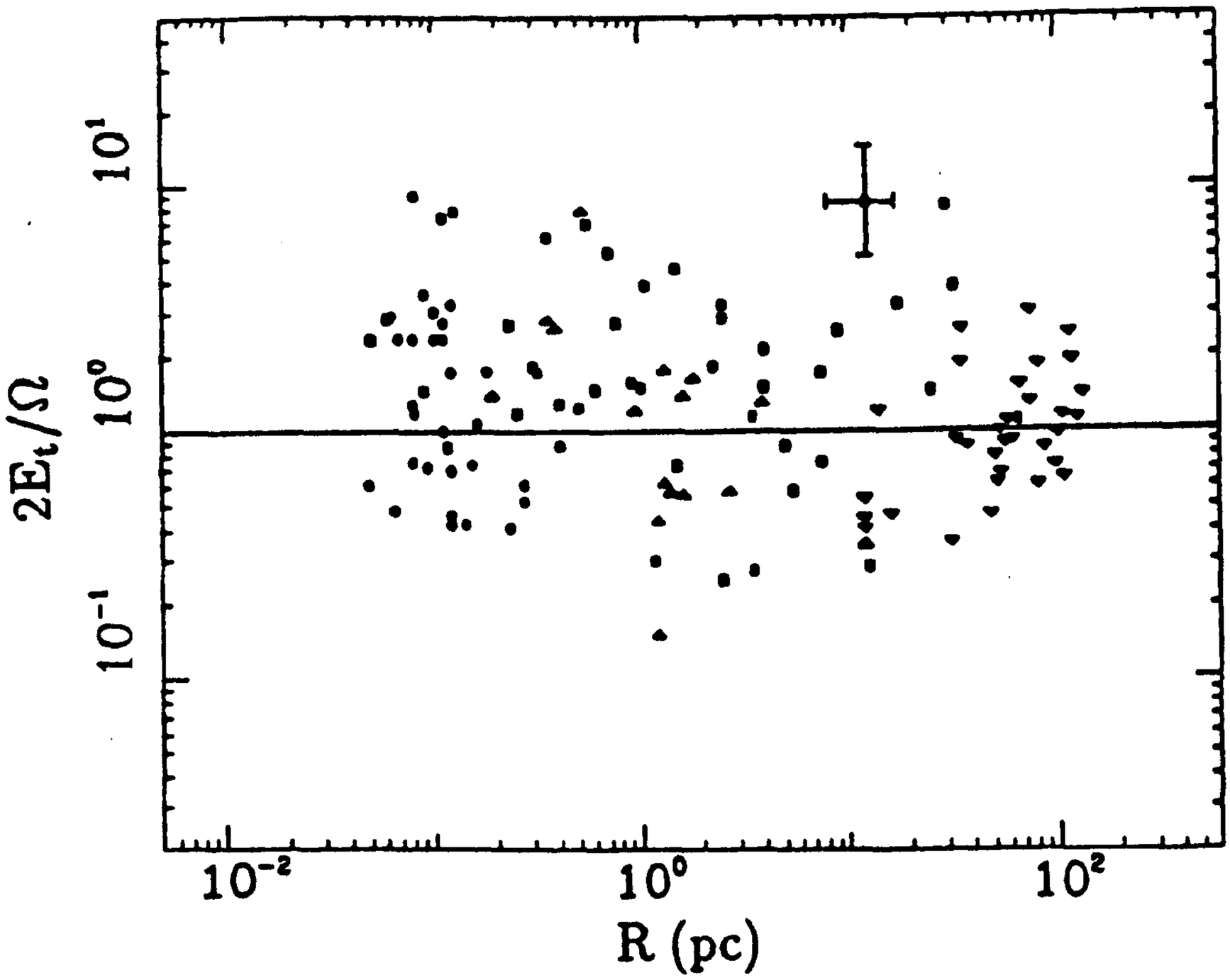

Fig 5.3 Ratio of kinetic energy-to-gravitational potential energy terms from the virial equation 5.1 as computed by Myers and Goodman (1988b). Cloud data were taken from:
Larson (1981) (squares); Leung, Kutner & Mead (1982) (triangles pointing up); Myers & Benson (1986) (circles); Dame et al. (1986) (triangles pointing down). The authors' 1σ error estimates are included.

The larger clouds in their sample originate in the CO survey of Dame et al. (1986). Some evidence that optical depth influences the CO linewidth was presented in *B* above. If correct, then E_t is overestimated by a factor of order ~ 2. A similar overestimate of Ω, caused by the use of an X_{20}-value which is higher than appears likely for the inner Galaxy, suggests the ratios from the Dame et al. data may not, in fact, be unreasonable. Myers and Goodman estimate random and systematic uncertainties in their result to be a factor of ~ 2. Thus their analysis is suggestive, but not compelling.

Scoville et al. (1987) present evidence that, for diameters $D \lesssim 30\,\mathrm{pc}$, the 'HII region clouds' in their catalogue have a higher CO-derived velocity dispersion than the general cloud population. They infer that either (i) these clouds are more dense (by a factor of ~ 5) than the non-HII region clouds, or (ii) HII regions contribute significantly to the cloud internal motions, this being more noticeable in smaller clouds, or (iii) they have recently undergone collisions with other GMCs. Estimated densities lie in the range $80 - 625\,\mathrm{cm}^{-3}$, with $\bar{n}(\mathrm{H_2}) \propto D^{-0.9}$. Scoville et al. argue that tidal disruption is unlikely since the minimum density for stability against Galactic tidal forces at $R \gtrsim 3\,\mathrm{kpc}$ is about $15\,\mathrm{cm}^{-3}$. However these conclusions follow from the use of equation (5.3) with CO linewidths. Considering all the above uncertainties and including a similar uncertainty in the tidal limit, the Scoville et al. conclusion is far from secure for the largest clouds.

Myers and Goodman (1988b) considered the case when the non-thermal KE term in

equation (5.3), defined as $E_{NT} = M\sigma_{NT}^2$, satisfies

$$2E_{NT} \sim \Omega \sim M$$

for a uniform cloud. The results were consistent with magnetic fields in the range $15-40\,\mu$G, which are comparable to observed fields in self-gravitating clouds.

A similar concept was applied to 14 molecular clouds, for which the magnetic field strengths were known, by Myers and Goodman (1988a). They showed that the model equilibrium and measured fields generally agreed within a factor of ~ 2 for a wide range of conditions. Though the two studies have different biases (the latter toward large fields and massive, dense cores and the former toward smaller fields, extended GMCs and dark clouds) they support the concept that molecular cloud masses are, within a factor of about two, predicted by equation (5.3) and that observed linewidths are predominantly magnetic in origin. This may mean that non-magnetic motions, such as turbulence and cloud-collapse, are not dominant, but the large uncertainties cannot exclude such contributions. If, for example, $2E_t \sim E_M$ and both terms originate from independent effects, then $2E_t/\Omega \sim 0.5$ which is only just outside the uncertainties. Cloud masses in this case are overestimated by a factor of ~ 2 if the magnetic term is ignored. Several other analyses (e.g., Heyer 1986) have also shown that magnetic fields play an important role in GMC physics.

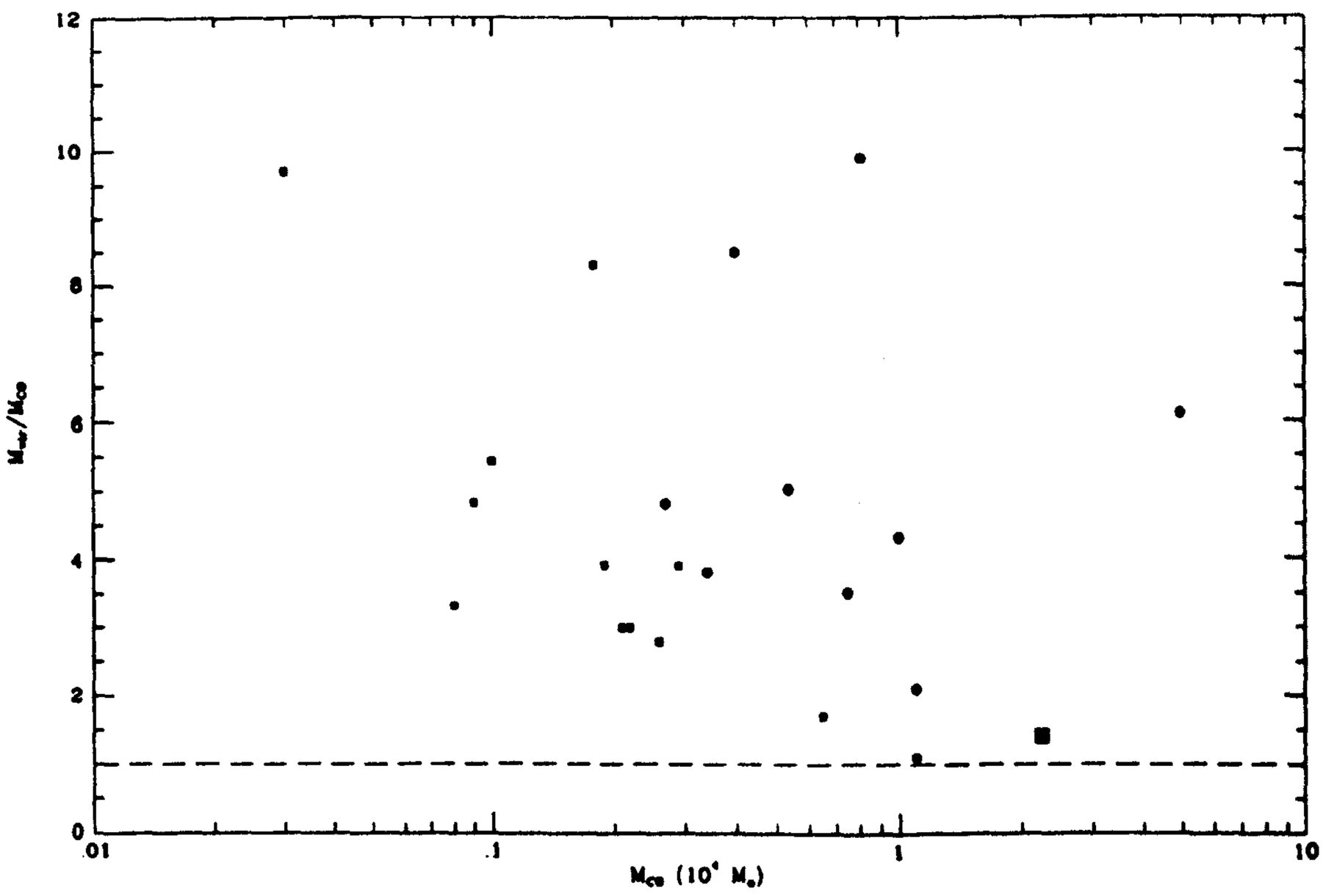

Fig 5.4 The ratio M_{vir}/M_{CO} as given by Ungerechts & Thaddeus (1986) for clouds in the Taurus-Perseus-Auriga region. M_{vir} was calculated using CO data; M_{CO} using $X_{20} = 2.6$. Clearly there would be little change if linewidths were corrected for saturation as in the text and $X_{20} = 1.5$ was used. However, the ratios should be reduced by a factor 190/210 since Ungerechts and Thaddeus assumed uniform clouds. The small squares all refer to subclumps of a larger cloud (labelled with a large square). This may suggest that the smaller condensations considered by these authors are not in virial equilibrium.

Compared to inner Galaxy molecular clouds, background emission and line blending problems are far less severe in local GMCs, and other mass estimators are available. Ungerechts and Thaddeus (1986) observed the local Taurus-Perseus-Auriga clouds in CO using

the Columbia telescope. Their data, comparing $M_{\rm CO}$ ($X_{20} = 1.5$) and corrected for He abundance, with M_{vir} are given in Fig (5.4). Virial masses in this case were computed using Δv(CO) in equation (5.3), and assuming n = constant. Clouds with uncertain distances or large velocity fluctuations, to which equation (5.3) is particularly sensitive, have been excluded from the figure. The agreement between the two mass estimators is clearly not good; this is true even if CO linewidths are corrected for saturation effects as above. The authors argue that the clouds are probably not in equilibrium.

However, this conflicts with ^{13}CO observations of 5 clouds in the Taurus complex by Heyer (1986) who derived luminosity masses by calibrating $W_{^{13}CO}$ vs A_v in two of the clouds. He obtained

$$W_{^{13}CO} = 1.3 A_v \,\mathrm{K\,km\,s^{-1}} \tag{5.9}$$

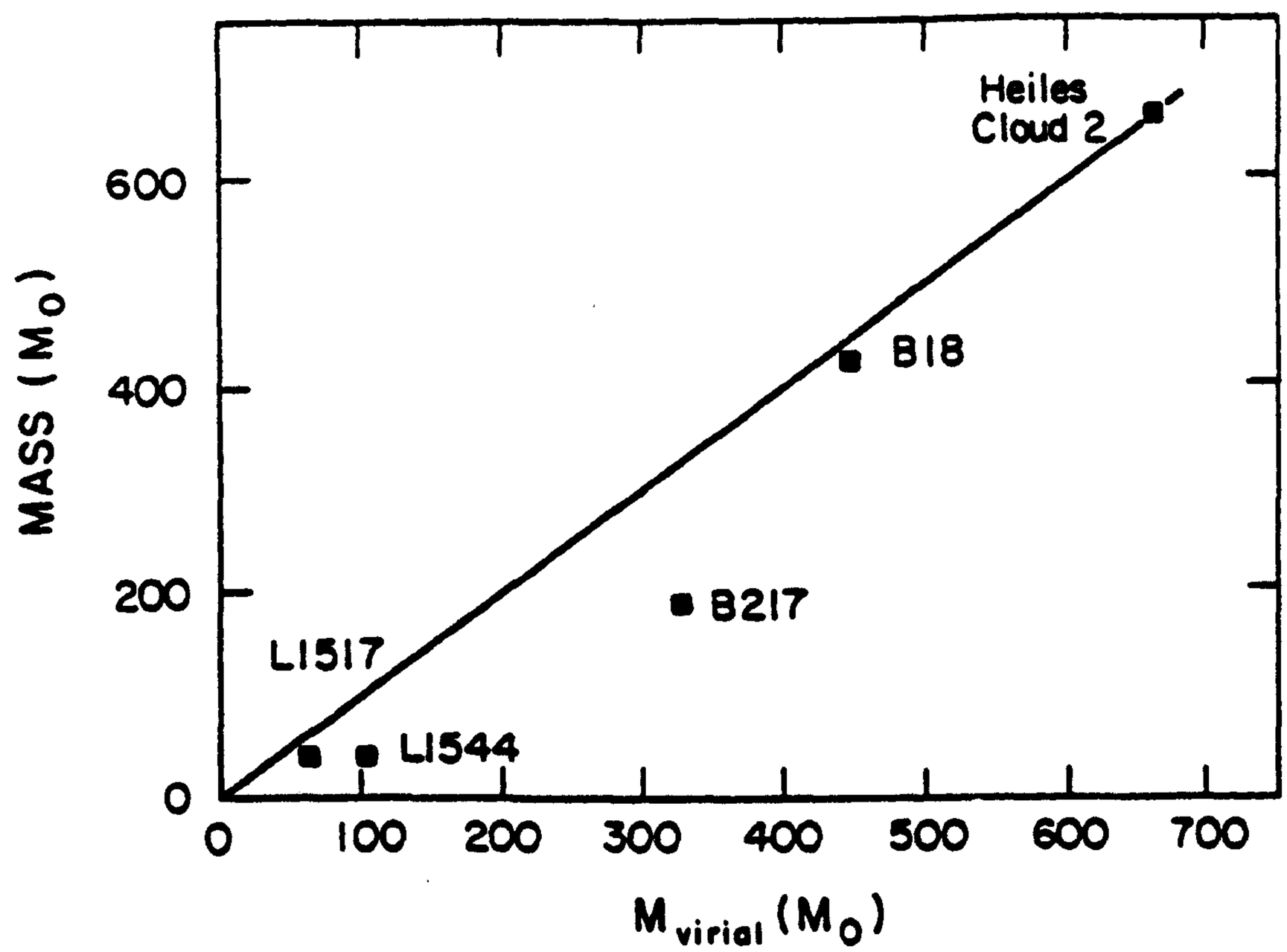

Fig 5.5 $M_{^{13}CO}$ luminosity mass versus M_{vir} (calculated with ^{13}CO linewidths and sizes) from Heyer (1986).

and compared these with virial masses derived using equation (5.3). Figure (5.5) reproduces his data and indicates the clouds are close to virial equilibrium, though there is some doubt about equation (5.9). Guélin and Cernicharo (1988) found a $W_{^{13}CO}/A_v$ ratio of $2.2\,\mathrm{K\,km\,s^{-1}mag^{-1}}$ from a much larger set of observations in the Taurus complex. Using this relation suggests Heyer's virial masses are larger than cloud luminosity masses by at most a factor of ~ 2 since the contribution to the gravitating mass from material not seen in ^{13}CO should be included. The Ungerechts and Thaddeus conclusions are therefore a little puzzling.

Maddalena (1986) quotes CO-derived virial masses for the Orion clouds. He finds $M_{vir} \sim M_{\rm CO}$, where $M_{\rm CO}$ has been calculated using the X_{20}-value of Bloemen et al. (1984b). However, his ^{13}CO observations of the same clouds give LTE masses which, when corrected for the fraction not seen in ^{13}CO (see §3.4) are in agreement with $X_{20} \sim 1.5$. This suggests overestimates of the mass by factors of 3 and 2 in Orion A and B respectively when CO linewidths are used. Correcting this as above gives much closer agreement.

Myers (1983) utilised the ^{13}CO data of Leung et al. (1982) and the NH_3 observations of dense cloud cores obtained by Myers and Benson (1983) to study some of these questions. The Leung et al. data relate to isolated dark globules ($R \lesssim 10\,\mathrm{pc}$), whereas the dense cores have typical dimensions at least an order order of magnitude smaller. Thus their results are not directly comparable with GMCs. Nevertheless they are interesting because the ^{13}CO lines were corrected for optical depth using the microturbulent approximation discussed above. Myers found a linear correlation between $\Delta v \bar{n}^{\frac{1}{2}}$ and R_c in close agreement with that expected from equation (5.3) – see Fig (5.6). Cloud masses were calculated as $M = \frac{4}{3}\pi R_c^3 \bar{n}$ with $\bar{n}$ derived from the LTE approximation and assumptions about the ^{13}CO abundance.

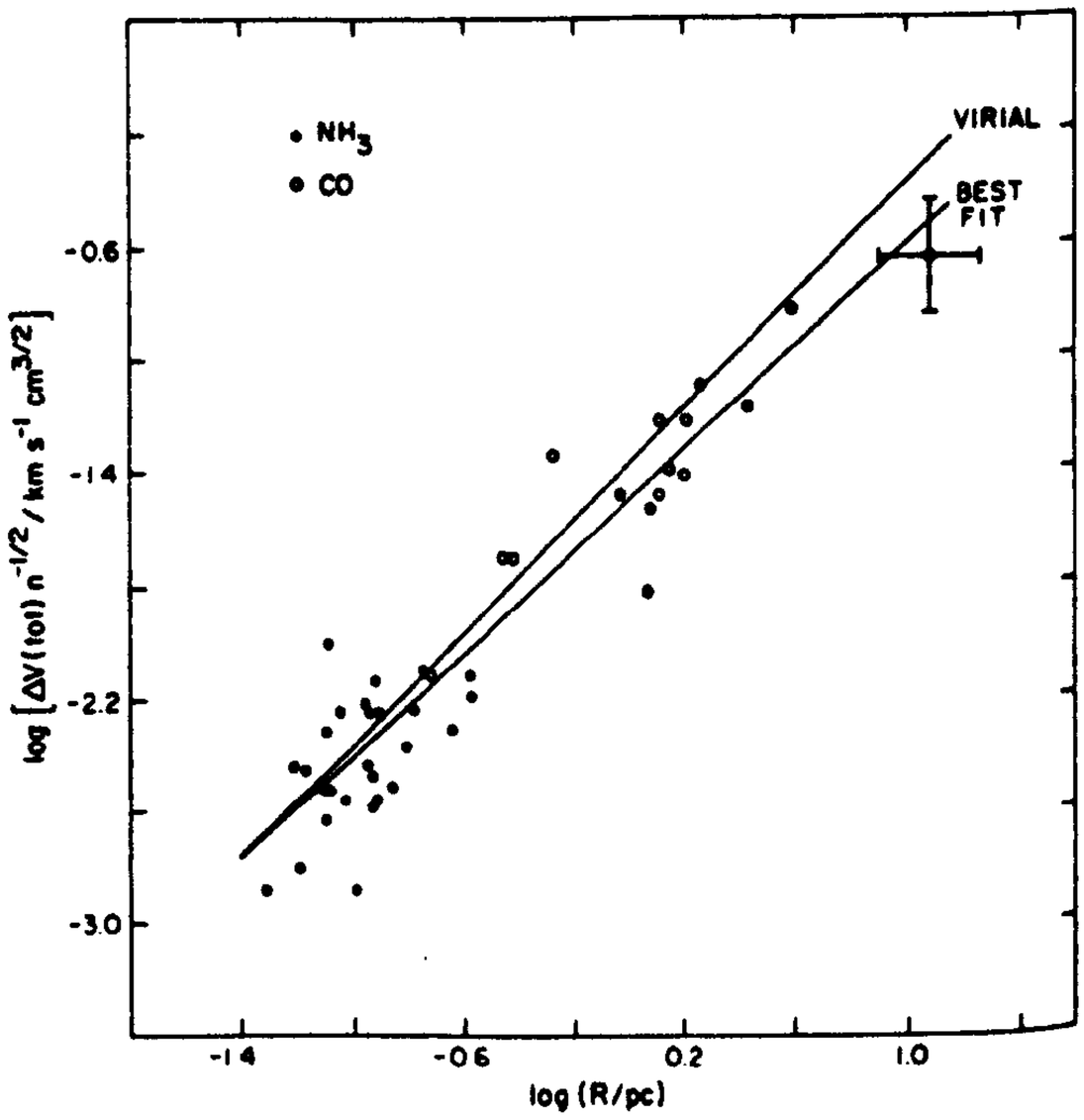

Fig 5.6 Log-log plot of $\Delta v\, n^{-1/2}$ versus R from Myers (1983). The best fit line (correlation coefficient 0.95) is in agreement with that expected assuming virial equilibrium.

Guélin and Cernicharo (1988) obtained good quality ^{13}CO and visual extinction data from part of the Taurus cloud complex, including HCL2. The average linewidth over the observed region was $1.4\,\mathrm{km\,s^{-1}}$, with a corresponding 'extinction' mass of $640\,M_\odot$. The authors suggest from this that the HCL2 cloud is very nearly in virial equilibrium. This contrasts with the CO observations of a somewhat larger region containing HCL2 by Ungerechts and Thaddeus (cloud 27f in their catalogue). Using $X_{20} = 2.8$, these authors found a virial mass nearly three times the luminosity mass i.e., 7200 and $2600\,M_\odot$ respectively. These CO-derived values would be comparable if the Guélin and Cernicharo linewidths were applicable across the whole of cloud '27f', and the conversion factor $X_{20} = 1.5$ were used to estimate the luminosity mass.

Observations of the Rosette molecular cloud in CO and ^{13}CO by Blitz (1987) show the same trend. Mass estimates were derived in three ways in this analysis: (1) Using the LTE approach (2) Using the OH observations of Wouterloot (1981) and (3) Using the virial theorem, with $\Delta v(^{13}\mathrm{CO})$ and $R_c(^{13}\mathrm{CO})$. All the estimates give $1.1 \times 10^5\,M_\odot$, which Blitz considers somewhat fortuitous considering the uncertainties inherent in all the methods. If $R_c(\mathrm{CO})$ and $\Delta v(^{13}\mathrm{CO})$ (see Table 5.2) were used instead, as argued above, the virial mass estimate would increase to $1.8 \times 10^5\,M_\odot$, to be compared with $2.7 \times 10^5\,M_\odot$ when all parameters are measured with the CO line.

Falgarone and Pérault (1987) mapped parts of the Galactic plane and some of the Taurus

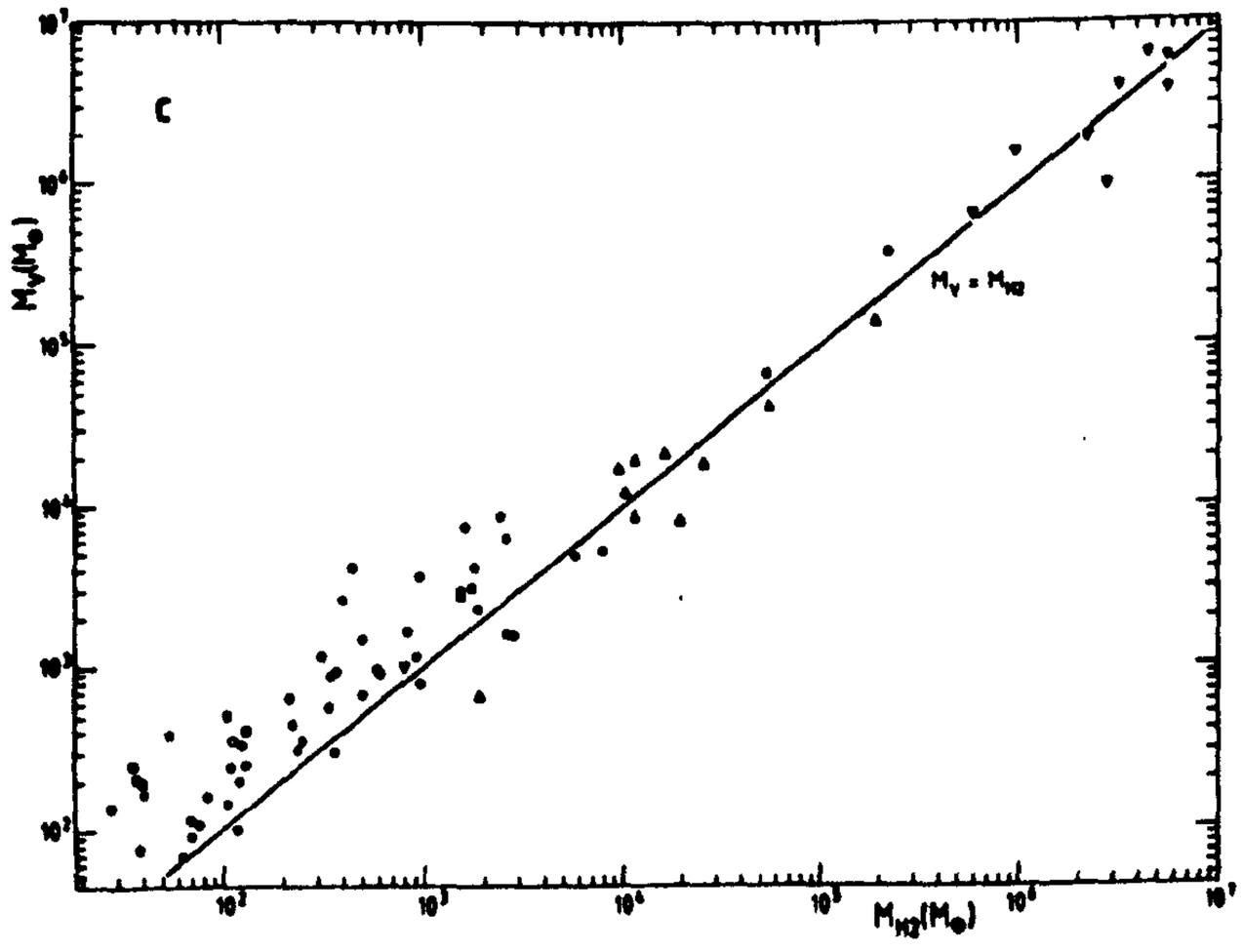

Fig 5.7 A comparison of M_{vir} (^{13}CO data) with $M(H_2)$ as determined using $W_{^{13}CO}$ (from Falgarone & Pérault 1987). The solid line assumes $M_{vir} = M(H_2)$.

complex with the Bordeaux telescope in ^{13}CO. The clouds were defined as resolved connected volumes in l, b, v-space in which $W_{^{13}CO} > 1\,K\,km\,s^{-1}$ so that, perhaps excepting the Taurus clouds, this survey is subject to the same cloud definition and background problems detailed above. They found $\sigma_v = 0.36R^{0.5}$ which, for the cloud size range $10 < R < 100\,pc$ in common with Dame et al. (1986), suggests

$$\frac{\sigma_v(^{13}CO)}{\sigma_v(CO)} \sim 0.69,$$

even lower than that obtained in Table (5.2). Figure (5.7) reproduces their plot of M_{vir} versus M_{H_2}, where the latter quantity is calculated from ^{13}CO intensities integrated over the cloud. This may indicate that clouds larger than about 10 pc are approximately virialised, but there is again some doubt about the conversion relation they used to estimate M_{H_2} which is equivalent to

$$\frac{W_{^{13}CO}}{A_v} = 3.8,$$

considerably higher than that obtained by Guélin and Cernicharo (1988) and Heyer (1986). If the former calibration is used, luminosity masses need to be divided by a factor of ~ 2.3, though a correction for 'unseen' molecular material could reduce this. A lower limit for the correction is ~ 1.4 since in the Rosette molecular cloud, the ratio of areas detected in ^{13}CO and CO is about 0.6. In this case, the Falgarone and Pérault conclusions are probably unchanged.

The general consensus of these various studies is that virial mass estimates using equation (5.3) and ^{13}CO linewidths are within a factor ~ 2 of the true mass. Even so, they must be regarded as upper limits since all the uncertainties conspire in that direction. The only possible exception arises if ^{13}CO is subthermally excited ($T_x < T$) over a large part of the cloud. The observations of Blitz (1987), Bally et al. (1987) and Falgarone and Pérault (1987) suggest that this is probably not the case, since they find a large fraction of GMC mass in very dense clumps.

5.3.1 Re-analysis of the MSB CO Survey

It is first of all necessary to summarise the SRBY and Scoville at al. arguments. Both analyses correlate virial masses computed according to equation (5.3) ($\alpha = 1$) with CO luminosity.

SRBY justify their use of CO velocity dispersions by noting that such lines, averaged over the cloud, have Gaussian shapes more typical of optically thin emission. They obtain a striking correlation, extending in virial mass over $\sim 100 - 2 \times 10^6\,\mathrm{M}_\odot$, viz.

$$M_{vir} = 39 L_{\mathrm{CO}}^{(0.81\pm0.03)}\,\mathrm{M}_\odot \tag{5.10}$$

where the cloud luminosity L_{CO} is in units of $\mathrm{K\,km\,s^{-1}\,pc^2}$, or

$$M_{vir} = 29 L_{\mathrm{CO}}^{(0.81\pm0.03)}\,\mathrm{M}_\odot \tag{5.11}$$

when corrected for He abundance, ignored by the authors. The conversion factor X_{20} follows, for M_{CO} in $\mathrm{M}_\odot$, as

$$\mathrm{X}_{20} = 58 M_{\mathrm{CO}}^{-0.23}$$

for the range in mass noted above.

A cloud model, related to that of Kwan and Sanders (1986), which claims to predict equation (5.10) is advanced by the authors. This 'mist' model considers GMCs to consist of a large number of discrete, optically thick droplets which are 'effectively optically thin' at each velocity. Observed line profiles averaged over a cloud then have a Gaussian appearance.

If CO emission is 'optically thin', however, then their relation (5.10) must be reinterpreted, since now the cloud mass is measured by its CO luminosity and X_{20} is a constant. Virial mass estimates then depend on GMC mass i.e., $M_{vir}/M_{\mathrm{CO}} \propto M_{\mathrm{CO}}^{-0.23}$, and the value of X_{20} depends on the proportionality constant, which cannot be determined unless an independent estimator of cloud mass is available.

It is possible that the problems of cloud definition etc. are partly responsible for the SRBY result. This suspicion is strengthened by the considerations of Scoville et al. who use the same database but find, with a different definition of a 'cloud',

$$M_{vir} = (6.7 \pm 0.4) L_{\mathrm{CO}}\,\mathrm{M}_\odot.$$

This relation was derived for all cloud types but refers only to the virial mass range $10^5 - 2 \times 10^6\,\mathrm{M}_\odot$. It predicts $\mathrm{X}_{20} = 3.1$ independent of cloud mass.

Inexplicably, Scoville et al. imply that this quantity varies with mass, being ~ 4.7 for $M_{vir} \sim 3 \times 10^4\,\mathrm{M}_\odot$ and ~ 1.6 for $M_{vir} \sim 5 \times 10^5\,\mathrm{M}_\odot$ which is not too different from that found using equation (5.11).

It is difficult to know whether these authors intend M_{vir} or M_{CO} to estimate cloud masses; clearly they cannot have both. Nevertheless, it illustrates the point that the correlation between M_{vir} and L_{CO} is sensitive to the definition of 'clouds' and their properties from CO emission features. Further evidence for this comes from the data of Dame et al. (1986) and Myers et al. (1986) who use quite different background subtraction techniques on the same first quadrant emission. Myers et al. do not give Δv or R for their clouds, but these can be estimated from the Dame et al. data as follows. Assuming a Gaussian line profile with velocity dispersion $\sigma_v\,\mathrm{km\,s^{-1}}$ and projected area $A\,\mathrm{deg^2}$, the cloud luminosity S_{CO} in $\mathrm{K\,km\,s^{-1}\,deg^2}$ is

$$S_{\mathrm{CO}} = A(2\pi)^{\frac{1}{2}} T_0 \sigma_v$$

where T_0 is the peak antenna temperature at line centre, averaged over the cloud. Therefore

$$\frac{S_{\rm CO}(T_{\rm min})}{S_{\rm CO}(2{\rm K})} = \left(\frac{A(T_{\rm min})}{A(2{\rm K})}\right)\left(\frac{\sigma_v(T_{\rm min})}{\sigma_v(2{\rm K})}\right). \tag{5.12}$$

The ratios in area and velocity dispersion were derived by Scoville et al. (see Fig 5.1) by fitting a polynomial expression to the data for three relatively isolated clouds. Equation (5.12) then predicts $S_{\rm CO}(2.5\,{\rm K})/S_{\rm CO}(1.5\,{\rm K}) \sim 0.5$ whereas Myers et al. quote 0.4, in reasonable agreement considering the differences between the two surveys. Hence, an effective $T_{\rm min}$ for the Dame et al. clouds was estimated from the ratio $S_{\rm CO}({\rm Dame})/S_{\rm CO}({\rm Myers})$ by interpolating equation (5.12); Δv, R_c for the Myers et al. clouds followed from Fig (5.1). Virial masses and luminosities (in $\rm K\,km\,s^{-1}\,pc^2$) can then be computed for the two datasets giving

$$M_{vir} = (0.32 \pm 0.36) L_{\rm CO}^{1.20\pm0.09}$$

and

$$M_{vir} = (38.3 \pm 36.1) L_{\rm CO}^{0.80\pm0.08}$$

for the Dame et al. and Myers et al. clouds respectively. The former result would imply

$$\rm X_{20} = 0.19 M_{CO}^{0.17}$$

or, conversely, assuming $\rm X_{20}$ to be constant, $M_{vir}/M_{\rm CO} \propto M_{\rm CO}^{0.17}$. The second result should not be taken too seriously because of the assumptions that have gone into it, but it is sufficient to cast some doubt on the technique. Interestingly, it is in reasonable agreement with the SRBY results.

5.3.2 Re-calculated Masses from the Virial Theorem

Inspection of the $k(\alpha)$ values in Table (5.1) demonstrates a considerable sensitivity to the density profile. For example, assuming uniform density when in actuality $n(r) \propto r^{-2}$ leads to an overestimate of mass by a factor 1.65.

Although departure from spherical symmetry is not too important, the often complicated CO emission structure raises difficulties, particularly when a cloud has more than one 'centre'. Thus the CO-derived profiles for the Orion A, Orion B, Taurus and Rosette clouds are given in Fig (5.8) as a function of radius ($\propto A^{\frac{1}{2}}$). All the data is normalised to the outer radius R_c, and to the same column density for $r = R_c$. Of course, CO is expected to trace the mass distribution well only in the 'envelope', but this is of little consequence if most of the mass is contained therein. Comparison is made with $n(r) \propto r^{-\alpha}$, derived assuming spherical symmetry, for various α.

Clearly, there are variations in α from one cloud to another. In what follows, $\alpha = 1.0$ is adopted as a conservative estimate because of the problems with multiple cloud centres and enhanced CO luminosities from embedded stars. It is unlikely to be much less than one in the outer regions of the cloud where $\rm X_{20}$ is probably low (§3.5), since the density gradient may be greater than that indicated in the Figure (5.8).

The values for $\rm X_{20}$ given above can now be compared with what might be expected using an identical analysis but with ^{13}CO linewidths (assuming the average presented in Table 5.2 to be correct) and CO-estimated sizes. Figure (5.9) shows the results for the SRBY and Scoville et al. (1987) data for both the original and corrected velocity dispersions. Note that the SRBY values have been reduced by the usual correction for He abundance. The differences are indicative of the dependence on cloud definition, background

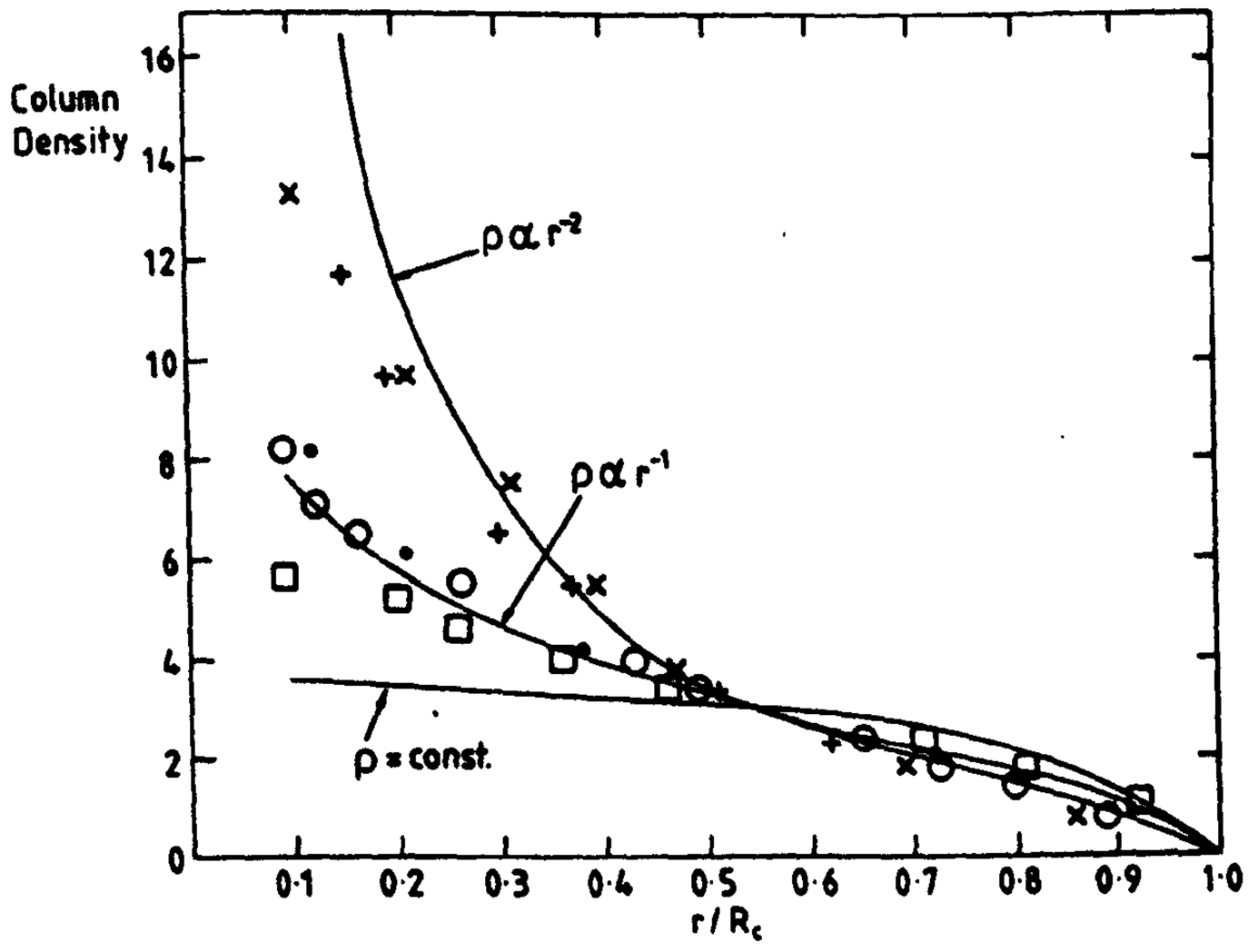

Fig 5.8 Column densities of hydrogen (in arbitrary units) derived from CO data versus normalised cloud radius r for several local GMCs. The radius is computed assuming that the area within a given column density $A(\mathrm{N}) = \pi r^2$, and normalised so that $A(r/R_c = 0.55) = 3$ units. R_c is defined by the total projected cloud area as measured in CO. The solid curves are column densities vesus r/R_c for idealised spherical clouds with density profiles $\propto r^{-n}$ for $n = 0, 1, 2$.
Key: Orion(A + B)(+): Maddalena (1986); Taurus(O) & Perseus(X): Ungerechts & Thaddeus (1986); Rosette (CO, dots) & (^{13}CO, squares): Blitz (1987).

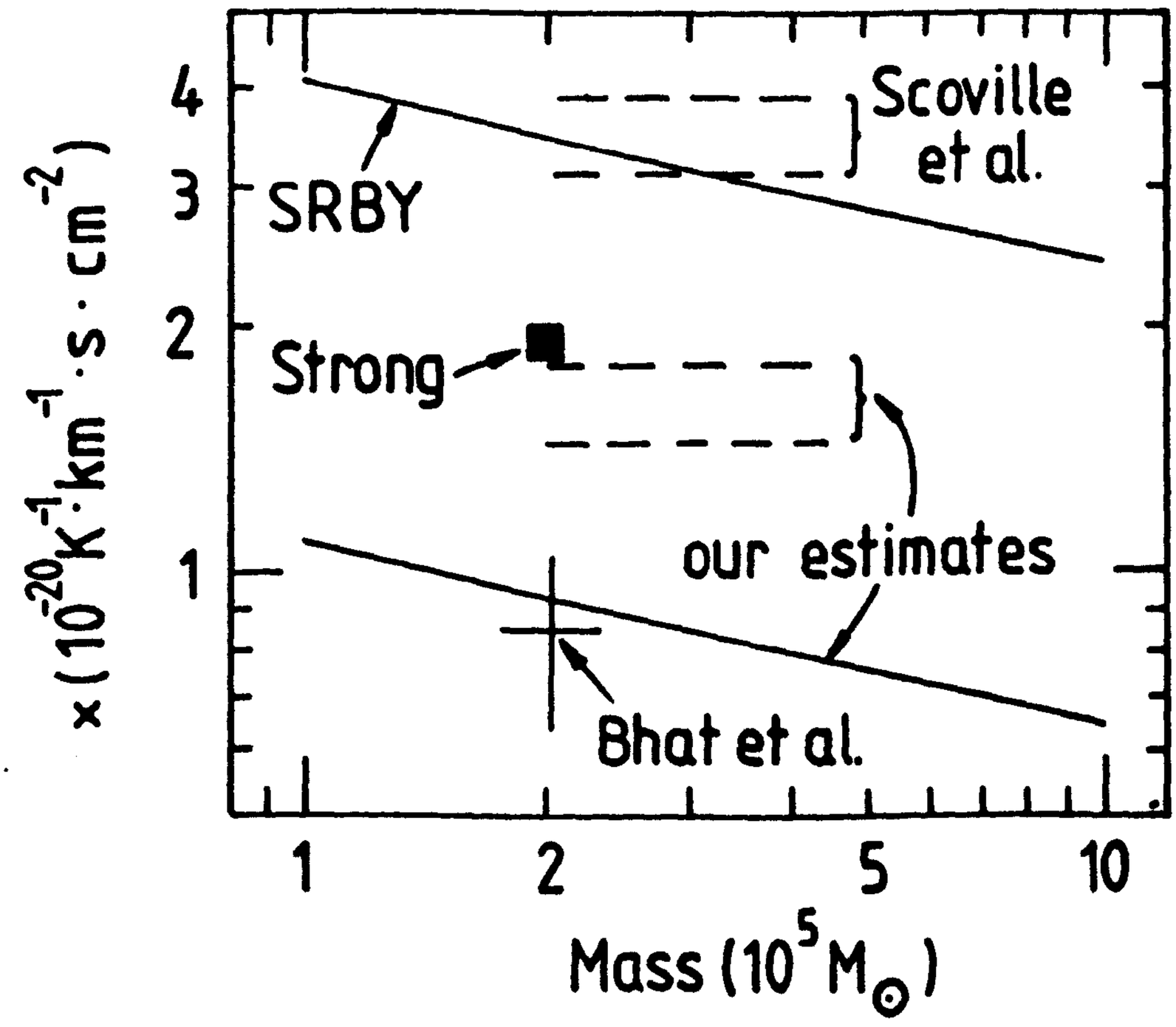

Fig 5.9 The conversion factor X as a function of cloud CO luminosity mass, as derived by SRBY (upper line) and after corrections for helium and conversion to ^{13}CO linewidths (lower line).
Key: *filled square*, Strong et al. (1987), the updated COS-B result, after allowing for the 20% calibration difference between the Columbia and MSB CO surveys; +, Bhat et al. (1986c).
Note that the data points are plotted at $M = 2 \times 10^5\,\mathrm{M}_\odot$, reduced from the median virial mass quoted by SRBY ($5 \times 10^5\,\mathrm{M}_\odot$).

subtraction, choice of T_{min} etc. Obviously the disagreement between the SRBY and Scoville et al. corrected estimates would be even greater if the latter's $T_{min} = 2\,K$ level were reduced to 1 K.

Comparing the above with X_{20} derived from $\gamma-$ray data merits careful consideration. For example, Bloemen et al. (1984b) found that $X_{20} = 2.6$ for Orion, but since the analysis was based on the Columbia CO survey which have W_{CO} values 20% less than the MSB observations, an appropriate value here is $X_{20} = 2.3$. Turning to the inner Galaxy, the latest COS-B estimate is $X_{20} = 2.2$ (Strong et al. 1987), which must be reduced to 1.8 before comparison. It is important to note, however, that the COS-B inner Galaxy values are actually upper limits to the real figure since they ignore the contribution of possible $\gamma-$ray sources and CR enhancements in GMCs.

The final corrected results for the various cloud datasets do not lie far from those of Bhat et al. (1986c), though there is uncertainty about which is the 'best' estimate for the reasons outlined above.

Chapter 6
SUMMARY AND PROSPECTS

6.1 The $\gamma-$ray Analysis

Local molecular clouds have been studied using $\gamma-$rays and molecular emission data in an effort to determine the CO-to-N(H_2) conversion factor X_{20}, and to understand the large variations between previous estimates of it. Nearby complexes were chosen to simplify the analysis and permit comparison with the results of other techniques. Large-scale variations in CR intensity are less important in this case, though some fluctuations are obviously expected.

Clear evidence for CR enhancements associated with molecular clouds has been obtained by comparing medium latitude regions containing GMCs with nearby mainly HI regions in the same latitude range. Some of the excess seen towards the Taurus-Perseus-Auriga clouds may be coincidental since there is a large $\gamma-$ray excess, but the emission from the molecular material is only weakly correlated with W_{CO}. Thus the 'best fit' Y_{20} values found in §3.3 for Taurus are often consistent with zero. Other evidence (e.g., from radio synchrotron observations) for an increase in CR intensity in this direction is lacking, however, and it must be ascribed to processes such as distributed acceleration at relatively low energies.

The CR variations complicate the derivation of X_{20}. The results of Bloemen et al. (1984b) in Orion are easily reproduced *if it is assumed that the CR excess is not significant.* This is important because it implies that $\gamma-$ray backgrounds, derived gas data etc. are comparable. However, the evidence for a CR enhancement in the direction of the Taurus clouds is stronger, and it is difficult to explain the very low X_{20} values derived under the assumption that the excess is not at least partly connected with the molecular complex. Furthermore, none of the $\gamma-$ray derived conversion factors obtained with this approach agrees with independent estimates using extinction data, or with LTE analyses of optically thin molecular emission surveys.

A more consistent interpretation implies $X_{20} \sim 1-2$ locally. The variations noted between the clouds must then be attributed to CR fluctuations associated with the cloud and/or coincident in the same direction. The CR enhancement is also associated with the more smoothly distributed neutral HI. Such a situation arises quite naturally in those models of CR enhancement which posit a neutral gas cloud, rather than a molecular cloud, since a GMC is typically embedded in an HI envelope of substantial mass and column density.

One consequence of this interpretation is that the values of X_{20} deduced by COS-B are too large because localised CR electron production occurs near GMCs. Further evidence that this may be the case was found by Riley and Wolfendale (1984), who noted a difference in the spectral shape of HI and H_2 $\gamma-$ray emission towards the inner Galaxy.

6.2 Other Estimates of X_{20}

There are also uncertainties about the alternative methods of deriving X_{20}. For example, any extinction analysis relies on the constancy of dust properties over the relevant distance scales. Similar assumptions are inherent in LTE calculations from ^{13}CO and CO emission (see Chapter 2). The variation in X_{20} computed using these techniques reflects this lack of knowledge. Broadly speaking, however, the values derived corroborate the $\gamma-$ray picture and $X_{20} \sim 1-2$ seems appropriate. Other recent evidence in support of such an interpretation is provided by Wilkinson (1987) who used a simple closed model of Galactic chemical evolution to derive $(X_{20})_{\odot} \sim 1.3 \pm 0.3$. Interestingly, the model predicted $X_{20} \sim M^{-c}$ where

$c = 0.8 - 0.9$ and M is the metallicity. Maloney and Black (1988) also obtained $(X_{20})_\odot = 1.8$ using chemical modelling techniques.

Significant trends in X_{20} as a function of its median integrated CO emission $< W_{CO} >$ were noted. Small clouds ($\sim 100\,M_\odot$), or the low density parts of GMCs with $< W_{CO} > \sim 1\,K\,km\,s^{-1}$, have relatively low conversion factors ($\lesssim 1$). This might also be true of very luminous cloud regions, a conclusion that is strengthened by theoretical predictions that X_{20} is approximately proportional to T^{-1} (Kutner and Leung 1985; van Dishoeck and Black 1987; Maloney and Black 1988). If the latter trend is confirmed, it may account for the decline in X_{20} found by Bhat et al. (1986) toward the inner Galaxy, since the more massive clouds there have higher mean temperatures (Scoville et al. 1987).

6.3 Cosmic Ray Acceleration near GMCs

Several models that predict increased CR fluxes associated with dense, neutral gas clouds were examined; the most attractive being that of Morfill (1982). In this picture, low energy electrons are generated in the cloud by few GeV CRs and are Fermi-accelerated by an Alfvén wave field produced by low energy (few hundred MeV) CRs streaming into the cloud to offset ionisation losses. Its predictions depend on the normalisation of the CR spectrum, but not on less well known quantities, such as the diffusion coefficient in the HIM. A substantial part of the excess in the $70-150$ and $150-300\,MeV$ energy bands (crudely estimated as $\gtrsim 50\%$) is accounted for if X_{20} is forced to take the value 1.5 in all clouds examined.

The model advocated by Völk (1983b) of CR compression in massive neutral clouds accreting gas from the HIM is also interesting, but can make no specific predictions about the enhancement expected in the electron component, for which it is viable energetically. If they do participate in the process, however, an excess flux over that in the HIM of $\lesssim 2-3$ might occur up to energies of $\sim$ few GeV and assist in explaining the small increase seen in the $300 - 500\,MeV$ $\gamma-$ray band. Both models would account for the observations of Riley and Wolfendale (1984) noted earlier.

6.4 The Virial Theorem and Molecular Clouds

An extensive survey of inner Galaxy GMCs obtained by workers at Massachusetts-Stony Brook has been subjected to a virial theorem analysis by SRBY and Scoville et al. (1987) who deduce values of $X_{20} \sim 3$ for clouds of mass $\sim 5 \times 10^5\,M_\odot$ and density profiles $n(r) \propto r^{-1}$. A reappraisal of the virial technique as often applied to GMCs has shown that derived masses are strict upper limits for the following reasons:

(i) Cloud definition, background subtraction and the estimation of velocity dispersions and sizes lead to overestimates of a factor of ~ 2 at least. The method used by SRBY seems particularly vulnerable to this problem.

(ii) The assumption of virial equilibrium introduces an uncertainty of a similar size. Comparison with extinction or LTE-derived masses, where available, suggests that these uncertainties tend to err on the high mass side (i.e., $M_{vir} > M_{cloud}$) even when a molecular line of moderate optical depth (e.g., ^{13}CO) is used to compute velocity dispersions. Ignoring the role of magnetic fields in GMCs may also cause considerable errors in the same direction.

(iii) Optically thick molecular lines, particularly CO, are widened by saturation effects.

An attempt to correct the SRBY and Scoville et al. conclusions for (iii) alone reduces their X_{20} estimates by ~ 2. A further correction to the SRBY value (for He) is also required and the final results are close to that of Bhat et al. (1986c), who found $X_{20} \sim 1.0$ for $R \sim 5\,kpc$. Even these reduced values might still be regarded as upper limits. The differences between them are probably attributable in part to points (i) and (ii). What is clear, however, is that

the claims by SRBY and Scoville et al. for values considerably in excess of those derived in Chapter 3 are not convincing. *A local figure of* $X_{20} \sim 1.5 \pm 0.5$, *reducing to* $X_{20} \lesssim 1.0$ *in the molecular ring, is indicated by the present work.*

Clearly this supports the arguments of Bhat et al. both in terms of the local value for X_{20} and its radial variation. However, it is not yet known whether the gradient is caused by metallicity or temperature variations; both may be important – see, for example, Kutner and Leung (1985); Williams (1985); Maloney and Black (1987).

One important consequence of relevance to CR studies is that the Bhat et al. H_2 distribution implies a modest large-scale CR gradient to be consistent with observed $\gamma-$ray fluxes towards the inner Galaxy. Not only would the much higher SRBY H_2 surface densities rule out such a gradient, but they would require CRs to be excluded from GMCs at much higher energies than theoretically expected, and in sharp contrast to what is found here.

6.5 Prospects

It is evident from the foregoing discussion that the $\gamma-$ray data presently available offer no simple solutions to the determination of X_{20}. Similarly, the radial variation in the nuclear CR component at GeV energies has proved to be a contentious issue, though most authors are now agreed that a small gradient exists (see Cesarsky 1987). Significant improvements in present understanding will undoubtedly occur with the deployment of two $\gamma-$ray satellites in the near future: Gamma 1 and the Gamma Ray Observatory (GRO). Both will have much improved spatial and energy resolution ($10'$ and 15% respectively for the GRO) and, just as important, a low isotropic background level. The influence of $\gamma-$ray sources in, for example, the estimation of X_{20} will be clarified by an order-of-magnitude better sensitivity ($\sim 10^{-7}\,\mathrm{cm}^{-2}\,\mathrm{s}^{-1}$) over COS-B.

With regard to the local ISM, such instruments offer the prospect of probing in far more detail the CR variations between cloud and cloud-free regions, the relation between $\gamma-$ray emission and tracers of the molecular gas, and $\gamma-$ray spectral variations on cloud size scales. Intensive observations at medium latitudes are required to reduce the statistical noise and make the best use of the improved detector characteristics. This should be regarded as an integral part of Galactic plane observations that sample the CR and gas distributions over distances of several kpc.

The next major step will be the launching of the GRASP telescope (Bignami et al. 1987) which is to combine high resolution ($\sim 6'$) with a wide field-of-view ($\sim 6°$), and a point source sensitivity of $\sim 10^{-8}\,\mathrm{cm}^{-2}\,\mathrm{s}^{-1}$.

A better understanding of the distribution of molecular gas is also of the greatest importance. Surveys in less optically thick molecular lines are just becoming available (e.g., Stark 1987); data are in hand for some local clouds and is imperative that these be extended both in longitude and latitude to cover the most important regions of Galactic emission. Observations of higher excitation transitions in CO (e.g., $J = 2 \rightarrow 1$) are required to clarify the variation of kinetic temperature in the Galactic disc, of some importance if X_{20} is strongly temperature-dependent. Finally, it is to be hoped that much greater theoretical insight into the formation of molecular lines, and the physics of GMCs themselves will emerge from these observations.

The next decade promises to be one in which $\gamma-$ray astronomy comes of age!

APPENDIX A

Table A.1: Gamma-ray emissivities for the predominantly HI regions A, C and F estimated separately. R is the multiple correlation coefficient.

Region	ΔE	$\frac{q}{4\pi} \times 10^{-26}$	R
	MeV	ph atom^{-1} s^{-1} sr^{-1}	
$A+C+F$	70−150	1.01 ± 0.08	0.40
A	"	1.01 ± 0.11	0.39
C	"	0.93 ± 0.25	0.38
F	"	1.01 ± 0.14	0.42
$A+C+F$	150−300	0.77 ± 0.05	0.46
A	"	0.78 ± 0.07	0.45
C	"	0.74 ± 0.17	0.44
F	"	0.73 ± 0.48	0.48
$A+C+F$	300−5000	0.58 ± 0.05	0.38
A	"	0.63 ± 0.07	0.38
C	"	0.57 ± 0.14	0.41
F	"	0.58 ± 0.08	0.42
$A+C+F$	800−5000	0.30 ± 0.04	0.30
A	"	0.30 ± 0.05	0.29
C	"	0.35 ± 0.10	0.20
F	"	0.35 ± 0.06	0.34

Table A.2: Y_{20} values derived using equation (3.3) assuming $q_{B+D} = q_{A+C+F}$ and $q_E = q_{A+C+F}$. R is the multiple correlation coefficient.

Region	ΔE	$\frac{q}{4\pi} \times 10^{-26}$	Y_{20}	R
	MeV	ph atom^{-1} s^{-1} sr^{-1}	10^{20} mol cm^{-2} (K km s^{-1})$^{-1}$	
$B+D$	70−150	1.01 ± 0.08	9.3 ± 2.0	0.24
"	150−300	0.77 ± 0.05	4.4 ± 1.0	0.20
"	300−5000	0.58 ± 0.05	6.5 ± 1.2	0.29
"	800−5000	0.30 ± 0.04	4.3 ± 1.4	0.16
E	70−150	1.01 ± 0.08	4.6 ± 1.2	0.24
"	150−300	0.77 ± 0.05	4.7 ± 0.9	0.32
"	300−5000	0.58 ± 0.05	4.1 ± 1.0	0.26
"	800−5000	0.30 ± 0.04	1.1 ± 1.0	0.06

Table A.3: HI and H_2 emissivities from equation 3.2 assuming $X_{20} = 1.5$, with $q_{H_2} = a/3 \times 10^{20}$, for all cloud regions. HI emissivities using the model cloud of §3.3 are given in brackets for $b = 0.5$.

Region	ΔE	$\frac{q(HI)}{4\pi} \times 10^{-26}$	$\frac{q(H_2)}{4\pi} \times 10^{-26}$
	MeV	ph atom^{-1} s^{-1} sr^{-1}	
$B + D$	70–150	(1.61) 1.31 ± 0.14	2.03 ± 0.80
"	150–300	(1.03) 0.90 ± 0.08	0.79 ± 0.33
"	300–5000	(0.72) 0.65 ± 0.07	1.12 ± 0.24
"	800–5000	0.28 ± 0.05	0.60 ± 0.18
E	70–150	(2.37) 1.69 ± 0.12	−0.18 ± 0.47
"	150–300	(1.35) 1.06 ± 0.08	0.66 ± 0.24
"	300–5000	(1.40) 0.99 ± 0.06	0.12 ± 0.19
"	800–5000	(0.42) 0.36 ± 0.04	0.09 ± 0.13
$B + D + E$	70–150	(2.07) 1.54 ± 0.09	0.49 ± 0.40
"	150–300	(1.19) 0.98 ± 0.05	0.73 ± 0.19
"	300–5000	(1.10) 0.84 ± 0.05	0.52 ± 0.15
"	800–5000	0.32 ± 0.03	0.29 ± 0.11

Table A.4: $q/4\pi$ estimated using equation (3.4) assuming $X_{20} = 1.5$. R is the multiple correlation coefficient.

Region	ΔE	$\frac{q}{4\pi} \times 10^{-26}$	R
	MeV	ph atom^{-1} s^{-1} sr^{-1}	
$B + D$	70–150	1.39 ± 0.10	0.61
"	150–300	0.88 ± 0.05	0.64
"	300–5000	0.73 ± 0.05	0.61
"	800–5000	0.34 ± 0.04	0.44
E	70–150	1.39 ± 0.08	0.72
"	150–300	0.98 ± 0.05	0.75
"	300–5000	0.82 ± 0.05	0.73
"	800–5000	0.31 ± 0.03	0.51
$B + D + E$	70–150	1.39 ± 0.06	0.67
"	150–300	0.94 ± 0.04	0.70
"	300–5000	0.78 ± 0.03	0.68
"	800–5000	0.32 ± 0.02	0.47

A.5 Gamma Ray Correlation Plots

A.5.1 $I_\gamma = I_\gamma(obs) - I_b$ versus $\tilde{N}$(HI) for region $A + C + F$.

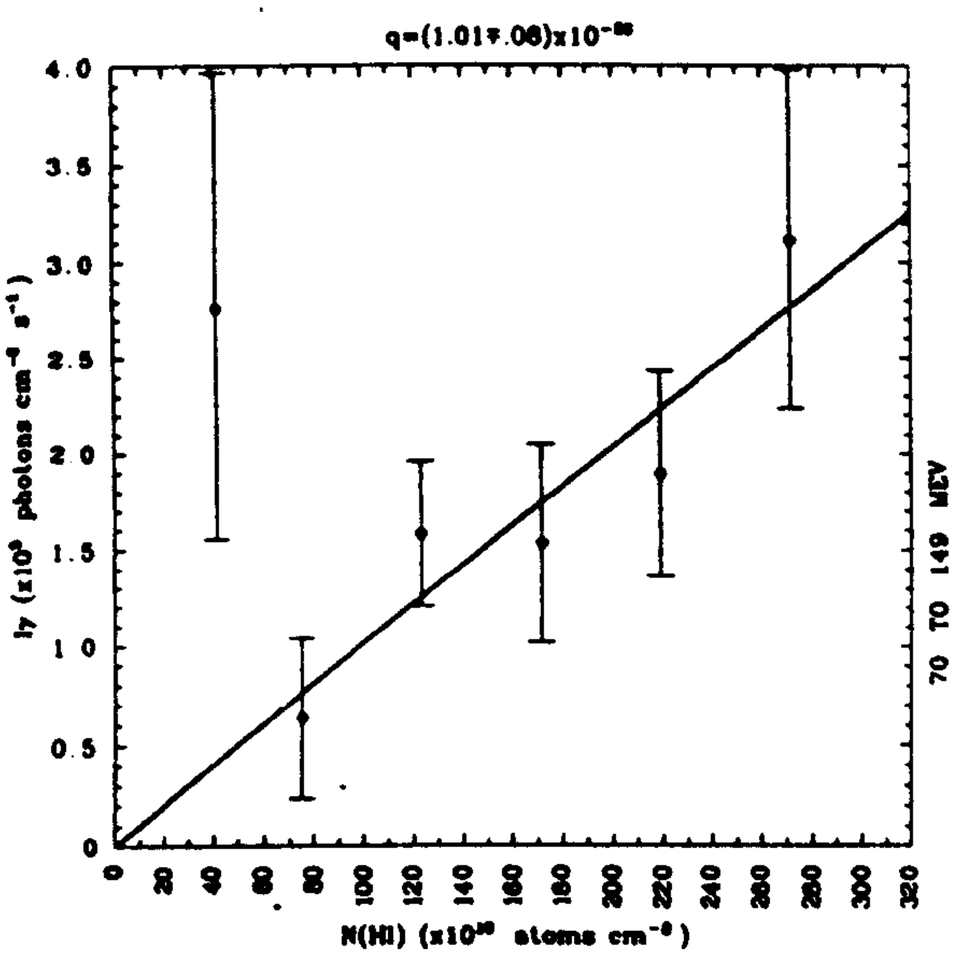

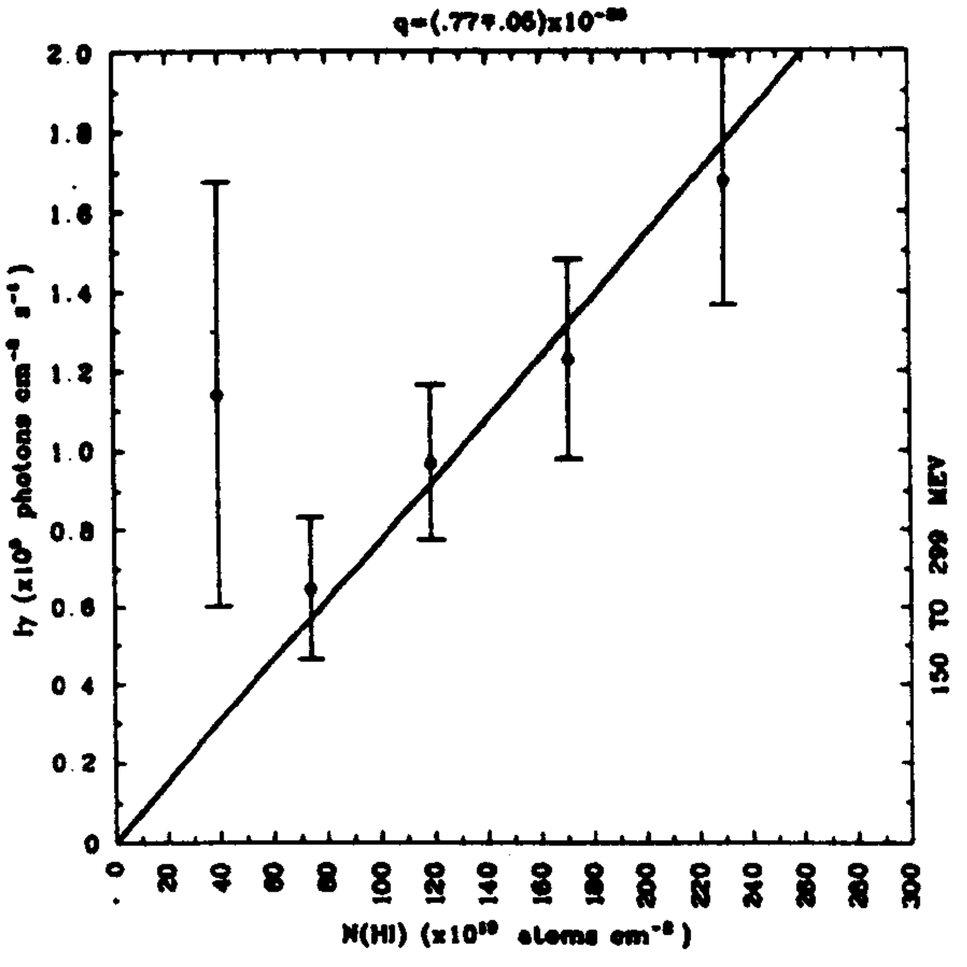

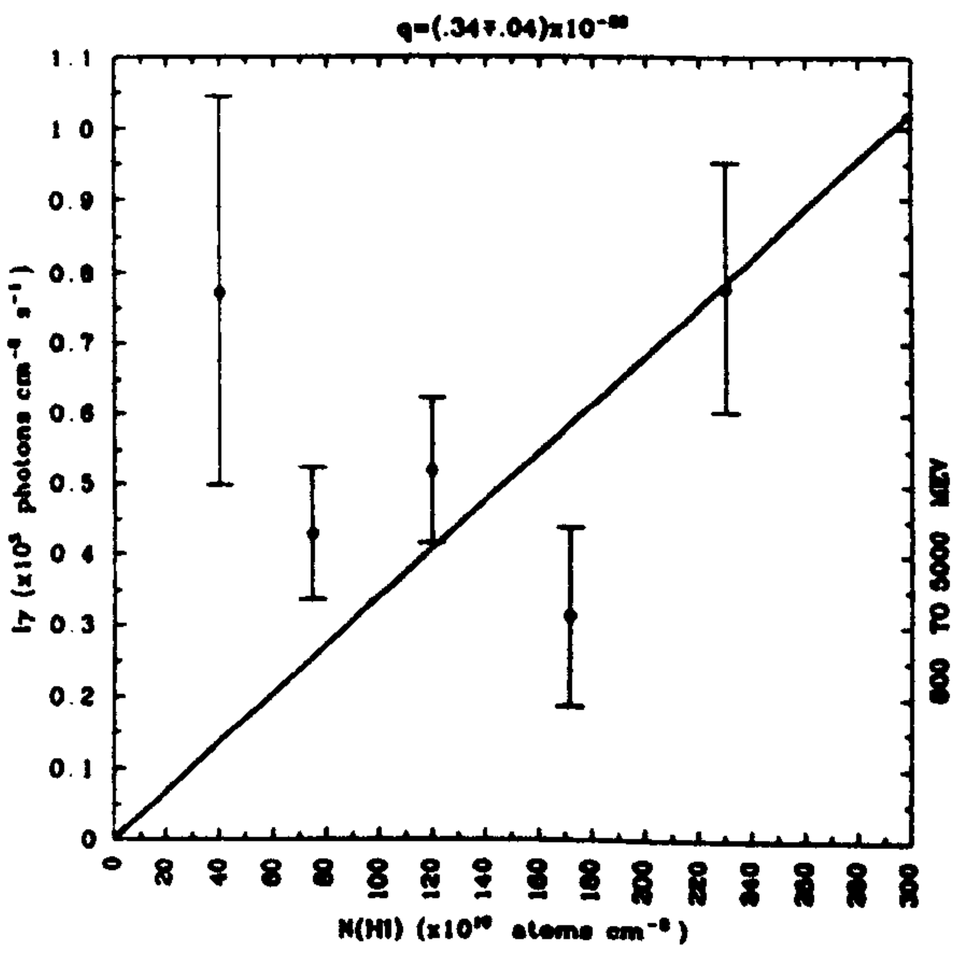

A.5.2 $\Delta I_\gamma = I_\gamma(obs) - \frac{q}{4\pi}\tilde{\mathrm{N}}(\mathrm{HI}) - I_b$ **versus** $\tilde{\mathrm{W}}_{\mathrm{CO}}$ **for region** E; q **and** X_{20} **estimated from equation 3.2.**

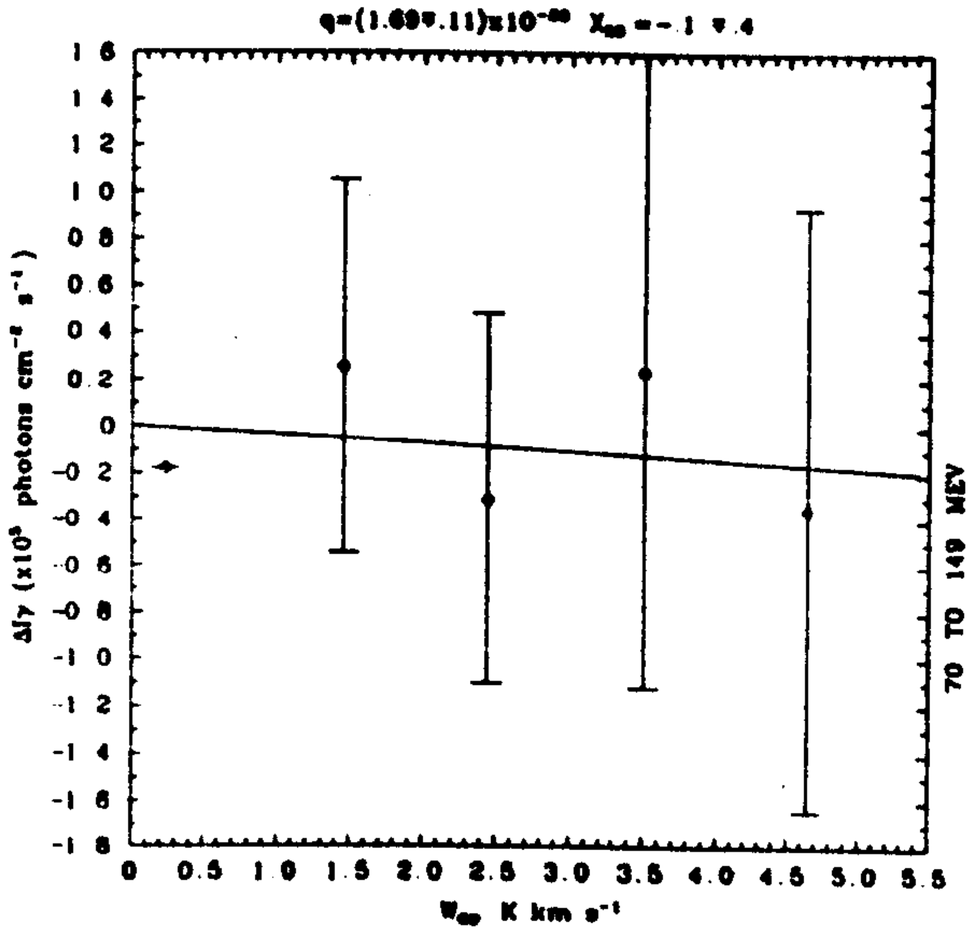

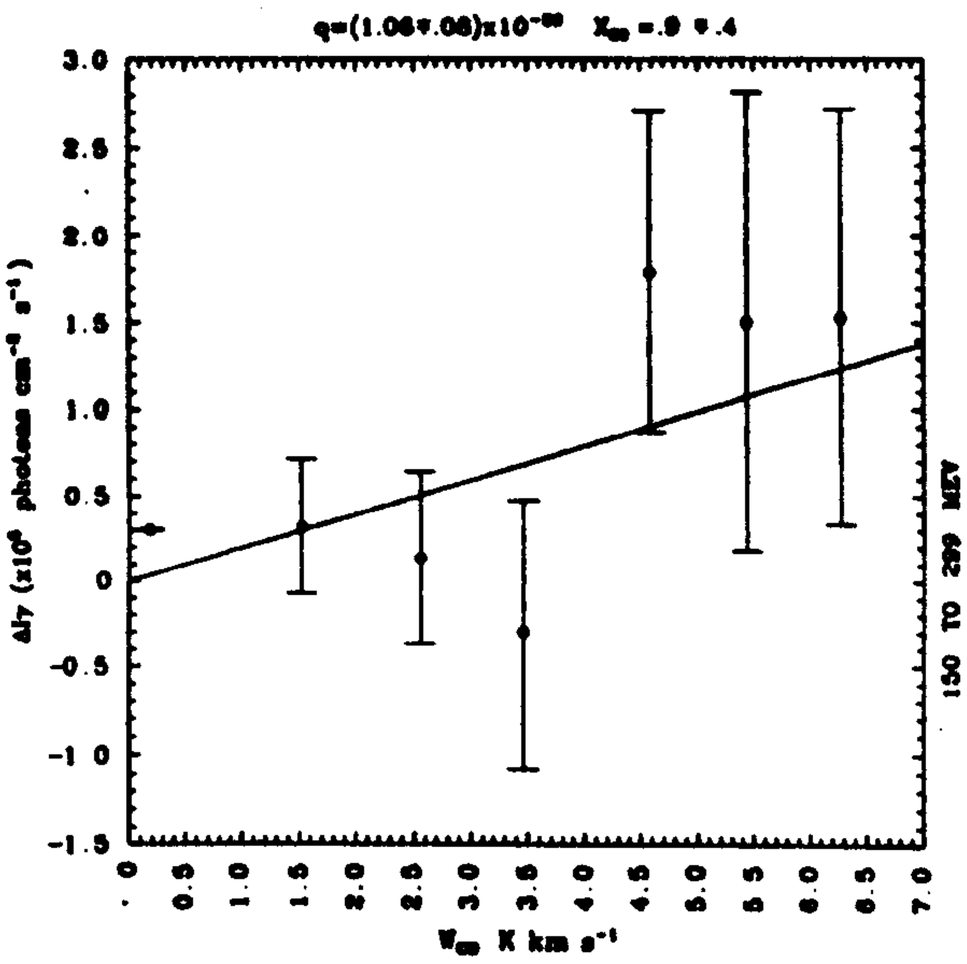

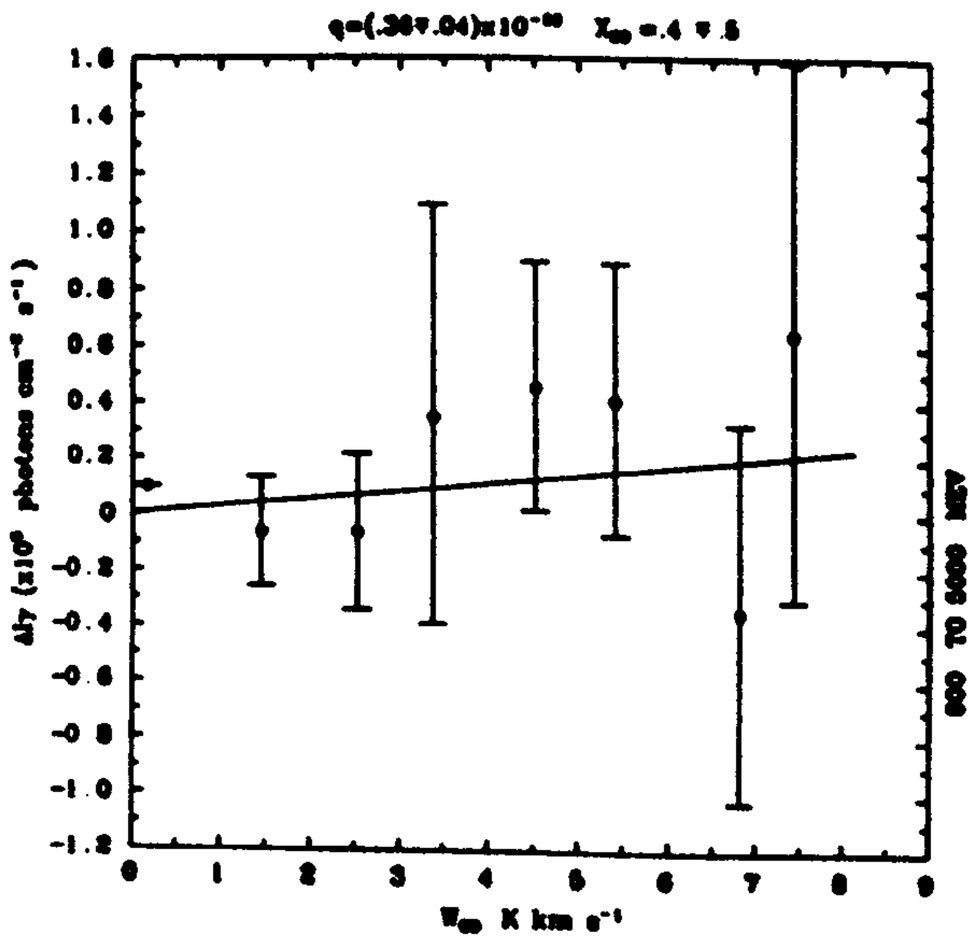

A.5.3 $\Delta I_\gamma = I_\gamma(obs) - \frac{q}{4\pi}\tilde{N}(HI) - I_b$ versus $\tilde{W}_{CO}$ for region $B + D$; q and X_{20} estimated from equation 3.2.

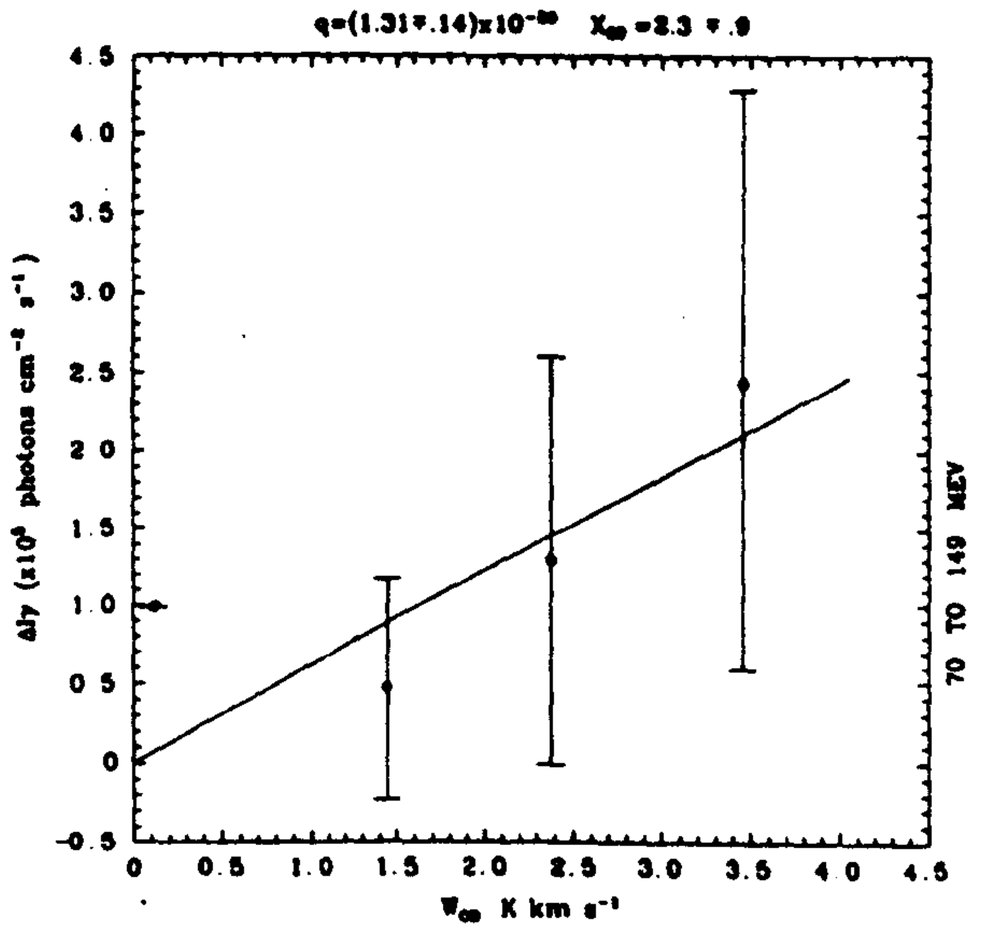

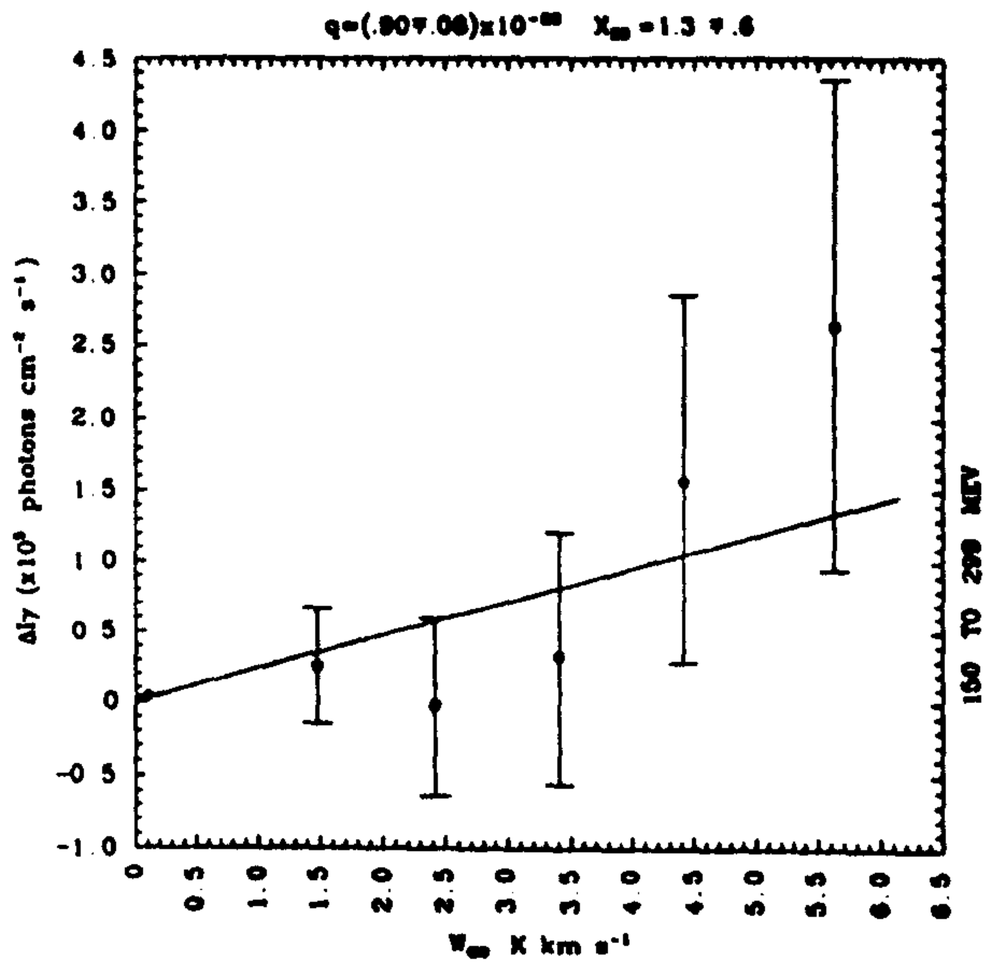

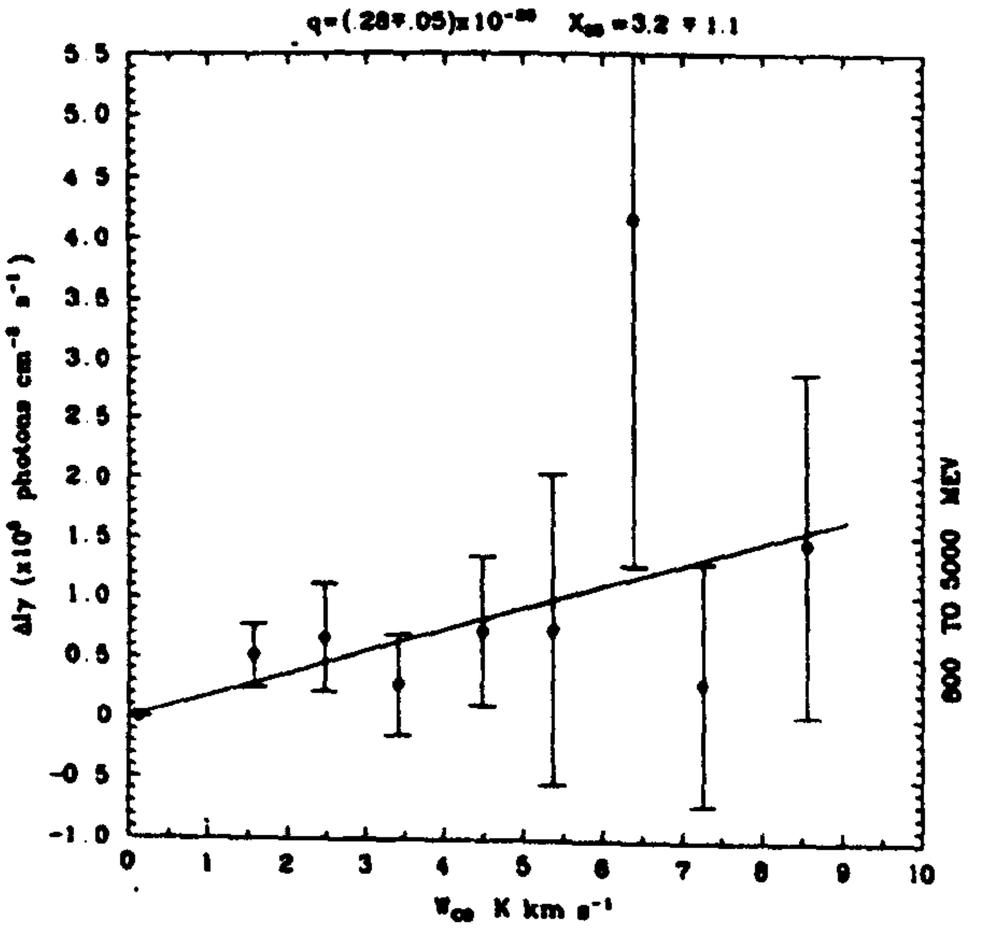

A.5.4 $\Delta I_\gamma = I_\gamma(obs) - \frac{q}{4\pi}\tilde{\mathrm{N}}(\mathrm{HI}) - I_b$ versus $\tilde{\mathrm{W}}_{\mathrm{CO}}$ for region $B+D+E$; q and X_{20} estimated from equation 3.2.

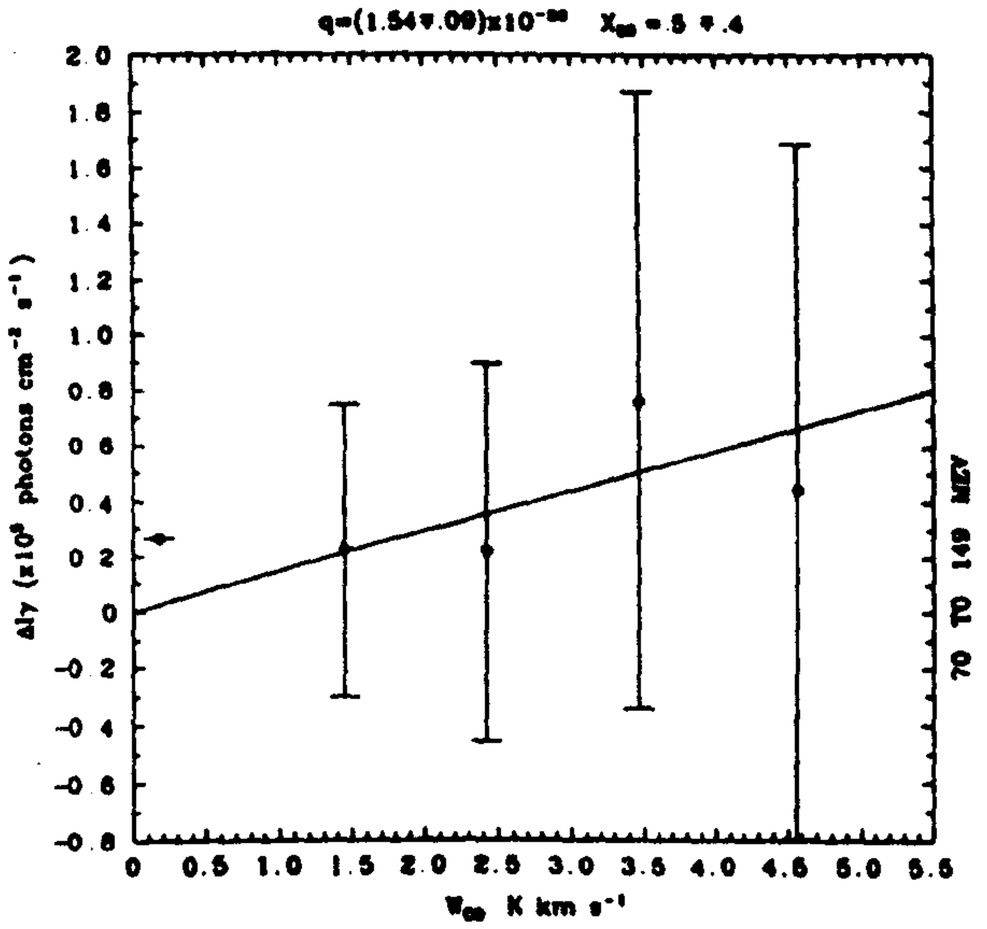

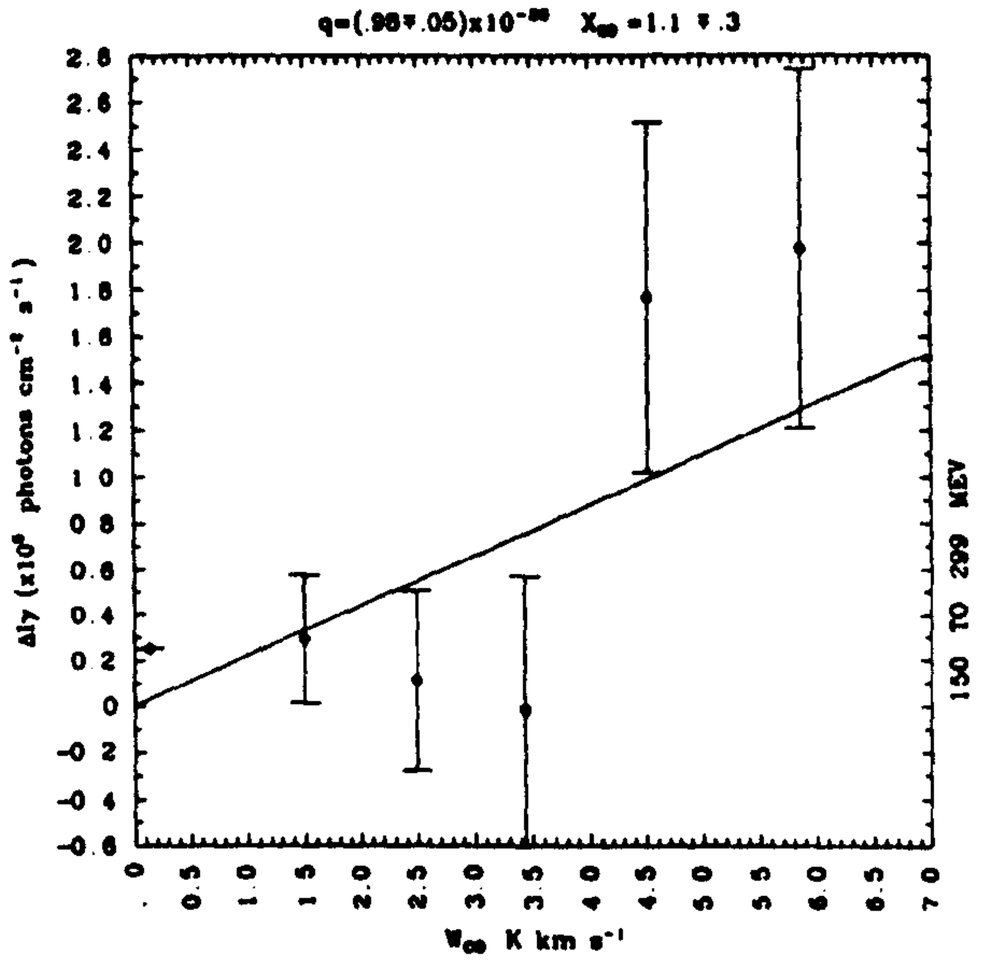

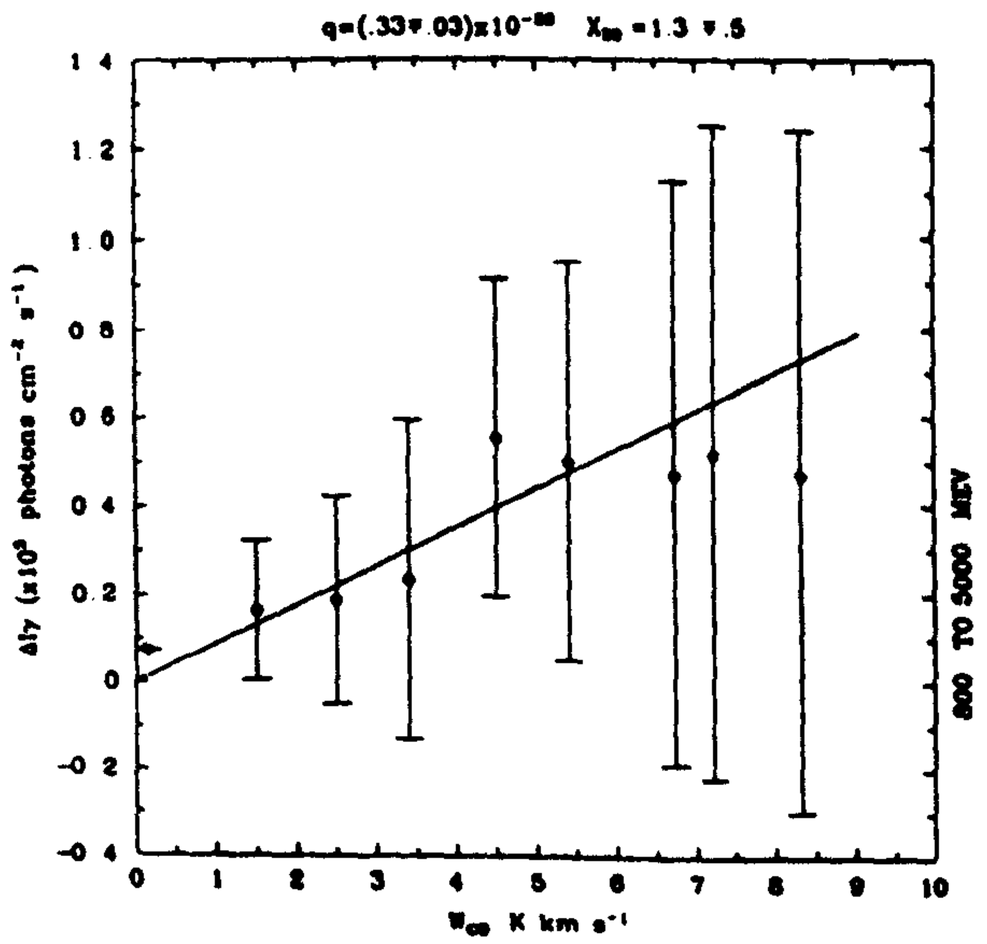

A.5.5 $\Delta I_\gamma = I_\gamma(obs) - \frac{q}{4\pi}\tilde{N}(HI) - I_b$ versus $\tilde{W}_{CO}$ for region E; q estimated in region $A + C + F$ and X_{20} derived from equation 3.2.

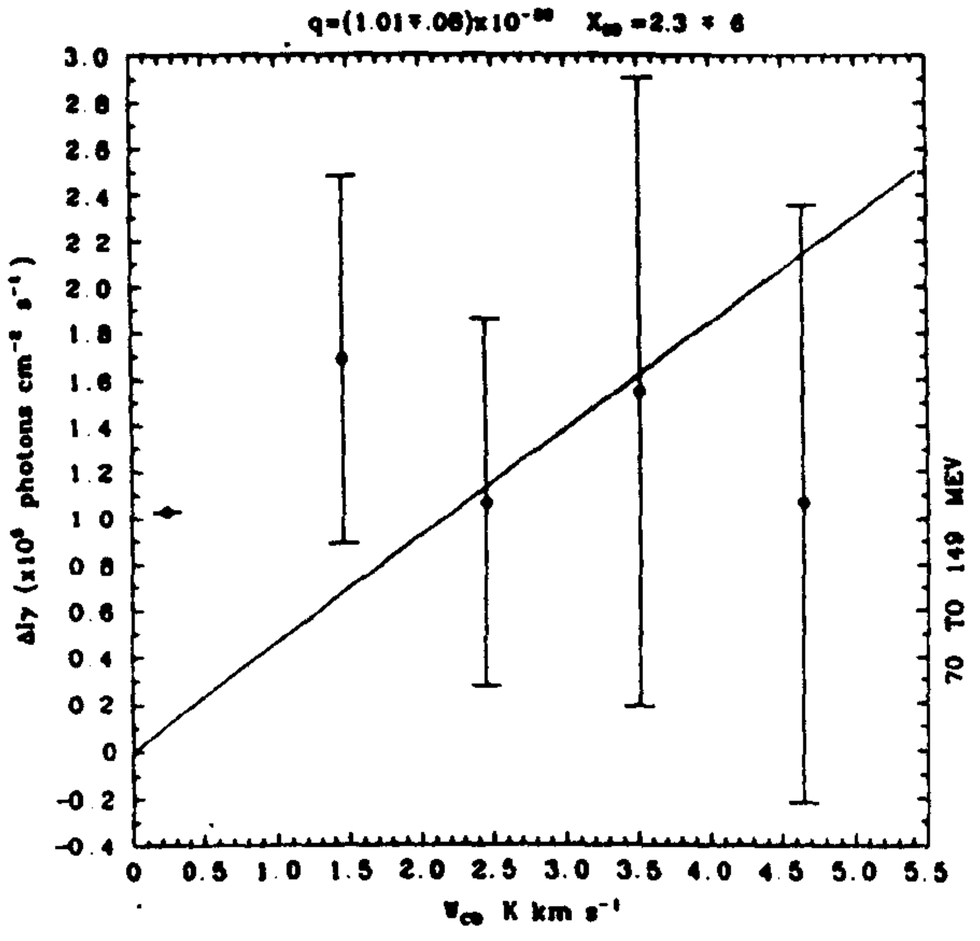

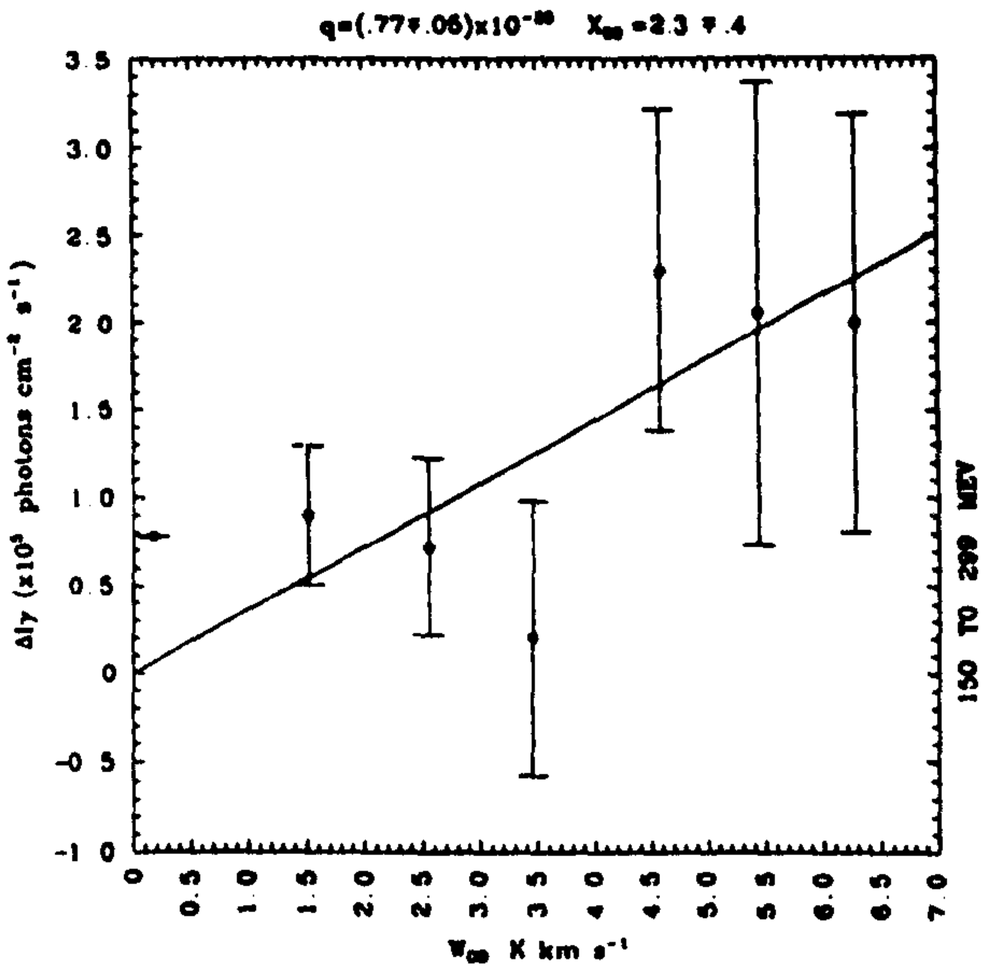

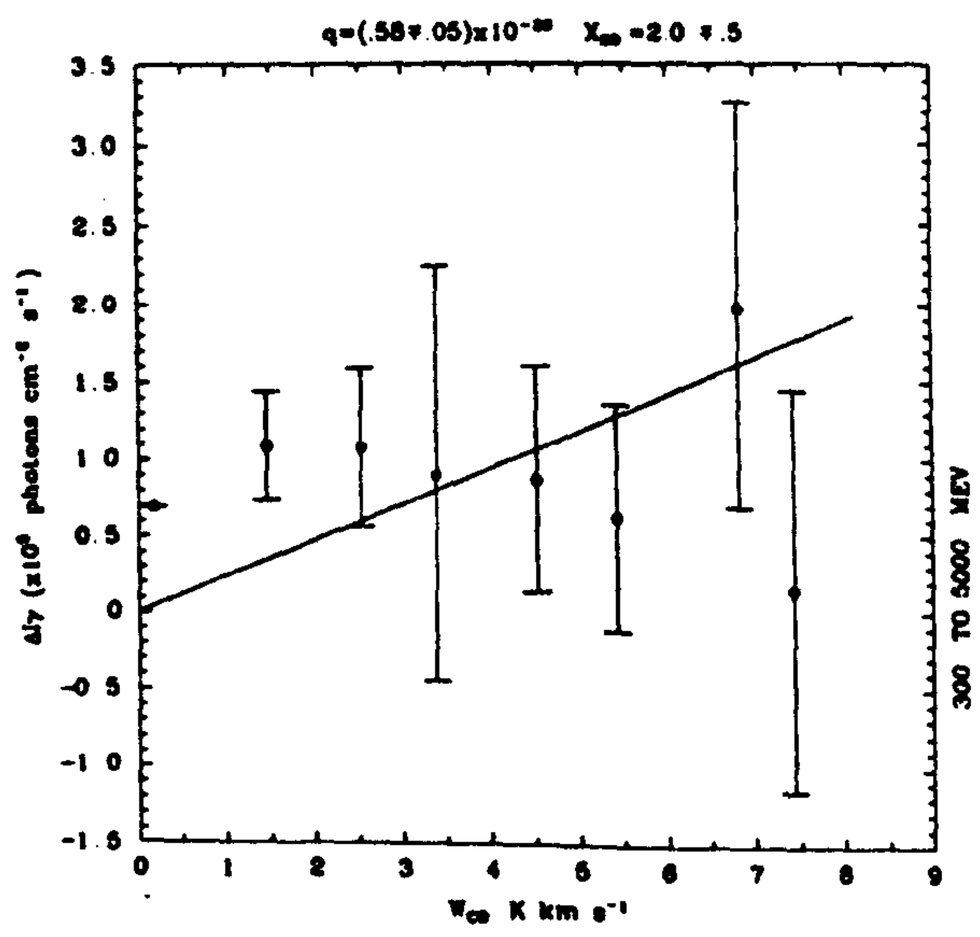

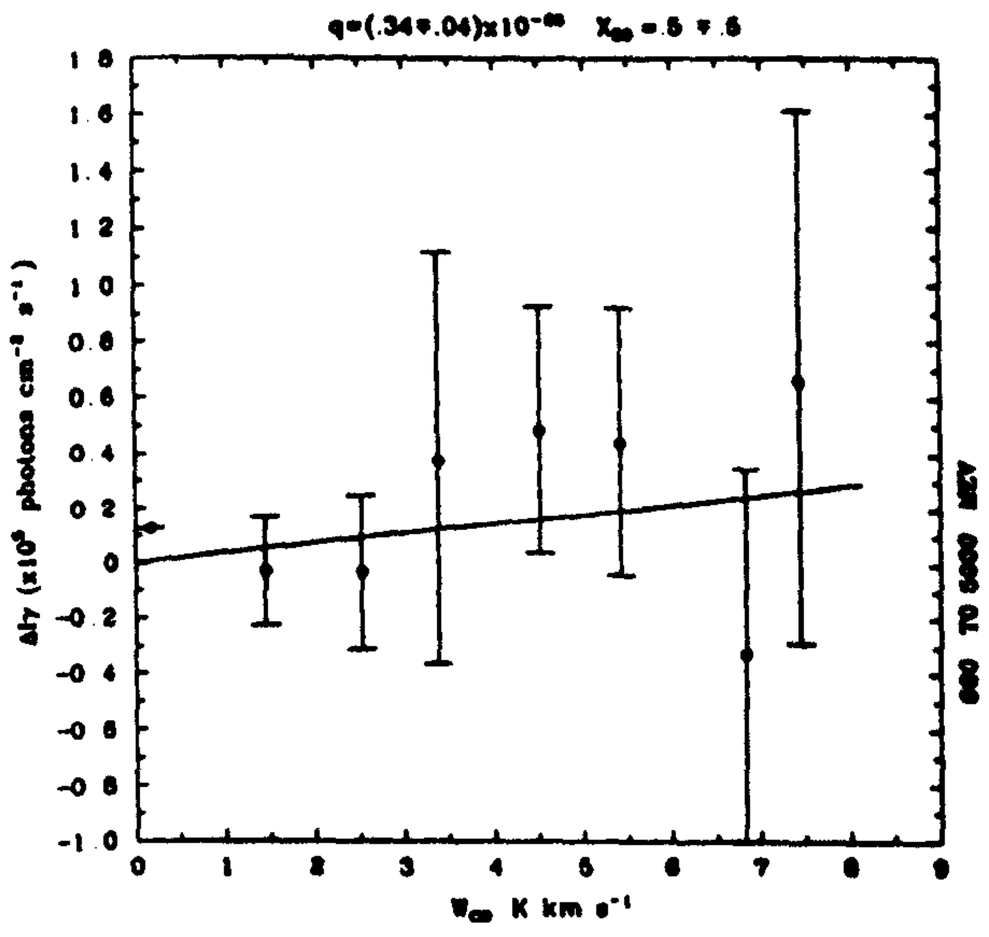

A.5.6 $\Delta I_\gamma = I_\gamma(obs) - \frac{q}{4\pi}\tilde{\mathrm{N}}(\mathrm{HI}) - I_b$ versus $\tilde{\mathrm{W}}_{\mathrm{CO}}$ for region $B + D$; q estimated in region $A + C + F$ and X_{20} derived from equation 3.2.

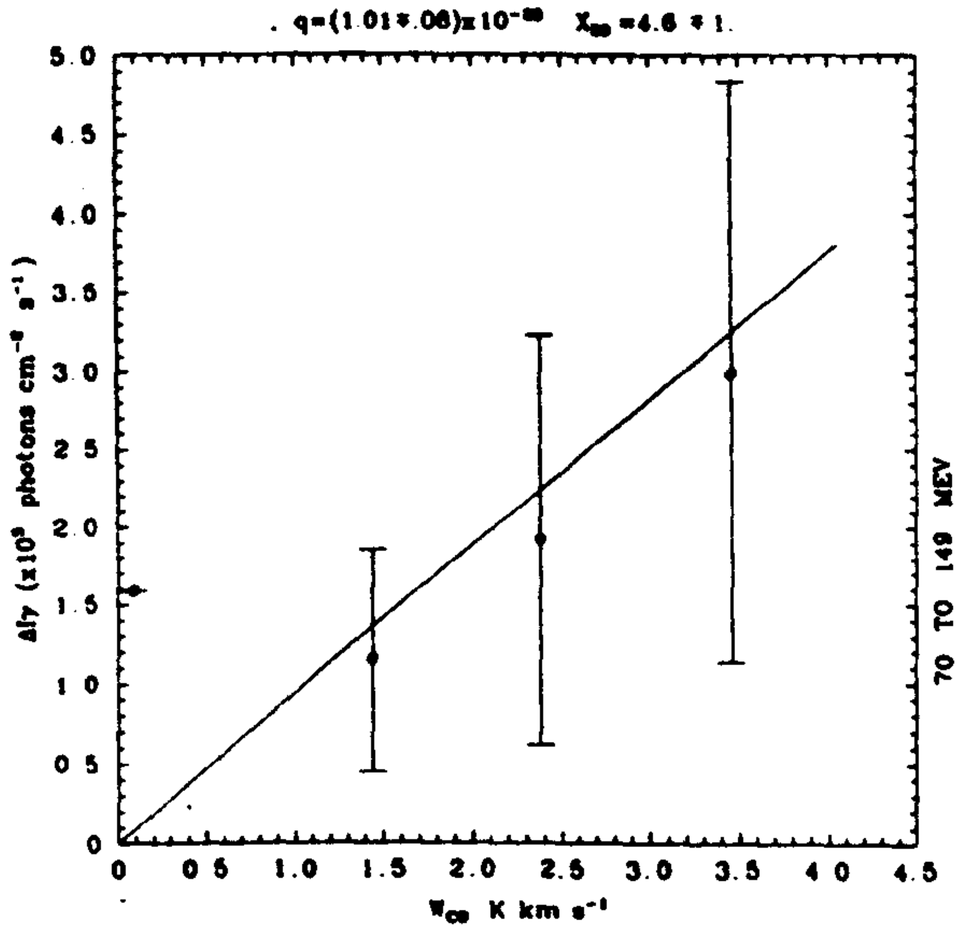

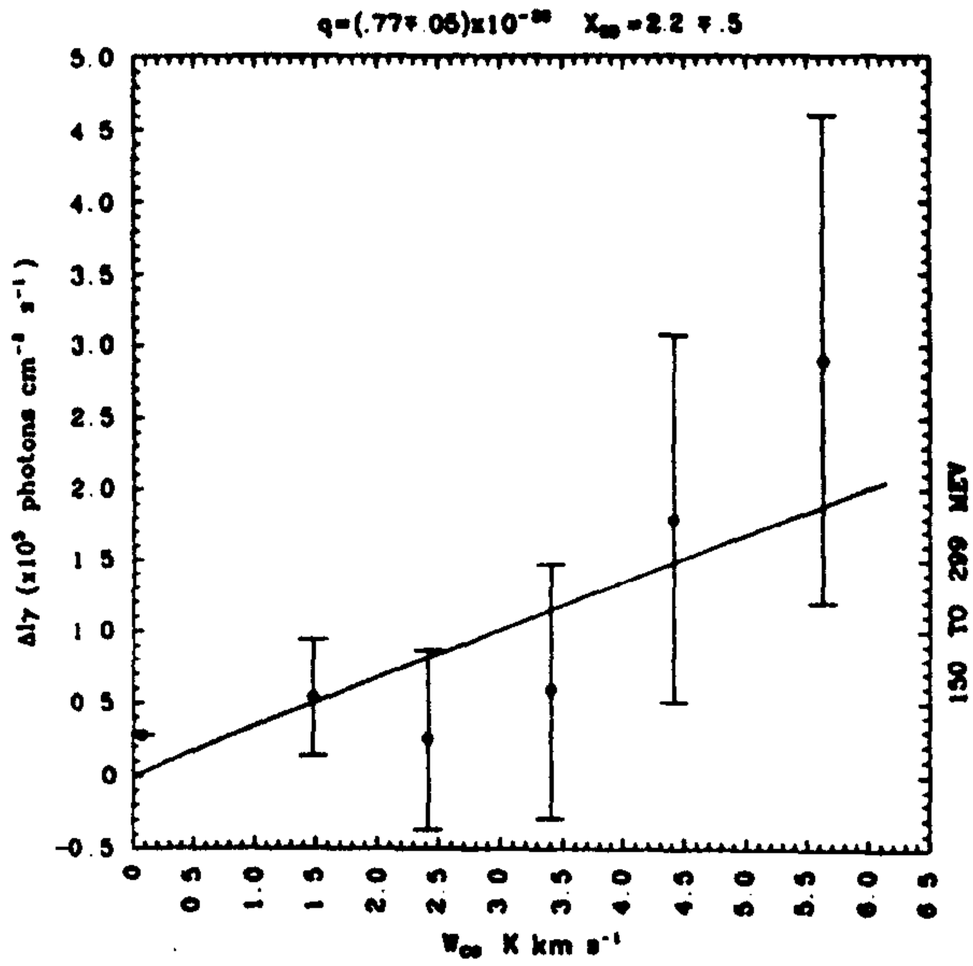

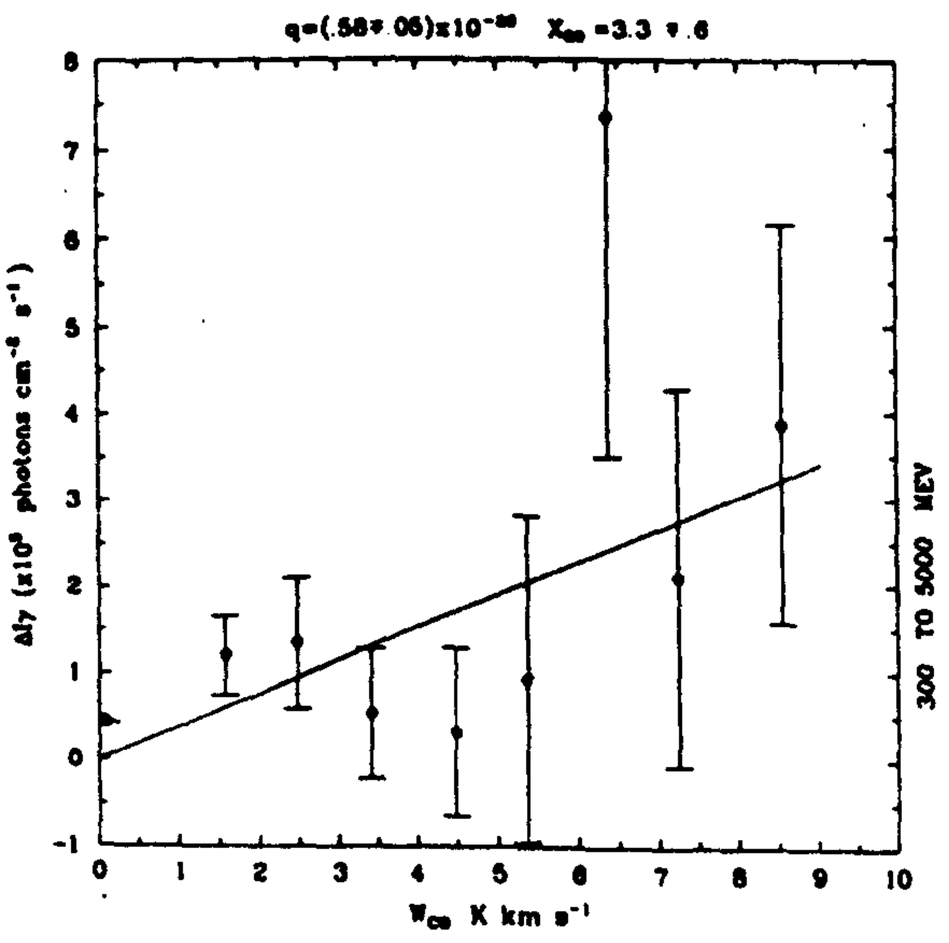

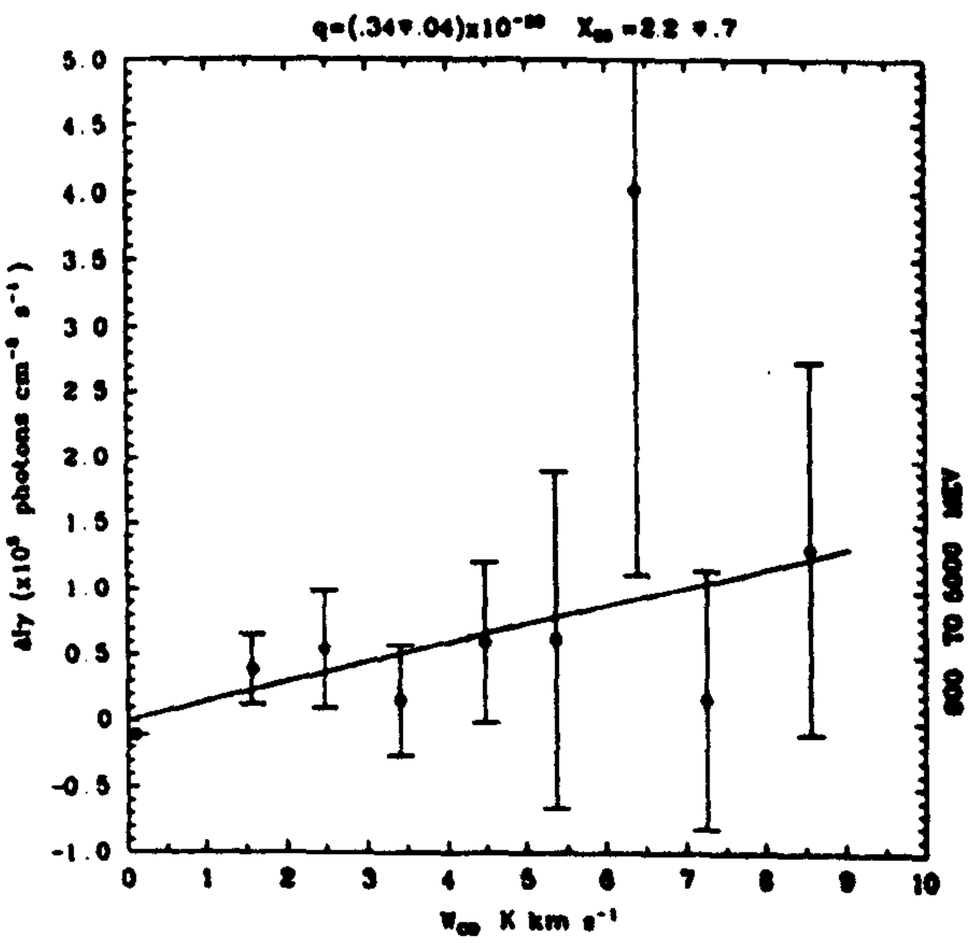

A.5.7 $\Delta I_\gamma = I_\gamma(obs) - \frac{q}{4\pi}\tilde{N}(HI) - I_b$ versus $\tilde{W}_{CO}$ for region $B + D + E$; q estimated in region $A + C + F$ and X_{20} derived from equation 3.2.

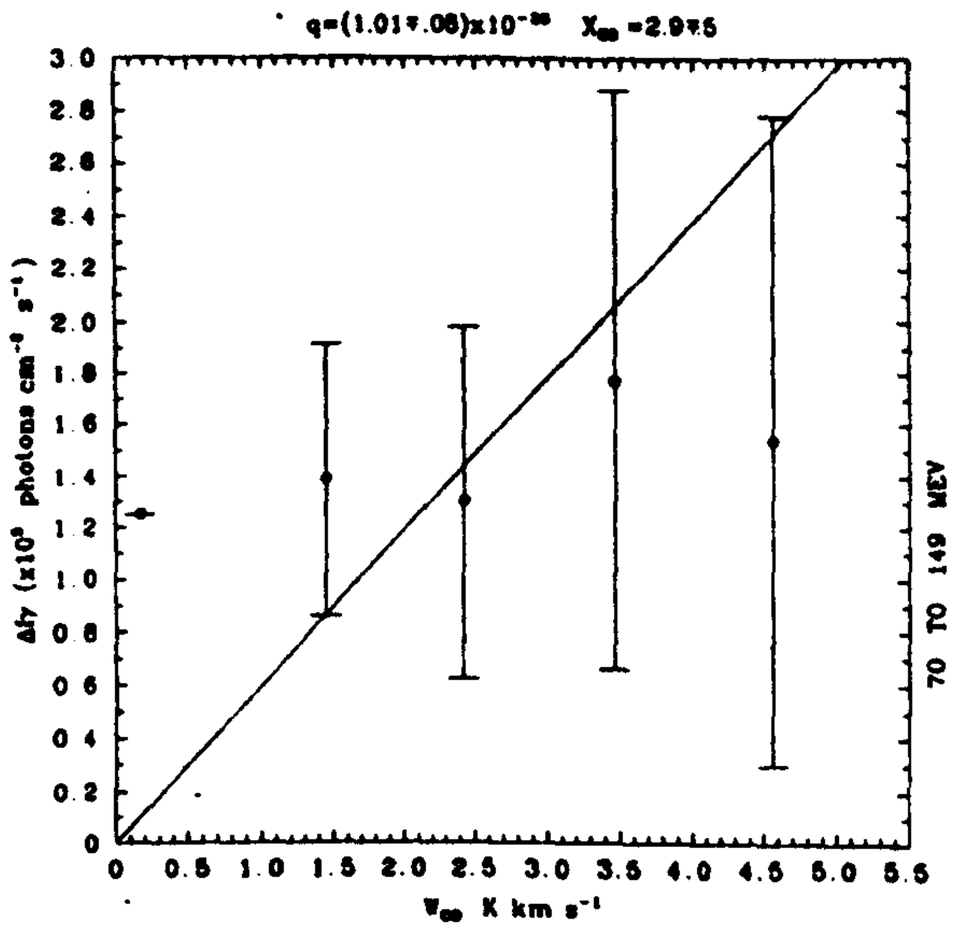

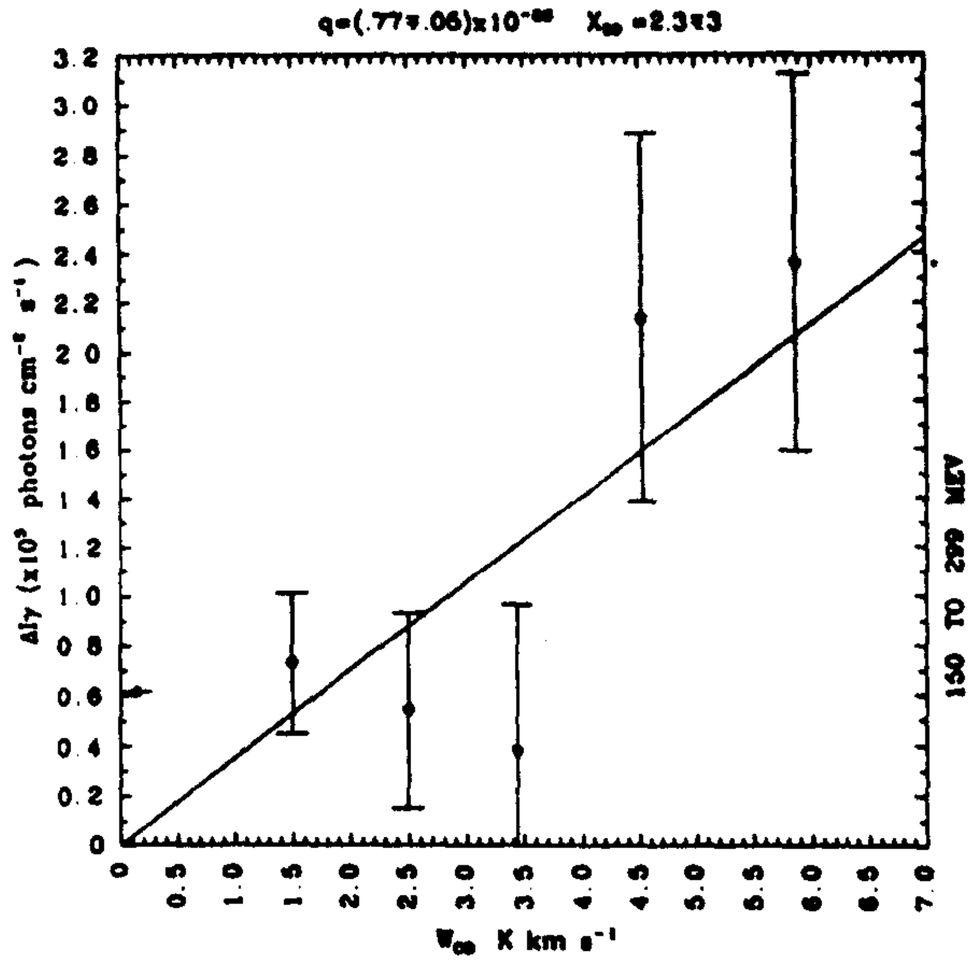

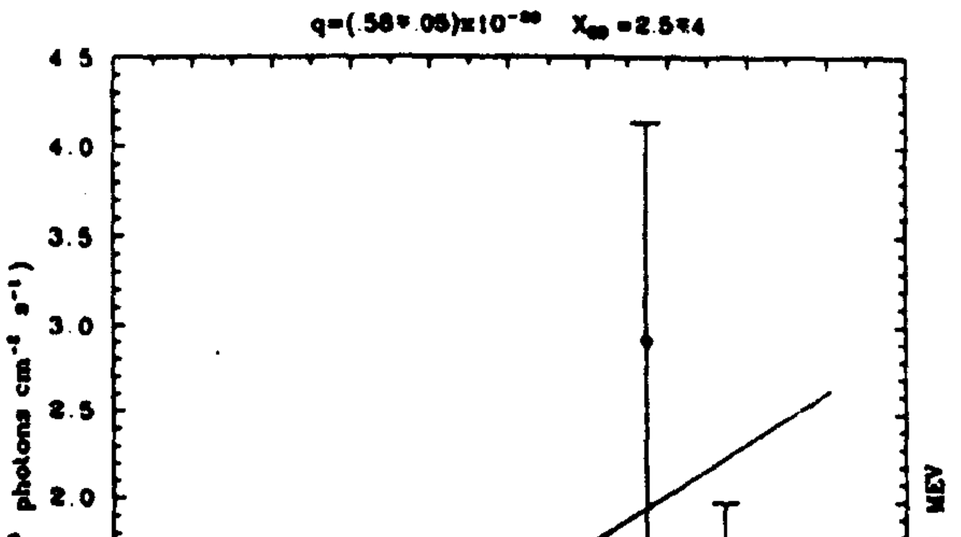

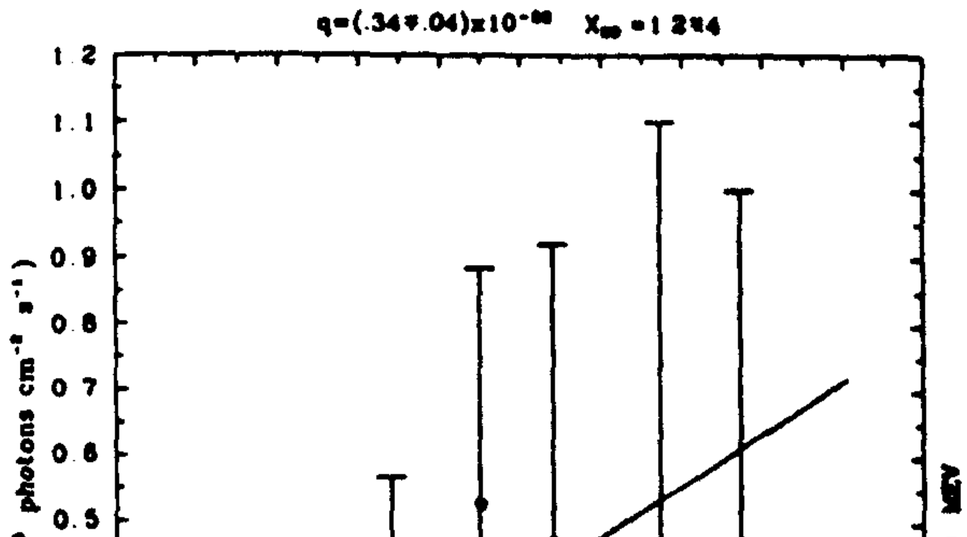

REFERENCES

Arquilla, R., 1987, *Ph.D. Thesis,* University of Massachusetts.

Aarseth, S.J. & Saslaw, W.C., 1972, *Astrophys. J.*, **172**, 17.

Bally, J. & Langer, W.D., 1982, *Astrophys. J.*, **255**, 143.

Bally, J., Langer, W., Stark, A.A. & Wilson, R., 1987, *Astrophys. J. Letters,* **312**, L45.

Bennett, K., Bignami, G.F., Boella, G., Buccheri, R., Burger, J.J., Cuccia, A., Hermsen, W., Higdon, J., Kanbach, G., Koch, L., Lichti, G.G., Masnov, J., Mayer-Hasselwander, H.A., Paul, J., Scarsi, L., Shukla, P.G., Swanenburg, B.N., Taylor, B.G., & Wills, R.D., 1976, in *The Structure and Content of The Galaxy and Galactic Gamma Rays*, Goddard Space Flight Centre, X-662-76-154, p.23.

Berezinsky, V.S., Ginzburg, V.L., & Ptuskin, V.S., 1985, *Proc. 19th Int. Cosmic Ray Conf.*, **1**, 305.

Bhat, C.L., Issa, M.R., Mayer, C.J. & Wolfendale, A.W., 1985, *Nature,* **314**, 515.

Bhat, C.L., Issa, M.R., Mayer, C.J. & Wolfendale, A.W., 1986a, *J. Phys. G: Nucl. Phys.*, **12**, 1067.

Bhat, C.L., Mayer, C.J., Rogers, M., Wolfendale, A.W. & Zan, M., 1986b, *J. Phys. G: Nucl. Phys.*, **12**, 1087.

Bhat, C.L., Mayer, C.J. & Wolfendale, A.W., 1984, *Astron. Astrophys.*, **140**, 284.

Bhat, C.L., Mayer, C.J. & Wolfendale, A.W., 1986c, *Phil. Trans. R. Soc.Lond.*, **319**, 249.

Bignami, G., Villa, G., Dean, A.J., Ramsden, D., Durouchoux, Ph., Hurley, K., Vedrenne, G., Lund, N., McBreen, B., Schönfelder, V., Swanenburg, B.n., Winkler, C. & Tomaschek, G., 1987, *Proc. 20th Int. Cosmic Ray Conf.*, **2**, 327.

Blandford, R.D. & Cowie, L.L., 1982, *Astrophys. J.*, **260**, 625.

Blitz, L., 1978, *Ph.D. Thesis*, Columbia University.

Blitz, L., 1980, in *Giant Molecular Clouds in the Galaxy*, eds. Solomon, P.M. & Edmunds, M.G., Pergammon, Oxford, p. 1.

Blitz, L., 1987, in *Physical Processes in Interstellar Clouds*, eds. Morfill, G.E. & Scholer, M., Reidel, Dordrecht, Holland, p.35.

Blitz, L., Fich, M. & Stark, A.A., 1982, *Astrophys. J. Suppl.*, **49**, 183.

Blitz, L. & Stark, A.A., 1986, *Astrophys. J. Letters,* **300**, L89.

Blitz, L. & Thaddeus, P., 1980, *Astrophys. J.*, **241**, 676.

Bloemen, J.B.G.M., 1985, *Ph.D. Thesis*, Leiden University.

Bloemen, J.B.G.M., 1987, *Proc. 20th Int. Cosmic Ray Conf.*, **1**, 121.

Bloemen, J.B.G.M., Bennett, K., Bignami, G.F., Blitz, L., Caraveo, P.A., Gottwald, M., Hermsen, W., Lebrun, F., Mayer-Hasselwander, H.A. & Strong, A.W., 1984a, *Astron. Astrophys.*, **135**, 12.

Bloemen, J.B.G.M., Caraveo, P.A., Hermsen, W., Lebrun, F., Maddalena, R.J., Strong, A.W. & Thaddeus, P., 1984b, *Astron. Astrophys.*, **139**, 37.

Bloemen, J.B.G.M., Reich, P., Reich, W. & Schlickeiser, R., 1988, *Astron. Astrophys.*, submitted.

Bloemen, J.B.G.M., Strong, A.W., Blitz, L., Cohen, R.S., Dame, T.M., Grabelsky, D.A., Hermsen, W., Lebrun, F. & Thaddeus, P., 1986, *Astron. Astrophys.*, **154**, 25.

Bohlin, R.C., Savage, B.D. & Drake, J.F., 1978, *Astrophys. J.*, **224**, 132.

Bronfman, L., Cohen, R.S., Alvarez, H., May, J. & Thaddeus, P., 1987, *Astrophys. J.*, **324**, 248.

Burton, W.B. & Gordon, M.A., 1978, *Astron. Astrophys.*, **63**, 7.

Burton, W.B., Gordon, M.A., Bania, T.M. & Lockman, F.J., 1975, *Astrophys. J.*, **202**, 30.

Cassé, M. & Paul, J.A., 1980, *Astrophys. J.*, **237**, 236.

Cernicharo, J. & Bachiller, R., 1984, *Astron. Astrophys. Suppl.*, **58**, 327.

Cernicharo, J. & Guélin, M., 1987, *Astron. Astrophys.*, **176**, 299.

Chin, G., 1978, *Ph.D. Thesis*, Columbia University.

Chin, Y. & Wentzel, D.G., 1972, *Ap. Space. Sci.*, **16**, 465.

Cohen, R.J., Matthews, N., Few, R.W. & Booth, R.S., 1983, *Mon. Not. R. astr. Soc.*, **203**, 1123.

Cohen, R.S., Cong, H., Dame, T.M. & Thaddeus, P., 1980, *Astrophys. J. Letters,* **239**, L53.

Cohen, R.S. & Thaddeus, P., 1977, *Astrophys. J. Letters,* **217**, L155.

Cowie, L.L., 1981, *Astrophys. J.*, **245**, 66.

Cowie, L.L. & McKee, C.F., 1977, *Astrophys. J.*, **211**, 135.

Cowsik, 1981, in *Origin of Cosmic Rays* eds. Setti, G., Spada, G. & Wolfendale, A.W., Reidel, Dordrecht, Holland, p.93.

Dame, T.M., 1984, *Ph.D. Thesis*, Columbia University.

Dame, T.M., Elmegreen, B.G., Cohen, R.S. & Thaddeus, P., 1986, *Astrophys. J.*, **305**, 892.

Dame, T.M., Ungerechts, H., Cohen, R.S., de Gues, E.J., Grenier, A., May, J., Murphy, D.C., Nyman, L.-A. & Thaddeus, P., 1987, *Astrophys. J.*, **322**, 706.

Dermer, C.D., 1986, *Astron. Astrophys.,* **157**, 223.

de Vries, H.W., 1987, in *Molecular Clouds in the Milky Way and External Galaxies*, Reidel (in press).

Dickman, R.L., 1978, *Astrophys. J. Suppl.*, **37**, 407.

Dickman, R.L., 1985, in *Protostars and Planets II*, eds. Black, D.C., & Matthews, M.S., University of Arizona Press, Arizona, p. 150.

Dickman, R.L. & Clemens, D.P., 1983, *Astrophys. J.*, **271**, 143.

Downes, D., Wilson, T.L., Beiging, J. & Wink, J., 1980, *Astron. Astrophys. Suppl.*, **40**, 379.

Drury, L.O'C., 1983, *Rep. Prog. Phys.*, **46**, 973.

Duvert, G., Cernicharo, J. & Baudry, A., 1986, *Astron. Astrophys.,* **164**, 349.

Elmegreen, B.G., 1985, in *Protostars and Planets II* eds. Black, D.C. & Matthews, M.S., University of Arizona Press, Arizona.

Falgarone, E. & Pérault, M., 1987, in *Physical Processes in Interstellar Clouds*, eds. Morfill, G.E. & Scholer, M., Reidel, Dordrecht, Holland, p.59.

Feitzinger, J.V. & Stüwe, J.A., 1986, *Vistas in Astron.*, **29**, 291.

Feitzinger, J.V., & Stüwe, J.A., 1986a, *Astrophys. J.*, **305**, 534.

Fichtel, C.E. & Kniffen, D.A., 1984, *Astron. Astrophys.,* **134**, 13.

Frerking, M.A., Langer, W.D. & Wilson, R.W., 1982, *Astrophys. J.*, **262**, 590.

Fukui, Y. & Hayakawa, S., 1981, *Proc. 17th Int. Cosmic Ray Conf.*, **2**, 226.

Giler, M., Szabelska, B., Wdowczyk, J. & Wolfendale, A.W., 1987, *Proc. 20th Int. Cosmic Ray Conf.*, **2**, 211.

Ginzburg, V.L. & Syrovatskii, S.I., 1964, *The Origin of Cosmic Rays*, New York, Pergamon, p.205.

Grabelsky, D.A., Cohen, R.S., Bronfman, L. & Thaddeus, P., 1987, *Astrophys. J.*, **315**, 122.

Guélin, M. & Cernicharo, J., 1988, in *Molecular Clouds in the Milky Way and External Galaxies*, Reidel (in press).

Guetter, H.M., 1977, *Astron. J.*, **82**, 598.

Hartquist, T. & Morfill, G.E., 1983, *Astrophys. J.*, **266**, 271.

Heiles, C., 1967, *Astrophys. J.*, **149**, 97.

Heiles, C., 1976, *Astrophys. J.*, **204**, 379.

Heiles, C. & Cleary M.N., 1979, *Aust. J. Phys. Astrophys. Suppl.*, **47**, 1.

Heiles, C. & Habing, H.J., 1974, *Astron. Astrophys. Suppl.*, **14**, 1.

Heiles,C. & Kulkarni, S.R., 1987, in *Physical Processes in Interstellar Clouds*, eds. Morfill, G.E. & Scholer, M., Reidel, Dordrecht, Holland, p.13.

Henderson, A.P., Jackson, P.D. & Kerr, F.J., 1982, *Astrophys. J.*, **263**, 116.

Hermsen, W., 1980, *Ph.D. Thesis*, University of Leiden.

Heyer, M.H., 1986, *Ph.D. Thesis*, University of Massachusetts.

Houston, B.P., 1985, *Ph.D. Thesis*, University of Durham.

Houston, B.P. & Wolfendale, A.W., 1983, *Astron. Astrophys.,* **126**, 22.

Houston, B.P. & Wolfendale, A.W., 1984, *J. Phys. G: Nucl. Phys.*, **10**, 1587.

Houston, B.P. & Wolfendale, A.W., 1985, *J. Phys. G: Nucl. Phys.*, **11**, 407.

Issa, M.R., Riley, P.A., Strong, A.W. & Wolfendale, A.W., 1980, *Nature*, **287**, 810.

Issa, M.R. & Wolfendale, A.W., 1981, *Nature*, **292**. 430.

Kulkarni, S.R., 1983, *Ph.D. Thesis*, U.C. Berkeley.

Kulsrud, R.M. & Pearce, W.P., 1969, *Astrophys. J.*, **156**, 445.

Kutner, M.L., 1984, *Fund. Cosmic Phys.*, **9**, 233.

Kutner, M.L. & Leung, C.H., 1985, *Astrophys. J.*, **291**, 188.

Kutner, M.L. & Mead, K.N., 1981, *Astrophys. J. Letters*, **249**, L15.

Kutner, M.L,, Tucker, K.D., Chin, G. & Thaddeus, P., 1977, *Astrophys. J.*, **215**, 521.

Kwan, J. & Sanders, D.B., 1986, *Astrophys. J.*, **309**, 783.

Larson, R.B., 1981, *Mon. Not. R. astr. Soc.*, **194**, 809.

Lebrun, F., 1986, *Astrophys. J.*, **306**, 16.

Lebrun, F. & Huang, Y.-L., 1984, *Astrophys. J.*, **281**, 634.

Leung, C.M., Kutner, M.L. & Mead, K.N., 1982, *Astrophys. J.*, **262**, 583.

Li, T.P. & Wolfendale, A.W., 1981, *Astron. Astrophys.*, **103**, 19.

Li, T.P., Riley, P.A. & Wolfendale, A.W., 1983, *Mon. Not. R. astr. Soc.*, **203**, 87.

Liszt, H.S., Xiang, D. & Burton, W.B., 1981, *Astrophys. J.*, **249**, 532.

Lockman, F.J., 1984, *Astrophys. J.*, **283**, 90.

Longair, M.S., 1981, *High Energy Astrophysics*, Cambridge Univ. Press.

Lynds, B.T., 1962, *Astrophys. J. Suppl.*, **7**, 1.

Lyne, A.G., Manchester, R.N. & Taylor, J.H., 1985, *Mon. Not. R. astr. Soc.*, **213**, 613.

Maddalena, R.J., 1986, *Ph.D. Thesis*, Columbia University.

Maloney, P. & Black, J.H., 1988, *Astrophys. J.*, **325**, 389.

Marscher, A.P. & Brown, R.L., 1978, *Astrophys. J.*, **221**, 558.

Martin, H.M., Sanders, D.B. & Hill, R.E., 1984, *Mon. Not. R. astr. Soc.*, **208**, 35.

Mayer-Hasselwander, H.A., Bennett, K, Bignami, G.F., Buccheri, R., Caraveo, P.A., Hermsen, W., Kanbach, G., Lebrun, F., Lichti, G.G., Masnou, J.L., Paul, J.A., Pinkau, K., Sacco, B., Scarsi, L., Swanenburg, B.N. & Wills, R.D., 1982, *Astrophys. J.*, **105**, 164.

McCray, R.,1987, in *Physical Processes in Interstellar Clouds*, eds. Morfill, G.E. & Scholer, M., Reidel, Dordrecht, Holland, p.95.

McKee, C.F. & Ostriker, C.P., 1977, *Astrophys. J.*, **218**, 148.

Meyer, P., 1981, in *Origin of Cosmic Rays*, eds. Setti, G., Spada, G. & Wolfendale, A.W., Reidel, Dordrecht, Holland, p.7.

Montmerle, T., 1979, *Astrophys. J.*, **231**, 95.

Montmerle, T., 1981, *Phil. Trans. R. Soc. Lond.*, **301**, 505.

Montmerle, T., 1985, *Proc. 19th Int. Cosmic Ray Conf.*, **1**, 209.

Morfill, G.E., 1982, *Astrophys. J.*, **262**, 749.

Morfill, G.E., Forman, M. & Bignami, G., 1984, *Astrophys. J.*, **284**, 856.

Mouschovias, T.CH., in *Physical Processes in Interstellar Clouds*, eds. Morfill, G.E. & Scholer, M., Reidel, Dordrecht, Holland, p.453.

Myers, P.C., 1983, *Astrophys. J.*, **270**, 105.

Myers, P.C. & Benson, P.J., 1986, *Astrophys. J.*, **266**, 309.

Myers, P.C., Dame, T.M., Thaddeus, P., Cohen, R.S., Silverberg, R.F., Dwek, E. & Hauser, M.G., 1986, *Astrophys. J.*, **301**, 398.

Myers, P.C. & Goodman, A.A., 1988a, *Astrophys. J.*, (in press).

Myers, P.C. & Goodman, A.A., 1988b, *Astrophys. J.*, (in press).

Ormes, J.F., 1987, *Proc. 20th Int. Cosmic Ray Conf.*, **1**, 95.

Osborne, J.L., Parkinson, M.L., Richardson, K.M. & Wolfendale, A.W., 1987, in *Physical Processes in Interstellar Clouds*, eds. Morfill, G.E. & Scholer, M., Reidel, Dordrecht, Holland, p.81.

Poon, C.B., 1983, *Ph.D. Thesis*, University of Hong Kong.

Protheroe, R.J., Strong, A.W., Wolfendale, A.W. & Kiraly, P., 1979, *Nature*, 277, 542.

Reynolds, R.J., 1984, *Astrophys. J.*, 282, 191.

Richardson, K.M. & Wolfendale, A.W., 1988, *Astron. Astrophys.*, (in press).

Riley, P.A. & Wolfendale, A.W., 1984, *J. Phys. G: Nucl. Phys.*, 10, 1149.

Rogers, M.J., Sadzinska, M., Szabelski, J., van der Walt, D.J. & Wolfendale, A.W., 1988, *J. Phys. G: Nucl. Phys.*, (in press).

Rogers, M.J. & Wolfendale, A.,W., 1987, *Proc. 20th Int. Cosmic Ray Conf.*, 1, 81.

Sacher, W. & Schonfelder, V., 1984, *Astrophys. J.*, 279, 817.

Sanders, D.B., 1981, *Ph.D. Thesis*, State University of Stony Brook.

Sanders, D.B., Scoville, N.Z. & Solomon, P.M., 1985, *Astrophys. J.*, 289, 373.

Sanders, D.B., Solomon, P.M. & Scoville, N.Z., 1984 (SSS), *Astrophys. J.*, 276, 182.

Savage, B.D., Bohlin, R.C., Drake, J.F. & Budich, W., 1977, *Astrophys. J.*, 216, 291.

Scoville, N.Z., Min Su Yun, Clemens, D.P., Sanders, D.B. & Waller, W.H., 1987, *Astrophys. J. Suppl.*, 63, 821.

Scoville, N.Z. & Solomon, P.M., 1975, *Astrophys. J. Letters*, 199, L105.

Sibson, R.A., 1981, *Interpreting Multivariate Data*, ed. Barnett, A.D., Wiley, New York, ch. 2.

Simpson, G. & Mayer-Hasselwander, H.A., 1987, *Proc. 20th Int. Cosmic Ray Conf.*, 1, 89.

Skilling, J. & Strong, A.W., 1976, *Astron. Astrophys.*, 53, 253.

Solomon, P.M., Rivolo, A.R., Barrett, J.W. & Yahil, A., 1987 (SRBY), *Astrophys. J.*, 319, 730.

Solomon, P.M. & Sanders, D.B., 1980, in *Giant Molecular Clouds in the Galaxy*, eds. Solomon, P.M. & Edmunds, M.G., Pergamon, New York, p.41.

Solomon, P.M. & Sanders, D.B., 1985, in *Protostars and Planets II*, eds. Black, D.C. & Matthews, M.S., University of Arizona Press, Arizona, p.59.

Solomon, P.M., Sanders, D.B. & Scoville, N.Z., 1979a, in *The Large-scale Characteristics of the Galaxy*, ed. Burton, W.B., Reidel, Dordrecht, Holland, p.35.

Solomon, P.M., Sanders, D.B. & Rivolo, A.R., 1985, *Astrophys. J. Letters*, 292, L19.

Solomon, P.M., Scoville, N.Z. & Sanders, D.B., 1979b, *Astrophys. J. Letters*, 232, L89.

Spitzer, L., 1978, *Physical Processes in the Interstellar Medium*, John Wiley & Sons, New York.

Stark, A.A., 1979, *Ph.D. Thesis*, Princeton University.

Stark, A.A., 1987, in *Molecular Clouds in the Milky Way and External Galaxies*, Reidel, (in press).

Stecker, F.W., 1971, *Cosmic Gamma Rays*, Mono Book Corporation, Baltimore, M.D.

Stecker, F.W., 1975, in *Origin of Cosmic Rays*, eds. Osborne, J.L. & Wolfendale, A.W., Reidel, Dordrecht, Holland, p.267.

Stephens, S.A. & Badhwar, G.D., 1981, *Astrophys. and Space Sci.*, 76, 213.

Strong, A.W., 1985a, *Astron. Astrophys.*, 145, 81.

Strong, A.W., 1985b, private communication, cited in Bhat et al. (1986b)

Strong, A.W. & Wolfendale, A.W., 1981, *Phil. Trans. R. Soc. Lond.*, 301, 541.

Strong, A.W., Bignami, G.F., Bloemen, J.B.G.M., Buccheri, R., Caraveo, P.A., Hermsen, W., Kanbach, G., Lebrun, F., Mayer-Hasselwander, H.A., Paul, J.A. & Wills, R.B., 1982, *Astron. Astrophys.*, 115, 404.

Strong, A.W., Bloemen, J.B.G.M., Dame, T.M., Grenier, I.A., Hermsen, W., Lebrun, F., Nyman, L-A., Pollock, A.M.T. & Thaddeus, P., 1987, *Proc. 20th Int. Cosmic Ray Conf.*, 1, 125.

Strong, A.W., Bloemen, J.B.G.M., Lebrun, F., Hermsen, W., Mayer-Hasselwander, H.A. & Buccheri, R., 1987a, *Astron. Astrophys. Suppl.*, 67, 283.

Terndrup, D., 1981, unpublished Thesis, U.C., Berkeley.

Thaddeus, P. & Dame, T.M., 1984, *Occasional Reports of Royal Observatory, Edinburgh*, ed. Wolstencroft, R., 13, p.15.

Ungerechts, H. & Thaddeus, P., 1986, *Astrophys. J. Suppl.*, 63, 3, 645.

van Dishoeck, E.F. & Black, J.H., 1987, in *Physical Processes in Interstellar Clouds*, eds. Morfill, G.E. & Scholer, M., Reidel, Dordrecht, Holland, p.241.

van Hoof, A., 1969, *Bull. Astr. Inst. Netherlands Suppl.*, **3**, 137.

Völk, H.J., 1983a, *Proc. 18th Int. Cosmic Ray Conf.*, **1**, 173.

Völk, H.J., 1983b, *Space Sci. Rev.*, **36**, 3.

Vrba, F.J. & Rydgren, A.E., 1985, *Astron. J.* **90**, 1490.

Wdowczyk, J. & Wolfendale, A.W., 1987, *J. Phys. G: Nucl. Phys.*, **13**, 411.

Wentzel, D.G., 1974, *Ann. Rev. Astron. Astrophys.*, **12**, 71.

Wilkinson, D.A., 1987, *Ph.D. Thesis*, University of Durham.

Williams, D.A., 1985, *Q. J. R. astr. Soc.*, **26**, 463.

Wolfendale, A.W., 1983, *Q. Jl. R. astr. Soc.*, **24** 122.

Wolfendale, A.W., 1984, in *Proc. Advanced Studies Institute on Cosmic Rays*, Erice.

Wolfendale, A.W., 1986, in *Cosmic Radiation in Contemporary Astrophysics*, ed. Shapiro, M.M., Reidel, Dordrecht, Holland, p.135.

Wolfendale, A.W. & van der Walt, D.J., 1988, *Space Sci. Rev.*, (in press).

Wouterloot, J.G.A., 1981, *Ph.D. Thesis*, University of Leiden.

ACKNOWLEDGEMENTS

I am indebted to Professor Arnold Wolfendale for providing the resources and guidance that have made this work possible. His broad insight into every aspect of cosmic ray physics and astrophysics, and the enthusiasm and energy with which he conducts his research constantly inspire his colleagues and students.

Many others in the department and collaborating institutions have offered both their friendship and invaluable advice during my two years at Durham:
Alison Broadbent, Margaret Chipchase, Desmond Evans, Maria Giler, Tadashi Kifune, Peter Kiraly, Mike Lee, Alan Lotts, Iain MacLaren, Chris Mayer, John Osborne, Mike Parkinson, Martin Rogers, Pauline Russell, Maria Sadzinska, Rajiv Shingal, Jacek Szabelski, George Wdowczyk, David Wilkinson, Johan van der Walt and Kevin Yau to name a few. Since I cannot adequately express my gratitude in so short a space, I am content to merely list their names.

The staff of St Mary's College deserve special mention for the kindness and hospitality thay have shown to me and my family.

Thanks also to Dr Tom Dame and colleagues at the Smithsonian Institute for Astrophysics, Dr Leo Blitz and Dr Hans Bloemen for useful discussions.

Finally, to Liz, Tae, Alex, Mum, Doris, Mita and Ron who put up with all the problems and difficulties and are still smiling, I can only say 'IT'S FINISHED, AT LAST'!